

## Broadband wireless LANs : a feasibility study

**Citation for published version (APA):**

Smulders, P. F. M. (1995). *Broadband wireless LANs : a feasibility study*. [Phd Thesis 1 (Research TU/e / Graduation TU/e), Electrical Engineering]. Technische Universiteit Eindhoven. <https://doi.org/10.6100/IR450978>

**DOI:**

[10.6100/IR450978](https://doi.org/10.6100/IR450978)

**Document status and date:**

Published: 01/01/1995

**Document Version:**

Publisher's PDF, also known as Version of Record (includes final page, issue and volume numbers)

**Please check the document version of this publication:**

- A submitted manuscript is the version of the article upon submission and before peer-review. There can be important differences between the submitted version and the official published version of record. People interested in the research are advised to contact the author for the final version of the publication, or visit the DOI to the publisher's website.
- The final author version and the galley proof are versions of the publication after peer review.
- The final published version features the final layout of the paper including the volume, issue and page numbers.

[Link to publication](#)

**General rights**

Copyright and moral rights for the publications made accessible in the public portal are retained by the authors and/or other copyright owners and it is a condition of accessing publications that users recognise and abide by the legal requirements associated with these rights.

- Users may download and print one copy of any publication from the public portal for the purpose of private study or research.
- You may not further distribute the material or use it for any profit-making activity or commercial gain
- You may freely distribute the URL identifying the publication in the public portal.

If the publication is distributed under the terms of Article 25fa of the Dutch Copyright Act, indicated by the "Taverne" license above, please follow below link for the End User Agreement:

[www.tue.nl/taverne](http://www.tue.nl/taverne)

**Take down policy**

If you believe that this document breaches copyright please contact us at:

[openaccess@tue.nl](mailto:openaccess@tue.nl)

providing details and we will investigate your claim.

# Broadband Wireless LANs: A Feasibility Study

PROEFSCHRIFT

ter verkrijging van de graad van doctor aan de  
Technische Universiteit Eindhoven, op gezag  
van de Rector Magnificus, prof.dr. J.H. van Lint,  
voor een commissie aangewezen door het  
College van Dekanen in het openbaar te  
verdedigen op maandag 4 december 1995 om  
16.00 uur

door

Petrus Franciscus Maria Smulders

geboren te Eindhoven

Dit proefschrift is goedgekeurd  
door de promotoren:  
**prof.dr.ir. G. Brussaard**  
en  
**prof.ir. J. de Stigter**

CIP-DATA KONINKLIJKE BIBLIOTHEEK, DEN HAAG

Smulders, Petrus Fransiscus Maria

Broadband wireless LANs : a feasibility study / Petrus  
Fransiscus Maria Smulders. - Eindhoven : Eindhoven  
University of Technology. - Fig., photos, tab.  
Thesis Technische Universiteit Eindhoven. - With ref. -  
With summary in Dutch.

ISBN 90-386-0100-X

NUGI 832

Subject headings: wireless LANs / indoor radio / millimetre wave propagation.

© 1995 by P.F.M. Smulders, Veldhoven

All rights reserved. No part of this publication may be reproduced or transmitted in any form or by any means, electronic, mechanical, including photocopy, recording, or any information storage and retrieval system, without the prior written permission of the author.

**Broadband Wireless LANs:  
A Feasibility Study**



Cover: Stock exchange crash on "Black Monday", Oct. 1987: Reliability and delay-free access should be a key feature with respect to data transfers on a stock exchange where crucial decisions must be taken within parts of seconds. A wireless LAN for such applications should not become congested under peak-traffic conditions.

aan Gerdi, Tessa en Remco

aan mijn ouders

## Abstract

This dissertation treats the potentials and limitations of wireless LANs intended for the support of services as envisioned for Broadband ISDN. The treatment is based on the assumption that the transmission takes place via millimetre-wave indoor radio channels.

A method is discussed for the measurement of the wideband characteristics of millimetre-wave indoor radio channels. Measurements results obtained with this method are presented. These results are used for the development of a statistical model of the millimetre-wave indoor radio channel. In addition, a deterministic channel model is developed based on Geometrical Optics. A discussion concerning the applicability, limitations and accuracy of such a model is included. Results of simulations based on the deterministic model developed are presented. These results give an indication of the influence of the environment and antenna radiation patterns on the channel characteristics.

Using the measurement results, the maximum feasible bit rate is evaluated for millimetre-wave indoor radio transmission assuming QPSK modulation. In addition, the improvement by channel equalization is examined. The evaluation includes the influence of noise, number of equalizer taps, antenna diversity and antenna directivity pattern.

It is shown in which way efficient, reliable and flexible information transfer can be achieved in broadband wireless LANs on the basis of the Asynchronous Transfer Mode. In this context a contention-free multi-access protocol is proposed.

---

# Contents

<b>Abstract</b>	i
<b>Chapter 1 General introduction</b>	1
1.1 Introduction	1
1.2 Use of millimetre-wave frequency bands	2
1.2.1 Availability of required bandwidth	2
1.2.2 Safety aspects	2
1.2.3 Frequency reuse aspects	3
1.2.4 Technology aspects	3
1.2.5 Applications	4
1.3 Use of infra-red	6
1.4 Research activities in Europe	7
1.5 Framework of research activities at EUT	7
1.6 Scope of thesis and survey of contents	7
References in Chapter 1	11
<b>Chapter 2 Digital transmission over millimetre-wave indoor radio channels</b>	15
2.1 Introduction	15
2.2 Representation of linear time-variant multipath channels	16
2.2.1 Relationship between time domain and frequency domain channel description	16
2.2.2 Time domain representation	17
2.2.2.1 Characterization of impulse responses as a deterministic process	17
2.2.2.2 Characterization of impulse responses as a statistical process	18
2.2.2.3 Characterization of individual sample functions	19
2.2.3 Frequency domain representation	21
2.3 Time dependence of millimetre-wave indoor radio channels	23
2.3.1 Fading	23
2.3.2 Effects of movement	23
2.3.3 Effects of displacement	25
2.3.3.1 Scales of displacement	25
2.3.3.2 Small-scale effects	25
2.3.3.3 Large-scale effects	26
2.4 Narrowband transmission	28

---

2.5	Review of diversity techniques	33
2.6	Wideband transmission	37
2.7	Summary and conclusions	39
	References in Chapter 2	41
<b>Chapter 3</b>	<b>Wideband measurements of millimetre-wave indoor radio channels</b>	<b>45</b>
3.1	Introduction	45
3.2	Measurement setup and procedures	49
3.2.1	Measurement setup	49
3.2.2	Calibration procedure	51
3.2.3	Equipment settings	52
3.2.4	Alignment of time axis	53
3.3	Antenna design	53
3.3.1	Desired antenna properties	53
3.3.2	Design procedure	55
3.3.2.1	General approach	55
3.3.2.2	Achievement of the desired elevation dependence of the radiation pattern	56
3.3.2.3	Achievement of the desired azimuth independence of the radiation pattern	61
3.3.2.4	Achievement of the desired polarization state of the radiated field	62
3.3.3	Dimensioning of the biconical-horn antennas	63
3.3.4	Characteristics of the biconical-horn antennas	64
3.3.5	The circular-horn antenna	66
3.4	Description of the indoor environments under consideration	68
3.4.1	Transmissivity properties	70
3.4.2	Reflection properties	70
3.5	Determination of normalized received power and rms delay spread	71
3.6	Measurement results and discussion	74
3.6.1	Results obtained with the 57-59 GHz biconical-horn antennas	75
3.6.1.1	Normalized received power	75
3.6.1.2	Rms delay spread	79
3.6.2	Results obtained with the 41-43 GHz biconical-horn antennas	81
3.6.2.1	Normalized received power	82
3.6.2.2	Rms delay spread	82
3.6.3	Results obtained with the 57-59 GHz circular-horn antenna	84
3.6.3.1	Normalized received power	85
3.6.3.2	Rms delay spread	87

---

3.7 Summary and conclusions	88
References in Chapter 3	90
<b>Chapter 4 Statistical modelling of millimetre-wave indoor radio channels</b>	<b>93</b>
4.1 Introduction	93
4.2 Ray determination for statistical modelling	96
4.3 Distribution of ray phases	96
4.4 Distribution of ray amplitudes	97
4.4.1 Assumptions	97
4.4.2 Average power delay profile	98
4.4.3 Goodness-of-fit test for the ray amplitudes	103
4.5 Distribution of ray interarrival times	105
4.6 Comparison with results obtained at UHF frequencies	110
4.7 Summary and conclusions	110
References in Chapter 4	112
<b>Chapter 5 Deterministic modelling of millimetre-wave indoor radio channels</b>	<b>115</b>
5.1 Introduction	115
5.2 Considerations concerning the model choice	116
5.2.1 Determination of reflection coefficients	117
5.2.2 Significance of diffraction	122
5.3 Simulation of millimetre-wave indoor radio channels	126
5.3.1 Geometric optical ray tracing	127
5.3.2 Coordinate system	130
5.3.3 Determination of field vectors	130
5.3.4 Determination of ray parameters	132
5.4 Implementation of antenna directivity functions	134
5.4.1 Sectorial-horn antennas	134
5.4.2 Biconical-horn antennas	138
5.5 Simulation results and discussion	139
5.5.1 Comparison of simulation results with measurement results	139
5.5.2 Additional simulations	142
5.5.2.1 Simulated configurations	142
5.5.2.2 Simulation results and discussion	144
5.6 Summary and conclusions	151
References in Chapter 5	153

<b>Chapter 6 Performance of millimetre-wave indoor radio transmission</b>	155
6.1 Introduction	155
6.2 Performance of QPSK	156
6.3 Calculation results and discussion with respect to QPSK	160
6.3.1 Parameters under consideration	160
6.3.2 Comparison of lower and upper Milewski bounds	160
6.3.3 Influence of timing algorithm	162
6.3.4 Influence of probability of bit error threshold	163
6.3.5 Influence of SNR	165
6.3.6 Influence of measurement configuration	167
6.3.7 Influence of external diversity	168
6.4 Performance of QPSK/DFE	168
6.5 Calculation results and discussion with respect to QPSK/DFE	173
6.5.1 Parameters under consideration	173
6.5.2 Influence of timing algorithm	174
6.5.3 Influence of SNR	174
6.5.4 Influence of number of forward taps	175
6.5.5 Influence of number of backward taps	178
6.5.6 Influence of measurement configuration	178
6.5.7 Influence of external diversity	178
6.6 Implementation aspects	179
6.6.1 Adaption of equalizer coefficients	179
6.6.2 Achievement of fast convergence	181
6.6.3 Achievement of low complexity	182
6.6.4 Achievement of accurate tracking	183
6.6.5 Adaptive lattice filtering	183
6.6.6 Achievement of accurate carrier recovery	184
6.6.7 Achievement of accurate clock recovery	185
6.6.8 Fractional tap spaced equalization	185
6.6.9 Off-line processing	186
6.7 Summary and conclusions	187
References in Chapter 6	190
<b>Chapter 7 Application of the Asynchronous Transfer Mode in indoor wireless LANs</b>	195
7.1 Introduction	195
7.2 Basic network concepts	198
7.2.1 Evolution of system concepts	198
7.2.2 ATM concept	199

---

7.2.2.1	Protocol reference model	199
7.2.2.2	Physical layer	200
7.2.2.3	ATM layer	200
7.2.2.4	ATM adaptation layer	201
7.2.3	Mapping of protocol data units	202
7.2.4	B-ISDN Reference points	203
7.3	Wireless LAN concepts based on ATM	204
7.3.1	Distributed B-NT2	204
7.3.2	Duplexing methods	205
7.3.3	Error control	208
7.3.4	Feasibility of reliable ATM-cell transmission	211
7.4	Medium-Access Control	217
7.4.1	General concept	217
7.4.2	Requests	218
7.4.3	Permits	219
7.4.4	Capacity allocation algorithm	220
7.4.5	Robustness of the protocol	223
7.4.6	Initiation of equalizer tap coefficients	223
7.5	Summary and conclusions	223
	References in Chapter 7	225
<b>Chapter 8</b>	<b>Summary and conclusions</b>	<b>229</b>
	<b>List of acronyms</b>	<b>233</b>
	<b>Korte samenvatting</b>	<b>237</b>
	<b>Epilogue</b>	<b>239</b>
	<b>List of scientific publications</b>	<b>241</b>
	<b>Account of scientific results</b>	<b>245</b>
	<b>Acknowledgements</b>	<b>247</b>
	<b>Curriculum Vitae</b>	<b>249</b>



## CHAPTER 1

### GENERAL INTRODUCTION

#### 1.1 Introduction

Today's telecommunication networks are passing through a rapid evolution as a result of the ever continuing advances in enabling technologies and the new demands on telecommunication services. In addition to the development of fibre-based networks, this evolution is characterized by two major trends; *service integration* and *radio networking*.

An important result of *service integration* is the advent of the Integrated Services Digital Network (ISDN). The main feature of the ISDN concept is the support of a wide range of voice and non-voice applications in the same network. A connection to the ISDN allows the user to have at his disposal different services such as voice, data or picture communication services from the same access point. All types of signals are transmitted in digital form from terminal to terminal across the network. To provide new attractive services like digital TV, digital HDTV, high quality videophone, high speed data transfer and video on demand, a further step to a broadband network (B-ISDN) is necessary and under discussion.

The developments in *radio networking* are spurred by the need for mobility and flexibility. The systems that are currently under development are based on digital

technology and can be gathered into two broad classes: cordless systems and cellular networks. Cordless systems are suitable for customers with limited mobility within short ranges from the base stations and with limits on roaming and mobile terminal speed. Cellular networks meet the demand of high mobility, whereas the set of services that can be provided is relatively limited.

A combination of these two trends, i.e., the provision of real broadband services to the mobile user seems to be a logical step. However, to date, developments in the field of radio-based broadband networks are still in a stage of preliminary research. One possible reason might be a lack of interplay between the two entirely different disciplines. A second reason is a technical one: In radio-based networks the spectral space available for information transport is a scarce resource, so that even with a carefully designed frequency plan the user capacity is limited. The pan-European digital cellular network GSM (Global System for Mobile communications), for instance, features 124 bi-directional 271 kbit/s TDMA data streams, thus providing an aggregate user capacity of 34 Mbit/s per coverage cell. This capacity must be shared among 992 simultaneous users. In contrast, the information transport capacity of fibre-based networks is an abundant resource so that the B-ISDN basic user interface could be standardized on 155 Mbit/s. Thus, about five times the total transmission capacity of a GSM coverage cell would be necessary to serve only one B-ISDN subscriber!

## **1.2 Use of millimetre-wave frequency bands**

### **1.2.1 Availability of required bandwidth**

From the above, it occurs that the conventional frequency bands for mobile communications, lying around 900 MHz and 1800 MHz, are not suitable for mobile broadband applications since broadband systems with an aggregate network capacity of hundreds of Mbit/s will require on the order of hundreds of MHz spectral space. Uncongested bandwidths of this order are only available at radio frequencies above about 25 GHz.

### **1.2.2 Safety aspects**

For many European countries, the general public exposure limits to radiofrequency electromagnetic fields are laid down in the Recommendations of the International Non-Ionizing Radiation Committee, a working group of the International Radiation Protection Association (IRPA/INIRC) [1]. The maximum power density for continuous exposure for

the general public is  $1 \text{ mW/cm}^2$  for millimetre (mm) waves<sup>1</sup>. Assumed that this limit is set at 6 cm of an antenna with 9 dBi (dB referred to isotropic) directivity of its radiation pattern, the transmitted power is limited to about 50 mW at the remote stations.

### 1.2.3 Frequency reuse aspects

Limiting transmitter power levels to some tens of mW is not only a safety requirement, but it is also a measure to limit the coverage range in order to improve the frequency reuse capabilities, with the final goal again to gain network capacity. With respect to indoor applications, high traffic density can be achieved by using frequency bands above approximately 40 GHz due to the possibility of frequency reuse between neighbouring rooms because of the severe attenuation of electromagnetic waves at these frequencies by most inner walls. With respect to frequency reuse in outdoor cells, the band around 60 GHz is especially advantageous because of the specific attenuation characteristic due to atmospheric oxygen of about 15 dB/km. The 60 GHz band is also of special interest for indoor systems since radio energy in the mm-wave range might still go through windows with the potential to interfere with neighbouring outdoor cells and other indoor systems operating in neighbouring buildings. It has been shown that a considerable performance enhancement is obtained by using the 60 GHz oxygen absorption band [2].

### 1.2.4 Technology aspects

The safety limit of 50 mW transmitted power is about the power level that is feasible with state-of-the-art technology [3]. A preliminary feasibility study reported in [4] shows that this 50 mW might be sufficient for reliable broadband communication in a typical office environment. This may be realizable by taking advantage of advances in Very High Speed Integrated Circuit (VHSIC) technology and analog Micro-wave and Millimetre-wave Monolithic ICs (M<sup>3</sup>ICs), which will supply the signals to the VHSIC-chips at a rate that is compatible with the high processing speeds. The maturity of these technologies has already been demonstrated, although the initial costs of producing such systems can be quite high. However, with large-volume manufacturing of individual circuit functions, the costs can be competitive when compared with installing new copper or fibre networks [5]-[8].

---

<sup>1</sup> For comparison: the exposure limits for 900 MHz and 1800 MHz are  $0.45 \text{ mW/cm}^2$  and  $0.9 \text{ mW/cm}^2$ , respectively.

At first sight, low-power transmission at mm-wave frequencies enables improved portability of hand-held equipment since power transmission at a low level implies light and small-sized batteries whereas the use of mm waves enables the use of small radio-frequency components and antennas with dimensions in the order of only a few centimetres. However, it is important to realize that radio receivers for high bit rate signals have to perform complex signal processing in order to combat radio channel imperfections and in order to meet the performance requirements for B-ISDN services. These requirements are much more stringent than requirements for "ordinary" low speed data and coded speech as supported by the present radio networks. Although the intensive signal processing may be performed by sophisticated VHSIC technology we might expect that the complexity required will contribute significantly to the size and weight of initial broadband radio equipment. To get around these difficulties, the scope of our work is limited to systems in which the remote stations are portable but not mobile. This means that they are fixed during operation. Commonly used terms for such a system are *radio Local Area Network (radio LAN, RLAN)*, *cableless (or cordless) LAN (CLAN)* or *wireless LAN (WLAN)*. We will use the term *broadband wireless LAN* throughout this thesis for a system that supports services with rates in excess of 10 Mbit/s for a single user.

### 1.2.5 Applications

Now let us consider the application field of broadband wireless systems. Many applications are envisaged in numerous publications [9]-[15].

In general, wireless networks greatly ease the work required to install a system. Wireless networks can be installed rapidly, often by users themselves whereas installation and rewiring of cable-based networks typically consume one to five months from initial planning to actual installation [9]. The latter is due to the time consuming process that entails providing precise specifications, selecting a reliable contractor, negotiating with building owners, managing the project and waiting for a convenient time -usually at night or in the weekend- during which to install the cabling. Annually, approximately 30 per cent of local networks must be relocated or rearranged in that way. Sometimes, wireless applications are even unavoidable, for instance in case local regulations prohibit cabling in historic buildings or in those buildings that have significant amounts of asbestos in the walls and ceilings, or between sealed areas in nuclear power plants. In addition, wireless technology is an ideal way to address *temporary* network needs or highly *flexible* connectivity.

More specific applications for *broadband* wireless systems can easily be imagined. Many probable uses can be found in environments such as ship-yards, air bases, in- and outdoor factory sites, railway stations, sport arena's, hospitals, magazines, vehicle

guidance/traffic control and in security and surveillance with video cameras linked to control centres by mm-wave radio links. Further applications can be found in the military field where fast and efficient operations in the open field must be coordinated, demanding reliable high capacity and flexible means of communication. In the medical field, video communication between ambulances and medical specialists in the hospital might contribute to efficient emergency handling. Another application is a network of wireless cameras, within studios but also outdoors, for flexible (HD)TV recording. Such networks are also useful for flexible live reporting; in distant areas only the base station needs to have a satellite connection with a dish antenna critically pointed towards the satellite, whereas the wireless cameras are equipped with omnidirectional antennas thus allowing much more flexible handling. With respect to the domestic market the M<sup>3</sup>VDS (Millimetre-wave Multichannel Multipoint Video Distribution Service) concept will become viable [10]. In this concept, TV signals from satellite, UHF etc. are gathered at a head-end before being retransmitted from some suitable high point/building. The multichannel signal is then received by a small, unobtrusive, receiver/downconverter mounted on each viewer's home.

Interesting market opportunities can also be envisaged in the introductory phase of B-ISDN; in the beginning of the B-ISDN era, not every company will have installed a fibre-based network for which B-ISDN is actually meant and many company managers will be reluctant to make the expensive switch to a fibre-based B-ISDN. For such companies it would be a good thing to have a trial with a leased, easy-to-install broadband network on a limited scale and with interworking facilities with their "good-old" twisted pair ethernet, for instance, in order to discover the relative merits and unique features offered by B-ISDN at their own premises. Wireless broadband networks can also be used at the edges of the backbone B-ISDN where "fibre-to-the-home" is not yet realized.

It is important to note, that a large user capacity does not only provide the opportunity to run bandwidth-hungry services such as videophone, but it can also be used to achieve highly reliable and secure communication (by additional channel coding). It can also be used to achieve immediate access (by creating congestion-free networks). Reliability and security are of prime concern for instance for the exchange of financial data as with Electronic Funds Transfer at Point of Sale (EFTPOS) providing direct debit of bank accounts at purchase or direct credit transfer if agreed by one's bank via mm-wave radio links between bank and supermarkets and stores. For such applications, point-to-point or point-to-multipoint mm-wave radio can be very cost effective when compared with leased circuits, especially when the rental charge for a leased circuit is considered over a period of several years [11].

In addition to reliability and security, delay-free access is a key feature with respect to data transfers on a stock exchange where crucial decisions must be taken within parts of seconds. The network for such applications should not become congested under

peak-traffic conditions as encountered at the time of an exchange crash for instance. They also may not be vulnerable to deliberate interference.

With respect to small remote stations like laptops, a significant amount of disk space can be saved by transferring software from a LAN each time it is actually needed and only keeping it in disk space for a limited time. Physically connecting or disconnecting a laptop to a LAN, however, can be inconvenient. A solution of this problem might be a reliable high-speed flexible wireless interface.

For the more distant future, it can be foreseen that cells with high traffic density will be created in both indoor and outdoor areas, which might ultimately lead to an infrastructure on a world scale supporting mass use of portable video phone in both the business and the public area.

### 1.3 Use of infra-red

So far, we have discussed the use of mm-wave frequency bands for broadband applications. As an alternative for millimetre waves, the use of the infra-red spectrum can be considered. Infra-red has an abundance of bandwidth, and infra-red components are small and inexpensive. As with millimetre waves, infra-red penetrates glass, but not walls, allowing neighbouring cells to co-exist without interference. However, an essential drawback, when compared with the use of the mm-wave bands, is the relatively high level of transmit power (i.e., in the order of watts) required for acceptable performance. This is because the levels of noise and interference due to common ambient light sources are relatively high. On the other hand, stringent power limitations on infra-red transmitters are imposed by safety considerations. These safety considerations are dictated by eye safety. The human eye focuses the energy density of light incident on the retina by factors of 100,000 or more. Therefore, the Maximum Possible Exposure (MPE) levels are quite small. The cornea, the outer layer of the eye, filters out all wavelength except those in the visible and near infra-red range. The eye thus forms a window for infra-red light whereas reflections which normally appear as a response to fluctuating levels of visual light are absent. In the medical professional world it is commonly agreed that continuous exposure to extraordinary high levels may damage the eye leading to cataract-like disorders. Various governmental, nongovernmental and standards organizations worldwide have therefore specified MPE levels for infra-red [16]-[18]. They are nearly in consensus. The power limits on infra-red transmitters imposed by safety considerations eliminate the possibility to use infra-red for reliable broadband communications in cells with radii in excess of about a few metres [19]. Therefore, the use of infra-red can be ruled out for our applications. In what follows, we shall therefore consider the use of the mm-wave bands only.

## 1.4 Research activities in Europe

In Europe, research activities in the field of mm-wave radio communication have been carried out in the European Community research programs COST (European COoperation in the field of Scientific and Technical research) within Working Group 3 of the COST 231 project, DRIVE (Dedicated Road Infrastructure for Vehicle safety in Europe) and RACE (Research into Advanced Communications Europe) within project 2067 (Mobile Broadband Systems). In ACTS (Advanced Communications Technologies and Services), the follow up of RACE, emphasis is put on demonstration of broadband wireless LAN system concepts and field trials. Harmonisation of the mm-wave spectrum is carried out by the ERC (European Radiocommunication Committee) whereas the harmonization of mm-wave radio equipment specifications are being formulated by ETSI (European Telecommunications Standards Institute) within committee TM4 (Transmission-radio). ETSI is open to manufacturers, user groups, administrations and research bodies.

## 1.5 Framework of research activities at EUT

Since 1990 the research programme of the Telecommunications Division of EUT (Eindhoven University of Technology) includes a project in which various mm-wave radio items are studied. With this project EUT actively participates in Working Group 3 of COST 231 in which the use of mm-wave frequency bands is investigated. This investigation is directed towards the generation of propagation models for small coverage cells with cross section dimensions of a few hundreds metres at maximum, and towards the development of high capacity transmission methods. Besides the Netherlands, universities and PTT's from Finland, France, Germany, Greece, Norway, Spain, Sweden, Portugal and United Kingdom are actively involved in this field. There is also cooperation and exchange of results with national institutes, i.e., Dutch PTT, DUT (Delft University of Technology), TNO (Applied Physical Research) and Philips Research.

## 1.6 Scope of thesis and survey of contents

This thesis reflects the output of the research activities in the field of indoor mm-wave radio channel modelling and networking carried out at EUT by the author during the period 1990 - 1995. Numerous graduate students have worked in this area resulting in substantial contributions to the final output [20]-[31]. This thesis is intended as a contribution to the development of wireless LANs for broadband communications. It is not intended to advocate the use of specific transmission techniques, but the results may assist

in weighing design options as antenna use, channel equalizer complexity, application of external diversity and choice of transfer mode.

It was decided to restrict the research topics to *indoor* applications in order to limit the scope of the project to reasonable proportions. However, it should be noted that the output of the project may also be useful to outdoor applications.

The research plan carried out included *channel*, *transmission* and *network* aspects which can be summarized as follows:

- Design of an equipment setup for the measurement of broadband propagation characteristics of mm-wave indoor radio *channels*.
- Design of antennas for application in the measurement setup and evaluation of the characteristics of manufactured prototypes afterwards.
- Application of the measurement setup to measure the mm-wave channel characteristics of a sufficient number of indoor radio channels to allow statistically significant conclusions.
- Development of software tools for the simulation of broadband propagation characteristics of mm-wave indoor radio channels.
- Application of these software tools to assess the influence of environment (configuration, wall reflectivity, antenna radiation patterns, etc.) on the characteristics of the mm-wave indoor radio channel.
  
- Development of mathematical tools and models that enable the calculation of the obtainable performance of mm-wave indoor radio *transmission*.
- Application of these tools and models to analyze the sensitivity of transmission performance to transmitted signal, channel and receiver parameters.
  
- Determination of an information transfer method tailored to handle broadband information traffic in a wireless LAN. This topic includes items as transfer mode, duplex method, error control and multi-access control.

These topics are covered by the various chapters as follows:

## **Chapter 2: Digital transmission over millimetre-wave indoor radio channels**

The first part of Chapter 2 treats the propagation characteristics expected to occur in a typical reflective indoor environment. Next, digital transmission over mm-wave channels is discussed, including some performance improvement methods and the suitability of some figures-of-merit that are commonly used to quantify transmission performance.



Furthermore, the parameters and terms which are used throughout this thesis are defined.

### **Chapter 3: Wideband measurements of millimetre-wave indoor radio channels**

Chapter 3 describes the wideband mm-wave channel measurements carried out in eight different indoor areas in various buildings at the EUT. In the first part, the measurement method is discussed, including equipment setup, calibration procedure and equipment settings for acceptable time-domain resolution and dynamic range. In addition, the design of the antennas to be applied in the measurement setup is treated and the measured characteristics of manufactured prototypes are evaluated. Finally, the measurement results are presented in terms of the channel parameters defined in Chapter 2.

### **Chapter 4: Statistical modelling of millimetre-wave indoor radio channels**

In Chapter 4, a statistical model of the mm-wave indoor radio channel is developed on the basis of measurement results as well as physical reasoning.

### **Chapter 5: Deterministic modelling of millimetre-wave indoor radio channels**

Chapter 5 treats the deterministic modelling of mm-wave indoor radio channels. The first part of Chapter 5 contains a discussion and description of the principles on which the modelling is based. Results are given indicating the influence of the environment and antenna radiation patterns on the channel characteristics.

### **Chapter 6: Performance of millimetre-wave indoor radio transmission**

Chapter 6 contains a performance evaluation of mm-wave indoor radio transmission. The performance is evaluated for transmission with/without antenna diversity and with/without the application of a Decision Feedback Equalizer (DFE) with a finite number of taps. In addition, implementation issues (clock and carrier recovery, tracking, convergence properties) of the most promising adaption algorithms for DFE's are discussed.

### **Chapter 7: Application of the Asynchronous Transfer Mode in indoor wireless LANs**

In the first part of Chapter 7, the physical configuration of the network is discussed and functions are identified and positioned in a suitable protocol reference model. In addition the transfer mode applied in B-ISDN is outlined and its suitability for wireless LANs is discussed. In the second part, the duplex method to be applied is determined and the application of error control is discussed. Finally, a contention-free multi-access protocol

is proposed for reliable and flexible information transfer in broadband wireless LANs.

### **Chapter 8: Summary and conclusions**

Finally, in Chapter 8, the main results of this dissertation are summarized and conclusions are drawn.

---

**References in Chapter 1**

- [1] INIRC, "Guidelines on limits of exposure to radiofrequency electromagnetic field in the frequency range 100 kHz to 300 GHz", *Health Phys.*, Vol. 54, pp. 115, 1988.
- [2] R. Prasad and B.C. van Lieshout, "Cochannel interference probability for micro- and picocellular systems at 60 GHz", *Electronic Letters*, Vol. 29, No. 22, pp. 1909-1910, 1993.
- [3] M. Muraguchi et al., "26 GHz-Band Full MMIC Transmitters and Receivers", *IEEE MTT-S Intern. Microwave Symp.*, pp. 873-876, 1990.
- [4] P.F.M. Smulders, "Feasibility considerations of broadband indoor radio networks", *Proc. IX Intern. Symp. on Subscriber Loops and Services*, Amsterdam, pp. 76-80, April 1991.
- [5] P.G. Wilson and J.H. Palmer, "Design of millimetre wave monolithic balanced diode mixer", *Colloquium on Microwave devices, fundamentals and applications*, *IEE Digest No. 43*, March 1988.
- [6] P.G. Wilson and I.G. Gosling, "Low-cost downconverter for UK demonstration of TV distribution by millimetre waves", *18th Eur. Microwave Conf.*, Sept 1988.
- [7] M. Pilgrim, R.D. Carver and B.C. Barnes, "M<sup>3</sup>VDS - 40 GHz multichannel TV delivery to the home", *20th Eur. Microwave Conf.*, Sept. 1990.
- [8] T.E. O'Ciardha, "40 GHz low noise amplifier", *Colloquium on Radiocommunications in the range 30-60 GHz*, *IEE Digest*, No 1991/012, Jan. 1991.
- [9] C. Hallinan, "Cableless LANs: The Network of the Future?", *Telecommunications.*, Vol. 25, No. 6, pp. 51-53, June 1991.
- [10] M. Pilgrim, R.P. Searle and R.P.I. Scott, "M<sup>3</sup>VDS - The cheapest, quickest and least obtrusive means of providing multichannel domestic TV?", *Proc. IEE Intern. Broadcasting Convention 1988*, pp. 284-288, Sept. 1988.
- [11] P.W. Hawkins, "The millimetric opportunity - how real is the hype?", *Proc. Intern. Conf. on Commun. '91*, pp. 1196-1200, 1991.

- 
- [12] M.J. Mehler, "Planning local access millimeter wave systems", Proc. Intern. Conf. on Commun. '91, pp. 1191-1195, 1991.
- [13] D. Postlethwaite, "Wireless office systems", Commun. Intern., Vol. 18, No. 2, pp. 37-42, 1991.
- [14] A.H. Aghvami, I.D. Robertson, S.A. Mohamed, "High bit-rate indoor radio communications", Proc. 3rd IEE Conf. on Telecomm. pp.101-106, March 1991.
- [15] R.D. Carver, "Millimetre-wave radio for broadband local access". Proc. Intern. Conf. on Commun. '91, pp. 1187-1190, 1991.
- [16] D.H. Sliney, "Deriving Exposure Limits, Laser Safety, Eyesafe Laser Systems, and Laser Eye Protection", Proc. SPIE, Vol. 1,207, pp. 2-13, Jan. 1990.
- [17] "Threshold Limit Values and Biological Exposure Indices for 1988-1989", ACGIH, Cincinnati, OH, 1988.
- [18] "American National Standard for the Safe Use of Lasers", ANSI Z136.1, ANSI, 1986.
- [19] J.R. Barry, J.M. Kahn, Edward A. Lee and D.G. Messerschmitt, "High Speed Nondirective Optical Communication for Wireless Networks", IEEE Netw. Mag. 1991.
- [20] M.A.A. Melters, "Simulation of an indoor radio channel at mm-wave frequencies", EUT M.Sc.E.E. thesis, Telecommunications Division, EUT, Aug. 1990.
- [21] R. Sonnemans, "ATM in an indoor radio network; a feasibility study", M.Sc.E.E. Thesis, Telecommunications Division, EUT, Aug. 1990.
- [22] A.G. Wagemans, "Measurements and Statistical Modelling of Indoor Radio Channels in the mm-Wave Frequency Band PART 1", M.Sc.E.E. Thesis, Telecommunications Division, EUT, Febr. 1992.
- [23] A.G. Wagemans, "Measurements and Statistical Modelling of Indoor Radio Channels in the mm-Wave Frequency Band PART 2: Additional Figures", M.Sc.E.E. Thesis, Telecommunications Division, EUT, Febr. 1992.

- 
- [24] P.J. Hendriks, "On the performance of adaptive equalization in indoor radio networks", M.Sc.E.E. Thesis, Telecommunications Division, EUT, July 1991.
  - [25] R.B. Maessen, "The use of ATM in an inhouse radio network", M.Sc.E.E. Thesis, Telecommunications Division, EUT, June 1992.
  - [26] H.T. Müskens, Performance Evaluation of a DFE/QPSK Modem for Indoor Radio Applications at 60 GHz, M.Sc.E.E. Thesis, Telecommunications Division, EUT, Aug. 1992.
  - [27] G.J.A.P. Vervuurt, "Modelling and Simulation of Indoor Radio Channels in the mm-Wave Frequency Band", M.Sc.E.E. Thesis, Telecommunications Division, EUT, Jan. 1993.
  - [28] E.W.A.M. Ruis, "An Object-Oriented Programming approach to the modelling of mm-wave Indoor Radio Channels", M.Sc.E.E. Thesis, Telecommunications Division, EUT, Febr. 1994.
  - [29] E.W.A.M. Ruis, "An Object-Oriented Programming approach to the modelling of mm-wave Indoor Radio Channels, Part 2", M.Sc.E.E. Thesis, Telecommunications Division, EUT, Febr. 1994.
  - [30] Ch. J. Grolleman, "Simulation of a MAC Protocol for Indoor Wireless ATM-Based Network", M.Sc.E.E. Thesis, Telecommunications Division, EUT, Aug. 1994.
  - [31] A.C.J. van Workum, "Performance of DS-CDMA over millimetre wave indoor radio channels", M.Sc.E.E. Thesis, Telecommunications Division, EUT, Dec. 1994.

## CHAPTER 2

# DIGITAL TRANSMISSION OVER MILLIMETRE-WAVE INDOOR RADIO CHANNELS

### 2.1 Introduction

This chapter treats the basic elements of electromagnetic propagation that are relevant to the problem of narrowband and wideband transmission over mm-wave indoor radio channels. This treatment shows to what extent propagation effects in an indoor environment might influence the performance of high-capacity indoor wireless systems and it demonstrates the effectiveness of performance-improving measures for such systems. Furthermore, the parameters and terms that are used throughout this thesis are defined.

The treatment is based on the assumption that mm-wave propagation takes place between a transmission point and a reception point over a number of separate ray paths, simultaneously, where a *ray path* is a path along which electromagnetic energy propagates. This phenomenon is commonly denoted as *multipath propagation* [1]. A channel that is determined by multipath propagation is generally denoted as *multipath channel*. We further assume that for the environments and frequency bands under consideration the ray-optical approach is valid and that there is a limited number of individual rays. This implies that, when a pulse is transmitted, the received signal appears as a train of identically shaped pulses.

The assumption that a mm-wave indoor radio channel is essentially a multipath channel and that the channel response on a pulse consists of a train of a finite number of replicas is confirmed by measurement results (see Section 3.5) as well as considerations concerning the influence of typical indoor environment configurations on mm-wave propagation. (see Section 5.2).

The organization of this chapter is as follows: first, in Section 2.2, the representation of a linear time-variant band-limited channel and its response to a bandpass signal is treated in both time- and frequency domain. In Section 2.3, the underlying mechanisms of the multipath effects are clarified and the significance of time-variability for the mm-wave indoor radio channel is evaluated. Section 2.4 contains a treatment of narrowband transmission over multipath channels. Section 2.5 gives a review of diversity techniques and shows the improvement of communication performance that can be obtained by using such techniques. Section 2.6 evaluates the structure of the optimum receiver for processing a wideband signal. Furthermore, the favourable effect of the inherent diversity associated with this technique is demonstrated. Conclusions are summarized in Section 2.7.

## 2.2 Representation of linear time-variant multipath channels

### 2.2.1 Relationship between time domain and frequency domain channel description

The channel considered is actually a bandpass filter centred around frequency  $f_c$ . This central frequency will be taken equal to the carrier frequency throughout this thesis. The channel can be characterized in the time domain by its real impulse response  $v(\tau;t)$  at time  $t$  due to an impulse applied at time  $t-\tau$  or by its transfer function  $V(f;t)$ , i.e., the Fourier transform of  $v(\tau;t)$  with respect to  $\tau$ . The fact that  $v(\tau;t)$  is real implies that

$$V^*(-ft) = V(f;t) \quad . \quad (2.1)$$

If we define  $H(f-f_c;t)$  as

$$H(f-f_c;t) = \begin{cases} V(f;t) & f > 0 \\ 0 & f < 0 \end{cases} \quad , \quad (2.2)$$

then

$$V(f;t) = H(f-f_c;t) + H^*(-f-f_c;t) \quad . \quad (2.3)$$

Inverse Fourier Transformation of (2.3) yields

$$v(\tau;t) = h(\tau;t)e^{j2\pi f_c\tau} + h^*(\tau;t)e^{-j2\pi f_c\tau} = 2\text{Re}\{h(\tau;t)e^{j2\pi f_c\tau}\} \quad , \quad (2.4)$$

in which  $h(\tau;t)$  denotes the Inverse Fourier Transform of  $H(f;t)$  and is called the *complex equivalent lowpass impulse response*. This definition will be used throughout this thesis.

## 2.2.2 Time domain representation

### 2.2.2.1 Characterization of impulse responses as a deterministic process

Assume that we transmit a short modulated pulse  $s(\tau)$  over a multipath channel. This pulse can be formulated as

$$s(\tau) = \text{Re}\{u(\tau)e^{j2\pi f_c\tau}\} \quad , \quad (2.5)$$

in which  $u(\tau)$  represents the *complex equivalent lowpass transmitted pulse* which can in turn be written as

$$u(\tau) = b(\tau)e^{j\theta(\tau)} \quad , \quad (2.6)$$

in case  $b(\tau)$ , the real envelope of  $s(\tau)$ , varies slowly relative to the rapid variations exhibited by the carrier.

As already stated, the received signal is assumed to appear as a train of identically shaped pulses. According to this assumption, the complex equivalent lowpass received signal  $r(\tau;t)$  can be formulated as

$$r(\tau;t) = \sum_n \beta_n(t)e^{j\theta_n(t)}b(\tau-\tau_n(t)) \quad , \quad (2.7)$$

where  $\beta_n(t)$ ,  $\theta_n(t)$  and  $\tau_n(t)$  are the amplitude, phase and excess delay for the  $n$ th received pulse, respectively. Note, that  $\tau$  represents excess delay whereas the  $t$  dependence represents the changes with time of the very structure of the impulse response. From (2.7) it is evident that the complex equivalent lowpass impulse response  $h(\tau,t)$  is<sup>1</sup>

---

<sup>1</sup> It is implicitly assumed that the response of each individual ray is non-dispersive.



$$h(\tau;t) = \sum_n \beta_n(t) e^{j\theta_n(t)} \delta(\tau - \tau_n(t)) \quad , \quad (2.8)$$

with  $\delta(\cdot)$  denoting the Dirac Delta function. This is proved by convolving  $h(\tau;t)$  and  $b(\tau)$  yielding  $r(\tau;t)$ . From propagation point of view, each pulse may be considered to be the result of a ray following a certain path from the transmit antenna through the environment to the receive antenna. Furthermore, each ray is weighed by the antenna gain functions<sup>2</sup>. This means that  $\{\beta_n\}$ ,  $\{\theta_n\}$  and  $\{\tau_n\}$  are completely determined at time  $t$  by the (in general changing) environment and the position of the transceivers within that environment and by the antenna gain functions of the antennas applied. Relating  $r(\tau;t)$  and  $h(\tau;t)$  to the environment configuration and the antenna gain functions in such a deterministic way leads to a deterministic model of  $r(\tau;t)$  and  $h(\tau;t)$ , respectively.

### 2.2.2.2. Characterization of impulse responses as a statistical process

In addition to deterministic modelling, the processes  $r(\tau;t)$  and  $h(\tau;t)$  can also be considered as stochastic processes with limited reference to the causal relationship between the environment characteristics and these responses. In the following, we formulate a number of correlation functions that can be used to describe the multipath channel statistically.

In general, the autocorrelation function of  $h(\tau;t)$  for the excess delay time instants  $\tau_1$  and  $\tau_2$ , and the time instants  $t_1$  and  $t_2$  can be defined<sup>3</sup> as

$$\Phi_h(\tau_1, \tau_2; t_1, t_2) = E\{h^*(\tau_1; t_1) h(\tau_2; t_2)\} \quad , \quad (2.9)$$

where  $E\{\cdot\}$  denotes mathematical expectation.

---

<sup>2</sup> The fact that a channel is characterized in terms of impulse response (or transfer function) implies that it is considered as a two port. In order to define a radio channel as a two port in an unambiguous way, however, the antennas should be considered as being part of the channel. Hence; their antenna gain functions (which include radiation patterns and antenna losses) influence the channel characteristics.

<sup>3</sup> In the definition of the autocorrelation function of a complex valued stochastic process it is common practice to incorporate a normalization factor of  $1/2$ . This is an arbitrary but mathematically convenient normalization factor in advanced treatments of such processes as demonstrated in [3]. However, this factor is useless for our purposes so that we will omit it in our definition.

In order to achieve a convenient statistical description certain assumptions have to be made on forehand. A realistic assumption, which considerably facilitates the statistical description of the process  $h(\tau;t)$ , is the assumption that  $h(\tau;t)$  is a *wide-sense-stationary* process with respect to the  $t$  variable. This means that 1) the mathematical expectation with respect to  $t$  is a constant and 2) the autocorrelation function does not depend on the actual values of the time instants  $t_1$  and  $t_2$  but only on the difference  $t_1 - t_2 = \Delta t$ . In that case, the autocorrelation of  $h(\tau;t)$  can be written as

$$\Phi_h(\tau_1, \tau_2; \Delta t) = E\{h^*(\tau_1; t)h(\tau_2; t + \Delta t)\} \quad (2.10)$$

The process  $h(\tau;t)$  is not stationary with respect to the  $\tau$  variable and thus nonergodic. Because subsequent pulses in the received impulse response are the result of different rays following different paths we assume that the ray amplitude and phase of the ray associated with path delay  $\tau_1$  is uncorrelated with the ray amplitude and phase associated with path delay  $\tau_2$ . This property is usually called *uncorrelated scattering* (US). Incorporating the US-assumption into (2.10) yields

$$E\{h^*(\tau_1; t)h(\tau_2; t + \Delta t)\} = \Phi_h(\tau_1; \Delta t)\delta(\tau_1 - \tau_2) \quad (2.11)$$

For  $\Delta t = 0$ , the resulting autocorrelation  $\Phi_h(\tau) \triangleq \Phi_h(\tau; 0)$  with  $\tau = \tau_1$  is

$$\Phi_h(\tau) = \int_{-\infty}^{\infty} E\{h^*(\tau; t)h(\tau_2; t)\}d\tau_2 = E\{|h(\tau; t)|^2\} \quad (2.12)$$

This function is commonly called the *delay power spectrum* of the channel. An equivalent function  $\Phi_r(\tau) = E\{|r(\tau; t)|^2\}$  can be defined as the delay power spectrum of the received signal.

### 2.2.2.3. Characterization of individual sample functions

An individual sample function in an ensemble generated by the process  $r(\tau;t)$  for any given but fixed value of  $t$  can be described by

$$|r_k(\tau)|^2 = \sum_n \beta_{k,n}^2 b^2(\tau - \tau_{k,n}) + 2 \sum_n \sum_{m > n} \beta_{k,n} \beta_{k,m} b(\tau - \tau_{k,n}) b(\tau - \tau_{k,m}) \cos(\theta_{k,n} - \theta_{k,m}) \quad (2.13)$$

where index  $k$  indicates the specific unique sample function  $r_k(\tau)$  under consideration.  $|r_k(\tau)|^2$  is commonly denoted as the *power delay profile* (PDP) of the  $k$ th individual sample function of the process  $r(\tau;t)$ . The PDP is a convenient description since it can be determined relatively simply by power measurements without the need to determine the individual ray phases. It is, however, not a *complete* description of  $r_k(\tau)$  since

information concerning the ray phases is missing. However, this information is not necessary to describe the most important overall characteristics of the channel as we shall see in the following.

In case there is no overlap among pulses, (2.13) reduces to

$$|r_k(\tau)|^2 = \sum_n \beta_{k,n}^2 b^2(\tau - \tau_{k,n}) \quad (2.14)$$

In case there is overlap among pulses, a similar simplification as (2.14) can be obtained by considering the  $\{\theta_{k,n}\}$  as statistically independent random variables, uniformly distributed over  $[0, 2\pi]$ . In this case, the mathematical expectation of (2.13) with respect to the  $\theta$ 's yields

$$\mathbb{E}_\theta\{|r_k(\tau)|^2\} = \sum_n \beta_{k,n}^2 b^2(\tau - \tau_{k,n}) \quad (2.15)$$

which is identical to (2.14) but allows for overlap.

Two simple parameters can be derived from a power delay profile that are useful in describing the overall characteristics of the received signal. A useful parameter in estimating the signal to noise ratio of communication systems is the *normalized received power* which is defined as the ratio of the total received power  $P_{r,k}$  and the transmitted power  $P_t$ . This ratio can be written as

$$\frac{P_{r,k}}{P_t} = \frac{\int_{-\infty}^{\infty} |r_k(\tau)|^2 d\tau}{\int_{-\infty}^{\infty} |b(\tau)|^2 d\tau} \quad (2.16)$$

Substituting (2.14) into (2.16) simply yields

$$\frac{P_{r,k}}{P_t} = \sum_n \beta_{k,n}^2 \quad (2.17)$$

The other parameter is the *rms delay spread* which is a measure of the channel time dispersion (i.e., the temporal extent) of the power delay profile which relates to performance degradation caused by intersymbol interference (ISI). In accordance with common practice, we will define rms delay spread of the  $k$ th channel as

$$\sigma_{rms,k} \triangleq \sqrt{\overline{\tau^2} - (\overline{\tau})^2} \quad (2.18)$$

where

$$\bar{\tau}^i = \frac{\int_{-\infty}^{\infty} \tau^i |r_k(\tau)|^2 d\tau}{\int_{-\infty}^{\infty} |r_k(\tau)|^2 d\tau}, \quad i=1,2. \quad (2.19)$$

Note, that  $P_{r,k}/P_r$  as well as  $\sigma_{rms,k}$  are independent of the choice of the time origin. Hence; the time origin does not need to be specified.

An alternatively used, but considerably more loose, measure of the channel dispersion is the range over which the power delay profile is essentially nonzero. This measure is called the *multipath spread* and is denoted by  $T_m$ .

### 2.2.3 Frequency domain representation

In Section 2.2.2, we formulated an autocorrelation function for multipath channel representation in the time domain. Under the assumption that  $H(f;t)$  is a wide-sense-stationary process with respect to the  $t$  variable, a completely analogous characterization is possible in the frequency domain by defining the autocorrelation

$$\Phi_H(f_1, f_2, \Delta t) = E\{H^*(f_1; t)H(f_2; t + \Delta t)\} \quad (2.20)$$

The relationship between  $\Phi_H(f_1, f_2, \Delta t)$  and  $\Phi_h(\tau, \Delta t)$  is established by

$$\begin{aligned} \Phi_H(f_1, f_2; \Delta t) &= E\left\{ \int_{-\infty}^{\infty} h^*(\tau_1; t) e^{j2\pi f_1 \tau_1} d\tau_1 \int_{-\infty}^{\infty} h(\tau_2; t + \Delta t) e^{-j2\pi f_2 \tau_2} d\tau_2 \right\} \\ &= \int_{-\infty}^{\infty} \int_{-\infty}^{\infty} E\{h^*(\tau_1; t)h(\tau_2; t + \Delta t)\} e^{j2\pi f_1 \tau_1 - j2\pi f_2 \tau_2} d\tau_1 d\tau_2 \\ &= \int_{-\infty}^{\infty} \int_{-\infty}^{\infty} \Phi_h(\tau_1; \Delta t) \delta(\tau_1 - \tau_2) e^{j2\pi f_1 \tau_1 - j2\pi f_2 \tau_2} d\tau_1 d\tau_2 \\ &= \int_{-\infty}^{\infty} \Phi_h(\tau; \Delta t) e^{j2\pi(f_1 - f_2)\tau} d\tau \\ &= \int_{-\infty}^{\infty} \Phi_h(\tau; \Delta t) e^{j2\pi \Delta f \tau} d\tau \equiv \Phi_H(\Delta f; \Delta t) \quad (2.21) \end{aligned}$$

where  $\Delta f = f_1 - f_2$ . Hence;  $\Phi_H(\Delta f; \Delta t)$  is the Fourier transform of  $\Phi_h(\tau; \Delta t)$ . Furthermore, the US assumption implies that the autocorrelation function of  $H(f;t)$  in frequency is a function of the frequency difference  $\Delta f$  and does not depend on the actual values of  $f_1$  and  $f_2$ . The fact that we assume strictly US, which is expressed by the Dirac delta

function in (2.11), implies that this holds for the entire frequency range.

For  $\Delta t=0$ , the resulting autocorrelation function  $\Phi_H(\Delta f)\Delta\Phi_H(\Delta f;0)$  is the Fourier transform of  $\Phi_h(\tau)$ . This autocorrelation function is called the *spaced-frequency correlation function* of the channel. Its shape expresses the *frequency coherence* of the channel, i.e., the extent to which two different sinusoids with frequency separation  $\Delta f$  are affected differently by the channel.

The maximum frequency difference for which two sinusoids are still strongly correlated is called the *coherence bandwidth* and denoted as  $(\Delta f)_c$ . According to the definition given by Jakes [2] it corresponds to the frequency separation when  $\Phi_H(\Delta f)=0.5$ . In case  $\Phi_h(\tau)\sim e^{-\tau/\sigma_{ms}}$ , which is in many cases a good approximation [2], then it can be readily shown that

$$(\Delta f)_c = \frac{\sqrt{3}}{\pi\sigma_{ms}} \quad , \quad (2.22)$$

where  $\sigma_{ms}$  denotes the rms delay spread of the delay power spectrum  $E\{|h(\tau)|^2\}$ . When a *wideband* signal is transmitted through the channel, i.e. if  $W \gg (\Delta f)_c$ , where  $W$  is the bandwidth of the transmitted signal, the channel is said to be *frequency-selective*. In this case, the signal is severely distorted by the channel. On the other hand, if a *narrowband* signal is transmitted through the channel, i.e. if  $W \ll (\Delta f)_c$ , the channel is said to be *frequency-nonselective* since all of the frequency components in the transmitted signal undergo the same attenuation and phase shift [3]. This means that for narrowband transmission  $H(f;t) \approx H(0;t)$ . Thus, if  $u(t)$ , a narrowband equivalent lowpass signal, is transmitted over the channel, then the received signal is

$$r(t) = H(0;t) \int_{-\infty}^{\infty} U(f)e^{2\pi jft} df = H(0;t)u(t) \quad , \quad (2.23)$$

where  $U(f)$  represents the Fourier transform of  $u(t)$ . Hence; in the narrowband case, the received signal is simply the transmitted signal multiplied by the complex-valued process  $H(0;t)$ , which represents the time-variant characteristics of the channel. Note, that, in case of narrowband transmission, the individual multipath components in the received signal are not resolvable. According to the Central Limit Theorem, the sum of many mutually-uncorrelated variables is Gaussian distributed. The US-assumption, made in Section 2.2, therefore implies that  $H(0;t)$  is a complex-valued Gaussian random process.

## 2.3 Time dependence of millimetre-wave indoor radio channels

### 2.3.1 Fading

Movements of the objects and transceivers in the environment cause time variations in the channels impulse response and therefore in the received signal. This phenomenon is called *fading* [4]. If the narrowband condition  $W \ll (\Delta f)_c$  holds, then all frequency components fade "together" and  $H(f;t)$  has a varying amplitude which applies to the whole frequency range (within the transmission bandwidth), i.e.,

$$H(f;t) \approx H(0;t) = \alpha(t) \quad \text{for } |\Delta f| \leq W, \quad (2.24)$$

where  $\alpha(t)$  is called the channel gain being a complex variable in its time variations [3]. This has been termed *non selective fading* or *flat fading* [1]. In that case, we may write for the received signal

$$r(t) = \alpha(t)u(t) \quad (2.25)$$

A channel providing  $r(t)$  according to (2.25) is therefore called a *multiplicative fading channel*. If  $W$  is not small when compared with  $(\Delta f)_c$ , then the channel is called a *frequency-selective fading channel*.

Now let us consider the consequences of a movement on the characteristics of a mm-wave indoor radio channel. For this, it is convenient to distinguish between the consequences of the movement itself and the consequences of the final effect of the movement, i.e., the displacement.

### 2.3.2 Effects of movement

In order to relate Doppler effects to the time variations in the channel due to the movements itself we consider the Fourier transform of  $\Phi_H(\Delta f; \Delta t)$  with respect to the variable  $\Delta t$  to the frequency ( $\nu$ ) domain denoted as  $S_H(\Delta f; \nu)$ . That is

$$S_H(\Delta f; \nu) = \int_{-\infty}^{\infty} \Phi_H(\Delta f; \Delta t) e^{-j2\pi\nu\Delta t} d\Delta t \quad (2.26)$$

With  $\Delta f$  set to zero the function  $S_H(\nu) \triangleq S_H(0; \nu)$  is called the *Doppler power spectrum* of the channel. An equivalent function can be defined for the received signal.

In the case under consideration, the spectrum broadening due to Doppler effects is caused by scattering from randomly moving objects in the environment whereas the transceivers themselves are not moving. Therefore, we may expect  $S_H(\nu)$

to be bell-shaped like the Gauss curve. For this case, we can define a measure for the spectrum broadening due to Doppler effects, the Doppler spread  $B_d$ , as the frequency shift that corresponds to  $S_{ff}(v) = 0.5S_{ff}(0)$ . Furthermore, we define the *coherence time*  $(\Delta t)_c$  as the maximum time difference for which two impulse responses are still strongly correlated and let  $(\Delta t)_c$  correspond to the time separation for which  $\Phi_{ff}(\Delta t)/\Phi_{ff}(0) = 0.5$ . If we assume that  $S_{ff}(v)$  has the shape of a Gauss curve, then it occurs from (2.26) that

$$(\Delta t)_c = \frac{4}{B_d} \quad (2.27)$$

A rough estimation of the coherence time to be expected in a typical indoor environment for a carrier frequency  $f_c = 60$  GHz can be obtained as follows: a ray reflecting from a moving object having a speed of 5 m/s may experience a Doppler shift of  $2f_c \cdot v/c = 2$  kHz (with  $c$  the velocity of electromagnetic waves in vacuum). Hence; the presence of many objects moving at various speeds up to 5 m/s may result in a Doppler spread of about 4 kHz and, equivalently, a coherence time of about 1 ms. The fading experienced is termed *slow fading* with respect to a transmitted data stream in case its symbol time  $T_s$  is sufficiently short so that fading variations cause negligible loss of coherence within each waveform as received, i.e.  $T_s \ll (\Delta t)_c$ .<sup>4</sup> The " $\ll$ "-symbol has a loose meaning; it might mean  $T_s < 10^{-1}(\Delta t)_c$  or  $T_s < 10^{-2}(\Delta t)_c$ . Referring to the latter (most stringent) interpretation it implies that for  $(\Delta t)_c = 1$  ms a data signal transmitted at a symbol rate of 100 ksymb/s experiences a channel that remains (essentially) constant over a single symbol period. It also implies that a data signal transmitted at a symbol rate of 1 Msymb/s experiences a channel that remains constant over 10 symbol periods etc. In situations where the transceivers operate at substantially higher symbol rates, as in our case, the channel is constant over many more symbols. Therefore, the mm-wave channel under consideration can be regarded as constant over many symbol periods for the data rates of interest so that there is no significant loss of coherence over individual received symbols. This means that if, in addition, there is no substantial frequency selective distortion of the symbol, then the receiving system can be designed on the basis of optimal processing of the transmitted waveform with filters matched to the transmitted waveform or some suitable approximation.

---

<sup>4</sup> This interpretation of the adjective "slow" deviates from the official definition of slow fading given by the International Electrotechnical Commission [1] which reads: Fading for which the fading rate (the rate at which fading occurs) is characterized by a relatively long period of, for example, more than a few minutes. However, relating the term "slow" to the coherence time of the channel and the symbol time of the received data signal yields a considerably more meaningful interpretation for our purposes.

### 2.3.3 Effects of displacement

#### 2.3.3.1 Scales of displacement

With respect to the discussion of channel variabilities due to displacement of transceivers and/or objects in the environment, it is convenient to distinguish between *small scale* effects due to displacements in the order of the wavelength in free space  $\lambda_0$  and *large scale* effects due to displacements over distances that are large when compared with  $\lambda_0$ . In between those two scales there is, of course, a gradual transition. However, the distinction in those two extreme scales is useful in describing the different physical mechanisms that determine the narrowband and wideband characteristics of the channel.

#### 2.3.3.2 Small-scale effects

If the transceiver or one or more objects in the environment are displaced over a distance  $\Delta d \approx \lambda_0$ , then the ray phases  $\{\theta_n(t)\}$  undergo significant changes and a significant change of the channel may be the result. We therefore expect the  $\{\theta_n(t)\}$  to change in an unpredictable (random) manner. This implies that the impulse response  $h(\tau, t)$  and received signal  $r(\tau, t)$  be modelled as a random process as already stated. When there is a large number of rays, the central limit theorem can be applied. That is,  $h(t)$  and  $r(t)$  can be modelled as complex-valued Gaussian random processes. In case of narrowband transmission, the vectors  $\{\beta_n e^{j\theta_n}\}$  are not discernable at the receiver. The randomly varying phases  $\{\theta_n(t)\}$  associated with the vectors  $\{\beta_n e^{j\theta_n}\}$  at times result in rays adding destructively. When that occurs, the resulting received signal  $r(t)$  is very small or virtually zero. At other times, the rays  $\{\beta_n e^{j\theta_n}\}$  add constructively, so that the received signal is large. The resulting phenomenon of amplitude variations in the received signal is termed *multipath fading*, since the fading is caused by the time-variant multipath characteristics of the channel. The probability density function (pdf) of envelope  $A$  can be found by considering the transmission of an unmodulated carrier so that  $u(t)=1$ . It follows from (2.23) that  $r(t)$  and  $H(0;t)$  are identical processes so that

$$A = |r(t)| = |H(0;t)| = \left| \sum_n \beta_n e^{j\theta_n} \right| \quad (2.28)$$

Since  $H(0;t)$ , and thus  $r(t)$ , is modelled as a zero-mean complex-valued Gaussian process, the envelope  $A$  at any instant  $t$  is Rayleigh-distributed in case of narrowband transmission. In this case, the channel is said to be a *Rayleigh fading channel*. The Rayleigh pdf of the envelope  $A$  is



$$p(A) = \frac{A}{\bar{S}} \exp\left[-\frac{A^2}{2\bar{S}}\right], \quad 0 \leq A < \infty, \quad (2.29)$$

where  $\bar{S}$  denotes the average power.

In the case that there are also fixed scatterers, there is a single nonfading component along with a fading process. In that case,  $A$  can no longer be modelled as having a zero mean. The envelope  $A$  then has a Rician distribution and the channel is said to be a *Rician fading channel*. The Rician pdf of the envelope  $A$  is [5]

$$p(A) = \frac{A}{\bar{S}_f} \exp\left[-\frac{\bar{S}_0}{\bar{S}_f}\right] \exp\left[-\frac{A^2}{2\bar{S}_f}\right] I_0\left[\frac{A\sqrt{2\bar{S}_0}}{\bar{S}_f}\right], \quad 0 \leq A < \infty, \quad (2.30)$$

where  $\bar{S}_0$  denotes the average power in the nonfading component while  $\bar{S}_f$  represents the average power in the fading component and  $I_0(\cdot)$  is the modified Bessel function of the first kind and zero order. When there is a single dominant component, the phase is no longer uniformly distributed, but rather more concentrated around that of the nonfading component. If there is no dominant component,  $\bar{S}_0$  becomes zero and expression (2.30) is reduced to (2.29) for the special case of Rayleigh fading.

In the case of wideband transmission,  $r(\tau; t)$  consists of a number of resolvable components. The amplitude of such a resolvable component is Rayleigh distributed only if it is the result of sufficient non-resolvable rays in accordance with the central limit theorem.

### 2.3.3.3 Large-scale effects

If the transceiver or one or more objects in the environment are displaced over a distance  $\Delta d \gg \lambda_0$ , then a significant change of the channel may not only be the result of changed ray phases  $\{\theta_n(t)\}$ , but also of changed ray amplitudes  $\{\beta_n(t)\}$ . If, for instance, a transceiver is moved over a relatively large distance, then rays appear and disappear suddenly due to occasional obstruction (shadowing) of the direct ray and/or reflected rays. When dominant rays experience occasional obstruction the channel statistics may not comply with the above pdf's and may not be considered as stationary. In an indoor environment, however, one might expect that next to a dominant first ray, associated with the direct line-of-sight (LOS) path, many reflected rays are present in case the associated antenna radiation patterns have only low or moderate directivity (as in our case). In that case, shadowing effects have less influence on the impulse response statistics. This is confirmed by incidental LOS-

blocking experiments during our mm-wave indoor radio measurements and by the observation that the removal of the LOS component from the data of a measured response does not lead to a significant change of the associated (normalized) received power and rms delay spread value (see Chapter 3).

Another large-scale effect might be that with changing position of the antennas, ray amplitudes change gradually but significantly due to changing path lengths and associated path losses and eventually due to a changing antenna pointing error. It can be argued, however, that the large-scale variabilities can be described by channel statistics that are quite similar to the small-scale statistics, if some conditions are met.

One condition is that the indoor environment has a morphology in such a way that the ray distributions do not depend upon the position of the transceivers. This might be expected in rooms in which there are no dominant partitions which could possibly cause obstruction of the direct LOS-ray and in rooms in which many rays run between the transmit and receive antennas. It can be intuitively felt that such is not the case in a figure-U shaped room, for instance; the amount of rays will then be much less when the transmitter and receiver are positioned each in another extreme, when compared with the situation in which the transmitter and receiver are placed in each others immediate vicinity.

A second condition is that no significant antenna mispointing occurs. When high-directivity antennas are applied, a small amount of mispointing might significantly influence channel characteristics such as the (normalized) received power. In order to prevent performance deterioration due to antenna mispointing, the antenna beam pointing must be manually or automatically corrected. These corrections thus allow displacements of remote stations without changing the channels characteristics significantly.

If the conditions mentioned above are met, then the shape of the pdf's describing the channel characteristics are expected to be fairly independent of the spatial position of the antennas. However, the (normalized) received power might still exhibit a strong dependence on the separation distance between the antennas, due to significant path loss differences. This is the actual reason why it makes sense to consider statistics of (normalized) received power next to (but separately from) the statistics of the power delay profile details.

With respect to mobile communications, methods for channel modelling and transmission performance evaluations have received considerable attention [6]-[13]. It is common practice to examine mobile radio channels by using a setup in which a radio signal is transmitted by a fixed transceiver and received by a mobile transceiver having a certain speed (or vice versa). We obtain a sufficiently complete charac-

terization of the mm-wave indoor radio channel, however, by considering a less complicated setup in which both transceivers are fixed. This is because the channel considered is essentially static so that time fluctuations are of minor importance as indicated already. This implies that characterization of the channel dynamics (e.g., fade rate and fade duration) is not of primary concern for our situation. In addition, the selection of a suitable coding and interleaving strategy to exploit/overcome fades is of less importance since in a (quasi) static environment, fades are much too long to be handled adequately by coding.

## 2.4 Narrowband transmission

This section discusses the relation between the average signal-to-noise ratio at the receiver and the resulting transmission performance under narrowband conditions (i.e.,  $W \ll (\Delta f)_c$ ). Two commonly used performance measures are considered, viz. 1) the *maximum* probability of error for a given outage probability, which can also be regarded as the probability of (bit) error threshold for that given outage probability, and 2) the *average* probability of (bit) error. The objective of this discussion is to enable link budget calculations for the narrowband case. As a result of this discussion, it will occur that a maximum probability of error of  $10^{-5}$  required for an outage probability of  $10^{-2}$  is well feasible whereas a required average probability of error of  $10^{-5}$  is much more difficult to achieve (without the application of diversity techniques). The results for the narrowband case can be used as a reference for estimating the improvement effects of diversity techniques as treated in Section 2.5 and Section 2.6.

As a starting point we assume a symbol waveform with roughly unity time-bandwidth product and for which the symbol duration  $T_s$  satisfies

$$\sigma_{rms} \ll T_s \ll 1/B_D \quad . \quad (2.31)$$

For such key streams, we are in the regime of the quasi static (slow fading) channel and negligible frequency selectivity. In that case, (2.25) can be written as

$$r(t) = Ae^{j\theta}u(t) \quad , \quad 0 \leq t \leq T_s \quad . \quad (2.32)$$

Now let us assume that the received signal is corrupted by additive white Gaussian noise (AWGN) and let us consider the simplest case of binary keying with unity time-bandwidth product. Then, the signal-to-noise ratio (SNR) at the input of the receiving system is  $\gamma = E_b/N_0$ , where  $E_b$  is the ratio of the energy per received bit and  $N_0$  the (one-sided) spectral density of the noise. The probability of error can be expressed in

terms of  $\gamma$  by one of two forms:

$$\begin{aligned} P_b^{(1)}(\alpha\gamma) &= \frac{1}{2}\exp(-\alpha\gamma) \quad , \\ P_b^{(2)}(\beta\gamma) &= \frac{1}{2}\operatorname{erfc}\sqrt{\beta\gamma} \quad , \end{aligned} \quad (2.33)$$

where

- $\alpha=1/2$  for noncoherent orthogonal symbols (e.g., noncoherent FSK)
- $\alpha=1$  for differentially detected antipodal symbols (e.g., DPSK)
- $\beta=1/2$  for coherent orthogonal symbols (e.g., coherent FSK)
- $\beta=1$  for ideal coherent antipodal symbols (e.g., ideal PSK, coherently detected).

Both forms result in an asymptotic exponential dependence  $\exp(-\alpha\gamma)$  or  $\exp(-\beta\gamma)$  at SNR's high enough to result in sufficiently low probability of error figures. Similar dependencies are found for higher-order alphabets, but we shall use the simple binary cases for our considerations.

If there is no dominant ray, the amplitude  $\mathcal{A}$  has a Rayleigh distribution as explained in the previous section. As a consequence,  $\gamma$  will be exponentially distributed because  $\gamma \sim \mathcal{A}^2$ . In that case, the outage probability  $P_{out}$  for the SNR outage threshold  $\gamma_{th}$  is

$$P_{out}(\gamma_{th} | \bar{\gamma}) = P(\gamma < \gamma_{th} | \bar{\gamma}) = \int_0^{\gamma_{th}} \frac{1}{\bar{\gamma}} \exp\left[-\frac{\gamma}{\bar{\gamma}}\right] d\gamma = 1 - \exp\left[-\frac{\gamma_{th}}{\bar{\gamma}}\right] \quad , \quad (2.34)$$

where  $\bar{\gamma}$  denotes the average received SNR. We only consider  $P_{out}$ -values of practical interest, i.e.  $P_{out} \ll 1$ , so that we may take  $\ln(1-P_{out}) \approx -P_{out}$ . In that case, it follows from (2.34) that  $\gamma_{th} \approx \bar{\gamma}P_{out}$ . Substituting this for  $\gamma$  in (2.33) yields

$$\begin{aligned} P_b^{(1)}(\alpha\bar{\gamma} | P_{out}) &\approx \frac{1}{2}\exp(-\alpha\bar{\gamma}P_{out}) \quad , \\ P_b^{(2)}(\beta\bar{\gamma} | P_{out}) &\approx \frac{1}{2}\operatorname{erfc}\sqrt{\beta\bar{\gamma}P_{out}} \quad . \end{aligned} \quad (2.35)$$

$P_b^{(1)}$  and  $P_b^{(2)}$  express the probability of bit error that corresponds to the SNR threshold  $\gamma_{th}$  for a given  $\bar{\gamma}$  and  $P_{out}$ .

It would be interesting to compare the average SNR  $\bar{\gamma}$  for the multipath case (Rayleigh fading) with the SNR  $\gamma$  for the non-multipath case required to achieve the same  $P_b^{(1)}$  and  $P_b^{(2)}$ . The ratio  $\bar{\gamma}/\gamma$  can be denoted as the *multipath margin*. It occurs directly from (2.33) and (2.35) that, for the noncoherent FSK and DPSK keying formats, this margin can be written as

$$\frac{\bar{\gamma}}{\gamma} = \frac{1}{P_{out}} \quad (2.36)$$

Thus, a factor of 10 reduction in  $P_{out}$  requires a 10 dB increase of average SNR. A similar consideration can be given for coherent FSK and PSK which yields the same conclusion. Note, that this is independent of  $P_b^{(1)}$ , respectively  $P_b^{(2)}$ .

In Fig. 2.1,  $P_b^{(1)}$  for binary DPSK modulation ( $\alpha=1$ ) and  $P_b^{(2)}$  for binary PSK modulation ( $\beta=1$ ) are plotted against  $\bar{\gamma}$  in dB for different values of outage probability, according to (2.35), together with the non-multipath curves, according to (2.33). It occurs from (2.33) and (2.35) that the corresponding curves for coherent FSK and non-coherent FSK can be obtained by shifting the PSK and DPSK curves, respectively, 3 dB upwards the abscissa.

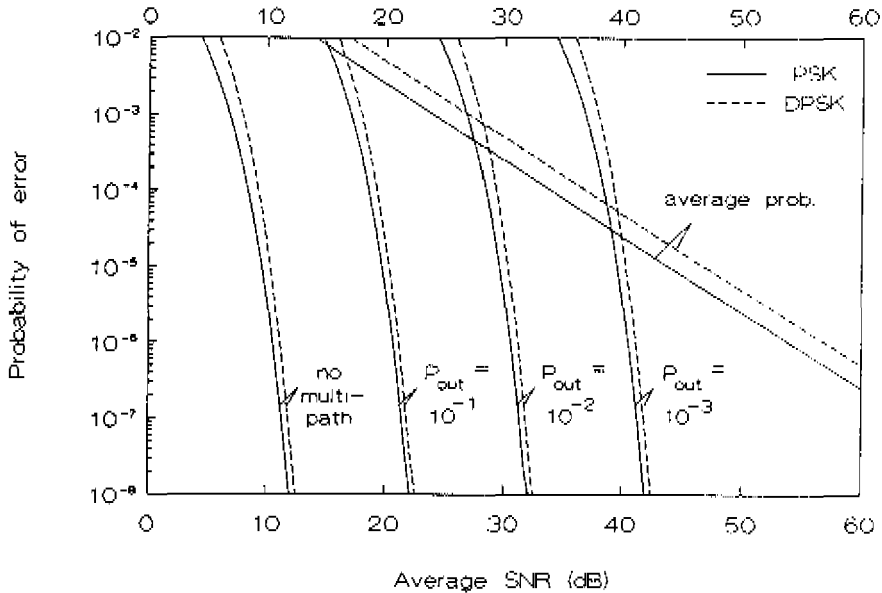


Fig. 2.1: Maximum probability of error for a given  $P_{out}$  and average probability of error in case  $\gamma$  is exponentially distributed. The probability of error for constant  $\gamma$  (no-multipath) is included as a reference.

The link budget listed in Table 2.1 is an example of a maximum data rate estimation for a 60 GHz indoor radio link consisting of a 50 mW transmitter and a basic DPSK receiver. Transmitter and receiver are located 40 metres apart.

Table 2.1 Example of a link budget for indoor mm-wave narrowband transmission

Transmit power [dBm]	17
Aggregate transmit and receive antenna gain [dBi]	13
Transmission loss at 40 metres separation distance [dB]	-100
Received signal power $C$ [dBm]	-70
Total available carrier to noise density ratio $C/N_0$ [dB-Hz]	104
Receiver noise figure [dB]	9
Additional losses [dB]	2
Required bit-energy-to-noise-density ratio $E_b/N_0$ for DPSK modulation, $P_b = 10^{-5}$ (see Fig. 2.1) [dB]	11
Multipath fading margin under Rayleigh fading conditions for DPSK modulation, $P_b^{(1)} = 10^{-5}$ with $P_{out} = 10^{-2}$ (see Fig. 2.1) [dB]	20
Implementation margin [dB]	2
Feasible data rate [Mbit/s]	1

The SNR required for DPSK modulation can be obtained from Fig. 2.1. The link budget estimation for DPSK modulation yields a maximum feasible data rate of 1 Mbit/s for an outage probability  $P_{out} = 10^{-2}$  with a probability of error threshold  $P_b^{(1)} = 10^{-5}$  under narrowband Rayleigh fading conditions.

Up to now, we considered the maximum probability of error as a measure for the transmission performance under multipath conditions. Alternatively, we could take the average probability of error  $\bar{P}_b^{(1)}$ , respectively  $\bar{P}_b^{(2)}$ , as a performance measure.  $\bar{P}_b^{(1)}$  and  $\bar{P}_b^{(2)}$  can be determined by regarding the non-multipath expressions in (2.33) as conditional probabilities of error conditioned on  $\gamma$ . Averaging these probabilities of error over the exponential pdf of  $\gamma$  yields

$$\begin{aligned} \bar{P}_b^{(1)}(\alpha\bar{\gamma}) &= \int_0^{\infty} P_b^{(1)}(\gamma) \frac{1}{\gamma} \exp\left(-\frac{\gamma}{\bar{\gamma}}\right) d\gamma = \frac{1}{2} \frac{1}{1+\alpha\bar{\gamma}} \quad , \\ \bar{P}_b^{(2)}(\beta\bar{\gamma}) &= \int_0^{\infty} P_b^{(2)}(\gamma) \frac{1}{\gamma} \exp\left(-\frac{\gamma}{\bar{\gamma}}\right) d\gamma = \frac{1}{2} \left[ 1 - \sqrt{1+1/\beta\bar{\gamma}} \right] \quad . \end{aligned} \quad (2.37)$$

Because the indoor radio channel is essentially static,  $\bar{P}_b^{(1)}$  and  $\bar{P}_b^{(2)}$  should be considered as the spatial expectation of error probability rather than the probability of error averaged over fading.

In Fig. 2.1,  $\bar{P}_b^{(1)}$  and  $\bar{P}_b^{(2)}$  are plotted against  $\bar{\gamma}$  in dB, according to (2.37), for the PSK and DPSK keying formats. Again, it occurs that the corresponding curves for coherent FSK and non-coherent FSK can be obtained by shifting the PSK and DPSK curves 3 dB upwards the abscissa, respectively.

For low probability of error figures both formulas of (2.37) exhibit an inverse algebraic dependence between the average probability of error and the average SNR of the form  $1/2\alpha\bar{\gamma}$  or  $1/4\beta\bar{\gamma}$ , respectively, instead of the exponential dependence on average SNR found for the maximum probability of error for a certain outage probability according to (2.35), and error probability for the non-multipath case according to (2.33). If one were to try to operate a system with  $10^{-5}$  average probability of error then, correspondingly, roughly 47 dB average SNR would be required. For this, measures must be implemented to gain an additional 16 dB when compared with the link budget given in Table 2.1, which might be an unacceptably stringent requirement. The reason for this is the nonzero probability of occurrence of signal values for which the SNR is so small that the probability of error approaches 0.5. Although this probability is small it forms a dominating contribution to the overall average. For these lowest levels the Rayleigh law is inversely dependent on the mean SNR, which is the inherent reason for the inverse dependence of average error probability on the average SNR. The  $P_b^{(1)}$  and  $P_b^{(2)}$  curves according to (2.35) do not show such inverse relation because these figures are not conditioned on  $\gamma$  and thus not on the occurrence of  $\gamma$  for  $\gamma \leq \gamma_{in}$ . Instead, this occurrence is catered for by an extra parameter, i.e.,  $P_{out}$ .

The "outage"-curves ( $P_b^{(1)}$  and  $P_b^{(2)}$  versus  $\bar{\gamma}$  for a fixed value of  $P_{out}$ ) and "average"-curves ( $P_b^{(1)}$  and  $P_b^{(2)}$ -versus  $\bar{\gamma}$ ) in Fig. 2.1 show that the requirement that  $P_b$  is maximally a certain threshold  $P_{in}=Q$  for a practical outage value (i.e., about  $10^{-2}$  to  $10^{-3}$ ) is much less stringent when compared with an average probability of error requirement  $P_b=Q$  in the range  $Q < 10^{-5}$ . Nevertheless, the "outage"-curves in Fig 2.1 yet show a large multipath margin up to 30 dB required for  $P_{out}=10^{-3}$ . An additional complication is the fact that, even if a sufficient amount of power could be transmitted to overcome the required multipath margin, irreducible errors remain due to phase distortions at the lowest SNR levels [2]. Examinations in a series of papers [14]-[16] show that the probability of error involves additional distortion-related factors, such that the probability of error becomes independent of SNR at very high SNR values. This is the so called *error-rate bottoming* effect. The error rate at which error-rate bottoming occurs depends strongly on factors involving the channel dispersion in time and the channel dispersion in frequency and may fall within the range  $10^{-3}$ - $10^{-6}$  [14]. Another familiar source is the distortion caused by properties of the non-ideal equipment, which again leads to occasional errors, independently of additive noise; the so called *irreducible errors*. A solution to the problem of a large required multipath margin due to channel dispersion and the appearance of bottoming effects is the use of redundancy, which can be obtained by means of diversity techniques, as will be discussed in the next section.

## 2.5 Review of diversity techniques

Diversity techniques are based on the fact that if the same information is received redundantly over two or more channels with mutually independent impulse responses called *diversity branches*, the probability that any individual symbol will be struck by a deep null of SNR coincidentally in every one of the branches is much smaller than the probability that this happens in any of the branches. With intelligent processing, each symbol decision can then be based primarily on the versions received at high SNR, thereby greatly reducing the overall probability of error. For  $L^{\text{th}}$ -order diversity, i.e., in case  $L$  uncorrelated diversity branches are used, with equal average SNR in each branch, the probability of error is essentially the  $L^{\text{th}}$  power of the probability of error for a single no-diversity channel. There are several ways to provide the receiver with  $L$  independent diversity branches.

One method is to employ *frequency diversity*. When a bandwidth  $W \gg (\Delta f)_c$  is available the same data signal can be transmitted on  $L$  carriers. This yields  $L$ -fold diversity in case the frequency spacing between successive carriers is chosen such that the impulse responses of the associated frequency channels are essentially uncorrelated.

A second method, called *time diversity*, is to transmit the signal in  $L$  different time slots, where the separation between successive time slots is sufficient to achieve uncorrelated impulse responses. This method is, however, only effective in combatting noise but it is not suitable for the quasi static indoor radio channel since the decorrelation requirement can not be met with acceptable small time separation.

A third method is *space diversity*. This method employs multiple antennas at the receiving end and is therefore also denoted as *antenna diversity*. It is a historical technique which has found many applications over the years. It is relatively simple to implement and does not require additional frequency spectrum as with frequency and time diversity. Space diversity therefore merits strong consideration for indoor radio applications. To fulfil the basic requirement of essentially uncorrelated individual impulse responses the receiving antennas should be spaced sufficiently far apart. It has been found that a minimum spacing of a half wavelength is sufficient for indoor reception [20].

A diversity technique that exploits the decorrelation of orthogonal field components is *polarization diversity*. It has been shown by [2], that signals transmitted on two orthogonal polarizations in a multipath environments exhibit uncorrelated multipath component statistics. One might consider polarisation diversity as a special case of space diversity since separate antennas are used.

Another special case of space diversity is *angle diversity*. This method has found some application in indoor radio. The diversity is provided by an arrangement of



antennas with directivity in widely different directions [21]-[23].

A variety of methods are known of combining the two or more signal replicas to obtain an improved signal [23]. In case the noise processes in the  $l$ th channel of  $L$  flat and slow fading channels are assumed to be mutually statistically independent AWGN processes, then the best performance is achieved if each diversity branch consists of a matched filter whereas each matched filter output is multiplied by the corresponding complex valued (conjugate) channel gain  $\alpha_l(t) = A_l(t)e^{j\phi_l(t)}$  [3]. The effect of this multiplication is to compensate for the phase shift in each channel and to weigh the received signal by the factor that is proportional to the SNR. Thus, a strong signal carries a larger weight than a weak signal. In case of binary transmission, two sums are formed after the complex-values weighing operation is performed. One consists of the real parts of the weighed outputs from the matched filters corresponding to a transmitted 0. The second consists of the real part of the outputs from the matched filters corresponding to a transmitted 1. This optimum combiner is called a *maximal ratio combiner*.

Let us consider the performance of a diversity system that performs maximal ratio combining with  $L$  uncorrelated diversity branches. For this, we assume for each diversity branch Rayleigh fading with  $\bar{\gamma}$  the average SNR. The resulting SNR after combining  $\gamma$  can be found via the characteristic function of  $\gamma$ , as indicated in [21]. The resulting probability density function can be written as

$$p(\gamma | \bar{\gamma}, L) = \frac{\gamma^{L-1} / \bar{\gamma}^L}{(L-1)!} e^{-\gamma/\bar{\gamma}} \quad (2.38)$$

The outage probability  $P_{out}$  for the SNR outage threshold  $\gamma_{th}$  is

$$P_{out} = P(\gamma < \gamma_{th} | \bar{\gamma}) = \int_0^{\gamma_{th}} p(\gamma) d\gamma = 1 - e^{-\gamma_{th}/\bar{\gamma}} \sum_{k=1}^L \frac{(\gamma_{th}/\bar{\gamma})^{k-1}}{(k-1)!} \quad (2.39)$$

which can also be written as

$$P_{out} = e^{-\gamma_{th}/\bar{\gamma}} \sum_{k=L+1}^{\infty} \frac{(\gamma_{th}/\bar{\gamma})^{k-1}}{(k-1)!} \quad (2.40)$$

The form (2.40) indicates that the approximations

$$P_{out} \approx e^{-\gamma_{th}/\bar{\gamma}} \frac{(\gamma_{th}/\bar{\gamma})^L}{L!} \approx \frac{(\gamma_{th}/\bar{\gamma})^L}{L!} \quad (2.41)$$

are accurate for sufficiently small  $\gamma_{th}/\bar{\gamma}$ . Substituting the explicitly written  $\gamma_{th}$  for  $\gamma$  in (2.33) yields

$$P_b^{(1)}(\alpha\bar{\gamma} | P_{out}, L) \approx \frac{1}{2} \exp(-\alpha\bar{\gamma}(P_{out}L!)^{1/L}) , \quad (2.42)$$

$$P_b^{(2)}(\beta\bar{\gamma} | P_{out}, L) \approx \frac{1}{2} \operatorname{erfc} \sqrt{\beta\bar{\gamma}(P_{out}L!)^{1/L}} .$$

The factor  $(P_{out}L!)^{1/L}$  in (2.42) can be regarded as the reciprocal value of the multipath margin required for  $P_{out}$  in case of  $L$ -fold diversity. With  $10\log(L!) \approx L^2$  for  $2 \leq L \leq 8$ , the multipath margin (MPM) can be written in dB as

$$10\log \frac{\bar{\gamma}}{\gamma} \approx -\frac{10\log(L!)}{L} - \frac{10\log P_{out}}{L} \approx -L - \frac{10\log P_{out}}{L} . \quad (2.43)$$

Hence; for  $2 \leq L \leq 8$  it can be roughly stated that

$$\{\text{MPM (dB) for } L\text{-fold diversity}\} \approx \frac{\{\text{MPM (dB) for no-diversity}\}}{L} - L ,$$

where "MPM for no-diversity" equals  $-10\log P_{out}$  dB.

Fig. 2.2 shows "outage"-curves with  $P_{out} = 10^{-2}$  and  $P_{out} = 10^{-3}$  according to (2.42) for DPSK ( $\alpha=1$ ) and  $L=1, 2$  and  $4$ .

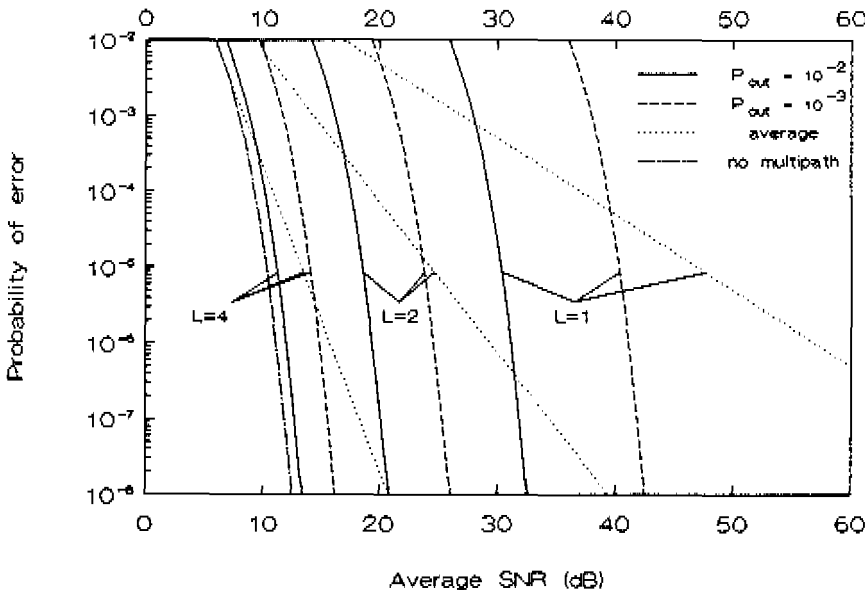


Fig. 2.2: Maximum probability of error for a given  $L$  and  $P_{out}$  and average probability of error for given  $L$  in case  $\gamma$  is exponentially distributed. The probability of error for constant  $\gamma$  (no-multipath) is included as a reference.

The "non-multipath"-curve according to (2.33) for DPSK is also shown in order to allow easy determination of the multipath margin for the various values of  $L$ . It occurs from (2.42) and Fig. 2.2 that the required average SNR depends strongly on  $P_{out}$  whereas it is rather insensitive to the probability of error itself. For outage probability values of practical interest many tens of dB's can be gained by applying diversity; a 2-fold diversity system yields a multipath margin of 8 dB instead of the 20 dB necessary if no diversity is implemented. Referring to the link budget of Table 2.1, the resulting gain due to diversity of 12 dB can be used to increase the feasible data rate to 16 Mbit/s, provided that the narrowband assumption  $W \ll (\Delta f)$ , still holds.

Expressions for average probability of error can be obtained by regarding the non-multipath expressions in (2.33) as conditional probability of error conditioned on  $\gamma$ . Averaging over the pdf of  $\gamma$  given in (2.38) yields

$$\begin{aligned} P_b^{(1)}(\alpha\bar{\gamma} | L) &= \frac{1-\mu}{2} \sum_{l=0}^{L-1} \left[ \frac{L-1+l}{l} \right] \left[ \frac{1+\mu}{2} \right]^l \quad \text{with } \mu = \frac{1}{1+1/\alpha\bar{\gamma}} \quad , \\ P_b^{(2)}(\beta\bar{\gamma} | L) &= \frac{1-\mu}{2} \sum_{l=0}^{L-1} \left[ \frac{L-1+l}{l} \right] \left[ \frac{1+\mu}{2} \right]^l \quad \text{with } \mu = \frac{1}{\sqrt{1+1/\beta\bar{\gamma}}} \quad . \end{aligned} \quad (2.44)$$

For  $\bar{\gamma} \gg 1$  these expressions can be simplified to

$$\begin{aligned} P_b^{(1)}(\alpha\bar{\gamma} | L) &= \frac{1}{(2\alpha\bar{\gamma})^L} \left[ \begin{matrix} 2L-1 \\ L \end{matrix} \right] \quad , \\ P_b^{(2)}(\beta\bar{\gamma} | L) &= \frac{1}{(4\beta\bar{\gamma})^L} \left[ \begin{matrix} 2L-1 \\ L \end{matrix} \right] \quad . \end{aligned} \quad (2.45)$$

It follows from these expressions that the multipath margin for  $2 \leq L \leq 8$  may be written as

$$\{\text{MPM (dB) for } L\text{-fold dvs}\} \approx \{\text{MPM (dB) for no-dvs}\} + \frac{L-1}{L} 10 \log \bar{P}_b + L \quad ,$$

with  $\bar{P}_b = P_b^{(1)}$  or  $\bar{P}_b = P_b^{(2)}$ . It can be easily verified that "{MPM (dB) for no-diversity}" equals about  $(-10 \log \bar{P}_b)/L + L - 10 \log 2\alpha - 11$  dB or  $(-10 \log \bar{P}_b)/L + L - 10 \log 4\beta - 11$  dB, respectively.

Fig. 2.2 includes "average"-curves according to (2.44) for DPSK ( $\alpha=1$ ) and  $L=1,2$  and 4. It occurs from (2.44) and Fig. 2.2 that the average probability of error strongly depends on the average SNR. In case very small values for the average probability of

error are required ( $< 10^{-6}$ ), many tens of dB's can be gained by applying diversity.

The improvements that occur to be feasible with the optimum combining technique (i.e., maximal ratio combining) can be closely approached by some alternative combining techniques which are much easier to implement. It has been shown by [2] that just phase locking without the additional amplitude weighing is almost as effective when the contributions from the individual diversity branches are of roughly equal mean strength. This method is commonly denoted as *equal gain combining*. It does not require the variable weighing capability as with true maximal ratio combining. However, it still requires phase locking which is necessarily a form of "predetection" (IF) combining. At the other extreme is *selection combining*, i.e., selection of the best diversity branch as judged by some criterion or *switched combining*, i.e., the use of one of the branches and switching only to another when the quality of this branch drops below a certain threshold. Selection or switching combining is often implemented after detection (postdetection combining).

## 2.6 Wideband transmission

In the previous section it was stated that, when a bandwidth  $W \gg (\Delta f)_c$  is available, a form of frequency diversity can be achieved by subdividing the available bandwidth  $W$  into  $L$  uncorrelated subchannels. A more direct method for achieving basically the same result is to employ a wideband signal covering the bandwidth  $W$ . In this method the fading is combatted by resolving the multipath contributions and combining them in an appropriate manner. Therefore, this kind of diversity is also denoted as multipath (or path) diversity. In this section, we consider the optimum receiver for processing the wideband signal, i.e., a signal with  $W \gg (\Delta f)_c$ . The symbol time  $T_s$  is such that  $T_s \gg T_m$ . Thus, we neglect any intersymbol interference (ISI) due to multipath. For a wideband signal this implies that  $T_s \gg W^{-1}$ . This can be achieved by spread-spectrum techniques as described in [3]. Application of the sampling theorem for the equivalent lowpass transmitted signal  $u(t)$ , bandlimited to  $|f| \leq W/2$ , yields

$$u(t) = \sum_{n=-\infty}^{\infty} u \left[ \frac{n}{W} \right] \frac{\sin \pi W(t - \frac{n}{W})}{\pi W(t - \frac{n}{W})} \quad (2.46)$$

The noiseless received signal can be written as the convolution sum of  $h(\tau; t)$  and  $u(t)$  in the form [3]

$$r(t) = \sum_{n=-\infty}^{\infty} h_n(t) u \left[ t - \frac{n}{W} \right] \quad \text{with } h_n(t) = \frac{1}{W} h \left[ \frac{n}{W}, t \right] . \quad (2.47)$$

The above form of the received signal implies that the frequency selective channel can be represented as a tapped delay line with tap spacing  $1/W$  and tap weight coefficients  $\{h_n(t)\}$ . The complex equivalent lowpass impulse response for the channel is

$$h(\tau, t) = \sum_{n=-\infty}^{\infty} h_n(t) \delta \left( \tau - \frac{n}{W} \right) . \quad (2.48)$$

Thus, an equivalent lowpass signal having a bandwidth  $W/2$ , where  $W \gg 1/T_m$ , yields a resolution of  $1/W$  in time domain. If the total multipath spread is  $T_m$ , then the tapped delay line model for the channel can be truncated at  $L = T_m W + 1$ . The noiseless signal can be expressed in the form

$$r(t) = \sum_{n=1}^L h_n(t) u \left[ t - \frac{n}{W} \right] . \quad (2.49)$$

The  $L$  tap weights  $\{h_n(t)\}$  are considered to be the result of the summation of many non-resolvable multipath components. According to the uncorrelated scattering assumption, made in Section 2.2, and the Central Limit Theorem they are thus zero mean complex-valued stationary Gaussian random processes. The magnitudes  $\{|h_n(t)|\}$  are therefore Rayleigh distributed. Since the  $\{h_n(t)\}$  represent the tap weights corresponding to the  $L$  different delays  $\tau_n = n/W$ ,  $n=1, 2, \dots, L$ , the uncorrelated scattering assumption implies that the  $\{h_n(t)\}$  are mutually uncorrelated. But the  $\{h_n(t)\}$  are Gaussian random processes, hence; they are statistically independent.

The form of (2.49) suggests, that the optimum demodulator for the received signal  $r(t)$  is a filter matched to the tapped delay channel model. That is, the matched filter is a tapped delay line having  $L$  taps with spacing  $n/W$ . In order to achieve that the various delayed replicas of  $u(t)$  all add constructively, their phases should be brought into common agreement. As already noted in the previous section, the SNR of a weighed sum, of which each term is the combination of a signal and an additive, independent noise of fixed power, is optimum when the amplitude weighing is done in proportion to the signal strength. Provided that  $W$  is large enough to isolate a number of independent echoes, the unfavourable effects of multipath are largely eliminated by such a scheme, since the path contributions are added algebraically, not vectorially. In effect, the tapped delay line receiver collects the signal energy from all the received

signal paths that fall within the span of the delay line and carry the same information. Its action looks like that of a garden rake, and is therefore called a *RAKE receiver* [25]. Note, that the  $L$ -taps RAKE receiver with perfect (noiseless) estimates of the channel tap weights is exactly equivalent to a maximal ratio combiner in a system with  $L$ -th order diversity. Thus, when all the tap weights have the same mean-square value, then the error rate performance of the RAKE receiver is given by (2.38) to (2.45).

A RAKE receiver is useful in case the data rate is low relative to either the coherence bandwidth or to the bandwidth utilized. If the data rate is not low relative to the coherence bandwidth, then ISI occurs which is statistically discriminated by the RAKE receiver. The RAKE receiver approach, however, resorts to bandwidth expansion to combat ISI and to achieve diversity gain. In this respect a RAKE receiver approach differs essentially from the application of adaptive channel equalization. Adaptive equalization enables operation at higher data rates by actually counteracting the ISI. Because adaptive equalizers can do this without expanding the bandwidth it may prove extra useful to have a closer look to the merits of channel equalizers for wideband communication over indoor radio channels. Considerable attention is devoted to this subject in Chapter 6.

## 2.7 Summary and conclusions

In this chapter, the basic elements of multipath and digital transmission are treated that are relevant to the problem of high speed transmission over millimetre-wave (mm-wave) indoor radio channels.

Considering the propagation aspects, it is assumed that the mm-wave indoor radio channel can be regarded as a discrete multipath channel. This assumption implies that the channel can be described by an ensemble of "rays" each characterized by an amplitude, phase and excess delay value. For wireless LAN applications in which the transceivers are fixed during operation, it is made plausible that the mm-wave indoor radio channel may be considered as practically constant over many symbol periods for symbol rates of interest ( $> 1$  Msymb/s).

For binary transmission, the relation between the average signal to noise ratio at the receiver and the resulting transmission performance is examined in order to enable link budget calculations. Two performance measures are considered, viz. 1) the maximum probability of error for a given outage probability and 2) the average

probability of error.

Under Rayleigh-fading conditions, the relation between the maximum probability of error for a certain outage probability and the average SNR shows an asymptotic exponential dependence at high average SNR's of practical interest. On the other hand, an inverse algebraic dependence is found for the relation between the average probability of error and average SNR. Because of this, an average probability of error requirement  $P_b = Q$  is much more stringent when compared with a maximum probability of error requirement  $P_b = Q$  for  $Q < 10^{-5}$  and in case we assume practical outage values ( $10^{-2}$  to  $10^{-3}$ ).

The average SNR required for acceptable transmission performance is considerably lower when some kind of diversity technique is applied. It is demonstrated that for the optimum diversity combining technique, i.e. maximal ratio combining with 2-fold diversity, the required average SNR is 12 dB lower while maintaining the same maximum probability of error and outage probability. This gain due to diversity does not depend on the actual value of the maximum probability of error considered. With respect to the average probability of error  $P_b$ , it occurs that the diversity gain is inversely proportional to the value of  $P_b$  considered.

With respect to wideband transmission, it is outlined how the inherent diversity of a multipath channel can be exploited. A bandwidth efficient method is adaptive channel equalization. Because adaptive equalizers cope with intersymbol interference without expanding the bandwidth they can be generally regarded as promising candidates for application in broadband wireless LANs.

---

**References in Chapter 2**

- [1] International Electrotechnical Commission, International Electrical Vocabulary, Chapter 705; Propagation, Geneva, July 1984.
- [2] W.C. Jakes "Microwave Mobile Communications", John Wiley and Sons, New York, 1978.
- [3] J.G. Proakis, "Digital Communications", McGraw-Hill, Singapore, 1983.
- [4] Recommendations of the CCIR, Vocabulary (CCV), Vol. XIII, CCIR, Geneva, 1990.
- [5] S.O. Rice, "Statistical properties of a sine wave plus random noise", Bell Sys. Techn. Journal, Vol. 24, No. 1, pp. 46-156, 1945.
- [6] W.C.Y. Lee, "Mobile communications design fundamentals", Howard W. Sams & Co., Indianapolis, 1986.
- [7] D.O. Cox, "Delay-Doppler characteristics of multipath propagation at 910 MHz in a suburban mobile environment", IEEE Trans. on Ant. and Propag., Vol. AP-20, No. 5, pp. 625-635, 1972.
- [8] H. Suzuki, "A statistical model for urban radio propagation", IEEE Trans. Commun., Vol. COM-25, No. 7, pp. 673-680, 1977.
- [9] M. Hata, "Empirical Formula for Propagation Loss in Land Mobile Radio Services", IEEE Trans. Veh. Technol., Vol. VT-29, pp. 317-325.
- [10] J. Walfish and H.L. Bertoni, " A theoretical model of UHF Propagation in Urban Environments. IEEE Trans. on Ant. and Propag., Vol. AP-36, pp. 1788-1796, 1988.
- [11] Y. Okumura et. al., "Field Strength and Its Variability in VHF and UHF Land-Mobile Radio Service", Review of the ECL, Vol. 16, pp. 825-873, 1968.
- [12] COST, "Urban transmission loss models for mobile radio in the 900- and 1800 MHz bands. COST 231 TS (91) 73.



- [13] J.P.M.G. Linnartz, "Effects of fading and interference in narrowband land-mobile networks", Ph.D. Thesis, Delft University of Technology, Nov. 1991.
- [14] P.A. Bello and B.D. Nelin, "Predetection diversity combining with selectively fading channels", IRE Trans. Commun. Syst., Vol. CS-10, pp. 32-42, 1962.
- [15] P.A. Bello and B.D. Nelin, "The influence of fading spectrum on the binary error probabilities of incoherent and differentially coherent matched filter receivers", IRE Trans. Commun. Syst., Vol. CS-10, pp. 160-168, 1962.
- [16] P.A. Bello and B.D. Nelin, "The effect of frequency selective fading on the binary error probabilities of incoherent and differentially coherent matched filter receivers", IEEE Trans. Commun. Syst., Vol. CS-11, pp. 170-186, 1963. (Corrections in Vol. CS-12, pp. 230-231, 1964.)
- [17] T.A. Freeburg, "Enabling Technologies for Wireless In-Building Network Communications - Four Technical Challenges, Four Solutions", IEEE Comm. Mag., pp. 58-63, 1991.
- [18] D. Buchholz et. al., "Wireless In-Building Network Architecture", IEEE Netw. Mag., pp. 30-38, 1991.
- [19] J.E. Mitzlaff, "Radio Propagation and Anti-Multipath Techniques in the WIN Environment", IEEE Netw. Mag., pp. 21-26, 1991.
- [20] J.G.W.M. Janssen, P.G.M. de Bot, A.J.M. Wijlaars, "Antenna Diversity for Digital Video Broadcasting", Proc. IEEE First Symp. on Comm. and Veh. Techn. in the Benelux, Delft, pp. 6.4.1-6.4.8., Oct. 1993.
- [21] D.G. Brennan, "Linear Diversity Combining Techniques", Proc. IRE, Vol. 47, pp. 1075-1102, 1959.
- [22] L. Turin, "On Optimal Diversity Reception", IRE Trans. Inform. Theory, Vol. 7, pp. 154-166, 1961.
- [23] L. Turin, "On Optimal Diversity Reception, II", IRE Trans. Commun. Syst., Vol. 10, pp. 22-31, 1962.

- 
- [24] M. Schwartz, W.R. Bennett and S. Stein, "Communication systems and techniques", McGraw-Hill, New York, 1966.
  
  - [25] R. Price and P.E. Green, "A Communication Technique for Multipath Channels", Proc. IRE, Vol. 46, pp. 555-570, 1958.

## CHAPTER 3

# WIDEBAND MEASUREMENTS OF MILLIMETRE-WAVE INDOOR RADIO CHANNELS

### 3.1 Introduction

In the previous chapter, we treated the fundamentals of electromagnetic wave propagation relevant to the problem of transmission over mm-wave indoor radio channels. In order to attain a more detailed insight in the characteristics of practical indoor radio channels at mm-wave frequencies, an extensive set of wideband measurements should be performed which allows for statistically significant conclusions. However, prior to this study, no results of extensive wideband measurements were reported in the (open) literature. Therefore, this research project included a large-scale measurement campaign which was carried out in different indoor areas. The main objective of these measurements was to obtain subsets of complex equivalent lowpass impulse responses from which the channel characteristics can be derived. These characteristics concern statistical distributions of

- 1) values of normalized received power (NRP). The NRP of a complex equivalent low-pass impulse response is defined by (2.16).
- 2) values of rms delay spread (RDS). The RDS of a complex equivalent low-pass impulse response is defined by (2.18) and (2.19).

- 3) values of impulse response details, i.e., amplitude, phase and interarrival-times of echo's distinguishable in an impulse response. In this chapter, these echo's will be referred to as *rays* in accordance with the ray-optical concept as formulated in Section 2.2.2.

For our purposes the 60 GHz absorption band, i.e., the frequency band around 60 GHz in which specific attenuation due to atmospheric oxygen occurs, is of particular interest. This is because this oxygen attenuation enables very short frequency-reuse distances as explained in Section 1.2.3. Therefore, we decided to centre the frequency band in which the measurements were performed around a frequency at which the oxygen attenuation is more or less representative for the entire 60 GHz absorption band. The width of the frequency band in which the measurements were performed is termed the *channel bandwidth* throughout this chapter. At 58 GHz, the oxygen attenuation is 12 dB/km which is 3 dB below the maximum attenuation which occurs at 60 GHz. For reasons explained later (in Section 3.2.3) we chose a channel bandwidth  $B=2$  GHz which was centred around 58 GHz. A practical consequence of this choice is the fact that the measurement setup must be based on WR-19 waveguide which is specified for U-band (40-60 GHz) or, alternatively, on WR-15 waveguide which is specified for V-band (50-75 GHz). We decided to choose in favour of the WR-19 option since for our purposes the 40-50 GHz frequency range is of more interest than the 60-75 GHz (see Section 1.2). The application of WR-19-based equipment enables additional measurements in the middle of the mm-wave frequency range of interest, i.e., 25-60 GHz. A reasonable assumption is that such measurements yield the most representative results for this frequency range. Therefore, we decided to perform additional measurements with the channel bandwidth  $B=2$  GHz centred around 42 GHz. Comparison of the results obtained in the 41-43 GHz band with those obtained in the 57-59 GHz band yields an indication of the frequency dependence of the channel characteristics.

Candidate measurement methods can be categorized in three groups, viz.: 1) time-domain methods, 2) frequency-domain methods and 3) correlation methods.

To date, *time-domain sounding* is the most commonly applied method for radio-channel measurement. In this method, the stimulus signal consists of a narrow and strong radio frequency (RF) pulse which is periodically transmitted. At the receiving end the pulse and its echo's, which result from reflections, are detected. By choosing a suitable pulse repetition period the power delay profile can be visualized on the display of an oscilloscope in real time. In addition, individual power delay profiles are digitized and stored on disk. Mostly, incoherent detection by means of a square law detector is applied. This implies that no phase information of the RF sig-

nals becomes available. The attained *time-domain resolution*, which we define as the minimum time spacing at which two neighbouring pulse echoes of equal amplitude are still discernable, is directly related to the width of the transmitted pulse and the bandwidth of the receiver. The dynamic range of the measurement equipment is directly related to the strength of the transmitted pulse. A problem with time-domain sounding of mm-wave channels is that narrow and strong RF pulses, necessary for sufficient time-domain resolution, are difficult to produce at mm-wave frequencies.

*Frequency-domain sounding* is a coherent measurement technique that can be performed with 1) a frequency-sweep stimulus or 2) a frequency-stepping stimulus. In the frequency-sweep technique the source is swept in a continuous fashion from the lower to the upper frequency and the received signal is sampled without stopping the sweep. In the frequency-stepping technique, a single sine wave originating from a synthesized source is transmitted and the received signal amplitude and phase are detected at the receiving end. Repeating this procedure by stepping through the frequency band with constant transmitted power produces the equivalent low-pass transfer function of the channel. Applying Inverse Fourier Transformation (IFT) yields the corresponding equivalent low-pass impulse response. The frequency-sweep method provides fast measurements in comparison with the frequency-stepping method. The frequency-stepping method, however, provides the benefit of improved frequency accuracy since the source is tuned and phase-locked to each frequency point. With both frequency-domain techniques, the achievable time-domain resolution depends only on the channel bandwidth and the frequency-domain window applied to improve the dynamic range in the time domain (see Section 3.2.3). Another advantage, when compared with time-domain measurements, is that phase information of the RF signals is available. A drawback of the frequency-stepping method is, in general, that the channel must be fixed during a complete measurement sweep in order to obtain meaningful results. As a consequence, no Doppler effects can be measured. Another drawback is the fact that a phase reference is needed.

With *correlation sounding*, the stimulus signal consists of a sine wave modulated with a pseudo-random binary sequence by means of Phase-Shift Keying. At the receiver this pseudo-random sequence is correlated with an identical sequence which runs at a slightly different clock frequency in comparison with the clock frequency of the sounding signal. The complex output signal of the correlator is proportional to the impulse response of the channel under test, but scaled in time. A similar technique is applied in the interleaved sampling oscilloscope, producing its output from successive samples of the impulse response. It is thus implicit that the channel under test does not change during the time required for each measurement. The time-domain resolution is determined by the chip rate of the transmitted sequence. The level of transmitted power is such that it does not significantly disturb other services when the

measurements are carried out in occupied frequency bands. In addition, this type of sounder is sometimes chosen for the simplicity of its construction.

After considering the relative merits and weaknesses of the different techniques mentioned above, we decided to choose in favour of the frequency-stepping technique. The main reasons<sup>1</sup> for this choice are that 1) an unprecedented time-domain resolution can be obtained, 2) a high measurement accuracy can be obtained and 3) a complete characterization (i.e., magnitude as well as phase) of the channel responses can be obtained.

The fact that the channel must be fixed during each measurement is not a serious restriction since the Doppler effects only cause *slow* fading as indicated in Section 2.3.2. A more annoying drawback is the fact that a phase reference is needed. This necessitates a waveguide connection between the transmitter and receiver. In practice, this makes the measurement setup more rigid and therefore it complicates the measurements.

The frequency-domain measurements were carried out in eight different indoor areas at the Eindhoven University of Technology. The measurement results consist of 14 subsets of (complex-valued) equivalent lowpass transfer functions. Each subset consists of  $K$  (about 20) transfer functions obtained in one and the same indoor area, i.e., a single room, hall or corridor. For each subset, the position of the receive antenna was fixed. The transfer functions were measured at  $K$  positions of the transmit antenna. The positions of the transmitter antenna were randomly chosen in one and the same horizontal plane. Hence, the height of this antenna was the same at all these positions. During the measurements people stopped moving to avoid channel variations. Since the channel is fixed we assume that a subset represents an ensemble of time-independent equivalent low-pass transfer functions  $\{R_k(f)\}$  called a *frequency-domain ensemble*. For each subset, such frequency-domain ensemble can be expressed as

$$R_k(f) = B(f)H_k(f) = B(f)\sum_n \beta_{k,n} e^{j\theta_{k,n}} e^{-j2\pi f\tau_{k,n}}, \quad k=1,2,\dots,K, \quad (3.1)$$

in which  $k$  represents the position of the transmit antenna.  $B(f)$  here represents the

---

<sup>1</sup> There is also a pragmatic reason for supporting this choice; the frequency-stepping technique (as well as the frequency-sweep technique) can be performed by a network analyzer which is a versatile general-purpose instrument for full two-port characterization; it can also be used for measuring many other types of communication channels and a broad scale of passive as well as active devices. Therefore, a network analyzer is a standard tool for microwave laboratories.

window function applied (see Section 3.2.3).

By employing IFT to each sample function  $R_k(f)$ , we obtain an ensemble of time-independent equivalent lowpass impulse responses  $\{r_k(\tau)\}$  which we call a *time-domain ensemble*. The IFT of (3.1) yields (2.7) with eliminated time-dependence, i.e.,

$$r_k(\tau) = \sum_n \beta_{k,n} e^{j\omega_n \tau} b(\tau - \tau_{k,n}) \quad , \quad k=1,2 \dots K \quad , \quad (3.2)$$

with  $b(\tau)$  representing the IFT of  $B(f)$ .

In Section 3.2, the measurement setup and procedures applied for conducting the indoor propagation experiments are described. In Section 3.3, the antennas and their connection to the waveguides are treated. In Section 3.4, the indoor environments under consideration are described. The measurement results are presented and discussed in Section 3.5. In Section 3.6, the accuracy of the measurement method applied is checked using the measurement results obtained. Results of additional transmissivity and reflectivity measurements are presented and discussed in Section 3.7 and Section 3.8, respectively. Finally, in Section 3.9, a summary is presented and the conclusions are given.

## 3.2 Measurement setup and procedures

### 3.2.1 Measurement setup

The system for wideband indoor radio propagation measurements is based on an HP 8510C network analyzer which is capable of measuring complex values of two-port  $S$  parameters. A schematic diagram of the setup is drawn in Fig. 3.1. The measurement system is essentially the same as an antenna measuring system. In fact, it was also used for determining the radiation patterns of the antennas applied. The network analyzer controls the RF source by an IEEE bus. The RF source is capable of generating sine waves up to a frequency of 50 GHz. To increase the frequency range of the setup, the output frequency of the RF source is tripled. A 20 dB amplifier must be inserted between the RF source and the frequency tripler to obtain the power level required for proper operation of the tripler. For the investigation of the frequency band of 40 to 60 GHz the RF source is thus used at 13.33 to 20 GHz. The output of the tripler is applied to a -10 dB directional coupler via an isolator. The directional coupler separates the incoming signal into the test signal and the reference signal which run via the test channel and reference channel, respectively. The reference channel provides the analyzer with a phase reference.

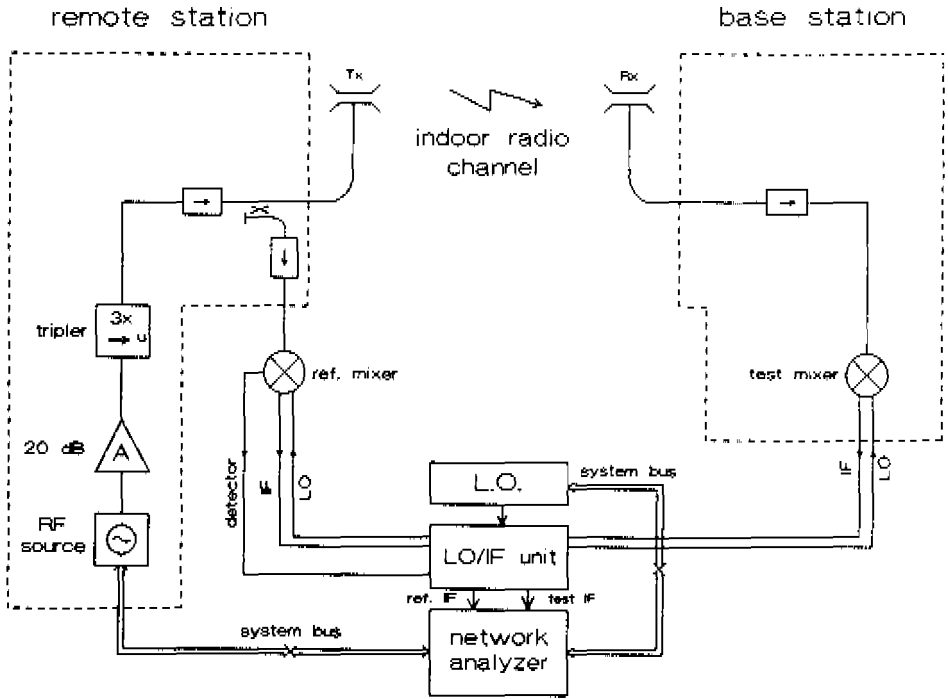


Fig. 3.1: Diagram of the measurement setup.

The reference output of the directional coupler is connected via an isolator and a rectangular WR-19 waveguide to an harmonic mixer (termed "reference mixer"). The test output of the directional coupler is connected to the transmit antenna via a piece of WR-19 waveguide. The receive antenna is connected to an harmonic mixer (termed "test mixer") via an isolator.

The LO/IF (Local Oscillator/Intermediate Frequency) unit uses a power splitter to feed one local oscillator signal which ranges from 4 to 6 GHz to both mixers. The mixers are connected to the LO/IF unit by coaxial cables (each 8 metres long). This allows flexible displacement of the transmitter and the receiver. The maximum separation distance that can be achieved between the transmit antenna and receive antenna is about 25 metres. The unit controls the level of LO power at the input of the reference mixer. This is possible by means of a feedback circuit which includes a detector at the mixers LO input. The harmonic mixers multiply the 10th harmonic of the LO signal with the RF frequency. The LO frequency is offset by 20 MHz. Hence; a 20 MHz IF signal is obtained from both reference and test channel. Both IF signals are fed back to the network analyzer, where the complex ratio of the signals is calculated and displayed as the  $S_{21}$  two-port transmission



parameter. The  $S_{21}$  parameter is defined as the (complex) ratio of the *received* sine wave at the output test port (i.e., the input of the test channel mixer) and the *transmitted* sine wave at the input test port (i.e., the output of the directional coupler).

The receiver bandwidth is 10 kHz, which results in a noise floor of approximately -100 dBm. At every measurement frequency the receiver noise floor was reduced further by taking the average of 128 responses. This resulted in a noise floor of -120 dBm, thus an increase of the dynamic range by 20 dB. The power level at the test output of the directional coupler was 0 dBm. The average level of received power was approximately -80 dBm for all measurements. Thus a 40 dB signal-to-noise ratio was attained. This means that multipath fades to a minimum level of -40 dB could be detected. The specification of the (linear) magnitude uncertainty, defined as the maximum relative error in the magnitude of the frequency response due to IF residuals, detector inaccuracies, mixer noise figure and conversion loss and due to the effects of cable instability, was approximately 0.02 [1]. This limits the difference between maximum and minimum ray amplitude to  $-20\log(0.02) = 34$  dB. In many impulse responses, however, differences in ray amplitude of about 40 dB could be observed.

### 3.2.2 Calibration procedure

Before any measurement can be done, calibration of the measurement equipment is necessary. A calibration quantifies and removes systematic errors introduced by the measurement equipment itself.

The first step in calibrating the setup is the removal of the transmit antenna and receive antenna from the coupler output and test-channel mixer input, respectively, since both antennas (including their mismatches) are part of the channel under test (see Note 2 in Section 2.2.2). The coupler output and test-channel mixer input are considered as the reference planes of the input port and output port, respectively, of the two-port under test (i.e., the channel under test).

The next step is the interconnection of these two ports and measurement of the  $S_{21}$  parameter for each frequency point  $f_i$ ,  $i=1,2,\dots,I$ , where  $I$  is the total number of frequency points within the channel bandwidth  $B$ . We denote the resulting  $S_{21}$  parameter values as  $S_{21,sys}(f_i)$ .

When the channel under test is measured, the  $S_{21}$  parameter of the actual channel at each frequency point  $f_i$  denoted as  $S_{21,chan}(f_i)$  is calculated according to

$$S_{21,chan}(f_i) = \frac{S_{21,meas}(f_i)}{S_{21,sys}(f_i)} \quad , \quad i=1,2,3 \dots I \quad , \quad (3.3)$$

where  $S_{21,meas}(f_i)$  is the measured value of the  $S_{21}$  parameter at each frequency point  $f_i$ .

### 3.2.3 Equipment settings

The HP 8510C network analyzer is capable of taking a maximum of 801 frequency samples. This number and the channel bandwidth determines the aliasing-free range  $T_{range}$  in the time domain, according to

$$T_{range} = \frac{1}{\nu} = \frac{I-1}{B}, \quad (3.4)$$

where  $\nu$  is the frequency spacing between the frequency points. In order to investigate the maximum excess delay in the impulse response, we performed preliminary experiments in various indoor environments which indicated that a total range of 400 ns should be sufficient for characterization of impulse responses. According to (3.4), the maximum channel bandwidth, necessary for a 400 ns aliasing-free range with full accuracy, is therefore  $B=2$  GHz. Discrete Fourier Transformation of the equally spaced frequency samples yields 801 complex time-domain data points which are also equally spaced at  $1/B = 0.5$  ns intervals.

The frequency response can be shaped (multiplied with a window function) in order to improve the dynamic range of the computed time-domain response. Because the measurements are bandlimited, no shaping is in fact applying a rectangular window. Multiplying a frequency-response function with a window function results in a convolution with the IFT of the window function in the time domain. For example: if no windowing is used, the time-domain response to the Dirac Delta function is the sinc function  $B(\sin(\pi B\tau))/(\pi B\tau)$ . Hence; if no window function is used and if the low-pass impulse response of the channel under test is described by (2.8) then the time-domain response can be written as (2.7) with  $b(\tau)$  being a sinc function. Because the maximum side-lobe level of a sinc function is 13 dB below the main-lobe level, the time-domain dynamic range will be limited to 13 dB in this case. A rectangular window, however, offers the highest *time-domain resolution*. Time-domain resolution is generally equated with the width of the main lobe of the IFT of the window function. With a rectangular window and  $B=2$  GHz, the time-domain resolution is  $1/B=0.5$  ns.

Generally, dynamic range and time-domain resolution are two opposing requirements. Using a window therefore means finding a compromise between required resolution and dynamic range. The HP 8510C network analyzer uses a Kaiser window for shaping frequency samples. Its formula and transform are given by

$$b(\tau) = \frac{\sin(\pi B \sqrt{\tau^2 - \tau'^2})}{\pi I_0(\pi B \tau') \cdot \sqrt{\tau^2 - \tau'^2}} \leftrightarrow B(f) = \begin{cases} \frac{I_0(\pi \tau' \sqrt{B^2 - 4f^2})}{I_0(\pi B \tau')} & |f| < \frac{B}{2} \\ 0 & |f| > \frac{B}{2} \end{cases}, \quad (3.5)$$

where  $\pi B \tau' = 0, 6, 13$  for a "minimum", "normal" and "maximum" window.  $I_0$  is the modified Bessel function of the first kind and order zero. The "minimum" window is simply a rectangular window. In our measurements, we used the "normal" window. With this window,  $b(\tau)$  has a highest side-lobe level of -44 dB and its main lobe is slightly broader than when a rectangular window is applied. With the "normal" window,  $b(\tau)$  has 99.988 % of its energy in the main lobe. With the "maximum" window,  $b(\tau)$  has side-lobes smaller than -90 dB. However, because the signal-to-noise ratio in our system is limited to 40 dB, a "maximum" window would not increase the dynamic range. With a "normal" window and  $B=2$  GHz, a time-domain resolution of 1 ns is achieved.

### 3.2.3 Alignment of time axis

When the reference port and test port are interconnected, the time-domain response after calibration shows as a unit pulse at  $\tau=0$  seconds excess delay. The moment  $\tau=0$  can therefore be considered as a common origin for all subsequent time-domain measurement results. Due to the varying distances between transmitter and receiver, measured impulse responses did not have the line-of-sight (LOS) ray displayed at  $\tau=0$ . In order to obtain an ensemble of impulse responses with mutually aligned  $\tau$ -axis, all profiles were shifted in time so that their LOS rays were all positioned at a common origin. If the LOS ray could not be clearly discerned in a response, its position was checked by placing a piece of absorber in the LOS path and noting the response change.

## 3.3 Antenna design

### 3.3.1 Desired antenna properties

The design of mm-wave antennas to be applied in the measurement setup should receive considerable attention since their radiation patterns will have a great impact

on the channel's propagation characteristics. This implies that the measurement results only reflect the channel characteristics with similar antennas. Hence; the antennas to be applied in the measurement setup should have a strong similarity to those expected to be applied in the actual radio networks. Therefore, we will focus on antennas with desirable properties for such applications. This means that we have to deal with the conflicting requirements of relatively high levels of transmitted power needed for reliable broadband transmission on the one hand, and technology, cost and safety constraints on the other. The requirement with respect to transmitted power can be relaxed by using antennas that exhibit radiation patterns with more directivity. The application of antennas with radiation patterns having some directivity in the elevation plane is illustrated in Fig. 3.2.

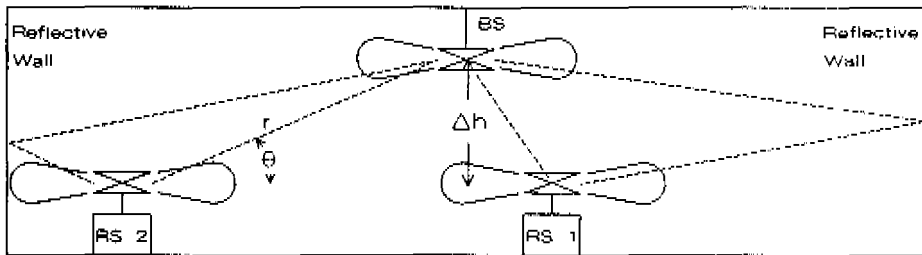


Fig. 3.2: Lay-out of the antenna setup.

This figure shows, schematically, a typical lay-out of an indoor radio network consisting of a central base station (BS) with its antenna located in the middle of the indoor area and two remote stations (RS<sub>1</sub> and RS<sub>2</sub>). All antennas exhibit an omnidirectional radiation pattern in the azimuth plane. This offers the advantage of avoiding cumbersome pointing of a remote station (RS) antenna towards the BS antenna after each significant displacement of the RS. The antenna gain functions thus solely depend on the elevation angle  $\theta = \arcsin(\Delta h/r)$ , where  $\Delta h$  is the mutual difference in height between the BS antenna and the RS antenna positions and  $r$  is the separation distance between the BS antenna and the RS antenna considered.

If only the direct ray is considered, then the received power  $P_r$  versus separation distance  $r$  can be determined by the well-known radio equation. We assume that the receive antenna and transmit antenna have an identical antenna gain function  $G_a(\theta)$ . Substituting this, together with  $\sin\theta = \Delta h/r$ , in the radio equation yields

$$P_r(\theta) = G_a^2(\theta) \left[ \frac{\lambda_0 \sin\theta}{4\pi\Delta h} \right]^2 P_t, \quad (3.6)$$

where  $\lambda_0$  is the wavelength in free space. In theory it is thus possible to achieve that the received power is independent of the (horizontal) position of the RS by taking  $G_e(\theta) \sim \text{cosec}\theta$ , provided that  $\Delta h \neq 0$ . The ability of the antennas to provide about equal received power for all RS positions would be a desirable feature since it would contribute to uniformity in performance of the various links in the radio network<sup>2</sup>.

Since we consider the design for antennas to be used for well-defined channel measurements, the antenna design should not only yield a well-defined radiation pattern but also a well-defined polarization state of the radiated field; in fact both these features are a prerequisite for measurement antennas.

### 3.3.2 Design procedure

#### 3.3.2.1 General Approach

We consider biconical-horn antennas with a geometry as depicted in Fig 3.3. They consist of the radial section, i.e., the spacing between the lower antenna part and upper antenna part with spacing distance  $a$  and diameter  $b$ , a circular waveguide with interior diameter  $d$ , and a biconical horn with length from the (virtual) horn apex in the radial section to the centre of the horn aperture  $L$  and aperture width  $A$ .

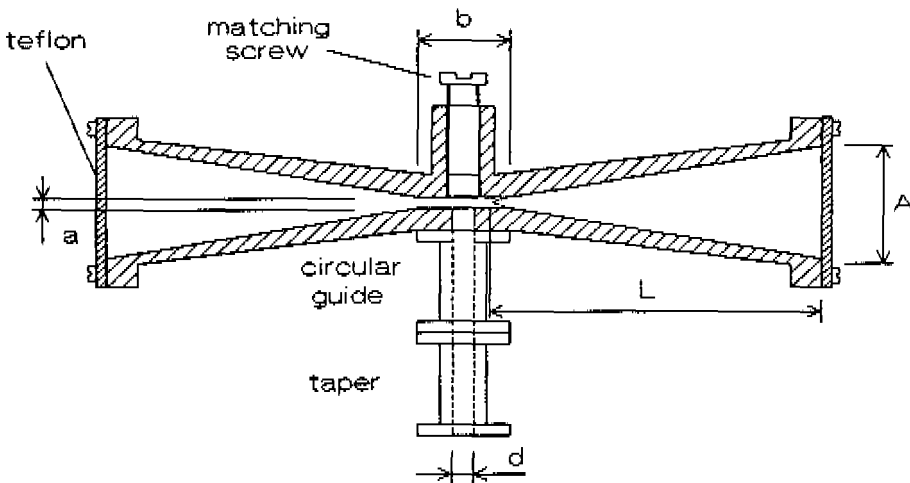


Fig. 3.2: Cross-section of a biconical-horn antenna.

<sup>2</sup> This, e.g., provides a measure to tackle the near-far problem which may occur in radio networks in which random access and/or spread spectrum is applied [2].

The design procedure can be subdivided in three parts corresponding to the following design objectives:

- 1) The achievement of the desired elevation dependence of the radiation pattern. (approximate cosec $\theta$  pattern).
- 2) The achievement of the desired azimuth independence of the radiation pattern. (rotationally symmetrical pattern).
- 3) The achievement of the desired polarization state of the radiated field.

In what follows, we show how each of these design objectives can be realized.

### 3.3.2.2 Achievement of the desired elevation dependence of the radiation pattern

In this section, it is shown how biconical-horn antennas can be designed to yield a radiation pattern that approaches a cosec $\theta$  dependence in elevation. This can be achieved for RS's that are located within a limited but sufficiently large area around the BS.

The elevation dependence of the radiation pattern is determined by the horn dimensions  $L$  and  $A$ . The path length  $l$  from the apex to the aperture increases toward the horn edges. Thus, a wave front, arriving at the aperture positions displaced from the aperture centre, lags in phase relative to its arrival at the centre. The phase variation in the aperture plane is given by  $\exp(-j2\pi(l-L)/\lambda_0)$ . This complies with the phase distribution in the aperture of an  $E$ -plane sectorial horn (i.e., a rectangular horn that is only flared out in the plane of the electric field  $E$ ) with length  $L$  and aperture width  $A$  in the  $E$ -plane. The radiation pattern can therefore be calculated by the methods described for sectorial horns excited with the corresponding mode, which is the  $TE_{01}$  mode in our case [3]. The normalized magnitude of the electric field in an elevation plane, i.e.,  $|F(\theta_s)| \equiv |E(\theta)|/|E(0)|$  with  $\theta = \arcsin(\Delta h/r)$  can be expressed as

$$|F(\theta_s)| = \frac{1 + \cos(\theta)}{2} \left[ \frac{[C(r_2) - C(r_1)]^2 + [S(r_2) - S(r_1)]^2}{4[C^2(2\sqrt{s}) + S^2(2\sqrt{s})]} \right]^{1/2}, \quad (3.7)$$

where  $C(x)$  and  $S(x)$  are the Fresnel integrals defined as

$$C(x) = \int_0^x \cos\left[\frac{\pi t^2}{2}\right] dt \quad , \quad S(x) = \int_0^x \sin\left[\frac{\pi t^2}{2}\right] dt \quad , \quad (3.8)$$

and

$$r_1 = 2\sqrt{s} \left[ -1 - \frac{1}{4s} \left[ \frac{A}{\lambda_0} \sin\theta \right] \right] \quad , \quad r_2 = 2\sqrt{s} \left[ 1 - \frac{1}{4s} \left[ \frac{A}{\lambda_0} \sin\theta \right] \right] \quad , \quad (3.9)$$

with parameter  $s$  being

$$s = \frac{1}{8} \left[ \frac{A}{\lambda_0} \right]^2 \frac{1}{L/\lambda_0} \quad . \quad (3.10)$$

The directivity  $D$  of the biconical antenna can be obtained by

$$D = \frac{4\pi}{\int_0^{2\pi} \int_{-\pi/2}^{\pi/2} |F(\theta)|^2 \cos\theta d\theta d\varphi} \quad , \quad (3.11)$$

while the antenna gain function  $G_a(\theta)$  can be written as

$$G_a(\theta) = L_a L_m D |F(\theta)|^2 \quad , \quad (3.12)$$

where  $L_a$  represents the antenna losses and  $L_m$  represents impedance mismatches. A typical value of  $L_a$  for horn antennas [3] is  $L_a = 0.8$ .

If only the direct ray is considered, then the received power versus separation distance can be determined by combining (3.7) to (3.12) and substituting the resulting  $G_a(\theta)$  in the radio equation. This yields

$$P_r(r, \theta) = G_a^2(\theta) \left[ \frac{\lambda_0}{4\pi r} \right]^2 P_t \quad . \quad (3.13)$$

In order to show how biconical-horn antennas can be dimensioned in such way that the level of (normalized) received power does not depend strongly on  $r$  within a certain region we define the (*directly-illuminated*) coverage area as the area around the BS in which the antenna of an RS must be located to meet

$$\beta_1^2 \geq 0.5\beta_{1,max}^2 \quad , \quad (3.14)$$

where  $\beta_1^2$  is the (normalized) received power. The subscript "1" expresses the fact that we only consider the received power associated with the direct ray.  $\beta_{1,max}^2$  is the maximum obtainable (normalized) received power associated with the direct ray.

Fig. 3.4 shows the level of received power (relative to the maximum level of received power considered) versus  $(\lambda_0/A)(r/\Delta h)$  for different values of the parameter  $s$ . The factor  $(1+\cos\theta)/2$ , which appears in (3.7), is not included in Fig. 3.4. It has only a small effect for most situations and may be neglected.

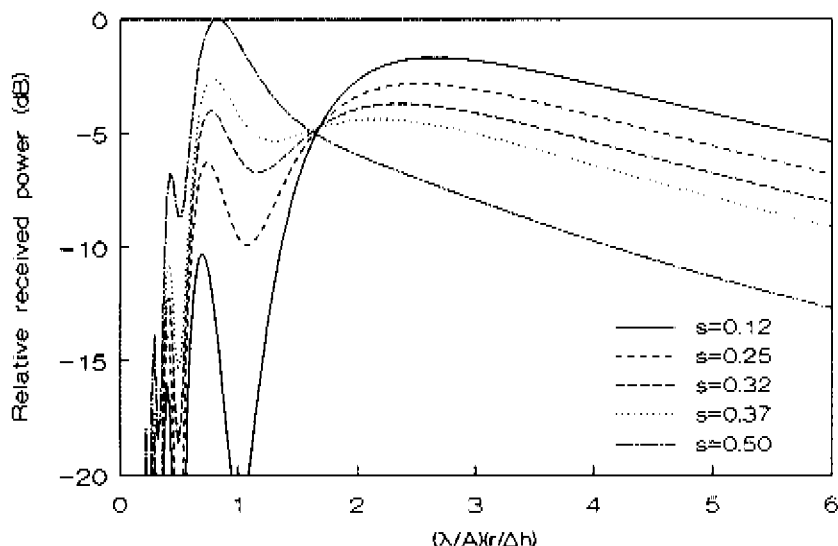


Fig. 3.4: Universal coverage curves.

The plots in Fig. 3.4 show a high dependence of received power on  $(\lambda_0/A)(r/\Delta h)$  as well as relatively low levels of received power in the range  $(\lambda_0/A)(r/\Delta h) < 0.6$ . Hence;  $r_{min}$  should be taken so that  $(\lambda_0/A)(r_{min}/\Delta h) > 0.6$ .

Within the range of interest, i.e.,  $(\lambda_0/A)(r/\Delta h) > 0.6$  each curve shows one or two local maxima. In accordance with (3.14), we can take the -3 dB values of  $(\lambda_0/A)(r/\Delta h)$  with respect to these maxima as the achievable minimum and maximum value associated with  $r_{min}$  and  $r_{max}$ , respectively. Table 3.1 lists these limits for each local maximum. In addition, values of  $r_{max}/r_{min}$  are given which determine the extent of the coverage area in case  $r_{max}$  or  $r_{min}$  is specified. Furthermore, Table 3.1 includes values of the local maxima themselves which provide an indication of the power penalty that must be paid for the achievement of a particular coverage area.

The fact that values of  $(\lambda_0/A)(r/\Delta h)_{max}$  do not exceed 5.5 is related to the fact that beyond this value the  $r$ -dependence of the curves asymptotically approaches -6 dB per doubling of  $r$ . Hence; the free space losses in this "distant" range are not effectively compensated by the gain function of both antennas.



Table 3.1: Coverage data

$s$	$(\lambda_0/A)(r_{min}/\Delta h)$	$(\lambda_0/A)(r_{max}/\Delta h)$	$r_{max}/r_{min}$	$P_{r,max}$ (dB)
0.12	0.6	0.9	1.5	-10.3
0.12	1.6	5.5	3.4	-1.7
0.25	0.6	1.1	1.8	-6.3
0.25	1.5	5.2	3.5	-2.8
0.32	0.6	5.0	8.3	-4.0
0.37	0.6	3.6	6.0	-2.3
0.37	1.0	4.2	4.2	-4.4
0.50	0.6	1.2	2.0	0

The fifth row is of special interest because the associated curve has two local maxima of equal value within the range  $(\lambda_0/A)(r_{min}/\Delta h) < (\lambda_0/A)(r/\Delta h) < (\lambda_0/A)(r_{max}/\Delta h)$  whereas the local minimum in between lies exactly 3 dB below these maxima. Variation of  $s$  learns that the value  $s=0.32$  is optimum in the sense that it provides the largest value of  $r_{max}/r_{min}$  and therefore, in case  $r_{max}$  or  $r_{min}$  is specified, the largest coverage area. It can be readily deduced from Table 3.1 that choosing parameter values according to the first, third and seventh row does not yield any advantage when compared with parameter values according to the fifth row. Therefore, these alternatives are not taken into consideration in what follows.

Now, we demonstrate how Table 3.1 can be used to find a compromise between antenna dimensions, extent of the coverage area and level of received power. For this we consider an example in which  $\lambda_0=5.2$  mm and  $\Delta h=1.6$  m while we want to create a coverage area around the BS in which an RS can be located with a maximum separation distance  $r_{max}=48$  m. From this requirement, we can readily calculate values of  $A$ ,  $L$  (by using (3.10)) and  $r_{min}$  for the remaining rows in Table 3.1. The result is listed in Table 3.2.

Dimensioning the antennas according to the first or fifth row of Table 3.2 leads to unpractically large antenna dimensions and a (relatively) large value of  $r_{min}$ . Therefore we discard these options.

Fortunately, it occurs that the choice that gives the best (smallest) value for  $r_{min}$  (third row of Table 3.2) also yields the smallest antenna dimensions. Choosing this option (among the three remaining alternatives), however, implies that a power penalty of 1.2 dB resp. 1.7 dB is payed.

Table 3.2: Design options

$s$	$A$ (mm)	$L$ (mm)	$r_{min}$ (m)	$P_{r,max}$ (dB)
0.12	173	600	32	-1.7
0.25	30.0	86.6	13.8	-2.8
0.32	31.2	73.1	5.8	-4.0
0.37	43.3	122	8.0	-2.3
0.50	130	813	24	0

So far, we only considered the direct ray. The reflected rays shown in Fig. 3.2 provide a coverage area in the same manner as the direct ray. We denote such region as *indirectly-illuminated coverage area* which we define as the area in which the antenna of an RS must be located to meet

$$\beta_n^2 \geq 0.5\beta_{n,max}^2, \quad n=2,3,\dots,N, \quad (3.15)$$

where  $\beta_n^2$  is the (normalized) received power associated with the  $n$ th reflected ray.  $\beta_{n,max}^2$  is the maximum obtainable (normalized) received power associated with the  $n$ th reflected ray. Indirectly-illuminated coverage areas can be determined by considering the directly-illuminated coverage area in case the assumption is made that the walls are fully transparent for the direct ray. We will call this area the *virtual (directly illuminated) coverage area*. Fig. 3.5 shows a map of a rectangular room (horizontal plane) and its mirrored versions (dashed) and the virtual coverage area. This area is specified by a minimum separation distance  $r_{min}$  and maximum separation distance  $r_{max}$  with respect to the position of the BS antenna which is located in the middle of the room at position O. We denote the area within the circle with radius  $r_{min}$ , which lies symmetrically around O, the *base station (BS) area*. An RS antenna at position P is located inside the BS area and thus outside the virtual (directly illuminated) coverage area. However, the reflected ray that runs via O-Rp-P provides a coverage area as defined by (3.15). The coverage area provided by this single-reflected ray equals the area for which P', i.e., the image of P when mirrored with respect to wall W1, is positioned within the virtual (directly illuminated) coverage area. The corresponding indirect coverage area is the mirror image of the virtual area thus defined. Similar coverage areas can be defined by considering multiple-reflected rays, e.g., the one that runs via O-Rq1-Rq2-Q with images Q' with respect to W2 and Q'' with respect to W4.

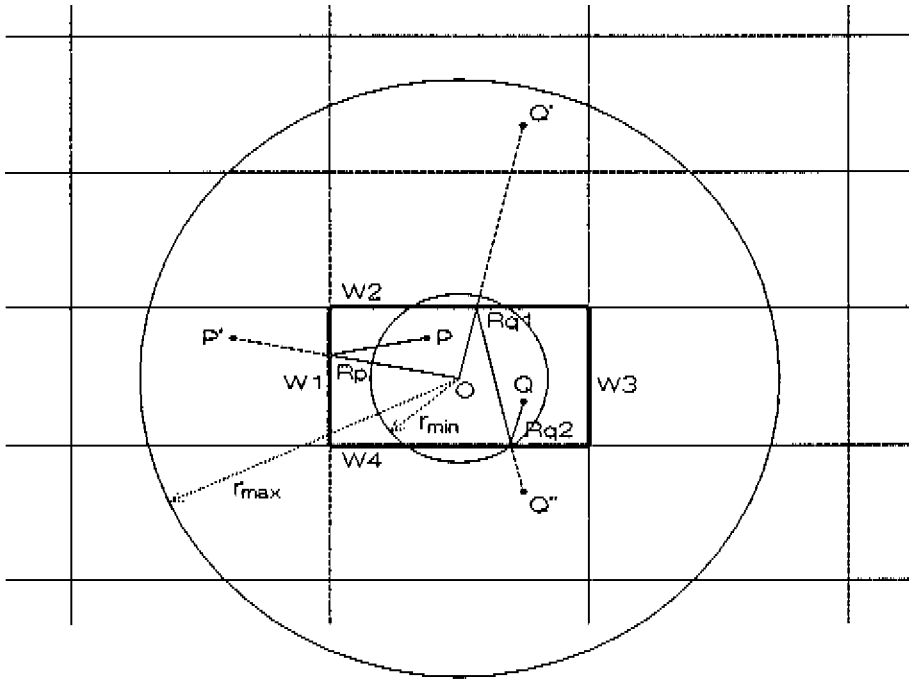


*Fig. 3.5: Map of a room, its mirrored versions and the virtual coverage area.*

In the BS area (thus for  $r < r_{min}$ ) the reflected rays are likely to dominate over the direct ray and they are therefore expected to determine the normalized received power  $P_r$ . In this area, the power contributions of reflected rays will thus yield higher values of received power than those observed when only the direct ray would be present (as in an anechoic room).

### 3.3.2.3 Achievement of the desired azimuth independence of the radiation pattern

In this section, it is shown how a rotationally symmetrical radiation pattern, with respect to the antenna axis (i.e., omnidirectional in the horizontal plane), can be achieved.

The biconical horn itself is rotationally symmetrical. This implies that a rotationally symmetrical radiation pattern with respect to the antenna axis can be achieved by ex-

citing the horn with a rotationally symmetrical mode pattern. The circular cylindrical entrance of the antenna exclusively supports the  $TE_{11}$  mode if  $0.585\lambda_0 < d < 0.764\lambda_0$  [3]. It can be readily shown that the  $TE_{11}$  mode pattern is rotationally symmetrical only in case it is circularly polarized<sup>3</sup>. Therefore, the linear  $TE_{11}$  mode has to be transformed to a circularly polarized  $TE_{11}$  mode. This can be established by a polarizer, i.e., a dielectric slab in the antenna entrance, rotated at  $45^\circ$  angle relative to the polarization vector of the incident wave. The incoming  $TE_{11}$  mode may be decomposed into two orthogonal  $TE_{11}$  modes, polarized parallel and perpendicular to the polarizer, respectively. The parallel mode has a larger propagation constant than the perpendicular mode. The length of the polarizer has to be chosen in such a way that the differential phase equals  $90 \pmod{180}$  degrees, or

$$(k_1 - k_2) \cdot l = (2n+1) \frac{\pi}{2}, \quad n = 0, 1, 2, \dots, \quad (3.16)$$

where  $l$  is the effective slab length and  $k_1$  and  $k_2$  are the propagation constants of the parallel and perpendicular mode, respectively.

### 3.3.2.4 Achievement of the desired polarization state of the radiated field

In this section it is shown how a well-defined polarization state of the radiated field can be achieved.

For  $\frac{1}{2}\lambda_0 < a < \lambda_0$ , the  $TE_{11}$  mode in the circular guide excites the  $TM_{10}$ ,  $TM_{11}$  and the  $TE_{11}$  mode in the radial section. The  $TM_{10}$  and  $TM_{11}$  modes are radiated through the biconical horn with vertical polarization whereas the  $TE_{11}$  mode is radiated with horizontal polarization [4]. As a consequence, the polarization state of the radiated field is elliptical. For  $a < \frac{1}{2}\lambda_0$ , the  $TE_{11}$  mode in the circular guide excites the  $TM_{10}$  mode in the radial section which is radiated through the horn with vertical polarization.

Suppression of the modes that support the vertical component for  $\frac{1}{2}\lambda_0 < a < \lambda_0$  is mechanically difficult so that a badly defined radiation field may be the result [5]. Such problem will not arise if we take  $a < \frac{1}{2}\lambda_0$  for the vertical polarization case.

---

<sup>3</sup> A circularly polarized  $TE_{11}$  mode implies that the entire mode pattern rotates, with respect to the waveguide axis, with angular frequency  $2\pi f$ . This is obvious when we realize that the  $TE_{11}$  mode pattern is the only pattern that can exist in the waveguide (if we assume  $0.585\lambda_0 < d < 0.764\lambda_0$ ) and consequently only the polarization state and not the pattern itself can be changed.

Therefore we consider a biconical-horn antenna with  $a < \frac{1}{2}\lambda_0$  which yields a vertically-polarized radiated field.

According to the reciprocity principle, the receive antenna transforms incident waves with vertical polarization into the circularly polarized  $TE_{11}$  mode in the circular cylindrical outlet (which supports the  $TE_{11}$  mode). By placing a slab (identical to the one at the transmitting end) in the outlet, the circularly polarized  $TE_{11}$  mode is transformed into the linearly polarized  $TE_{11}$  mode which is in turn transformed into the (linearly polarized)  $TE_{01}$  mode by a circular-to-rectangular taper.

It has to be emphasized that the transformation of linear polarization into circular polarization and vice versa is only provided in order to achieve a rotationally symmetrical radiation pattern in the azimuth plane. The circular polarization in the waveguide does not automatically generate the desired polarization state of the radiation field! As already noted, the polarization state of the radiation field is determined by the radial section spacing distance  $a$ .

### 3.3.3 Dimensioning of the biconical-horn antennas

For experimental verification, we constructed two pairs of biconical-horn antennas having a geometry as depicted in Fig. 3.3. One pair was designed to operate within a channel bandwidth of 2 GHz centered around 58 GHz ( $\lambda_0 = 5.2$  mm). The other pair was designed to operate within a channel bandwidth of 2 GHz centered around 42 GHz ( $\lambda_0 = 7.1$  mm). The design objective was to achieve the largest possible (directly illuminated) coverage area around the BS with  $r_{max} = 48$  m and  $\Delta h = 1.6$  m. In the previous section it was determined that this design objective can be met by choosing  $A = 31.2$  mm and  $L = 73.1$  mm for the 57-59 GHz band yielding  $r_{min} = 5.8$  m. For the 41-43 GHz band the dimensions are  $A = 43.1$  mm and  $L = 100$  mm. The biconical horns for the 41-43 GHz band are thus scaled versions of the biconical horns for the 57-59 GHz band. The fact that the resulting radiation patterns are nearly identical enables a fair comparison of the channel characteristics obtained in the two bands. The upper part of each antenna is fixed to the lower part by a Teflon support of  $t = \frac{1}{2}\lambda_t$  thickness enclosing the horn ( $\lambda_t$  denotes the wavelength in Teflon, being 3.7 mm and 5.0 mm for 57-59 GHz and 41-43 GHz, respectively). The matching screw is used to optimize the standing-wave ratio of the antenna.

In order to connect the biconical-horn antennas to the WR-19 waveguide hardware, rectangular to circular tapers with a length of 5 cm are used. These tapers transform the  $TE_{01}$  mode supported by the WR-19 waveguide into the  $TE_{11}$  mode

which is exclusively supported by the circular cylindrical entrance of the transmit antenna.

The polarizer in the antenna entrance is made of 0.5 mm thick Teflon ( $\epsilon_r=2$ ). Its ends are 2 mm tapered to a point in order to reduce reflections to a minimum. The effective length  $l$  is not equal to the point-to-point length, due to the slab tapering and has been determined experimentally with the mm-wave test set of the network analyzer. For this, both tapers were connected to its WR-19 test port flanges. The differential phase delay between the two modes was measured as follows: The dielectric slab was placed orthogonal with respect to the polarization of the incoming wave in the round wave guide. The phase response corresponding to a delay of  $k_1l$  was measured. After that, the slab was rotated  $90^\circ$  and the measured phase delay corresponding to  $k_2l$  was compared to that corresponding to  $k_1l$  by calculating the difference of the two phase responses. The slab length was adjusted until the differential phase equalled  $90^\circ \pm 1^\circ$  within the entire channel bandwidth. For the 57-59 GHz band, the total point-to-point slab length equalled 12 mm which corresponds to an effective slab length of 9.6 mm for  $n=1$ . The resulting differential amplitude was less than 0.01 dB.

The relevant dimensions of the various parts of the constructed biconical-horn antennas are listed in Table 3.3.

Table 3.3: Dimensions of biconical-horn antennas (mm)

Parameter	57-59 GHz	41-43 GHz
aperture width $A$	31.2	43.1
horn length $L$	73.1	100
radial section spacing distance $a$	2	3
radial section diameter $b$	10	20
antenna entrance diameter $d$	3	5
polarizer length $l$	12.0	16.6
support thickness $t$	3.7	5.0

### 3.3.4 Characteristics of the biconical-horn antennas

The standing-wave ratio (SWR) of all manufactured biconical-horn antennas could be tuned to an average value of about 1.4 over the channel bandwidth. With this

adjustment radiation patterns were measured in an anechoic room. The co- and cross-polarization radiation patterns in the azimuth plane of one of the 57-59 GHz biconical-horn antennas are depicted in Fig. 3.6.

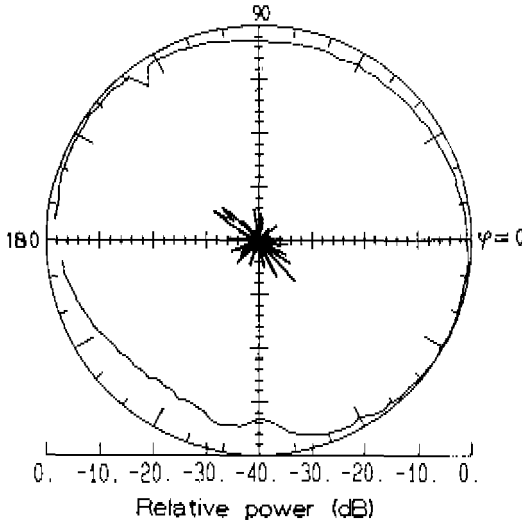


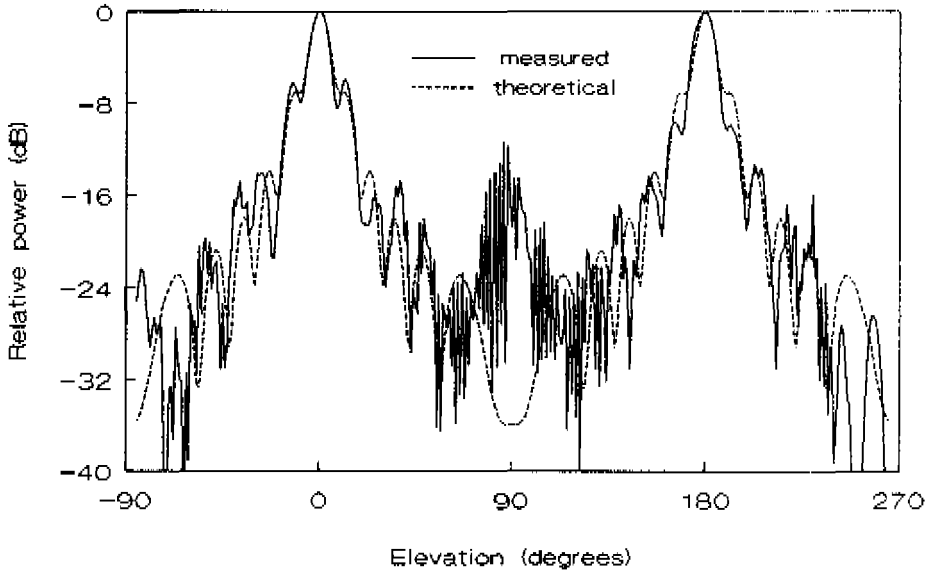
Fig. 3.6: Co- and cross polarization radiation pattern in the azimuth plane of a 57-59 GHz biconical-horn antenna.

Fig. 3.6 shows that the 2-mm spacing distance of the radial section results in vertically polarized waves with at least 25 dB suppression of the horizontally polarized components. This implies that the design objective to achieve a well defined polarization state of the radiated field, namely vertical polarization, is met. Furthermore, it shows a maximum deviation of about 2 dB from a perfectly omnidirectional radiation pattern, which implies that the design objective to achieve a rotationally symmetrical radiation pattern in the azimuth plane, is also met.

The measured radiation pattern in the elevation plane of the same antenna is depicted in Fig. 3.7 together with the theoretical pattern according to (3.7) to (3.10).

Good agreement between theoretical and measured results is shown for elevation angles in the range  $-60^\circ < \theta < 60^\circ$  (and  $120^\circ < \theta < 240^\circ$ ). Outside this range, diffracted rays originating from the horn edges become dominant [6]. These diffraction effects, which are not included in (3.7) to (3.10), might have a favourable effect since the diffracted rays cover the BS area so that they tend to extend the coverage area. The antenna directivity  $D(s)$  can be determined by pattern integration according to (3.11) which results for both measured and theoretical pattern in  $D(0.32) = 9$  dBi.

The 3 dB beamwidth of both patterns is  $9^\circ$ . The good agreement between theoretical and measured results is found for all manufactured biconical-horn antennas. This implies that the design objective to achieve an approximate  $\text{cosec}\theta$  elevation dependence of the radiation pattern is also met.



*Fig. 3.7: Measured and theoretical radiation pattern in the elevation plane.*

In conclusion, it is shown that biconical-horn antennas can be designed to yield a well-defined radiation pattern that approaches a  $\text{cosec}\theta$  dependence in elevation whereas the radiation pattern is approximately rotationally symmetrical with respect to the antenna axis. In addition, the design procedure presented yields a well-defined polarization state of the radiated field being vertical polarization.

### 3.3.5 The circular-horn antenna

In addition to the biconical-horn antennas, a circular-horn antenna was constructed for operation in a 2 GHz band centred around 58 GHz having a considerably smaller beamwidth than the radiation beams of the biconical antennas. With this antenna, additional measurement sessions were carried out in order to investigate the influence of antenna directivity on the channel characteristics. Its cross section is depicted in Fig. 3.8. The measured co-polar azimuth and elevation radiation patterns of this antenna are shown in Fig. 3.9a and Fig. 3.9b, respectively. From these figures a 3 dB



beamwidth of  $27^\circ$  in both planes can be derived. Theoretically, the beamwidths in these two planes are approximately  $24^\circ$  [4]. The directivity of this antenna is 15.2 dBi (theoretically 17 dBi). The average SWR ratio within the 57-59 GHz band is 1.4.

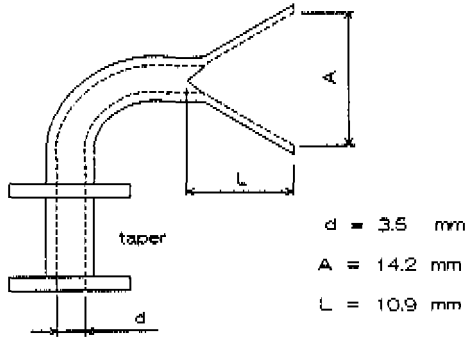


Fig. 3.8: Cross-section of the circular-horn antenna.

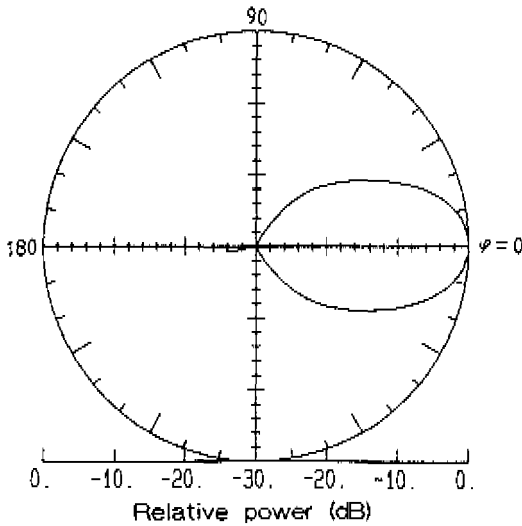


Fig. 3.9a: Measured co-polarization radiation patterns of the 57-59 GHz circular-horn antenna for the azimuth plane.

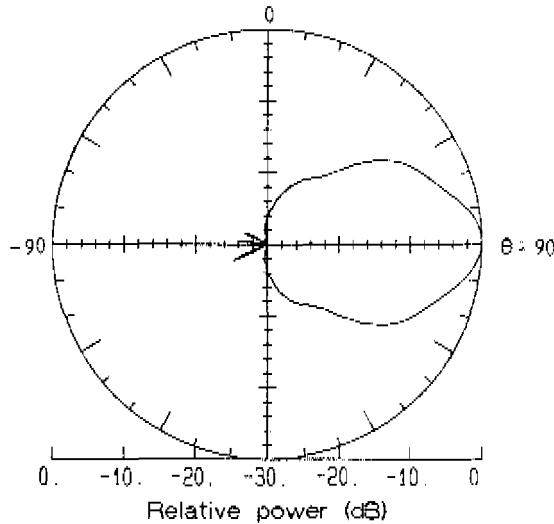


Fig. 3.9b: Measured co-polarization radiation patterns of the 57-59 GHz circular-horn antenna for the elevation plane.

### 3.4. Description of the indoor environments under consideration

With the antennas described above, measurements were carried out in eight different indoor environments at the University. These environments consist of one single room, a single corridor, or a single hall only, because millimetre waves are severely attenuated by most inner walls. In the following these environments are denoted A to H.

Environment A (Reception Room in the Auditorium Building, also denoted as "Room A") is an empty, almost perfectly rectangular room with dimensions  $24.3 \times 11.2 \times 4.5 \text{ m}^3$ . One (long) side is completely windowed with double thermopane glass in a steel framework from floor to ceiling. The walls are mainly made of wood. The concrete floor is covered with carpet. The ceiling is a complex structure made of plastic.

Environment B (Large Room in the Auditorium Building) is an amphi-theatre-shaped room with approximate dimensions of  $30 \times 21 \times 6 \text{ m}^3$ . The walls and ceiling are made of wood covered by acoustically soft material (rock wool). The central floor on which the measurement equipment was located is made of wood. Cushioned chairs are placed in an amphi-theatre-like manner on two sides of the central floor. A number

of chairs are also lined up on the central floor. The transmitter was moved randomly among them. The ceiling is covered with plastic panelling with lighting holders and spotlights.

Environment C (Large Hall in the Auditorium Building) has a complex structure with approximate dimensions  $43*41*7$  m<sup>3</sup>. Dominant objects are four staircases which lead to the balustrade of the second floor. The walls and ceiling consist of plastered concrete. The floor consists of linoleum glued on concrete. Some tables and chairs are placed throughout the hall.

Environment D (Vax Room in the Computing-Center Building also denoted as "Room D") has a complex structure with dimensions of  $33.5*32.2*3.1$  m<sup>3</sup>. The room has a bare concrete wall, one metal wall and two glass sides. The floor is linoleum glued on concrete. Many large mainframe computer and filing cabinets are dominant objects in this room.

Environment E (Corridor in the Computing-Center Building) is a straight, empty corridor with dimensions  $44.7*2.4*3.1$  m<sup>3</sup>. The long sides are smooth metallic walls up to a height of 2.5 m and windows above. Swivelling doors with glass in a wooden frame are located half way down the corridor. These doors were open during the measurements except for one additional experiment in which the transmissivity of the glass was measured. The floor is covered with thin carpeting and the ceiling is made of aluminum profiles with lighting holders.

Environment F (Computer Room in the Computer-Center Building, also denoted as "Room F") is a rectangular Room with dimensions  $9.9*8.7*3.1$  m<sup>3</sup>. One (long) side consists of large floor to ceiling double-glazed windows encased in a steel frame while the other sides are smooth metallic walls. Some 20 personal computers are lined up against these walls. Wooden chairs and tables with metal legs are lined up through the room.

Environment G (Lecture Room in the Auditorium Building also denoted as "Room G") is a typical rectangular class room with dimensions  $12.9*8.9*4.0$  m<sup>3</sup>. One (long) side consists of large windows in a steel framework from 1 m height to ceiling. Up to 1 m height there is concrete. The other sides are walls which are completely covered with wooden lathing. The concrete floor is covered with linoleum. The ceiling is covered with lighting holders. Tables and chairs are lined up throughout the room.

Environment H (Laboratory Room in the Faculty Building of Electrical Engineering, also denoted as Room H) is rectangular with dimensions 11.3\*7.3\*3.1 m<sup>3</sup>. One (short) side consists of a window from 1 m height to the ceiling and a metal heating radiator case below. The other walls consist of smoothly plastered concrete. The floor is linoleum on concrete. Four square (0.5\*0.5 m<sup>2</sup>) concrete pillars and a metal cupboard in a corner are dominant objects in this room. A number of large wooden benches with wooden shelves on top are located in this room. The ceiling consists of aluminum plates and lighting holders.

### 3.4.1 Transmissivity properties

In order to get an impression of the transmissivity properties of the superstructure of a typical indoor environment at 57-59 GHz, some ad-hoc transmission measurements have been carried out.

In Environment E, a transmission experiment was performed at 57-59 GHz by closing the two swivelling glass doors between the transmit and receive antenna. As a result the NRP dropped only 4.8 dB whereas the RDS increased from 64 to 68 ns. This propagation experiment shows that radio-waves at 57-59 GHz can pass through windows very well. The change in the RDS may be caused by some "new" rays which "bounce" between the glass doors.

An additional transmission experiment was performed for a 15 cm thick concrete wall at 57-59 GHz. The NRP level was -116 dB and thus barely exceeded the -120 dB receiver noise floor. Under LOS conditions the NRP would be -80 dB, hence; the transmission attenuation was about 36 dB.

Ganesh and Pahlavan [8] reported a transmission attenuation of 3-7 dB at 60 GHz through doubly-glazed windows. Tharek and McGeehan [9] reported a 27 dB transmission attenuation through a concrete wall at 60 GHz. These figures thus comply fairly well with our measurement results.

### 3.4.2 Reflection properties

In order to be able to relate the measurement results obtained to the reflection properties of the indoor environment we measured the *return loss* of some typical indoor walls. This parameter is defined in dB as

$$R_{dB} = 20 \log \left[ \frac{\beta_{reference}}{\beta_{test}} \right] , \quad (3.17)$$

in which  $\beta_{test}$  is the amplitude of the received echo pulse that originates from a perpendicular reflection against the wall under test whereas  $\beta_{reference}$  is the amplitude of the corresponding echo pulse in case the wall under test is covered by a metal plate obtained under the same measurement conditions. We used a 1 m<sup>2</sup> aluminium square-shaped plate, 1 mm thick, with its center located at the geometric optical reflection point. The results are listed in Table 3.4.

Table 3.4: Measured Return Loss.

Environment	Material	$R_{dB}$	
		41-43 GHz	57-59 GHz
Room A	windows	2.1	13.1
	wooden doors	3.2	3.9
	wooden panels	9.6	7.9
Room G	wooden laths	–	13.0
Room H	concrete walls	–	2.0
	metal	0	0

### 3.5 Determination of normalized received power and rms delay spread

NRP and RDS values of *measured* impulse responses cannot be determined exactly according to (2.16) and (2.18)-(2.19), respectively, since the span of the integral in the numerator of (2.16) and the span of both integrals in (2.19) are infinite whereas the aliasing-free range is finite. Moreover, the actual impulse response is contaminated with (additive) noise. The NRP can, however, be approximated by

$$\frac{P_{r,k}(\tau_{max})}{P_i} = \frac{\int_0^{\tau_{max}} |r_k(\tau) + n_k(\tau)|^2 d\tau}{\int_{-\infty}^{\infty} |b(\tau)|^2 d\tau}, \quad i=1,2 \quad (3.18)$$

where  $\tau_{max}$  is the maximum excess time up to which data points are included in the calculation of the impulse response.  $n_k(\tau)$  represents the noise component of the  $k$ th measured impulse response  $r_k(\tau) + n_k(\tau)$ . The RDS can be approximated by

$$\sigma_{ms,k}(\tau_{max}) \triangleq \sqrt{\tau_k^2 - (\bar{\tau}_k)^2} \quad , \quad (3.19)$$

with

$$\bar{\tau}_k(\tau_{max}) = \frac{\int_0^{\tau_{max}} \tau |r_k(\tau) + n_k(\tau)|^2 d\tau}{\int_0^{\tau_{max}} |r_k(\tau) + n_k(\tau)|^2 d\tau} \quad , \quad i=1,2 \quad . \quad (3.20)$$

For all NRP and RDS calculations we took  $\tau_{max}=390$  ns. The 390-400 ns range was excluded to avoid residual aliasing.

The maximum excess time has a more profound influence on the reliability of the RDS values obtained than on the reliability of NRP values obtained since the echo pulses are weighed more heavily with increasing excess time in the RDS calculation than in the NRP calculation where all echo pulses have equal weight. Hence; the "tail" of the impulse response yields a more significant contribution to the RDS than to the associated NRP. Therefore, we only examine the influence of maximum excess time on RDS. For this, we consider the measured *average power delay profile* (average PDP)  $p_{av}(\tau, \tau_{max})$  which is defined for each measurement subset consisting of  $K$  (about 20) impulse responses as

$$p_{av}(\tau, \tau_{max}) = \frac{1}{K} \sum_{k=1}^K \left[ |r_k(\tau) + n_k(\tau)|^2 \cdot \frac{P_i}{P_{r,k}(\tau_{max})} \right] \quad . \quad (3.21)$$

In calculating the average PDP, each individual PDP is thus weighed with the corresponding NRP value. This is done because a single PDP should not dominate in the average PDP.

We calculated the RDS of the average PDP as function of  $\tau_{max}$  for subsets obtained in the 57-59 GHz band with a configuration in which the transmit and receive antenna were the biconical-horn antennas with characteristics as described in Section 3.3.4. The transmit antenna was located at 1.4 m above the floor at  $K$  randomly-chosen (horizontal) positions. The receive antenna was placed in the centre of the environment under test at 3 m height. In what follows, this configuration is referred to as the *(57-59 GHz) standard configuration*. In each of the eight environments described in the previous section, one subset of impulse responses was obtained with this standard configuration. For each of these eight subsets, the RDS of the average PDP is calculated according to

$$\sigma_{rms,av}(\tau_{max}) \triangleq \sqrt{\overline{\tau^2} - (\overline{\tau})^2} \quad , \quad (3.19)$$

where

$$\overline{\tau}(\tau_{max}) = \frac{\int_0^{\tau_{max}} \tau p_{av}(\tau, \tau_{max}) d\tau}{\int_0^{\tau_{max}} p_{av}(\tau, \tau_{max}) d\tau} \quad , \quad i=1,2 \quad . \quad (3.20)$$

In Fig. 3.10a, the RDS of the average PDP is drawn as a function of  $\tau_{max}$  for the small rooms (i.e., environments A, F, G and H) whereas Fig. 3.10b shows similar plots for the large environments (i.e., B, C, D) and the corridor (i.e., Environment E).

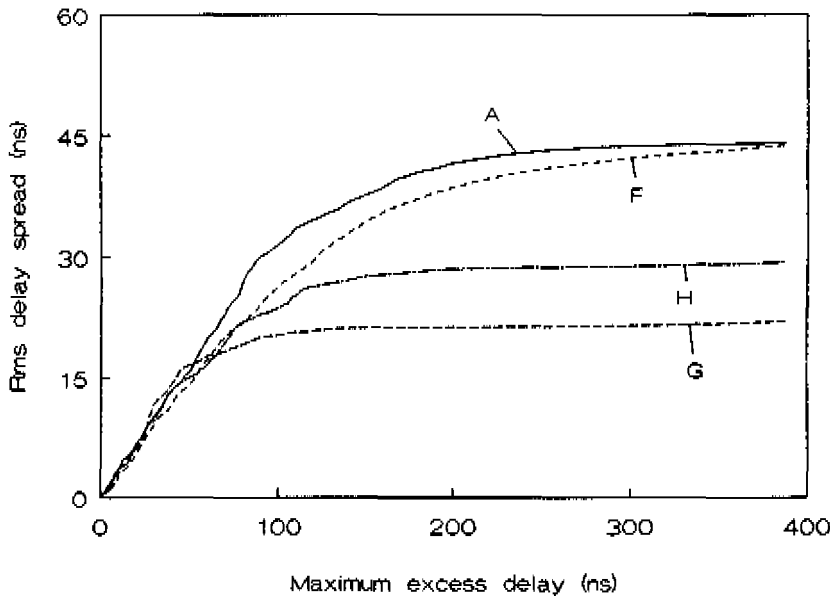
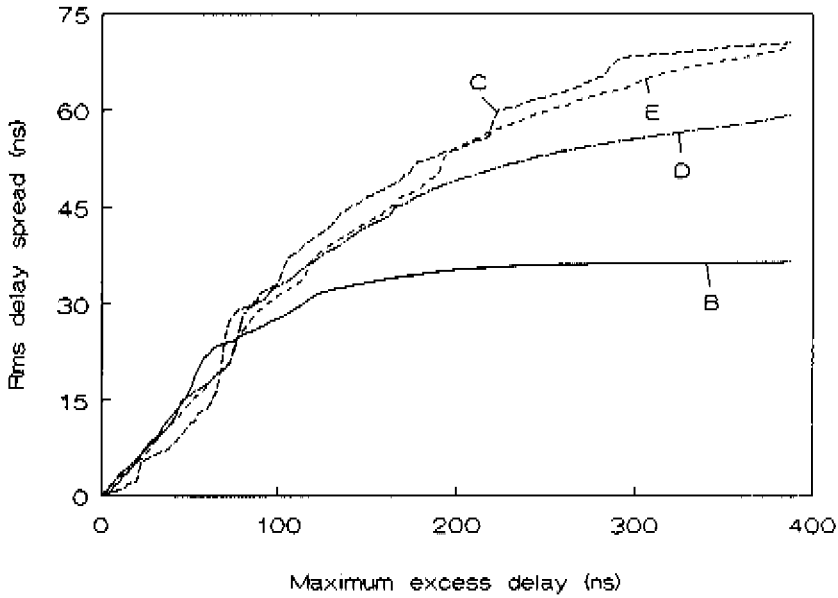


Fig. 3.10a: *Rms delay spread of the average PDP as function of the maximum excess delay considered for environments A, F, G and H obtained with biconical-horn antennas in the 57-59 GHz band.*



*Fig. 3.10b: Rms delay spread of the average PDP as function of the maximum excess delay considered for environments B,C,D and E obtained with biconical-horn antennas in the 57-59 GHz band..*

These figures demonstrate that the RDS of the average PDP does not drop sharply if  $\tau_{max}$  is reduced from 390 ns. This is also the case for the RDS of average PDPs associated with the subsets obtained with the remaining non-standard configurations. With respect to our measurement results this indicates that (3.18) to (3.23), with  $\tau_{max}=390$  ns, yield accurate RDS values. This also indicates that NRP values are determined accurately when they are calculated according to (3.18) with  $\tau_{max}=390$  ns.

### 3.6. Measurement results and discussion

In this section, the results are discussed of the large-scale measurement campaign carried out in the eight environments previously described by which some 300 impulse responses of mm-wave indoor radio channels were collected. In each environment, at least one subset of about 20 impulse responses was obtained. These impulse responses were measured in the 57-59 GHz band using the 9 dBi 57-59 GHz biconical-horn antennas. In two rooms (A and F), additional subsets of about 20 impulse responses



were obtained in the 41-43 GHz band with the 9 dBi 41-43 GHz biconical-horn antennas. Furthermore, we discuss the results of additional measurements performed in the 57-59 GHz band with the 15 dBi 57-59 GHz circular-horn antenna.

Practically all our measurements concerned line-of-sight (LOS) channels. The channels with obstructed LOS path will be designated as obstructed (OBS) channels. These OBS-channels are derived from the impulse responses obtained under LOS-conditions by mathematical removal of the direct ray. This method is justified by the experience that obstruction of the direct ray by a person, cabinet or piece of absorber caused a drop of the LOS-ray in such way that the LOS component could not be recognized anymore in the measured response. (For a discussion concerning the significance of a (partly) obstructed LOS ray see also Section 5.2.2.)

### 3.6.1 Results obtained with the 57-59 GHz biconical-horn antennas

Firstly, measurement results are presented that have been obtained in the standard configuration of each indoor environment under test (standard configuration: transmit antenna placed at randomly-chosen (horizontal) positions at 1.4 m height, receive antenna placed in the middle of each indoor area at 3 m height, frequency band is 57-59 GHz, transmit antenna and receive antenna are both 9 dBi 57-59 GHz biconical-horn antennas). With this configuration, a subset of about 20 impulse responses was obtained for each of the eight environments under test.

#### 3.6.1.1 Normalized received power

Fig. 3.11a shows scatter plots of NRP values versus separation distance on a logarithmic scale for both LOS and OBS situations obtained in the small rooms (i.e., A, F, G and H). Fig. 3.11b shows similar plots for the large environments B, C, D and E. The lines are linear fits based on the minimum mean square error (MMSE) with the relationship

$$10\log\left(\frac{P_r(r)}{P_t}\right) = 10\log\left(\frac{P_r(1)}{P_t}\right) - 10\alpha\log(r) \quad , \quad (3.24)$$

in which  $P_r(1)/P_t$  is the (fitted) value of NRP at the separation distance of 1 m, while  $\alpha$  represents the decay exponent of the fit. Parameter  $\alpha$  thus represents the slope of each regression line.

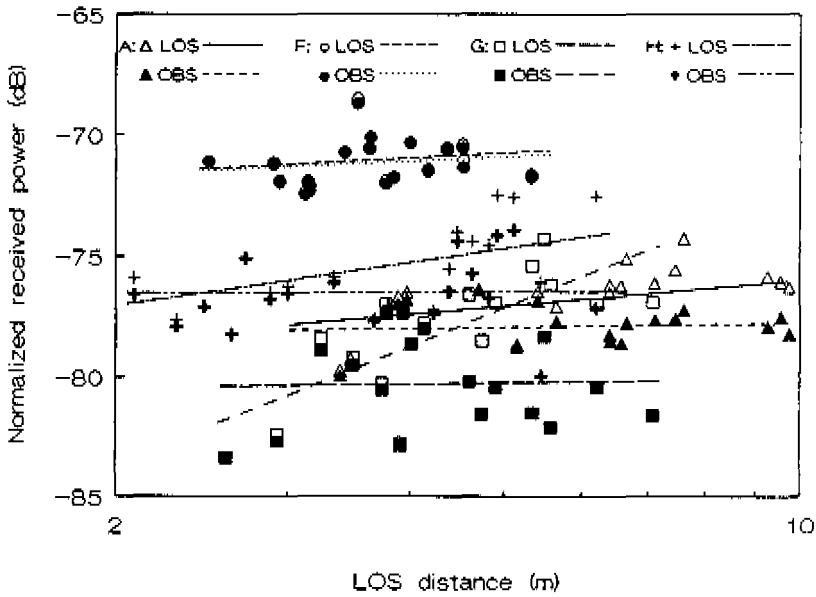


Fig. 3.11a: Normalized received power versus separation distance for environments A, F, G and H obtained with biconical-horn antennas in the 57-59 GHz band.

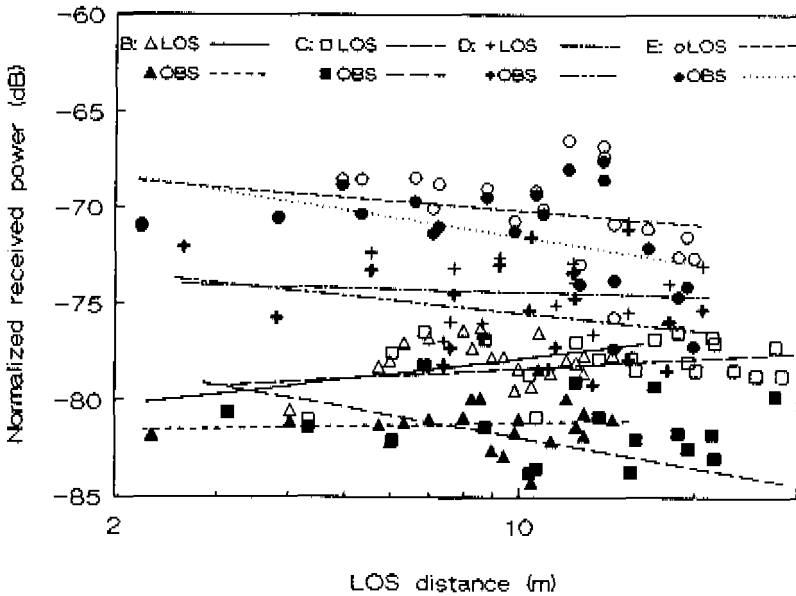


Fig. 3.11b: Normalized received power versus separation distance for environments B, C, D and E obtained with biconical-horn antennas in the 57-59 GHz band.

The decay-exponent values of all regression lines are determined and listed in Fig. 3.12 for each environment, together with average and standard deviation of the NRP values obtained. Fig. 3.12 also includes an overview of environment dimensions and return loss values in the 57-59 GHz band of the most dominant wall partitions so that the measurement results can be readily related to these environment properties.

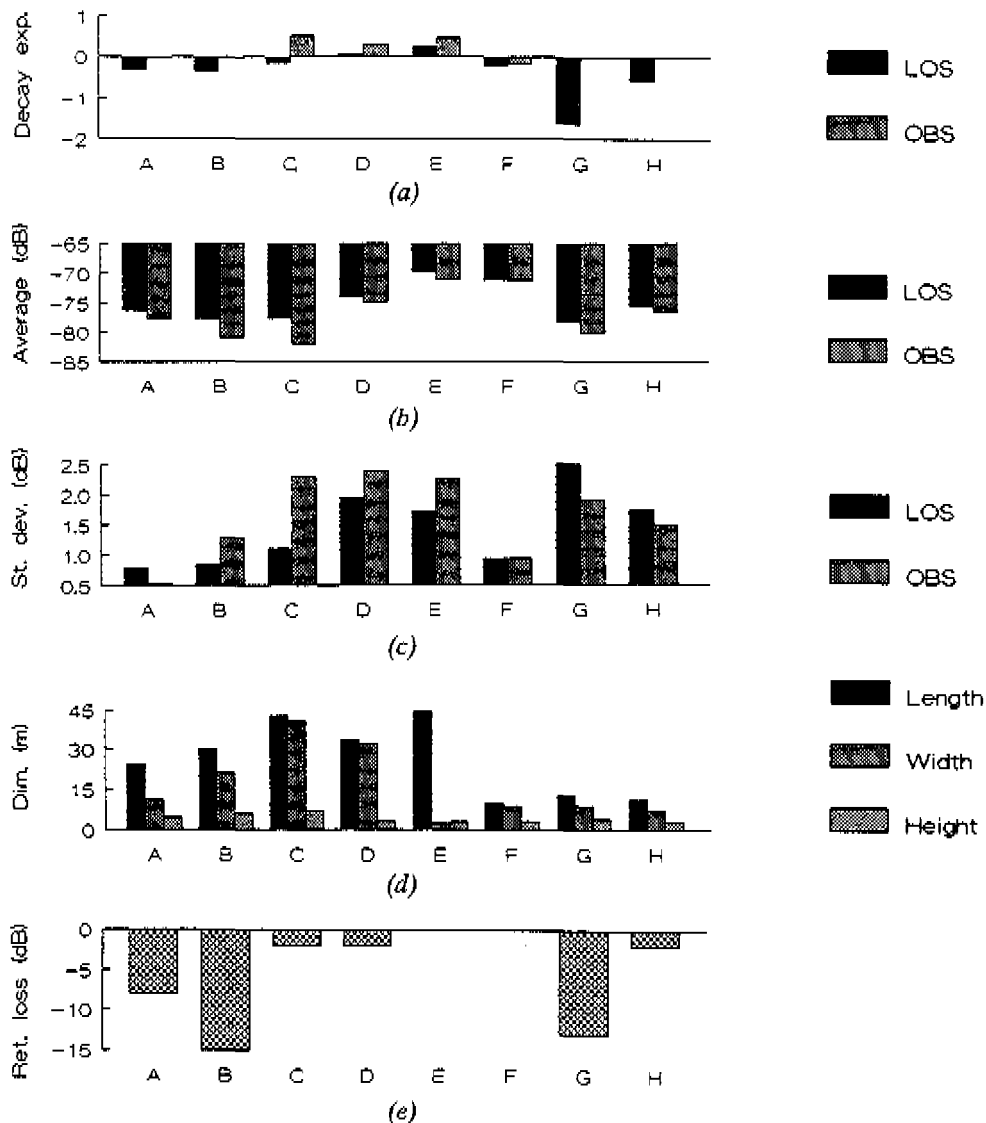


Fig. 3.12: (a) decay rate of NRP, (b) mean of NRP values, (c) standard deviation of NRP values, (d) environment dimensions, (e) return loss (57-59 GHz).

### *Decay rate of NRP with separation distance*

Especially for the large environments (B, C and D), Fig. 3.12a shows decay exponent values close to zero for LOS situations. This confirms the theory presented in Section 3.3.2.2 which predicts a ring-shaped virtual directly-illuminated coverage area (with minimum radius  $r_{min}=6$  m and maximum radius  $r_{max}=48$  m), lying symmetrically around the (horizontal) position of the centrally located antenna. The most negative value of  $\alpha$  (-1.65) is found for Room G. This can be explained by the fact that in this room: 1) the (virtual) directly-illuminated coverage area lies outside the room and 2) the reflected rays cannot dominate the direct ray because the walls of this room are made of wood, which has a return loss of 13 dB. The same effect, although less serious, can be observed for Room H with concrete walls having a return loss of 2 dB. This effect does not appear in Room F since this room has metal walls so that indirectly-illuminated coverage areas are provided by strong reflected rays. The NRP values obtained for LOS and OBS at the same position of the transmit antenna are virtually equal for this room. This indicates that the reflected rays in this small room dominate the direct ray in accordance with the principles given in Section 3.3.2.2.

### *Average of NRP values*

By mutually comparing the different average values in Fig. 3.12b for the different rooms we find high values for environments with metal walls (E and F) and environments in which highly reflective (metal) objects are present (Room D), whereas relatively low values are found in environments with only low reflective materials like wood (Room B and G). This confirms the idea that rays reflecting from metal walls and objects contribute significantly to the mean of NRP values.

In all environments, equal or lower NRP values are obtained for the BS area (i.e.,  $r < r_{min}=5.8$  m) when compared with the mean of NRP values obtained in the directly-illuminated coverage area ( $r > r_{min}=5.8$  m); in rooms with many metal walls and/or metal objects (D, E and F) no differences in mean NRP values for both areas were found, while lower values are obtained for the BS area in rooms without highly-reflective surfaces. This complies with what we expect when regarding the effects of power contributions of reflected rays (see Section 3.3.2.2).

### *Spread in NRP values*

One reason for the spread in NRP values is the irregularity of the environment; especially in Room D, in which many metal cabinets are present, reflected rays strongly depend on the specific position of the transmit antenna. In addition, the non-ideal radiation patterns (in the azimuth plane as well as in the elevation plane) of both antennas contribute to the spread in NRP values. Furthermore, constructive and destructive addition of the various (complex) rays contribute to the spread in received power.

### *Differences between LOS and OBS results*

In highly-reflective indoor environments (E and F), differences in NRP values between LOS and OBS situations are only small (a few dBs at maximum). This indicates that throughout such environments the level of NRP is maintained well in the case that the direct LOS-ray is blocked. In low-reflective environments (B, C and G), however, substantial differences between LOS and OBS can be observed due to the severe attenuation at each reflection. For separation distances in excess of the upper limit  $r_{max}$  of the indirectly-illuminated coverage area, there is also another mechanism responsible for these differences; outside this area, the power contributions of the reflected rays tend to decrease more rapidly with increasing separation distance ( $r^2$ -law) in comparison with the power contribution of the direct ray with path length below  $r_{max}$ . This explains the differences in excess of 7 dB between LOS and OBS situations which can be observed for some measurements positions at relatively large separation distances in Environment C.

#### **3.6.1.2 Rms delay spread**

From the measured responses, RDS values have been calculated according to (2.18)-(2.19) yielding values between 10 ns and 100 ns. In Fig. 3.13, the (complementary) cumulative distribution functions (CDFs) are shown for the RDS values obtained in the eight environments.

By comparing the curves G, H and F, it occurs that RDS values tend to increase with the increasing reflectivity of the walls. Room G has wooden walls ( $R_{dB}=13$  dB), Room H has concrete walls ( $R_{dB}=2$  dB) and Room F has highly-reflective walls ( $R_{dB}=0$  dB). RDS values found in the small Room F with metal walls are even larger than those found in the large Room B.

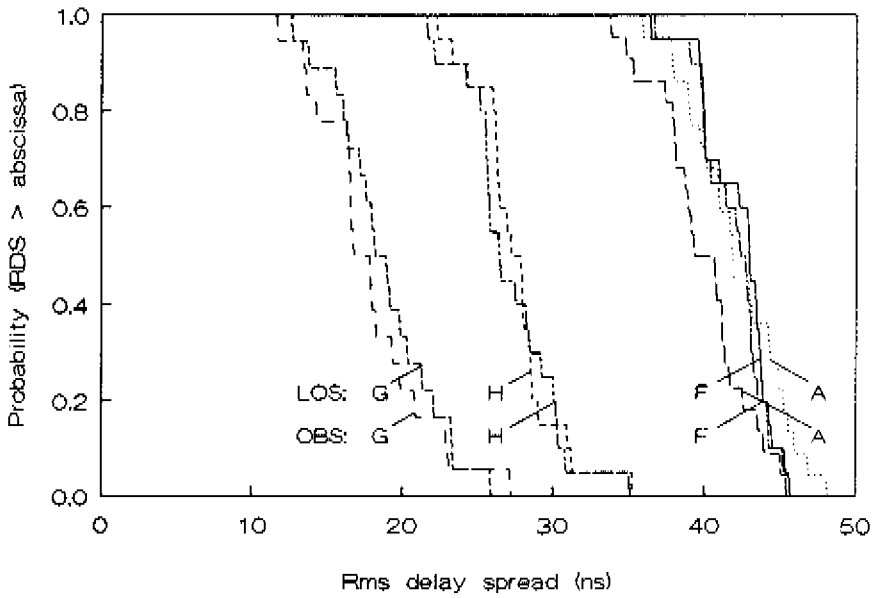


Fig. 3.13a: Distribution functions of RDS values in environments A, F, G and H obtained with biconical-horn antennas in the 57-59 GHz band.

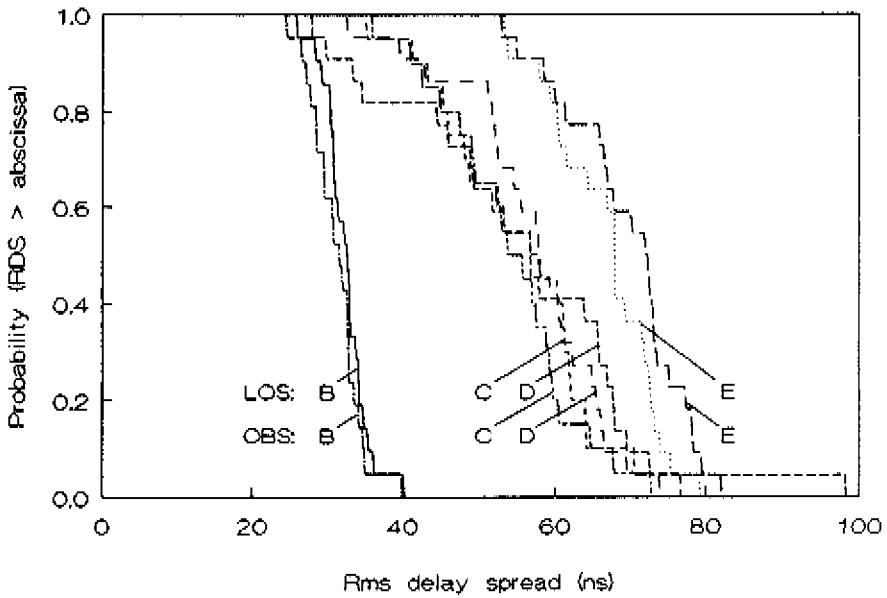


Fig. 3.13b: Distribution functions of RDS values in environments B, C, D and E obtained with biconical-horn antennas in the 57-59 GHz band.

It would be interesting to see how the RDS values alter at increasing separation distances. As an example Fig. 3.14 shows the relationship between the RDS and separation distance in Room A.

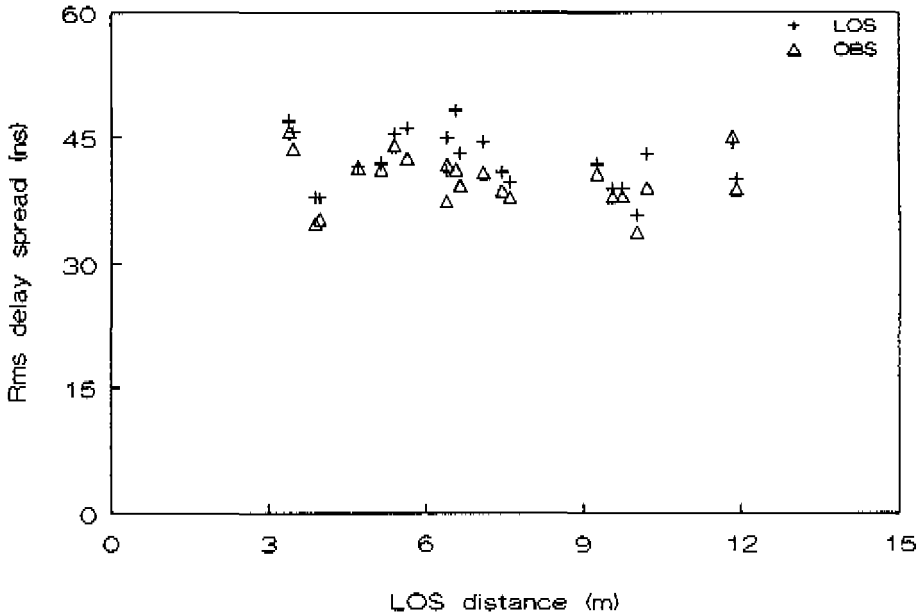


Fig. 3.14: RDS versus separation distance in Room A.

From this figure, it is clear that the RDS values also remain fairly constant for increasing distances in Room A. This property, which is also observed for the other environments, indicates that roughly the same performance degradation caused by ISI is experienced everywhere in a particular room<sup>4</sup>.

### 3.6.2 Results obtained with the 41-43 GHz biconical-horn antennas

Additional measurements in the 41-43 GHz band have been undertaken in a low and highly reflective room (Room A and Room F, respectively) with the 41-43 GHz

<sup>4</sup> Here, we mean performance degradation in terms of maximum feasible symbol rate  $r_{s,max}$ . In [10] it is shown that, for transmission systems in which no channel equalization is applied, there exists a direct, though approximate, relationship between  $r_{s,max}$  and the RDS which reads;  $r_{s,max} \approx 0.2/\sigma_{rms}$ .

biconical-horn antennas placed at the same positions as in the standard configuration.

### 3.6.2.1 Normalized received power

Fig. 3.15 shows a scatterplot of the NRP values obtained and associated MMSE regression lines.

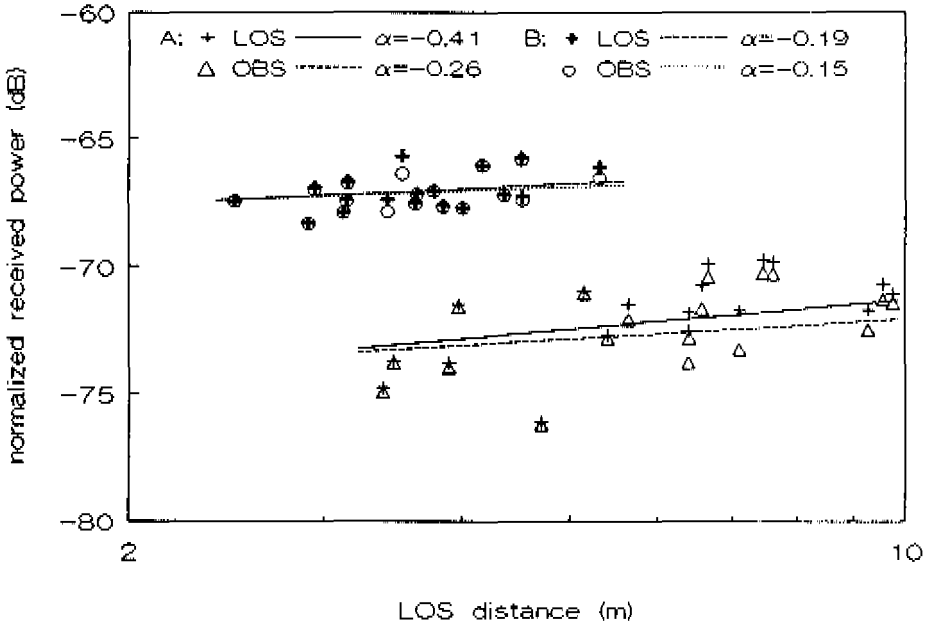


Fig. 3.15: NRP values for Room A and Room F obtained in the 41-43 GHz band.

It can be concluded that, for both rooms, the 41-43 GHz results are very similar to the 57-59 GHz results; the corresponding decay exponents are the same for both frequency bands whereas the mean of NRP values are 3 dB higher for the 41-43 GHz measurements. This 3 dB difference complies well with (3.12) which predicts an average increase in NRP of 2.8 dB at 41-43 GHz.

### 3.6.2.2 Rms delay spread

Fig. 3.16 shows CDFs of RDS values for LOS situations obtained in the 41-43 GHz band and 57-59 GHz band.



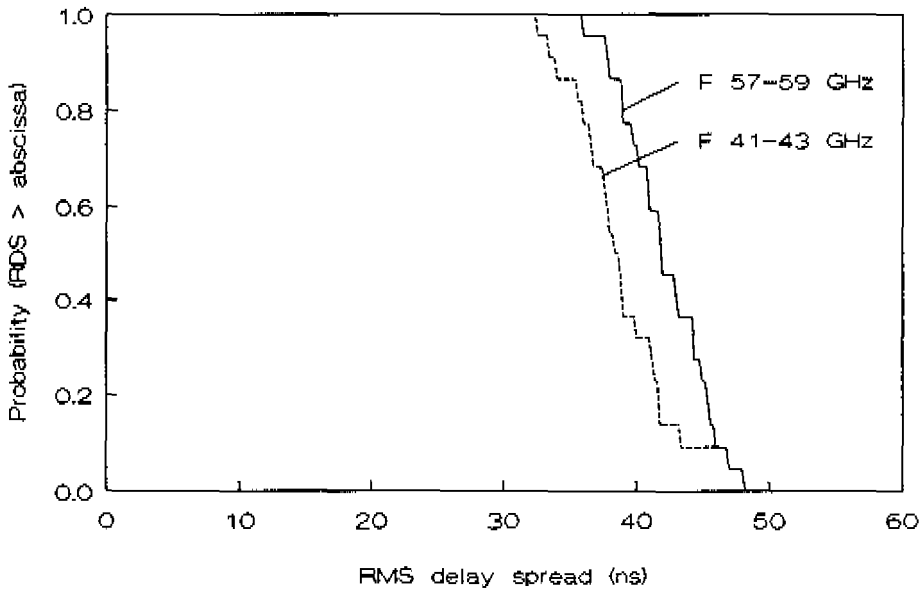


Fig. 3.16a: Distribution functions of RDS for 41-43 GHz and 57-59 GHz for Room A.

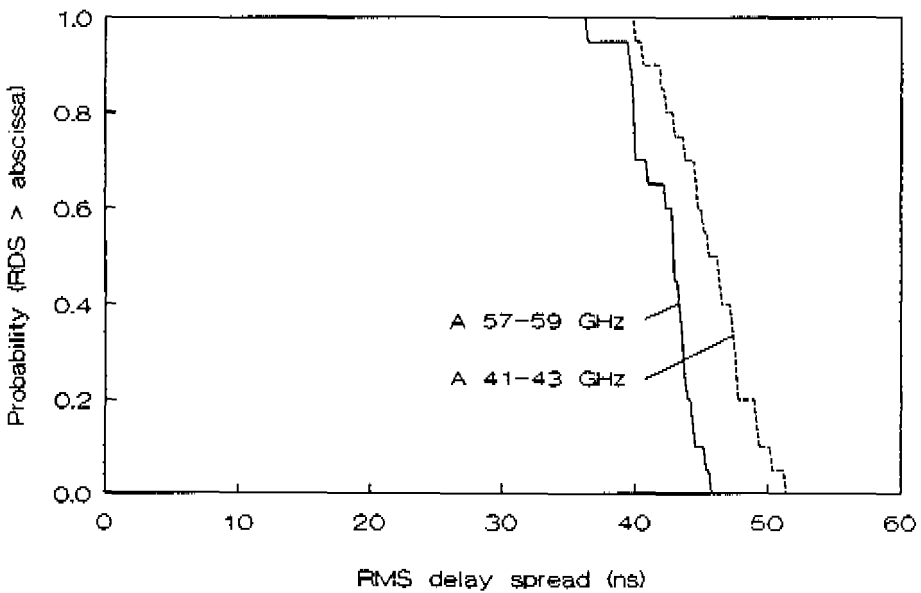


Fig. 3.16b: Distribution functions of RDS for 41-43 GHz and 57-59 GHz for Room F.

No significant differences between the two bands could be observed. This indicates that the reflectivity properties of wall material do not differ significantly for both frequency bands.

### 3.6.3 Results obtained with the circular-horn antenna in the 57-59 GHz band

In order to examine the influence of antenna radiation patterns on the NRP and RDS, we performed additional measurements in Room A using the directional (15 dBi) circular-horn antenna described in Section 3.3.5. We applied this antenna in two different measurement configurations as depicted in Fig. 3.17.

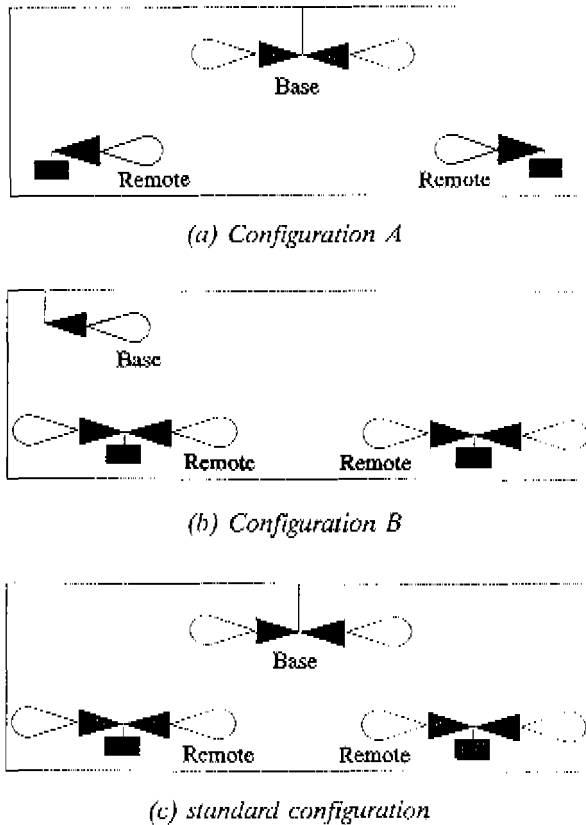


Fig. 3.17: Measurement configurations.

In one configuration the directional antenna was used as the transmit antenna. It was placed at 20 randomly-chosen (horizontal) positions 1.4 m above the floor. The receive antenna was a 9 dBi omnidirectional biconical-horn antenna positioned in the middle of the room at 3 m height. At each measurement position, the directional horn was pointing in the horizontal plane towards the receive antenna. This configuration is depicted, schematically, in Fig. 3.17a and will be denoted as "Configuration A".

In the second configuration the directional antenna was used as the receive antenna. However, it was not located in the middle of the room but in a corner at 3 m height. The boresight direction was horizontal towards the opposite corner of the (rectangular) room. The receive antenna was a 9 dBi biconical-horn antenna. It was placed at 20 randomly-chosen horizontal positions 1.4 m above the floor. This configuration is depicted in Fig. 3.17b and will be denoted as "Configuration B".

For each configuration we obtained a subset of 20 impulse responses. These two subsets will be mutually compared. In addition, these two subsets will be compared with the subset obtained in Room A with the standard configuration as defined in Section 3.5. The standard configuration is depicted in Fig. 3.17c.

### 3.6.3.1 Normalized received power

Fig. 3.18a and Fig. 3.18b are scatter plots of NRP values versus separation distance under LOS and OBS conditions for Configuration A and Configuration B, respectively. The lines are linear MMSE fits drawn for LOS and OBS situations.

Comparison of Fig. 3.18a, Fig. 3.18b and Fig. 3.11a yields the conclusion that Configuration A exhibits the highest NRP values under LOS conditions. Under OBS conditions, however, the standard configuration has the highest NRP values. The lowest spread in NRP values is observed for the standard configuration.

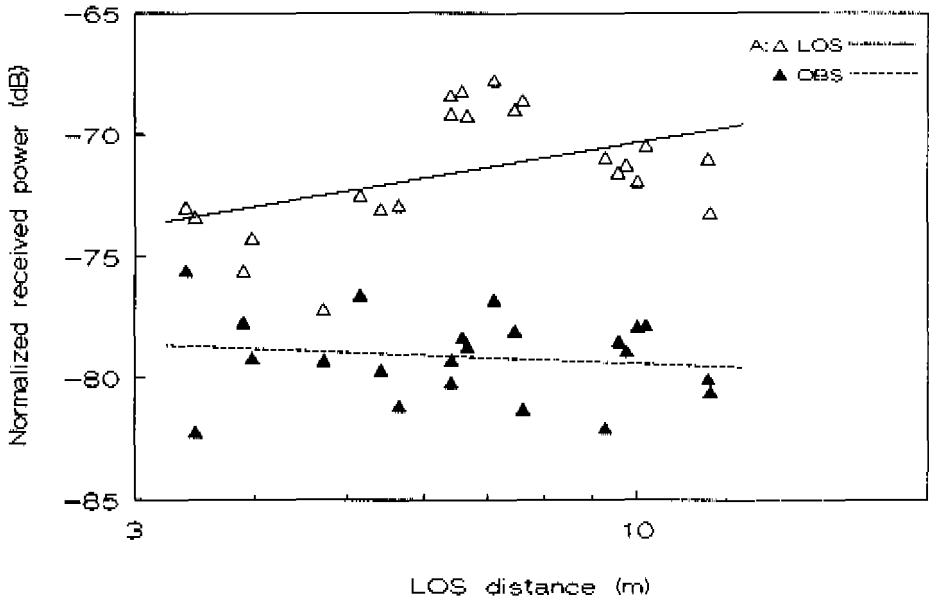


Fig. 3.18a: NRP values for Room A obtained with Configuration A.

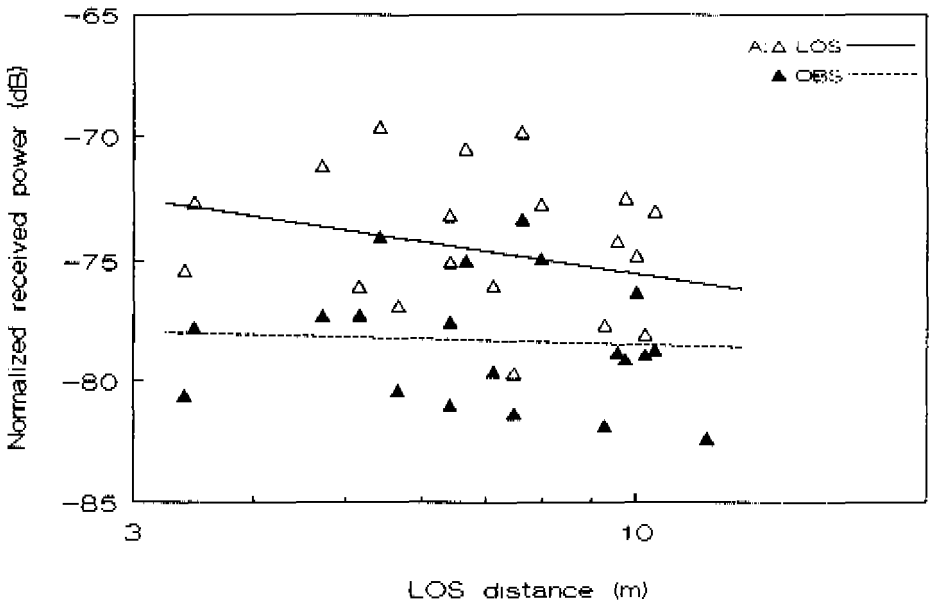


Fig. 3.18b: NRP values for Room A obtained with Configuration B.

## 3.6.3.2 Rms delay spread

Fig. 3.19 depicts the cumulative distribution functions of RDS for the three configurations considered under both LOS and OBS-conditions.

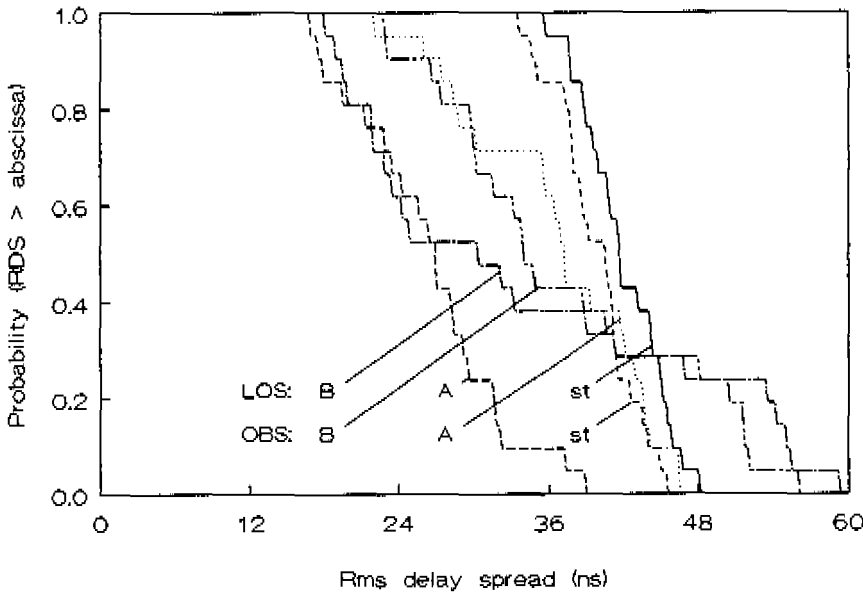


Fig. 3.19 Distribution functions of rms delay spread in Room A for the Configurations A and B and the standard configuration.

Fig. 3.19 shows that Configuration A and Configuration B both exhibit a larger spread in RDS values when compared with the standard configuration. The maximum RDS value found for Configuration A equals the maximum RDS value for the standard configuration. The maximum RDS value found for Configuration B exceeds the maximum RDS value for the standard configuration. This indicates that the use of more directive antennas does not automatically lead to lower RDS values as sometimes suggested in literature (see e.g., [11]). In fact, the use of more directive antennas might even lead to significantly higher RDS values when the directive antenna is not precisely directed towards the other antenna as in Configurations A and B. This effect of antenna mispointing is studied in more detail by means of simulations in Chapter 5.

### 3.7 Summary and conclusions

In this chapter, the measurements of the mm-wave indoor radio channels, carried out in eight indoor environments, are discussed. The main objective of these measurements was to obtain a large number of equivalent lowpass impulse responses from which channel characteristics can be derived.

We applied a frequency-stepping technique within a 2 GHz bandwidth centered around 58 GHz or 42 GHz yielding the equivalent lowpass transfer function of each channel under test. By applying Inverse Fourier Transformation, complex equivalent lowpass impulse responses could be obtained with a time-domain resolution of 1 ns whereas differences in ray amplitude of about 40 dB could be observed. The aliasing-free range in the time domain was 400 ns, which is sufficient for reliable channel characterization.

The antennas applied in the measurement setup receive considerable attention since their radiation patterns have great impact on the channel's characteristics. It is shown that biconical-horn antennas can be dimensioned in such way that the level of normalized received power (NRP) does not depend strongly on the (horizontal) position of the remote-station antenna.

In each environment, at least one subset of about 20 impulse responses was obtained. These impulse responses were measured at randomly-chosen positions of the transmit antenna at desktop height (1.4 m). The receive antenna was located in the middle of each environment at 3 m height. As predicted by theory the NRP values derived from the impulse responses obtained do not strongly depend on the horizontal position of the transmit antenna (i.e., the antenna that represents the remote-station antenna). Especially in highly reflective environments the level of NRP is maintained well in case the direct line-of-sight ray becomes obstructed.

Typical rms delay spread (RDS) values range between 15 and 45 ns for the small rooms and are between 30 to 70 ns for the larger ones. Obstruction of the direct path causes only slight changes in RDS. The largest value obtained is 100 ns.

A preliminary comparison with coverage results at 41-43 GHz shows similar RDS values for both frequency bands; the difference in atmospheric attenuation at 41-43 GHz and 57-59 GHz (0.1 dB/km and 12 dB/km, respectively) is not noticeable in our measurement results. This indicates that atmospheric attenuation has not a significant impact on the characteristics of mm-wave indoor radio channels.

---

In order to examine the influence of antenna radiation patterns on the NRP and RDS, we performed additional measurements in one room using a circular-horn antenna having 15 dBi antenna gain. The theoretical and empirical results indicate that application of biconical-horn antennas may yield clear advantages when compared with the use of more directive antennas. This topic deserves more extended examination. A thorough reconsideration of the effects of radiation patterns on NRP and RDS is presented in Chapter 5.

**References in Chapter 3**

- [1] "Millimeter-wave vector measurements using the 8510A network analyzer", Product Note No. 8510-1, Hewlett Packard, USA, Nov. 1984.
- [2] G.J.M. Janssen and R. Prasad, "Performance Improvement using Coherent Combining for Personal Communication Systems in Millimetre Wave Channels", Proc. 24th European Microwave Conference pp. 173-179, Cannes, 5-8 Sept. 1994.
- [3] W.L. Barrow, L.J. Chu and J.J. Jansen, "Biconical Electromagnetic Horns," Proc. I.R.E., Vol 28, pp. 769-779, 1939.
- [4] W.L. Stutzman and G.A. Thiele, "Antenna theory and design," John Wiley & Sons, NY, 1981, Chapter 8.
- [5] K. Uenakada and K. Yasunaga, "Horizontally polarized biconical horn antenna excited by TE<sub>11</sub> mode in circular waveguide," Trans. IECE, Vol. 54-B, pp. 125-126, 1971.
- [6] K. Uenakada, S. Yamashita and Y. Shibano, "Horizontally Polarized Biconical Horn Antenna Using Metal Plate Lens," Electronics and Communications in Japan, Vol. 59-B, No. 7, pp. 80-87, 1976.
- [7] C.A. Mentzer, L. Peters Jr. and R.C. Rudduck, "Slope Diffraction and Its Application to Horns," IEEE Trans. Antennas Propagat., Vol. AP-23, No. 2, pp. 153-159, 1975.
- [8] R. Ganesh and K. Pahlavan. "On the modeling of fading multipath indoor radio channels", IEEE, GLOBECOM '89, Vol. 3, pp.1346-1350, 1989.
- [9] A.R. Tharek and J.P. McGeehan, "Propagation and bit error measurements within buildings in the mm-wave band about 60 GHz", IEEE, IICC, pp. 318-321, 1988.
- [10] B. Glance and L.J. Greenstein, "Frequency-Selective Fading Effects in Digital Mobile Radio with Diversity Combining", IEEE Trans. on Commun., Vol. COM-31, No. 9, pp. 1085-1094, 1983.



- [11] J.E. Mitzlaff, "Radio Propagation and Anti-Multipath Techniques in the WIN Environment", IEEE Netw. Mag., pp. 21-26, 1991.

## CHAPTER 4

# STATISTICAL MODELLING OF MILLIMETRE-WAVE INDOOR RADIO CHANNELS

### 4.1 Introduction

In general, an idealized mathematical representation of the characteristics of a channel can be a useful tool in studies concerning the evaluation of transmission performance [1]-[5]. According to [6], such an idealized<sup>1</sup> representation may be termed a *channel model*. In principle, a channel model can be a *statistical* representation as well as a *deterministic* representation. A statistical channel model represents the statistical properties of the channel considered by describing the details of the impulse response in terms of probability distribution functions and their statistical moments. These distribution functions can be derived from measurements. A deterministic channel model is an algorithm to calculate the channel properties from a predefined environment. For an indoor multipath channel, the details of the impulse response can be determined on the basis of geometrical optics and eventually diffraction and scattering theory. The two modelling methods, statistical modelling

---

<sup>1</sup> The fact that a model is an *idealized* representation is expressed in the definition of the noun "modelling" given in [6] which reads; "technique of system analysis and design using mathematical or physical *idealizations* of all or a portion of the system". Completeness and reality of the model are dependent on the questions to be answered, the state of knowledge of the system, and its environment.

and deterministic modelling, have their own merits and complement each other; statistical modelling provides a compact summary of the overall characteristics for an environment or a class of environment types whereas deterministic modelling can provide more detail on a site-by-site basis. A statistical model is especially useful if system performance is to be evaluated through outage probabilities (see Section 2.4 and 2.5) since, for each calculation of an outage probability, this requires the generation of numerous individual channel responses. In this chapter, a statistical model for the impulse response of the mm-wave indoor radio channel is developed on the basis of physical reasoning and measurement data obtained from the measurements described in Chapter 3 whereas Chapter 5 deals with deterministic modelling of mm-wave indoor radio channels. The objective of the statistical modelling is to obtain a first-order model approximation that can eventually be refined further (in the sense that more environment and antenna effects are incorporated). This refinement can be based on a more detailed analysis of our measurement results and future results of other researchers in the field.

To date, no statistical models for mm-wave indoor radio channels have been reported in the literature. On the other hand, there have been several statistical models reported for microwave ( $< 3$  GHz) indoor radio channels [7]-[14]. Both continuous and discrete models are available. The continuous model corresponds to a situation where, at any excess delay, the channel impulse response actually consists of a number of individual rays which add up within the measurement time resolution. According to the Central Limit Theorem, the resulting process is Gaussian when a large number of ray components is assumed and when there is no ray component dominating all the others. The distribution of the ray amplitude matches a Rayleigh distribution so that the model is also sometimes referred to as a continuous Rayleigh model. The condition that, at any excess delay, the channel impulse response actually consists of a number of individual rays, which mutually overlap, may not be a valid assumption when wideband transmission is considered. In that case, multipath models are better described by discrete models. The discrete channel model of the complex equivalent-lowpass impulse response has the form of (2.8). Since the channel to be modelled is essentially static (see Section 2.3.2), the resulting discrete channel representation will have the form of (2.8) with eliminated time dependence, i.e.,

$$h(\tau) = \sum_n \beta_n e^{j\theta_n} \delta(\tau - \tau_n) \quad , \quad (4.1)$$

where  $\beta_n$ ,  $\tau_n$  and  $\theta_n$  are the real ray amplitude, excess delay and phase of ray  $n$ , respectively. Since we consider wideband transmission over multipath channels, we focus on discrete channel modelling.

In Fig. 4.1 a typical example of an observed complex equivalent-lowpass impulse response is shown (magnitude only).

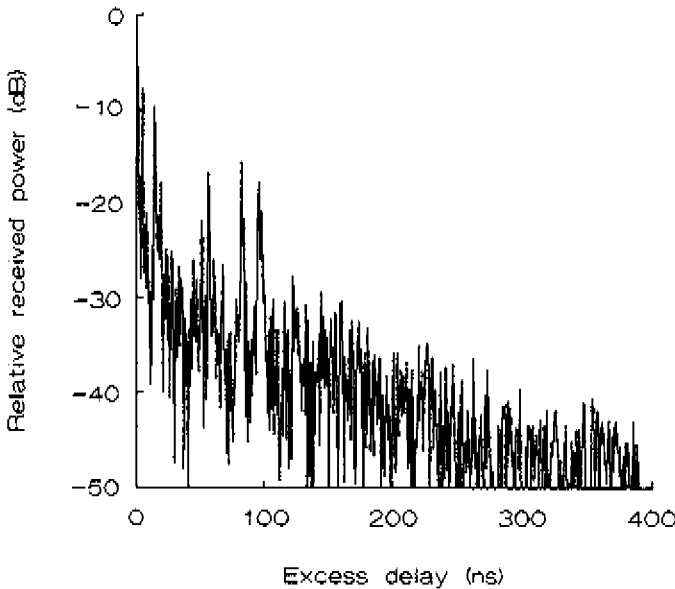


*Fig. 4.1: Typical impulse response obtained in Room A.*

Individual rays could be detected by blocking the associated ray by an absorbing mat, while other rays were not noticeably influenced. The measured channel impulse responses in which individual rays can be resolved with a measurement resolution of 1 ns show that a mm-wave indoor radio channel is indeed essentially a multipath channel, as assumed in Chapter 2. Hence; it occurs that the wavelengths considered are sufficiently short to be modelled as rays following discrete paths. The complex equivalent-lowpass impulse response of a mm-wave indoor radio channel can therefore be considered as discrete so that it may be written as (4.1).

In Section 4.2, the data reduction process is described that is applied to extract amplitude and time of arrival of individual rays in an impulse response. In Section 4.3, 4.4 and 4.5, respectively, the modelling of ray phases, ray amplitudes and ray interarrival times are treated. In Section 4.6, we briefly discuss the main difference between the modelling results obtained and results reported for UHF channels. Finally, in Section 4.7, the resulting statistical model is summarized.

## 4.2 Ray determination for statistical modelling

The first step towards statistical modelling of the channel impulse response is a data reduction by means of a filtering process of the 801 data points which make up a measured response. The filtering is necessary because not all data samples can be considered as being actual rays, since the responses also contain noise and side-lobes which result from the bandwidth restriction of 2 GHz. Also a ray will span more than one data sample, whereas in a discrete statistical model a ray is to be modelled as a Dirac delta pulse according to (4.1). The search for individual rays is therefore a search for local maxima in the responses. These local maxima are determined as follows: The first data point of each response is per definition a ray, because all measured responses were time-aligned so that the maximum of the line-of-sight ray is located at zero nanoseconds excess delay. From the second point onwards the excess-delay axis is looked at through a three-point "ray window", i.e., at a particular excess delay  $\tau$  three consecutive data points are considered. If the central point is greater than both its neighbours, the point is declared a possible ray. Next the "window" is shifted by 1 position and the process is repeated. To ensure that noise and pulse side-lobes (maximum pulse side-lobe level is -44 dB, with the Kaiser window applied in the measurements) are excluded from being modelled as genuine rays, only data values that exceed a certain threshold are candidate for a ray. For ray phase and ray amplitude considerations this threshold is chosen 30 dB below the maximum of a response (magnitude). In order to examine the influence of threshold value on ray interarrival times different threshold values (20, 30 and 40 dB) were considered in Section 4.5.

Since the data spacing is 0.5 ns the three-point "ray window" spans a 1 ns time interval which just equals the measurement resolution. If this "ray window" would span more than three points, some noise cancelation would be the result. However, less genuine rays would be detected too since the measurement resolution would not be used completely. Therefore, we decided to take the span of the "ray window" not larger than 1 ns.

## 4.3 Distribution of ray phases

A reasonable assumption for the ray phases is that they are mutually independent random variables which are uniformly distributed over  $[-180^\circ, 180^\circ]$ . This follows from the fact that the ray phase is critically sensitive to the path length, changing by the order of  $360^\circ$  as the path length changes by a wavelength of only a few millimetres.

To see if the assumption of uniformly distributed ray phases is reasonable it was checked for all measurement subsets and found to be true. An example of a typical probability density function (pdf) of all ray phase values in a measurement set is drawn in Fig. 4.2. The straight line corresponds to a uniform distribution over  $[-180^\circ, 180^\circ]$ .

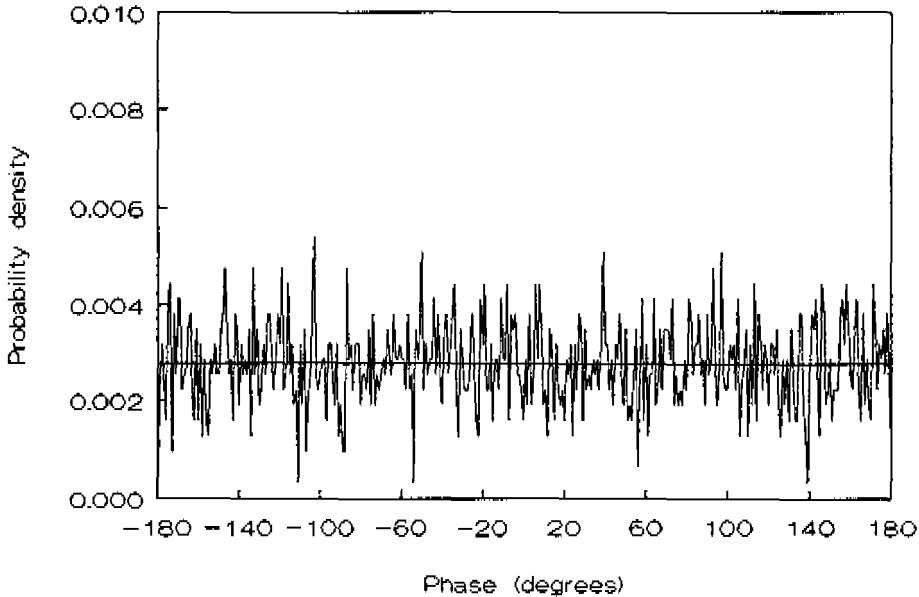


*Fig. 4.2: Typical ray phase distribution.*

## 4.4 Distribution of ray amplitudes

### 4.4.1 Assumptions

An important assumption in determining ray amplitude distributions is that per measurement subset all responses considered are generated according to the same statistical process. It is assumed that the ray generation process is a wide-sense stationary process with respect to the  $t$  variable. (see Section 2.2.2.2). In addition, we assume that the real part as well as the imaginary part of the ray phasor at a particular excess delay cross section are identically distributed random variables. Furthermore, it can be assumed that the rays that arrive at the same excess delay are mutually independent (and thus uncorrelated) since they arrive via independent ray paths. Reflected rays, however, may be composed of many different components

which add up within the measurement resolution. This is because in many cases the reflecting wall and objects have a layered and/or irregular structure at a scale smaller than (or comparable with) the measurement resolution which is 30 cm. According to the Central Limit Theorem, the real part as well as the imaginary part of a ray phasor that is built up of many random components is Gaussian distributed. This, together with the reasonable assumption of uniformly distributed ray phases, results in the assumption that the amplitudes of reflected rays have a Rayleigh distribution. The probability density function (pdf) of the Rayleigh distribution can be expressed as

$$p(\beta(\tau)) = \frac{2\beta(\tau)}{\overline{\beta^2(\tau)}} e^{-\frac{\beta^2(\tau)}{\overline{\beta^2(\tau)}}} \quad (4.2)$$

This results in an exponential pdf of ray power values, i.e.,

$$p(\beta^2(\tau)) = \frac{1}{\overline{\beta^2(\tau)}} e^{-\frac{\beta^2(\tau)}{\overline{\beta^2(\tau)}}} \quad (4.3)$$

which complies a unit-mean exponential CDF, i.e.,

$$P(\beta^2(\tau)/\overline{\beta^2(\tau)} > X) = e^{-X} \quad (4.4)$$

#### 4.4.2 Average power delay profile

The normalization parameter  $\overline{\beta^2(\tau)}$  can be identified as the *average power delay profile (average PDP)* defined as

$$\overline{\beta^2(\tau)} \triangleq \frac{1}{K} \sum_{k=1}^K \frac{p_k(\tau)}{\sum_{n=1}^N \beta_{k,n}^2} \quad (4.5)$$

where  $K$  denotes the total number of measured responses within the measurement subset considered and  $p_k(\tau) = |h_k(\tau)|^2$  represents the  $k$ th individual power delay profile (PDP) with  $k=1,2,\dots,K$ . The amplitude term  $\beta_{k,n}$  represents the  $n$ th ray of the  $k$ th individual impulse response with  $n=1,2,\dots,N$ . In calculating the average PDP, each individual PDP is thus normalized by its normalized received power value (according to (2.17)). This is done because a single PDP should not dominate in the average PDP.

An example of an average PDP with  $K=24$  is shown in Fig. 4.3. This profile is typical for all measurement subsets obtained. It can be modelled by a LOS ray followed by a constant-level part up to  $\tau=\tau_1$  which in turn is followed by a linear decrease (dB value) down to the noise floor. This general shape is depicted in Fig. 4.4.

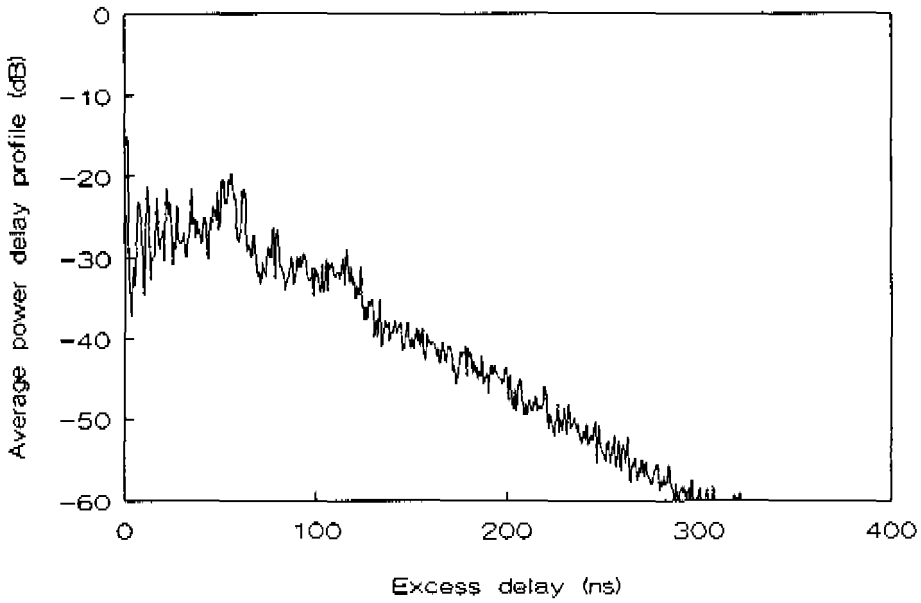


Fig. 4.3: Average power delay profile in Environment B.

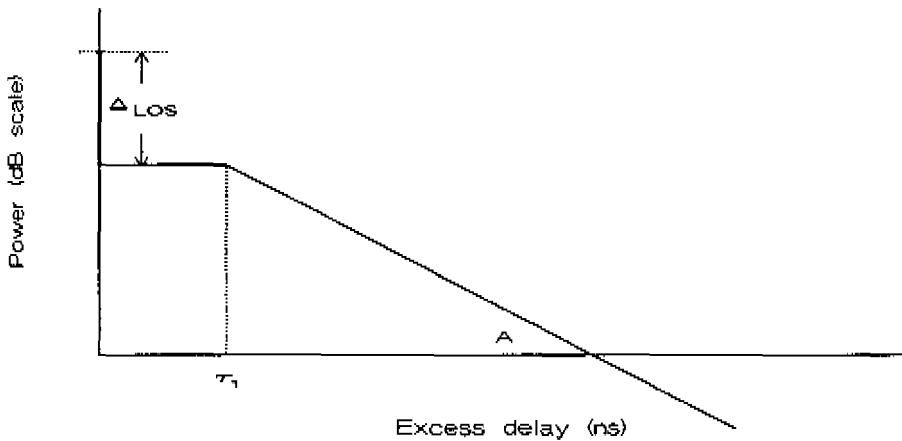


Fig. 4.4: Model of average power delay profile.



The normalized received power of the LOS component  $\overline{\beta^2(0)}$  can be calculated using the radio equation which for azimuth-independent radiation patterns is given by (3.6). OBS-situations are modelled by completely omitting the LOS-component (see the introduction of Section 3.6).

The constant-level part is caused by the compensation of free-space losses by antenna gain compensation due to the elevation dependence of the antenna radiation patterns and the difference between the transmit antenna and receive antenna height as explained in Section 3.3.2.2. The pulses in a response that immediately follow the first pulse (LOS pulse) are likely to come from single reflected rays. This suggests that we may use the approximation

$$10\log(\overline{\beta^2(\tau_1)}) = 10\log(\overline{\beta^2(0)}) - R_{dB} \quad , \quad (4.6)$$

where  $R_{dB}$  is the return loss of the most dominant wall partition.

There are two effects that determine the value of  $\tau_1$ . First, the compensation of free-space losses with antenna gain decreases with increasing path length (and thus with increasing excess delay). Second, the aggregate reflection loss for a ray increases with increasing number of reflections. Therefore,  $\tau_1$  is relatively small for small rooms with walls exhibiting a high return loss like Room G (50 ns). On the other hand,  $\tau_1$  will be relatively high for a large environment with walls having a low return loss like Environment C (70 ns). Vervuurt [15] showed that the rms delay spread values of the average PDPs as modelled are not significantly sensitive to variation of  $\tau_1$  in the range of the  $\tau_1$  values obtained, i.e.  $50 \text{ ns} < \tau_1 < 70 \text{ ns}$ . Therefore, we assume the general value  $\tau_1 = 60 \text{ ns}$  for all measurement subsets.

For the linearly decreasing part, the logarithm of  $\overline{\beta^2(\tau)}$  can be modelled as a linear fit according to

$$10\log(\overline{\beta^2(\tau)}) = 10\log(\overline{\beta^2(\tau_1)}) - A \cdot (\tau - \tau_1) \quad , \quad \tau > \tau_1 \quad . \quad (4.7)$$

Approximate expressions of parameter  $A$  as function of return loss and environment dimensions can be found by applying the radio equation. On the basis of this we can write

$$10\log(\overline{\beta^2(\tau)}) = 10\log \left[ G_{a,t} G_{a,r} \left[ \frac{\lambda}{4\pi} \right]^2 \right] + \quad (4.8)$$

$$- 10\log(\alpha(l(\tau))) - 20\log(l(\tau)) \quad , \quad \tau > \tau_1 \quad ,$$

where  $G_{a,t}$  and  $G_{a,r}$  are the antenna gain of the transmit antenna and receive antenna, respectively.  $\alpha(l(\tau))$  accounts for reflection losses with

$$l(\tau) \approx c(\tau + \overline{\tau_{LOS}}) , \quad (4.9)$$

where  $c$  is the velocity of electromagnetic waves in free space and  $l$  the pathlength that corresponds to the arrival time  $\tau + \overline{\tau_{LOS}}$ .  $\overline{\tau_{LOS}}$  is the average path delay associated with the LOS component in the average PDP.

Now let us consider those rays that are expected to dominate in a power delay profile obtained in a rectangular room whose walls all exhibit a return loss  $R_{dB}$ . Then, the rays that are expected to dominate in the profile are those rays that run in parallel with the longest wall since these rays have the lowest number of reflections among the rays that have about the same path length. It is obvious from simple image theory that the expected attenuation due to return losses of such a ray with path length  $l$  can be estimated as

$$10\log\alpha(l) \approx \frac{l}{L_{long}} R_{dB} , \quad (4.10)$$

in which  $L_{long}$  denotes the length of the longest side and in which the ratio  $l/L_{long}$  approximates the number of reflections.

Substituting (4.9) and (4.10) together with the approximation  $20\log l \approx C_1 + 0.2l$ , with  $C_1$  being a constant which turns out to be irrelevant, into (4.8) yields

$$\begin{aligned} 10\log\overline{\beta^2(\tau)} &\approx C_2 - \frac{c(\tau + \overline{\tau_{LOS}})}{L_{long}} R_{dB} - 0.2c(\tau + \overline{\tau_{LOS}}) \\ &\approx C_3 - \left[ \frac{R_{dB}}{L_{long}} + 0.2 \right] c\tau , \quad \tau > \tau_1 , \end{aligned} \quad (4.11)$$

where  $C_2$  is a constant representing the sum of  $C_1$  and the first term of the right part of (4.8).  $C_3$  represents the sum of  $C_2$  and the two terms in (4.11) associated with  $\overline{\tau_{LOS}}$ . Since  $\overline{\tau_{LOS}}$  only yields a constant contribution in (4.11) it does not contribute to the value of parameter  $A$  in (4.7). The result of (4.11) implies that

$$A \approx \left[ \frac{R_{dB}}{L_{long}} + 0.2 \right] c . \quad (4.12)$$

In order to examine how far the average PDPs comply with the approximations (4.6) and (4.12) we performed linear fitting of the "constant level part" by determining the mean value of the PDP curve in the excess delay range  $0 < \tau < \tau_1$ . For the same reason we performed linear fitting of the most linear section of the "linear decreasing part"

( $100 \text{ ns} < \tau < 200 \text{ ns}$ ) based on a minimum mean square error (MMSE) criterion. This yields values for  $\Delta_{LOS} \triangleq 10\log\bar{\beta}(0) - 10\log\bar{\beta}(\tau_1)$  (dB) and parameter  $A$ , respectively. These two parameters are listed in Table 4.1 for each measurement subset, together with the corresponding values calculated according to the relationship  $\Delta_{LOS} = R_{dB}$  (as indicated by (4.6)) and (4.12), respectively.  $R_{dB}$  is taken according to the values listed in Table 3.4 (the values for Room A are averaged). Although only values for four of the eight environments are listed they also refer to all environments considered<sup>2</sup>. In Table 4.1, the term "standard" refers to the standard configuration as defined in Section 3.5. "A" and "B" refer to "Configuration A" and "Configuration B", respectively, as defined in Section 3.6.3.

*Table 4.1: Values for  $\Delta_{LOS}$  and  $A$  according to  $\Delta_{LOS} = R_{dB}$  and (4.12), respectively, and according to fits of the average PDPs for all measurement subsets.*

Measurement subset			$\Delta_{LOS}$ (dB)	$\Delta_{LOS}$ (dB)	$A$ (dB/ns)	$A$ (dB/ns)
Env.	$f$ (GHz)	Config.	= $R_{dB}$	fitted	(4.12)	fitted
A	57-59	standard	8	7	0.16	0.12
B	57-59	standard	8	8	0.14	0.14
C	57-59	standard	2	5	0.07	0.07
D	57-59	standard	2	4	0.08	0.08
E	57-59	standard	0	10	0.06	0.06
F	57-59	standard	0	1	0.06	0.09
G	57-59	standard	13	10	0.36	0.27
H	57-59	standard	2	4	0.11	0.17
A	41-43	standard	5	6	0.18	0.12
A	57-59	A	8	12	0.16	0.11
A	57-59	B	8	12	0.16	0.10
F	41-43	standard	0	2	0.06	0.09
F	57-59	B	0	3	0.06	0.11

<sup>2</sup> Room A has wooden panels ( $R_{dB} = 8$  dB) at its head ends. The walls of Room B are covered with similar panels. Rooms C and D have bare concrete walls similar to the walls of Room H ( $R_{dB} \approx 2$  dB). Environment E has metal walls similar to the walls of Room F ( $R_{dB} \approx 0$  dB).

With respect to the values of  $\Delta_{LOS}$  obtained, we find that the values based on the fits of the average PDP match the return loss values with a maximum difference of 3 dB for all but one measurement subsets obtained with the standard configuration. The exception is the fit of the average PDP for Environment E which shows a considerable larger value of  $\Delta_{LOS}$  than what can be expected on the basis of  $\Delta_{LOS}=R_{dB}$ . This can be explained by the fact that Environment E is a narrow corridor with highly reflective walls so that many strong reflected rays are added with the actual LOS ray within (or almost within) the measurement resolution of 1 ns.

With respect to Configuration A and Configuration B considerably higher values of  $\Delta_{LOS}$  than those predicted by (4.6) are found. This can be simply explained by the fact that antennas are used that radiate mainly in the direction of the receiver so that the reflected rays are highly suppressed when compared with the direct ray.

With respect to the values of parameter  $A$  obtained we find that the values based on the fits of the average PDP do not depend strongly on the measurement configuration, as expected (compare the configurations in Environment A and also those in Environment F). Furthermore, we find that the values based on the fits of the average PDP match (4.12) with a maximum (relative) deviation of 30% for all measurement subsets obtained with the standard configuration. Especially for the large environments a good match is found. This can be explained by the fact that for these environments the effect of the free space losses which is accurately expressed in (4.12) dominates the effect of reflection losses. For the non-standard configuration the maximum deviation found is about 50%. The deviations can be attributed to the fact that the values of  $R_{dB}$  given in Table 3.4 are only global indications and that the values of  $A$  is highly sensitive to the value of  $R_{dB}$  especially for the small rooms. When, for instance, we take  $R_{dB}=1$  dB instead of  $R_{dB}=0$  dB for Room F ( $L_{img}=9.9$  m) then, according to (4.12),  $A$  becomes 0.09 dB/ns yielding a good match with the values based on the fits of the average PDP.

#### 4.4.3 Goodness-of-fit test for the ray amplitudes

The assumption that a Rayleigh distribution describes the amplitude statistics of reflected rays is verified with a goodness-of-fit test. The test is conditioned to the existence of a ray with exclusion of LOS rays. Thus, data values that are not recognized as (reflected) rays are not taken into consideration and each detected ray is represented as a single point having a particular amplitude and excess delay in the impulse response. With this approach, we obtain a meaningful amplitude distribution for each measurement subset since each resulting sample set contained only "non

zero" ray amplitudes. Hence; the test can be utilized to model the ray amplitude generation process independent from the ray arrival process.

This test was applied to each measurement subset. Per measurement subset all ray amplitude values in all responses are being lumped into a homogeneous random process which has a mean according to the average PDP.

The validity of the hypothetical (Rayleigh) distribution was examined by means of the chi-square test. For this test, the measurement data are divided into a number of classes. A measure of the discrepancy between the distribution of the measurement data and hypothetical distribution is defined as

$$\chi^2 = \sum_{j=1}^J \frac{(f_j - F_j)^2}{F_j} , \quad (4.13)$$

where  $J$  denotes the number of classes. In (4.13),  $f_j$  and  $F_j$  denote the measured and hypothetical frequency in class  $j$ . For large numbers of data values,  $\chi^2$  tends to a specific distribution, regardless of the hypothetical distribution. This distribution is generally known as the  $\chi^2$ -distribution. From this distribution the probability

$$\xi = P(\chi^2 < \chi_0^2) \quad (4.14)$$

is determined, where  $\chi_0^2$  is a function of  $J$ .  $\xi$  is denoted as the *significance level* and can be found by using a chi-square table. If  $\xi$  is smaller than some value, 95 % is common practice, then the hypothesis that the hypothetical distribution is the same as the distribution of the measurement data is rejected. For none of the measurement subsets the hypothetical Rayleigh distribution is rejected if a significance level of 95 % is used as a selection criterion except for the two measurement subsets obtained in Room F with the 41-43 GHz and 57-59 GHz standard configuration. For both these subsets the significance level is 89 %. In Fig. 4.5 the CDF of the ray-power values is drawn (dotted line) that represents the worst fits with respect to the 57-59 standard configuration, together with the unity mean exponential function (solid line). From the fact that the distribution of ray power values fits an exponential CDF for all measurement subsets with a minimum significance level as high as 89% we conclude that the associated distribution of ray amplitude values may indeed be modelled as a Rayleigh distribution.

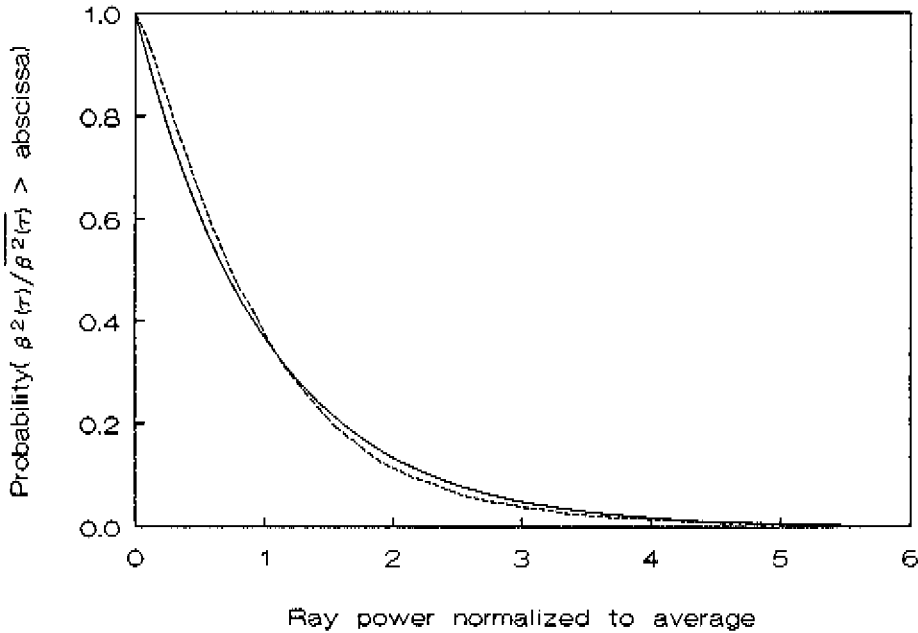


Fig. 4.5: Worst fit of ray power distribution.

#### 4.5 Distribution of ray interarrival times

The last item concerns the statistical distribution of the interarrival times between consecutive rays  $\Delta\tau$ . Because the data points of the measured responses are equally spaced at 0.5 ns intervals, the time of arrival of a detected ray is also a multiple of 0.5 ns, i.e.,

$$\Delta\tau \in \{i \cdot 0.5 \text{ ns}\}, \text{ where } i = 0, 1, 2, \dots \quad (4.15)$$

The 'three point' ray search algorithm automatically implies that interarrival times of 0.5 ns (two consecutive data points) cannot be detected. As with the ray phase and amplitude considerations, the interarrival time statistics are considered per measurement subset. In determining the ray arrival time distribution, we assume that, in each response, the ray arrival process is random and stationary with respect to the  $t$  variable as well as with respect to the  $\tau$  variable. As already stated in Section 4.4, we also assume that, per measurement subset, all responses considered are generated according to the same statistical process.

For each measurement subset all ray interarrival time values in all responses considered are lumped together, assuming a homogeneous random process. An example of an empirical pdf is shown in Fig. 4.6. The probability of an interarrival time  $\Delta\tau$  is simply the quotient of the number of times this interarrival time occurred and the total number of interarrival times found in a particular measurement subset. Not included in Fig. 4.6 are incidental high values found (up to 100 ns). These values were artefacts of the thresholding procedure applied in the ray determination. Because the area under a pdf must equal 1, the height of each bar in Fig. 4.6 is adjusted in such a way that height \* width = probability \* unit area.

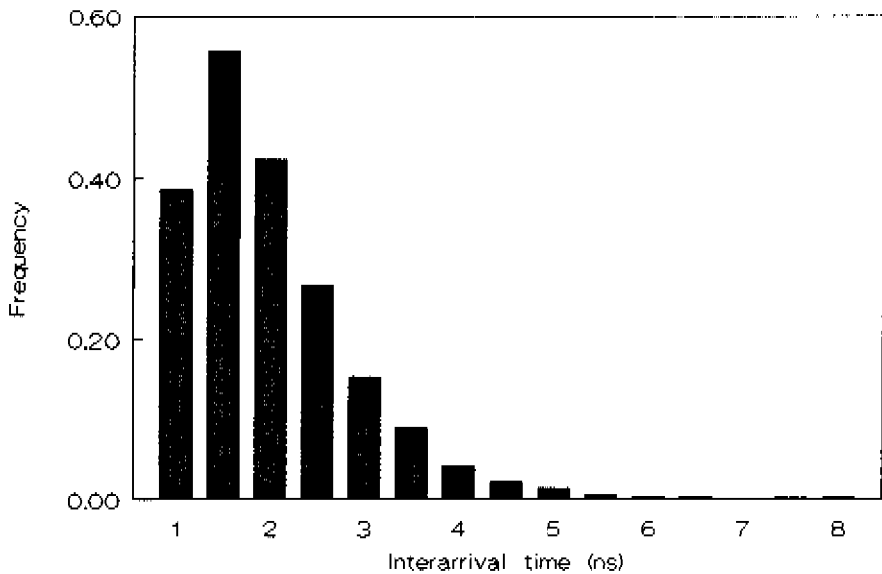


*Fig. 4.6: Typical interarrival time frequency histogram.*

The shape of the histogram in Fig. 4.6 is typical for those obtained for all environments and, as will be shown, the same for different threshold values. Because the probability of an interarrival time of 1 ns is smaller than the probability at 1.5 ns, the shape of the empirical pdf suggests that the interarrival time pdf should generally look like a Weibull function, i.e.,

$$f(\Delta\tau) = \begin{cases} \frac{\beta}{\alpha} \left(\frac{\Delta\tau}{\alpha}\right)^{\beta-1} \exp\left[-\left\{\frac{\Delta\tau}{\alpha}\right\}^\beta\right] & \Delta\tau \geq 0 \\ 0 & \text{otherwise} \end{cases}, \quad (4.16)$$

with  $\alpha > 0$  and  $\beta > 0$ . In [13]-[14], where UHF indoor radio channels in various manufacturing environments have been modelled, interarrival time pdf's with a similar shape are reported. In these references, these pdf's were modelled as Weibull pdf's with  $\alpha$  ranging from 17.5 to 50.5 and  $\beta$  lying between 1 and 2.9. Consequently

$$\lim_{\Delta\tau \rightarrow 0} f(\Delta\tau) = 0, \quad (4.17)$$

as in our case. This suggests that rays could not overlap. However, there is no conceivable reason why pulses should not overlap. Overlap does occur but cannot be detected because of the limited time domain resolution! Hence; a pdf with a shape according to (4.16) does not represent reality since it includes the characteristics of the measurement system. The significance of this is that modelling of the ray arrival process must not only be based on the pdf's obtained, but also on the reasonable assumption that rays arrive randomly, which means that each occurrence is independent from others and cannot be predicted exactly.

A process of random independent arrivals is described by a Poisson distribution. According to the Poisson distribution the probability of  $k$  arrivals in a time interval  $\xi$  equals

$$P_k(\xi) = P(k \text{ arrivals} \in \text{interval } \xi) \\ = \frac{e^{-\lambda\xi} \cdot (\lambda\xi)^k}{k!}, \quad k = 0, 1, 2, 3, \dots \quad (4.18)$$

This distribution is equivalent to a pdf of interarrival time  $\Delta\tau$  of

$$p(\Delta\tau) = \lambda e^{-\lambda\Delta\tau} \quad (4.19)$$

Parameter  $\lambda$  is the mean arrival rate, and the reciprocal value  $1/\lambda$  is the mean time between two consecutive arrivals. The fact that a Poisson distribution can be characterized by only one parameter implies that it is an easier representation and easier to use than the Weibull distribution for which two parameters need to be determined.

A pdf of measured interarrival times as depicted in Fig. 4.6 can be approximated by a negative exponential function starting from  $\Delta\tau = 1.5$  ns. If the assumption is made that the ray arrival process is in fact a Poisson process, then the following procedure can be used for finding the mean ray arrival rate: First, all interarrival values of 1 ns are removed from the data set. Next, an exponential



function  $A_0 \exp(-\lambda\tau)$  is fitted to the interarrival pdf of the measurement data according to a MMSE criterion. The third step is adapting the heights of the bars in the frequency histograms in such way that (4.19) is satisfied. In Fig. 4.7 the interarrival time pdf's for Environment B are depicted for three different threshold values: -40, -30 and -20 dB. In addition, the corresponding exponential fits are shown. Taking a higher threshold value yields higher values of  $\lambda$  for all environments since less data points are recognized as rays.

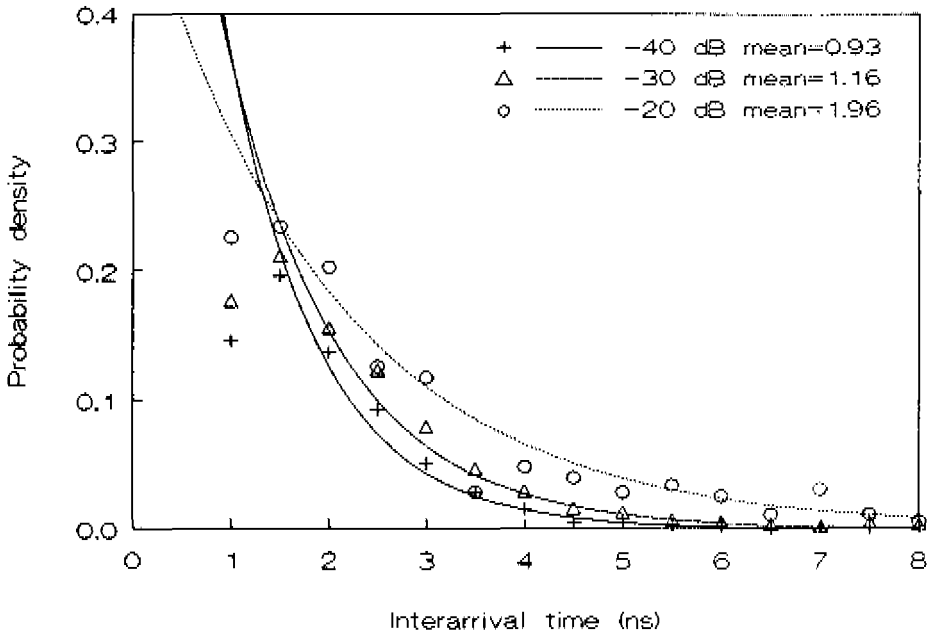


Fig. 4.7: Interarrival probability density functions and exponential fits for Room B.

The interarrival time pdf's were subjected to a chi-squared goodness-of-fit test. Unfortunately, this test failed to yield results of sufficient significance. This is mainly caused by the limited number of interarrival time classes, though the total number of values is considerable, typically several thousand values per measurement subset. (This was not the case for the ray amplitudes, since these data values are real continuous variables.) However, good correlation coefficients (MMSE) between exponential fit and empirical frequency distributions are found. Hence, we conclude that the ray arrival process approximates a Poisson process, i.e., the pdf of ray interarrivals is approximately exponential. Table 4.2 lists the mean of the interarrival times for all measurement subsets and for thresholds of -40, -30 and -20 dB. For each threshold the mean interarrival time tends to be relatively small for small environ-

ments and highly reflective environments and for the standard configurations. Obviously, a small and highly reflective environment as well as the omnidirectional radiating antennas applied in the standard configuration contribute to the scattering of the radio waves. The mean of the interarrival times varies from approximately 0.7 to 1.1 ns for the threshold of -40 dB, 0.9 to 2.0 ns for the -30 dB threshold and 1.3 to 3.1 ns for the -20 dB threshold. Especially the values for the -40 dB threshold are comparable to the measurement resolution. This suggests that the discrete multipath process of mm-wave indoor radio channels converges toward a continuous Rayleigh model and, at every excess delay, the amplitude of the response is statistically characterized by a Rayleigh pdf. However, since this threshold is in the order of the dynamic range of the measurement system also noise might contribute significantly to the result. In this respect, the results for the -20 dB threshold are most reliable. This implies that the mean interarrival time is most reliably characterized as being 1 to 3 ns for the case that those rays are excluded that have amplitude values that are more than -20 dB below the highest ray amplitude.

*Table 4.2: Mean interarrival time for diff. thresholds and for all measurement subsets.*

Measurement subset			$1/\lambda$ (ns) for threshold of		
Env.	f (GHz)	Config.	-40 dB	-30 dB	-20 dB
A	57-59	standard	0.8	1.1	1.9
F	57-59	standard	0.9	1.0	1.3
D	57-59	standard	1.0	1.2	2.0
C	57-59	standard	1.0	2.0	3.0
E	57-59	standard	0.7	1.2	1.5
B	57-59	standard	0.9	1.2	2.0
H	57-59	standard	0.9	1.0	1.4
G	57-59	standard	0.7	1.4	2.2
A	41-43	standard	0.9	1.0	1.9
A	57-59	A	1.1	1.6	3.1
A	57-59	B	1.1	1.5	3.0
F	41-43	standard	0.8	0.9	1.3
F	57-59	B	1.0	1.1	1.9

#### 4.6 Comparison with results obtained at UHF frequencies

Saleh and Valenzuela [7] have treated the modelling of UHF indoor radio channels. In this paper it was reported that rays arrive in clusters. The leading peaks of these clusters decay with excess time and so do rays within a single cluster. The clustering, they conclude, is related to the building superstructure; the rays that arrive at the receiver with approximately the same excess delay, come from the same direction (propagation through the same walls of a room for example) and consequently these rays will form a cluster. Their measurements covered a whole building floor.

For indoor radio communications at mm-wave frequencies, the signal coverage is limited to one room. Therefore, the individual clusters are not observed in our case. If a comparison should be made with the model of [7], then all our resolved rays belong to the same, first, cluster.

#### 4.7 Summary and conclusions

In this chapter, we develop a statistical model for the complex equivalent lowpass impulse response of the indoor mm-wave radio channel. The objective of the statistical modelling is only to obtain a first-order model approximation which can serve as a basis for further refinement. The resulting statistical model is mainly based on physical reasoning which is confirmed by the measurement data obtained from the measurements described in Chapter 3. The relation between the model parameters and environment properties (wall dimensions and return-loss figures) are described by simple first order approximations. This makes the model readily applicable to a variety of other comparable indoor environments.

The ray phases are modelled as independent random variables that are uniformly distributed over  $[-180^\circ, 180^\circ]$ .

The amplitude values of the LOS rays are not modelled since they can be determined easily on the basis of the radio equation.

The amplitude values of reflected rays are modelled as independent random variables that are Rayleigh distributed. The normalization parameter of this distribution are modelled as a function of excess delay by a constant level part followed by a linear decrease (dB value). The level of the constant-level part as well as the slope parameter of the linear decreasing part are related to the specific properties of the particular environment under consideration and the antennas applied.

The ray interarrival times are modelled as independent random variables that are exponentially distributed (i.e., a Poisson process). The relation between the

interarrival time and the threshold used for identification of rays as well as the relation between the interarrival time and the environment and antenna properties is described.

The statistical parameters derived from the measurement subsets that were performed at 41-43 GHz using the scaled biconical-horn antennas, are practically the same as those derived from the 57-59 GHz measurement results attained with a similar measurement configuration. This indicates that atmospheric attenuation has not a significant impact on the characteristics of mm-wave indoor radio channels and that the statistical model can be used for other frequencies in the mm-wave band as well.

The assumptions underlying the model are mainly based on geometric ray tracing. The fact that the measurement results confirm these assumptions suggests that geometric ray tracing performed by a simulation programme could yield reliable results. Chapter 5 deals with deterministic modelling based on geometric ray tracing.

**References in Chapter 4**

- [1] H. Hashemi, "Simulation of urban radio propagation channel", Ph. D. dissertation, Univ. Calif., Berkeley, 1977.
- [2] J.H. Winters and Y.S. Yeh, "On the performance of wide-band digital radio transmission within buildings using diversity", Proc. IEEE GLOBECOM, 1985.
- [3] P. Monsen, "Theoretical and measured performance of DFE modem on fading multipath channel", IEEE Trans. Commun., Vol. COM-25, pp. 1144-1153, 1977.
- [4] T.A. Sexton and Pahlavan K., "Effect of multi-cluster delay spectrum on wireless indoor communications", Proc. CISS, Johns Hopkins Univ., March 1987.
- [5] T.A. Sexton and Pahlavan K., "Channel Modeling and Adaptive Equalization of Indoor Radio Channels", IEEE, Journ. on Sel. Areas in Comm., Vol. SAC-7, No. 1, pp. 114-120, 1989.
- [6] IEEE Std 100-1977, "IEEE Standard Dictionary of Electrical and Electronics Terms", 2nd ed., IEEE Inc., New York, Dec. 1977.
- [7] A.A.M. Saleh and R.A. Valenzuela, "A statistical model for indoor multipath propagation", IEEE, Journ. on Sel. Areas in Commun., Vol. SAC-5, No. 2, pp. 128-137, 1987.
- [8] D.M.J. Devasirvatham, "Multipath time delay spread in the digital portable radio environment", IEEE Commun. Mag., Vol. COM-25, pp. 13-21, 1987.
- [9] P. Yegani and C.D. McGillem, "A statistical model for the factory radio channel", IEEE, Trans. on Comm., Vol. COM-39, pp. 1445-1454, 1991.
- [10] T.S. Rappaport, "Characterisation of UHF multipath radio propagation inside factory buildings", IEEE Trans. Antennas Propagat., Vol. AP-37, pp. 1058-1069, 1989.
- [11] G.L. Turin, et al., "A statistical model of urban multipath propagation", IEEE, Trans. on Veh. Tech., Vol. VT-21, No 1, pp 1-8, 1972.

- 
- [12] T.S. Rappaport and C.D. McGillem, "UHF fading in factories", *IEEE, Journ. on Sel. Areas in Comm.*, Vol. SAC-7, No. 1, pp.40-48, 1989.
  - [13] P. Yegani and C.D. McGillem, "A statistical model for line-of-sight (LOS) factory radio channels", *IEEE, Proc. 39th Veh. Tech. Conf.*, pp. 496-503, May 1989.
  - [14] P. Yegani and C.D. McGillem, "A statistical model for the obstructed factory radio channel", *IEEE, GLOBECOM '89*, Vol. 3, pp. 1351-1355, 1989.
  - [15] G.J.A.P. Vervuurt, "Modelling and Simulation of Indoor Radio Channels in the mm-Wave Frequency Band", *M.Sc.E.E. Thesis, Telecommunications Division, EUT*, Jan. 1993.

## CHAPTER 5

### DETERMINISTIC MODELLING OF MILLIMETRE-WAVE INDOOR RADIO CHANNELS

#### 5.1 Introduction

A deterministic channel model can be defined as an algorithm to calculate the channel properties from a predefined environment. The motivation for deterministic channel modelling is that it can be used to clarify the relationship between environment, antenna characteristics and positioning on one side and wave propagation characteristics on the other. It differs from statistical modelling in the sense that it provides more detail on a site-by-site basis whereas statistical modelling provides a compact summary of the overall characteristics for an environment or a class of environment types. Hence, as already stated in the previous chapter; the two modelling methods have their own merits and complement each other.

It will be shown that a deterministic model for mm-wave indoor propagation might be a reliable tool for at least comparative (parameter sensitivity) studies. It will also be shown that even absolute accuracy can be obtained, provided that reasonable accurate assessments of wall reflection coefficients are available. This is presumably because the characteristics of indoor mm-wave propagation lend themselves well to software implementation since the corresponding wavelengths (5 to 10 mm) are small in terms

of the dimensions of dominating walls and objects while they are large in terms of surface roughness dimensions of most building materials so that convenient high frequency approximations can be applied according to the concepts of classical geometrical optics.

In this chapter, the following subjects are discussed. Firstly, in Section 5.2, we introduce the basic principles of reflection including the effects of surface roughness. After that, we examine the significance of diffraction effects in comparison with reflection effects. We furthermore discuss in which way the effects that are identified as being significant should be incorporated in a deterministic indoor mm-wave propagation model. In Section 5.3, such a model is proposed and the basic algorithms underlying this model are presented. In Section 5.4, we treat the dimensioning of various antennas and their implementation in software to be used for mm-wave indoor radio channel simulations. Results of such computer simulations and comparisons with measurement results are presented and discussed in Section 5.5. Finally, in Section 5.6, a summary is presented and the conclusions are given.

## 5.2 Considerations concerning the model choice

In choosing a deterministic model for implementation in a simulation programme, there are some restrictions. First of all, the model must be based on a representation of the environment that is sufficiently accurate to predict at least the qualitative effects of environment and antenna parameter variations on the channel characteristics. On the other hand, the degree of refinement of the model must be in proportion to the accuracy of the model approximation. Additionally, the model must give some physical insight in the most important parameters that constitute the characteristics of the radio channel. For instance, it must be relatively easy to predict the changes in the radio channel when an object is moved from one place to another, or when a wall is coated with another material, changing the reflectivity.

These restrictions reduce the choice of a model greatly. Solving the Maxwell equations for a particular room configuration, for instance, is very difficult and hard to implement. Hence; this option is not considered here. An alternative is making use of Physical Optics (PO) to describe the reflections against walls and objects, as is commonly done for reflector antenna systems. This method includes an integration of the incident electromagnetic fields over all surfaces that are illuminated by the transmitter radiation and radiation reflected by one or more surfaces. If the room configuration becomes complicated, however, the computation of the integrals is very time consuming. This means that PO is also not suited as a model for the indoor



radio channel.

For the frequencies under consideration, there are some methods that are based on ray tracing. These are Geometrical Optics (GO) [1], Geometrical Theory of Diffraction (GTD) [2], Uniform geometrical Theory of Diffraction (UTD) [1,3,4] and Uniform Asymptotic Theory of diffraction (UAT) [5]. GO describes the field received directly from the transmit antenna and via reflections. This method is based on the assumption that the wavelength approaches zero. The other techniques assume that the wavelength is small in comparison with the dimensions of the objects the electromagnetic wave interacts with.

GO predicts zero fields in shadow regions. GTD supplies the GO with rays diffracted by edges or corners of objects. The major limitation of GTD is its failure at reflection and shadow boundaries, where it predicts infinite fields. UTD is in this context the wanted extension; it predicts smooth continuous fields at the boundaries and approaches GTD as the observation point moves away from these boundaries. UAT also predicts finite fields for the directions mentioned, not by adjusting the GTD coefficients, but by changing the GO field to infinite fields compensating the GTD infinite fields. This gives less physical insight and also causes problems when computing the fields. For these reasons and because UTD is very well described in literature, UTD seems an attractive candidate to incorporate diffraction in our model. However, it remains to be seen how far the UTD extension contributes to the accuracy already provided by GO alone, since the introduction of the UTD extension on top of GO implies a significant increase in software complexity and computer calculation time.

### 5.2.1. Determination of reflection coefficients

Firstly, we consider the reflection coefficients for an incident plane wave of an electromagnetically flat, infinite boundary between vacuum and some homogeneous material having material properties  $\epsilon'$ ,  $\mu'$ , and  $\sigma$ , i.e., the relative dielectric constant, the relative magnetic permeability and the conductivity, respectively. Expressions for the reflection coefficients can be extracted from the boundary conditions for the electric and magnetic field. They can be expressed in field components of the incident and reflected fields, namely the components perpendicular (resp.  $E_{\perp,i}$  and  $E_{\perp,r}$ ) and parallel (resp.  $E_{\parallel,i}$  and  $E_{\parallel,r}$ ) with respect to the incident plane. For the perpendicular and parallel electric field components of an incident plane wave expressions for the reflection coefficients, known as the Fresnel reflection coefficients, are given in any standard work on electromagnetic theory. For a vacuum-material boundary these expressions can be written as

$$R_{\perp}(\theta_i) = \frac{E_{\perp,r}(\theta_i)}{E_{\perp,i}(\theta_i)} = \frac{\cos \theta_i - \sqrt{\mu' \epsilon_r - \sin^2 \theta_i}}{\cos \theta_i + \sqrt{\mu' \epsilon_r - \sin^2 \theta_i}}, \quad (5.1)$$

$$R_{\parallel}(\theta_i) = \frac{E_{\parallel,r}(\theta_i)}{E_{\parallel,i}(\theta_i)} = \frac{\mu' \epsilon_r \cos \theta_i - \sqrt{\mu' \epsilon_r - \sin^2 \theta_i}}{\mu' \epsilon_r \cos \theta_i + \sqrt{\mu' \epsilon_r - \sin^2 \theta_i}},$$

$$\epsilon_r = \epsilon' - j \frac{\sigma}{2\pi f \epsilon_0}, \quad (5.2)$$

in which  $\epsilon_0 = 8.854 \cdot 10^{-12}$  As/Vm.  $R_{\perp}(\theta_i)$  and  $R_{\parallel}(\theta_i)$  are thus determined by  $\epsilon'$ ,  $\mu'$  and  $\sigma$  (or equivalently by  $\epsilon'$ ,  $\mu'$  and the loss tangent  $\tan(\delta) = \sigma / 2\pi f \epsilon_0 \epsilon' = 60 \sigma \lambda_0 / \epsilon'$  with  $\lambda_0$  the wavelength in vacuum).

When the material thickness is large (compared to the wavelength) and/or the material-related losses are high, reflection coefficients can be approximated according to (5.1). For media for which the validity of these conditions are not fulfilled the thickness must be taken into account. The results in Table 3.4 with respect to the glass windows with such substantial differences between the two frequency ranges, for instance, can only be understood by considering the thickness of the window glass. The reflection coefficient of a slab having thickness  $d$  can be determined as the addition of the simple reflection coefficient according to (5.1) with the sum of the infinite series of consecutive reflections departing inside the slab. This reflection coefficient can be expressed as

$$R_{slab}(\theta_i) = R - (1-R^2) \frac{R e^{-j2k_x d} e^{-2\alpha d} e^{-j k_x b \sin \theta_i}}{1 - R^2 e^{-j2k_x d} e^{-2\alpha d} e^{-j k_x b \sin \theta_i}}, \quad (5.3)$$

where  $R$  is  $R_{\perp}(\theta_i)$  or  $R_{\parallel}(\theta_i)$  for the field components perpendicular or parallel with respect to the incident plane, respectively. Furthermore,  $k_x$  is the propagation constant inside the slab which is

$$k_x = \frac{2\pi}{\lambda_s} = \frac{2\pi}{\lambda_0} \sqrt{\epsilon'}, \quad (5.4)$$

where  $\lambda_s$  is the wavelength inside the slab and  $\lambda_0$  is the wavelength in free space. Parameter  $\alpha$  is the attenuation coefficient inside the slab which can be expressed as

$$\alpha = \pi f \left[ 2\mu_0 \epsilon_0 \epsilon' \left[ \sqrt{1 + \left( \frac{\sigma}{2\pi f \epsilon_0 \epsilon'} \right)^2} - 1 \right] \right]^{1/2}, \quad (5.5)$$

with  $c$  the velocity of electromagnetic waves in vacuum. Parameter  $k_0$  in (5.3) is the free space propagation constant, i.e.,

$$k_0 = \frac{2\pi}{\lambda_0}, \quad (5.6)$$

and  $s$  is the pathlength inside the slab between the two surfaces, thus

$$s = \frac{d}{\sqrt{1 - \frac{\sin^2(\theta_i)}{\epsilon'}}}, \quad (5.7)$$

and  $b$  the path length difference on the slab of two consecutive departing reflections:

$$b = \frac{2d}{\sqrt{\frac{\epsilon'}{\sin^2\theta_i} - 1}}. \quad (5.8)$$

In order to be able to use the approximations (5.1)-(5.3), we need to have estimates of the parameters  $\epsilon'$ ,  $\mu'$  and  $\sigma$  for the most commonly used building materials. In [6] results are reported for several building materials obtained from power reflection and transmission measurements at 0.14 GHz and 10 GHz in terms of  $\epsilon'$ ,  $\mu'$  and  $\sigma$ . These are listed in Table 5.1. In [7], estimates are reported of  $\epsilon'$  and  $\tan(\delta)$  based on power reflection and transmission measurements at 62 GHz. These are listed in Table 5.2. This table shows considerably higher values for the conductivity of concrete at 62 GHz when compared with the values in Table 5.1 for concrete at 0.14 GHz. This indicates that the conductivity of concrete highly depends on frequency<sup>1</sup>.

---

<sup>1</sup> In [6], it is reported that the conductivity of *brick* highly depends on frequency, especially when the relative humidity is high; For 15% relative humidity  $\sigma$  equals  $8.9 \Omega^{-1}\text{m}^{-1}$  for 0.1 GHz whereas it amounts to  $5507 \Omega^{-1}\text{m}^{-1}$  at 30 GHz. In [7], no data concerning the relative humidity of the materials considered are given. A discussion with the authors revealed, however, that the humidity of these materials was 0%.

Table 5.1: Material characteristics according to [6].

Material	$f$ (GHz)	$\epsilon'$	$\mu'$	$\sigma$ ( $\Omega^{-1}m^{-1}$ )
Concrete				
Humidity 0%	0.14	4.5		$1.4 \cdot 10^{-3}$
Humidity 5%	0.14	6.5		$5.6 \cdot 10^{-3}$
Humidity 15%	0.14	14		$2.8 \cdot 10^{-2}$
Glass	10	5-10		
Wood	10	3-7		
Perspex	10	3		
Aluminium	0.14	1	1	$3.7 \cdot 10^7$
Iron	0.14	1	$10^4-10^5$	$9.5 \cdot 10^6$

Table 5.2 Material characteristics at 62 GHz according to [7].

Material	$\epsilon'$	$\tan(\delta)$	$\sigma$ ( $\Omega^{-1}m^{-1}$ )
Aerated concrete	3.7	0.034	25.2
Concrete	11.5	0.026	60.0
Glass	4.9	0.026	25.6
Plasterboard	2.8	0.016	9.2
Wood (chipboard)	2.8	0.056	31.9

Let us furthermore examine the applicability of (5.1) and (5.3) for deterministic modelling by estimating to what degree surfaces as expected to be present in a typical indoor environment can be considered as "flat" and "infinite".

To distinguish between electromagnetically flat and rough surfaces the well-known Rayleigh criterion can be used [8]. According to this criterion, an irregular surface can be considered as being "flat" if

$$h < \frac{\lambda_0}{8 \cos \theta_i} , \quad (5.9)$$

and "rough" otherwise. The parameter  $h$  denotes the maximum irregularity height difference of the surface while  $\theta_i$  represents the angle of incidence. Hence; the roughness of the surface depends on the free-space wavelength  $\lambda_0$  and  $\theta_i$ .

The worst case value for the irregularity height, which divides "rough" from "flat" surfaces according to the Rayleigh criterion, appears at perpendicular incidence ( $\theta_i=0^\circ$ ) and equals about 0.6 mm for  $f=60$  GHz and 0.9 mm for  $f=40$  GHz. Therefore, most materials of walls and furniture etc., as encountered in an indoor environment, can be considered as electromagnetically flat for the frequency range of interest. In this context, a favourable fact with respect to the accuracy of our simulations is, that metal surfaces which have the simplest reflection characteristics and which can be certainly considered as electromagnetically flat also produce the strongest reflections. Hence; the most dominant reflections are most accurately calculated.

For rough surfaces the effects of surface roughness can be taken into account by a factor yielding an *effective* reflection coefficient. In [8], a reduction factor  $\rho_r$  is derived for a normal distributed surface roughness yielding the most general solution of the rough-surface scatter problem known to date. This factor, which has to be applied to (5.1) and (5.3), reads

$$\rho_r = \exp \left[ -\frac{1}{2} \left[ \frac{4\pi\sigma_h \cos \theta_i}{\lambda_0} \right]^2 \right] , \quad (5.10)$$

where  $\sigma_h$  is the standard deviation of the surface roughness. In deterministic modelling one does not need to incorporate this factor in case a reflection coefficient value is used which is obtained from measurements, since this factor is already incorporated in the measurement result. The same holds for the effects of layering and inhomogeneity of the material underneath the surface on the *strength* of an individual reflected ray.

The *time dispersion* of a reflected ray induced by material layering and inhomogeneities is not noticeable in practice since a path length difference of at least 30 cm is necessary to exceed the measurement resolution of 1 ns, whereas transmission measurements showed that millimetre waves cannot travel such distance in building materials without losses of tens of dB's.

In principle, radio waves incident on rough surfaces are not completely

reflected in the specular direction but there is also a diffuse reflection component. Measurements of scattering profiles at 60.2 GHz are reported in [9]. Distinct reflection scattering has been observed for  $\sigma_h > 0.3$  millimetre ( $\sigma_h$  estimated). For rough materials that are commonly used in indoor environments, like aerated concrete, it occurred that for all directions of reflection the power associated with the diffuse component is about 15 dB below the power of the specular component.

### 5.2.2 Significance of diffraction

In order to estimate the significance of diffraction, the contribution of the diffracted ray power to the total received power in a particular observation point is examined for 5 mm wavelength (60 GHz). For this, we consider diffraction by a perfectly conducting internal edge as well as diffraction by a perfectly conducting external edge. Both these configurations are depicted in Fig. 5.1. The point source and observation point are located at a distance of 10 m and 5 m from the edge, respectively. The incidence angle  $\phi' = 30^\circ$ .

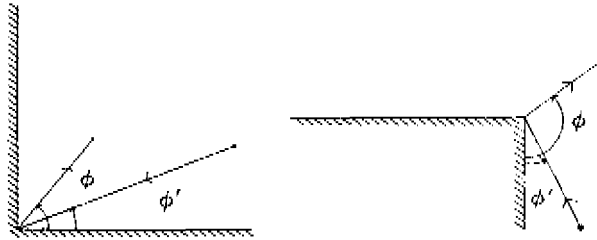


*Fig. 5.1: Configurations for calculating the power of diffracted rays: (a)  $92^\circ$  internal edge and (b)  $90^\circ$  external edge.*

The diffracted component at the observation point has been calculated for both soft and hard polarizations as a function of angle  $\phi$ . These calculations are based on the diffraction coefficients of UTD for a perfectly conducting edge as defined in [3]. Fig. 5.2 shows the difference (in dB) between the diffracted power as function of  $\phi$  and the GO reflected power near the reflection boundary. With "GO reflected power near the reflection boundary" we mean the power in the lit region just near the reflection boundary calculated according to (5.1), thus on the basis of GO alone. Fig. 5.2a shows the results for the interior edge of  $92^\circ$ . (For a  $90^\circ$  interior edge UTD predicts, correctly, zero diffracted fields.)

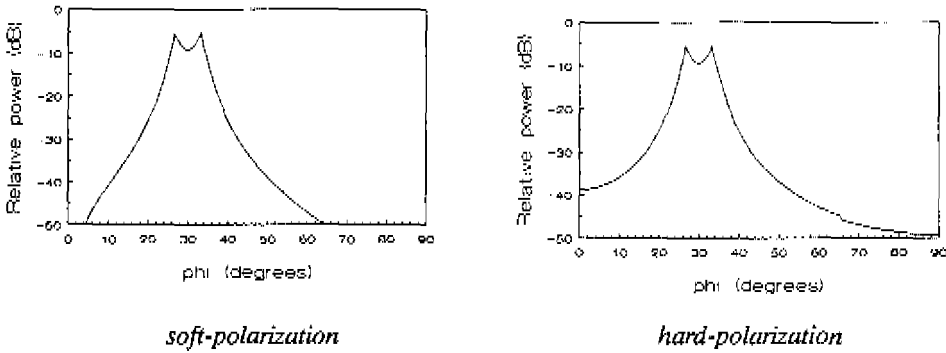


Fig. 5.2a: Diffracted power normalized on reflected power at reflection boundary for the  $92^\circ$  interior edge.

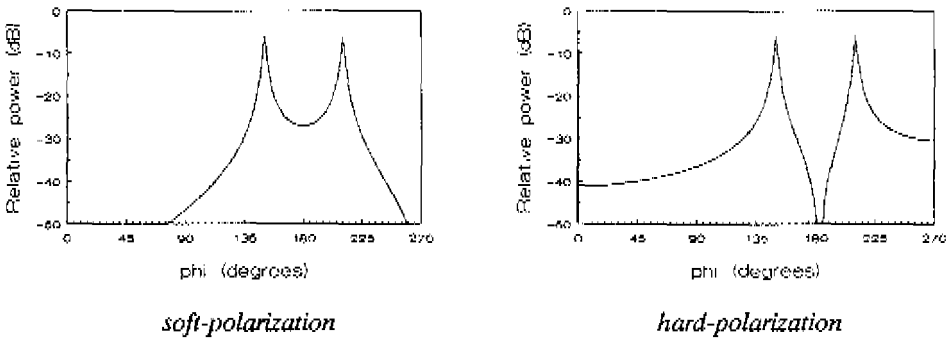


Fig. 5.2b: Diffracted power normalized on reflected power at reflection boundary for the  $90^\circ$  exterior edge.

The double peaking is due to the choice of the edge angle close (but not equal) to  $90^\circ$ . In Fig. 5.2b the results for the  $90^\circ$  exterior edge are depicted. These figures show that at 60 GHz the difference between the diffracted and reflected component remains above -10 dB over a range of observation angles that spans only a few degrees around the shadow and reflection boundaries. This indicates that in many cases diffracted rays at 60 GHz do not carry a significant amount of power in the reflective environments we consider. On the other hand, there may be incidental situations in which there are (one or more) edges within the first few Fresnel zones of

(one or more) reflection points which may result in significant diffraction<sup>2</sup>. Then, the electric field vector at the observation point cannot be calculated reliably on the basis of eq. (5.1)-(5.3) alone. For such situations, it would be useful to incorporate diffraction in our model. However, as already said, the calculation of diffraction on top of GO implies a significant increase in software complexity and computer calculation time. Therefore, we resort to an alternative approach that does not involve these drawbacks. According to this approach, the dimensions of the first  $n$  Fresnel zones are calculated for each reflection along with the actual ray calculations, e.g. for  $n=2$ . In addition, it is determined for each reflection whether or not these Fresnel zones completely fit the object face considered. To obtain an estimate of the possible significance of the reflections near edges, normalized received power (NRP) as well as rms delay spread (RDS) is calculated in two different ways, namely

- 1) All rays, wherever their reflection points are located on the various object faces, are calculated according to (5.1)-(5.3).
- 2) Only rays for which edges do not lie within the first  $n$  Fresnel zones of each reflection are taken into account.

If comparison of the two results does not yield a significant difference, then it is concluded that diffraction does not play a dominant part for the parameter under consideration (i.e., NRP or RDS). In other words, it is indicated that the result is reliable. However, if comparison of the two results yields a significant difference then it can be concluded that diffraction may yield a significant contribution to the parameter to be calculated so that the result is unreliable. In that case, the objects defined should be enlarged and/or repositioned and the whole procedure described above should be repeated.

In what follows, we estimate the minimum required dimensions of the surface area around a reflection point that allow application of (5.1)-(5.3) for sufficiently accurate calculation of electric field vector at the observation point. For this, we consider the dimensions of the  $n$ th Fresnel zone ellipse of a family of Fresnel zones around a reflection point as shown in Fig. 5.3.

---

<sup>2</sup> It is exactly when these Fresnel zones exceed an edge that diffraction comes in. In the case of perpendicular incidence, the Fresnel zones are concentric circles. It is pointed out by Kerr [8] that, in that case, the significant diffraction only occurs from edges that lie within half of the first Fresnel zone. In case of small grazing angles, the eccentricity of the zones is large and it is not evident a priori that, in that case, only diffraction from edges in half of the first Fresnel zone contributes effectively to the total field. Instead, it is widely agreed that the first few Fresnel zones act as the principal contributors to the total field in case of grazing incidence [8].



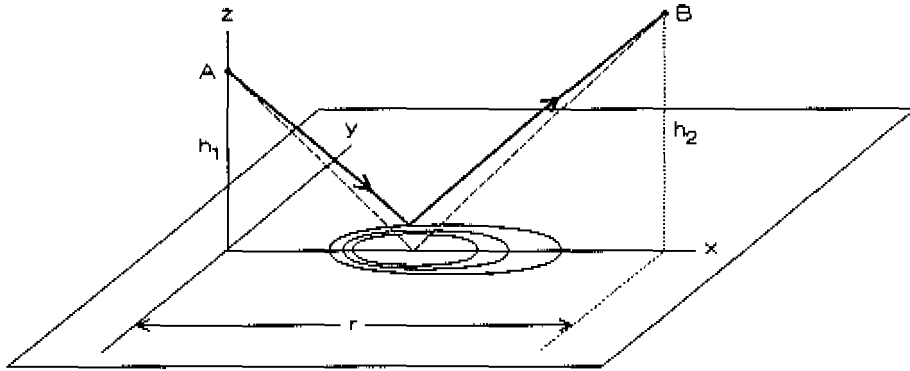


Fig. 5.3: Fresnel zones on a reflecting plane.

Hence; we consider the lengths  $l_{min,n}$  and  $l_{maj,n}$  of its (full) minor axis and (full) major axis, respectively. Exact expressions for  $l_{min,n}$  and  $l_{maj,n}$  are given in [8], but these expressions are rather complex. However, convenient approximations result in case we make the assumption that the free-space wavelength  $\lambda_0$  as well as the perpendicular distance  $h_1$  from source point  $A$  to surface and perpendicular distance  $h_2$  from observation point  $B$  to surface are much smaller than the distance  $r$  between the projection of the source point and the projection of the observation point on the surface (see Fig. 5.3). This is a reasonable assumption for the worst case situation of small grazing angles which dictates the minimum allowed object dimensions for reliable ray-tracing results when neglecting diffraction. The resulting approximations for  $l_{min,n}$  and  $l_{maj,n}$  read

$$l_{min,n} \approx \sqrt{n\lambda_0 r} \sqrt{\frac{1 + \frac{4h_1 h_2}{n\lambda_0 r}}{1 + \frac{(h_1 + h_2)^2}{n\lambda_0 r}}}, \quad (5.11)$$

and

$$l_{maj,n} \approx r \sqrt{\frac{1 + \frac{4h_1 h_2}{n\lambda_0 r}}{1 + \frac{(h_1 + h_2)^2}{n\lambda_0 r}}}. \quad (5.12)$$

For  $h_1 = h_2$ , eq. (5.11) can be simplified to

$$l_{min,n} \approx \sqrt{n\lambda_0 r} \quad . \quad (5.13)$$

For  $h_1 \approx h_2 \gg \sqrt{n\lambda_0 r}$ , eq. (5.12) can be simplified to

$$l_{maj,n} \approx \frac{r}{2h_1} \sqrt{n\lambda_0 r} \quad , \quad (5.14)$$

whereas for  $h_1 \approx h_2 \ll \sqrt{n\lambda_0 r}$ , eq. (5.12) can be simplified to

$$l_{maj,n} \approx r \quad . \quad (5.15)$$

For  $r=10$  m,  $h_1 \approx h_2=50$  cm and  $\lambda_0=5$  mm, for instance, we get  $l_{min,2} \approx 0.3$  m and  $l_{maj,2} \approx 3$  m.

The software package that we developed for GO ray tracing (see next section) includes a "Fresnel zone check" procedure as described above, based on (5.11) and (5.12). By means of this procedure the significance of diffraction has been checked for the simulation results presented in Section 5.5. The differences with respect to NRP as well as RDS values are typically less than 5% for  $n=2$ . Therefore, we conclude that diffraction does not play a significant part for the simulation results we obtained.

### 5.3 Simulation of millimetre-wave indoor radio channels

In general, ray-tracing programmes are used extensively for the examination of radio propagation characteristics. In order to investigate the propagation characteristics in an indoor environment, various algorithms have been developed taking into account the effect of transmission through walls and polarization [10,11]. In addition, more sophisticated techniques have been developed incorporating the effects of diffraction [12].

For simulation of the indoor propagation of millimetre waves, we developed the simulation package PROagation SIMulation (PROSIM). The basic algorithms and procedures underlying the PROSIM simulation package are based on GO. From the previous section it occurs that calculation of the mm-wave propagation on the basis of GO yields a good compromise between calculation accuracy and complexity. Using GO means that ray paths have to be calculated along which electromagnetic power travels from transmitter to receiver. Reflection coefficients have to be applied, electromagnetic field polarization states have to be considered and rays have to be

weighed with the radiation patterns of the transmit and receive antenna. PROSIM only considers the reflectivity of walls and objects (representing furniture etc.) but not the transmissivity. The walls (and windows) of the room are assumed to be infinitely thick and the objects within the room do not allow an electromagnetic wave to travel through them. The room and the objects within can be represented by smooth faces. Objects are assumed to stand on the ground and can be arbitrarily oriented with respect to the horizontal plane.

### 5.3.1 Geometric optical ray tracing

This section provides the foundations for a ray-tracing algorithm tailored to examine the propagation characteristics of mm-wave indoor radio channels. The ray-tracing algorithm traces possible rays between transmit and receive antenna according to Snell's reflection law which states that the angle of incidence is equal to the angle of departure. An example of a multiple reflection is depicted in Fig. 5.4.

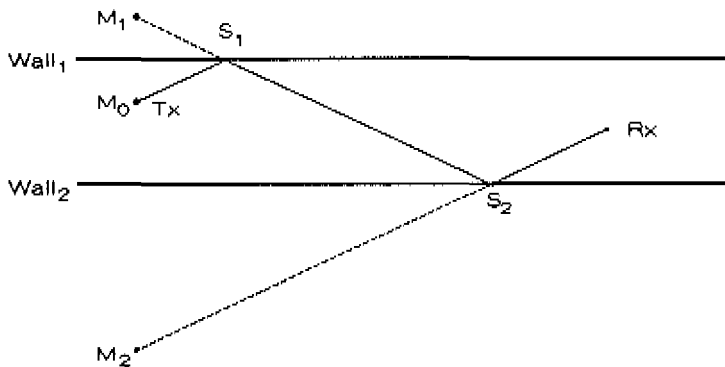


*Fig. 5.4: Example of a multiple reflection.*

In this figure, Tx and Rx are the positions of the transmit antenna and receive antenna, respectively. S<sub>1</sub> and S<sub>2</sub> are the reflection points at Wall<sub>1</sub> and Wall<sub>2</sub>, respectively. M<sub>1</sub> is the image of Tx with respect to Wall<sub>1</sub>. M<sub>2</sub> is the image of M<sub>1</sub> with respect to Wall<sub>2</sub>.

If we know the number of reflections in advance, we can find a possible ray from Tx to Rx, for this configuration, by repeating the following algorithm:

```

// ray trace
M0 = Tx; i=1; j=1;
while i < "desired number of reflection points" do
{
    Mi = Wallj.Mirror(Mi-1); // where j=1 if i=odd and j=2 if i=even
    i=i+1; j=(j+1) mod 2;
}

// ray verification
P1 = Rx; P2 = Mi;
do
    if (Wallj.InterSection(P1,P2,si)) then
    {
        P1 = si; P2 = Mi-1;
        i=i-1; j=(j+1) mod 2;
    }
    else
        "intersection point not on wall. Not a valid ray ";
until i=1;

```

The function  $Wall_j.Mirror(M_{i-1})$  mirrors vector  $M_{i-1}$  with respect to  $Wall_j$ , where  $j$  is the index of the wall under consideration. The point between  $Wall_j$  and the function  $Mirror(\cdot)$  denotes that  $Mirror(\cdot)$  is a member of object  $Wall^1$ . The function  $Wall_j.InterSection(P_1, P_2, s_i)$  returns TRUE if there's an intersection point  $s_i$  between  $Wall_j$  and the line between  $P_1$  and  $P_2$ . In what follows, the equations needed are developed to implement a ray-tracing algorithm, that can accomodate any configuration of planes.

Two functions are used intensively; firstly the calculation of the image of some point in space with respect to the illuminated face of an object, and secondly the calculation of the intersection point between some line section and a face of an object. For these calculations each wall can be described as a plane  $V$ :

$$V : (\underline{n}, \underline{x}), \text{ where } \underline{n} = \frac{\underline{u} \times \underline{v}}{|\underline{u} \times \underline{v}|}, \quad (5.16)$$

which is known as the normal equation of a plane.  $\underline{u}$  and  $\underline{v}$  denote the direction

<sup>1</sup> The Object Oriented Programming technique has been used to structure the specification of the simulation software [13].

vectors of the plane and  $\underline{x}$  denotes the place vector with respect to the origin  $Q$ . The resulting normalized outer product is called the normal vector  $\underline{n}$ . By making use of this normal vector, the mirror point  $\underline{m}$  of the original point  $\underline{q}$  with respect to plane  $V$  can be written as

$$\underline{m} = \underline{q} - 2[\underline{n}, (\underline{q} - \underline{x})] \cdot \underline{n} \quad (5.17)$$

Let us consider a line section that begins at  $\underline{q}$  and ends at  $\underline{p}$ . If that line section intersects the plane  $V$ , then  $\underline{q}$  has to be on one side and  $\underline{p}$  on the other, hence

$$[\underline{n}, (\underline{q} - \underline{x})] \cdot [\underline{n}, (\underline{p} - \underline{x})] < 0 \quad (5.18)$$

If this property holds, then the intersection point  $\underline{s}$  can be calculated according to

$$\underline{s} = \underline{q} - \frac{[\underline{n}, (\underline{q} - \underline{x})]}{[\underline{n}, (\underline{q} - \underline{p})]} (\underline{q} - \underline{p}) \quad (5.19)$$

for an infinite plane  $V$ . Let  $V$  be bounded by the length of its direction vectors  $\underline{u}$  and  $\underline{v}$  and let  $(\underline{u}, \underline{v}) = 0$ . Then, an intersection point exists if the projections of  $\underline{s} - \underline{x}$  on the direction vectors  $\underline{u}$  and  $\underline{v}$  are both smaller than the length of the direction vectors, i.e., if

$$0 < \left[ \frac{\underline{u}}{|\underline{u}|}, (\underline{s} - \underline{x}) \right] < |\underline{u}| \quad \wedge \quad 0 < \left[ \frac{\underline{v}}{|\underline{v}|}, (\underline{s} - \underline{x}) \right] < |\underline{v}| \quad (5.20)$$

In the ray-tracing algorithm, we have to check whether or not a ray is obstructed by any of the objects in the room. We can do this in 3-D, but then we will have to check every face of every object to determine whether a ray intersects some object. The calculation efficiency can be considerably improved by applying a preselection in 2D. For this, each object in the room is wrapped in a rectangular box and all these boxes are projected to a horizontal plane. The line section from  $\underline{q}$  to  $\underline{p}$  is also projected to that horizontal plane. The preselection then results from 2D intersection checks in that plane.

Let us consider a reflected ray with  $K$  reflection points. We denote the  $k$ th reflection point (counted from the transmitting end) as  $\underline{s}_k$ ,  $k \in \{1, 2 \dots K\}$ . Then, the ray path consists of  $K+1$  (straight) path sections. Let  $\underline{r}_k$  be the propagation direction vector of the  $k$ th path section, i.e., the path section between  $\underline{s}_{k-1}$  and  $\underline{s}_k$  for  $k \in \{2, 3 \dots K\}$ . Furthermore, let  $\underline{r}_1$  and  $\underline{r}_{K+1}$  be the propagation direction vectors associated with the path section between  $\underline{T}_x$  and  $\underline{s}_1$  and the path section between  $\underline{s}_K$  and  $\underline{R}_x$ , respectively.

For each reflected ray the vector set  $\{\underline{r}_1, \underline{r}_2, \dots, \underline{r}_{K+1}\}$  must be known for calculation of the field contribution at the receive antenna. Furthermore, we have to determine the normal vectors of the reflecting planes. Thus, with  $\underline{n}_{ref,k}$  being the normal vector of the reflecting plane of  $\underline{r}_k$  the vector set  $\{\underline{n}_{ref,1}, \underline{n}_{ref,2}, \dots, \underline{n}_{ref,K}\}$  needs to be determined. In addition, the total path length  $l_{path}$  must be determined.

### 5.3.2 Coordinate system

It is most convenient to define the environment configuration with respect to a Cartesian coordinate system  $\langle e_x, e_y, e_z \rangle$  with the floor lying in the  $xy$  plane. With respect to this coordinate system, we define the position of the transmit antenna as  $\underline{T}_t = (T_x, T_y, T_z)$  whereas the position of the receive antenna is  $\underline{R}_r = (R_x, R_y, R_z)$ .

In PROSIM antenna beam directivity functions can be defined in the spherical coordinate system  $\langle e_\theta, e_\phi \rangle$ . The directivity functions are defined in a convenient way in the sense that the antenna beams as defined are symmetrical with respect to the  $z$ -axis or  $xy$  plane. The directivity pattern can be pointed arbitrarily by a rotation operation: The directivity function is defined as

$$\underline{F}_{def}(\theta, \phi) = F_{def,\theta}(\theta, \phi) \underline{e}_\theta + F_{def,\phi}(\theta, \phi) \underline{e}_\phi \quad (5.21)$$

Its rotated version is

$$\underline{F}(\theta, \phi) = F_{def,\theta}(\theta - \Delta\theta, \phi - \Delta\phi) \underline{e}_\theta + F_{def,\phi}(\theta - \Delta\theta, \phi - \Delta\phi) \underline{e}_\phi \quad (5.22)$$

where  $\Delta\theta$  is the rotation angle in the elevation plane in the positive  $\theta$ -direction, and  $\Delta\phi$  is the rotation angle in the azimuth plane in the positive  $\phi$ -direction.

### 5.3.3 Determination of field vectors

In order to calculate the field strength and polarization changes at the reflection points and the resulting electric field components at the receive antenna we define a reference plane  $V_{ref}(\underline{n}_{ref}, \underline{Q})$ . For convenience, the  $xy$  plane (i.e., the floor) is chosen as the reference plane. Hence;  $\underline{n}_{ref} = \underline{e}_z$ . Let us consider a reflected ray and let us introduce a vector  $\underline{A}_k$  representing the electric field vector along the  $k$ th ray section, with exclusion of the free space loss. The polarization components of  $\underline{A}_k$ , being  $A_{\theta,k}$  and  $A_{\phi,k}$ , are in the direction of the unity vectors  $\underline{e}_{\theta,k}$  and  $\underline{e}_{\phi,k}$ , respectively, as depicted in Fig. 5.5;  $\underline{e}_{\theta,k}$  lies parallel to the reference plane while  $\underline{e}_{\phi,k}$  is perpendicular to  $\underline{e}_{\theta,k}$

and  $\underline{z}_k$  which points in the direction of propagation.

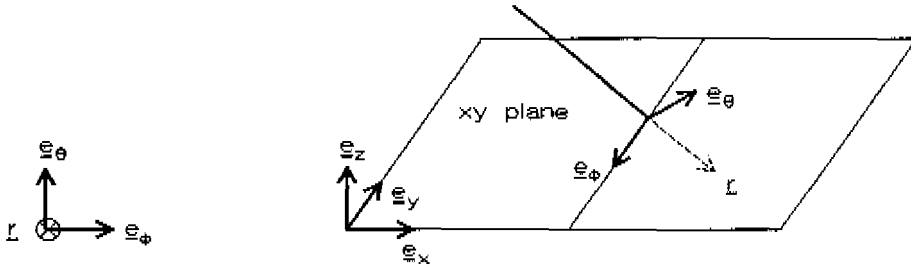


Fig. 5.5: Definition of field components of a ray.

The direction vectors can be described with respect to the plane  $V_{ref}$  as

$$\underline{e}_{\phi,k} = \frac{\underline{n}_{ref} \times \underline{r}_k}{|\underline{n}_{ref} \times \underline{r}_k|}, \quad \underline{e}_{\theta,k} = \frac{\underline{e}_{\phi,k} \times \underline{r}_k}{|\underline{e}_{\phi,k} \times \underline{r}_k|}. \quad (5.23)$$

Let us consider a reflection at  $\underline{s}_k$  as depicted in Fig. 5.6.

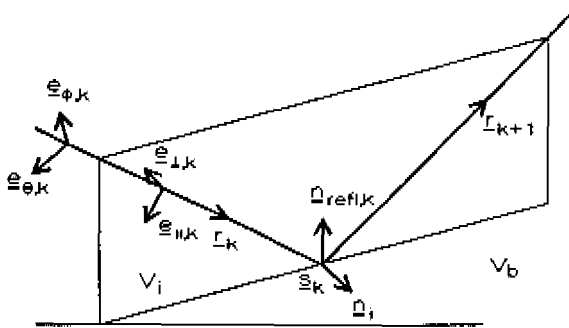


Fig. 5.6: Reflection against a plane boundary.

In order to allow determination of  $A_{\theta,k+1}$  and  $A_{\phi,k+1}$  by applying eq. (5.1) we first have to determine the components of  $\underline{A}_k$  perpendicular and parallel to the plane of incidence associated with the  $k$ th ray section.

The perpendicular unity vector  $\underline{e}_{\perp,k}$  can be found by using the fact that the incidence plane  $V_i(\underline{n}_i, \underline{s}_k)$  is perpendicular to the reflecting plane of the  $k$ th reflection  $V_{ref,k}(\underline{n}_{ref,k}, \underline{s}_k)$ , and by using the fact that the ray lies in the incidence plane. The parallel unity vector  $\underline{e}_{\parallel,k}$  is perpendicular to  $\underline{r}_k$  and  $\underline{e}_{\perp,k}$ . Hence;

$$\underline{e}_{\perp,k} = \frac{\underline{n}_{refl,k} \times \underline{r}_k}{|\underline{n}_{refl,k} \times \underline{r}_k|}, \quad \underline{e}_{\parallel,k} = \frac{\underline{e}_{\perp,k} \times \underline{r}_k}{|\underline{e}_{\perp,k} \times \underline{r}_k|}. \quad (5.24)$$

At the  $k$ th ray section the reference rotation from  $\langle \underline{e}_{\theta,k}, \underline{e}_{\phi,k} \rangle$  to  $\langle \underline{e}_{\parallel,k}, \underline{e}_{\perp,k} \rangle$  thus yields

$$\begin{bmatrix} A_{\parallel,k} \\ A_{\perp,k} \end{bmatrix} = \begin{bmatrix} (\underline{e}_{\parallel,k}, \underline{e}_{\theta,k}) & (\underline{e}_{\parallel,k}, \underline{e}_{\phi,k}) \\ -(\underline{e}_{\perp,k}, \underline{e}_{\theta,k}) & (\underline{e}_{\perp,k}, \underline{e}_{\phi,k}) \end{bmatrix} \begin{bmatrix} A_{\theta,k} \\ A_{\phi,k} \end{bmatrix}, \quad (5.25)$$

The incidence angle to the plane  $V_{refl,k}(\underline{n}_{refl,k}, \underline{s}_k)$  is equal to the arccosine of the inner product of the normal vector  $\underline{n}_{refl,k}$  with  $\underline{r}_k$ . Using this property, we can write the reflection coefficient for the  $k$ th reflection as

$$R_{\perp,k} = \frac{|\underline{n}_{refl,k}, \underline{r}_k| \cdot \sqrt{\mu'_k \epsilon_{r,k} - 1 + (\underline{n}_{refl,k}, \underline{r}_k)^2}}{|\underline{n}_{refl,k}, \underline{r}_k| + \sqrt{\mu'_k \epsilon_{r,k} - 1 + (\underline{n}_{refl,k}, \underline{r}_k)^2}}, \quad (5.26)$$

$$R_{\parallel,k} = \frac{\mu'_k \epsilon_{r,k} |\underline{n}_{refl,k}, \underline{r}_k| - \sqrt{\mu'_k \epsilon_{r,k} - 1 + (\underline{n}_{refl,k}, \underline{r}_k)^2}}{\mu'_k \epsilon_{r,k} |\underline{n}_{refl,k}, \underline{r}_k| + \sqrt{\mu'_k \epsilon_{r,k} - 1 + (\underline{n}_{refl,k}, \underline{r}_k)^2}},$$

in which the subscript " $k$ " refers to the material properties of the reflection surface of reflection point  $\underline{s}_k$ . Multiplying  $A_{\parallel,k}$  and  $A_{\perp,k}$  by their reflection coefficients yields

$$\begin{aligned} A_{\parallel,k+1} &= R_{\parallel,k} A_{\parallel,k} \\ A_{\perp,k+1} &= R_{\perp,k} A_{\perp,k} \end{aligned} \quad (5.27)$$

$A_{\theta,k+1}$  and  $A_{\phi,k+1}$  with respect to  $\langle \underline{e}_{\theta,k+1}, \underline{e}_{\phi,k+1} \rangle$  are obtained by

$$\begin{bmatrix} A_{\theta,k+1} \\ A_{\phi,k+1} \end{bmatrix} = \begin{bmatrix} (\underline{e}_{\theta,k+1}, \underline{e}_{\parallel,k+1}) & (\underline{e}_{\theta,k+1}, \underline{e}_{\perp,k+1}) \\ -(\underline{e}_{\phi,k+1}, \underline{e}_{\parallel,k+1}) & (\underline{e}_{\phi,k+1}, \underline{e}_{\perp,k+1}) \end{bmatrix} \begin{bmatrix} A_{\parallel,k+1} \\ A_{\perp,k+1} \end{bmatrix}. \quad (5.28)$$

### 5.3.4 Determination of ray parameters

Let the reflection at  $\underline{s}_k$  be characterized by the matrix operation  $\underline{R}_k$  which transforms



$\begin{bmatrix} A_{\theta,k} \\ A_{\phi,k} \end{bmatrix}$  into  $\begin{bmatrix} A_{\theta,k+1} \\ A_{\phi,k+1} \end{bmatrix}$  according to (5.25) to (5.28). Then, the actual electric field vector at the receive antenna

$$\underline{E}_{rec}(l_{path}) = E_{rec,\theta}(l_{path})\underline{e}_{\theta,K+1} + E_{rec,\phi}(l_{path})\underline{e}_{\phi,K+1}$$

can be calculated according to

$$\underline{E}_{rec}(l_{path}) = \underline{R}_1 \underline{R}_2 \dots \underline{R}_K \underline{E}_{rad}(l_{path}) \quad , \quad (5.29)$$

in which  $\underline{E}_{rad}(l_{path})$  is the far-zone electric field at distance  $l_{path}$  from the transmit antenna in the direction of radiation.  $\underline{E}_{rad}(l_{path})$  incorporates the directivity function of the transmit antenna as well as a factor  $l_{path}^{-1} e^{-j\beta l_{path}}$ , which accounts for the free space propagation.

$\underline{E}_{rad}(l_{path})$  is weighed with the directivity function of the receive antenna, which can be written as  $\underline{E}_{rec} = F_{rec,\theta}\underline{e}_{\theta} + F_{rec,\phi}\underline{e}_{\phi}$  with  $\underline{e}_{\theta} = \underline{e}_{\theta,K+1}$  and  $\underline{e}_{\phi} = -\underline{e}_{\phi,K+1}$ . Therefore, the ray amplitude  $\beta$ , phase  $\psi$  and excess delay  $\tau$  are<sup>2</sup>

$$\begin{aligned} \beta &= C \left| F_{rec,\theta} E_{rec,\theta} - F_{rec,\phi} E_{rec,\phi} \right| \quad , \\ \psi &= \arg\{F_{rec,\theta} E_{rec,\theta} - F_{rec,\phi} E_{rec,\phi}\} \quad , \\ \tau &= \frac{l_{path} - l_{min}}{c} \quad , \end{aligned} \quad (5.30)$$

in which  $C$  is a constant whereas  $l_{min}$  is the shortest ray path (i.e., the direct ray in the LOS case) and  $c$  is the velocity of light in free space. The constant  $C$  may incorporate antenna losses and impedance mismatches and can be determined on the basis of the radio equation. When, for example, the standard configuration as described in Section 3.5 is considered we can apply (3.13) and (5.30) to express the received power of an arbitrary LOS ray as

$$\beta^2 = G_a^2 \left[ \frac{\lambda}{4\pi r} \right]^2 = C^2 |F_{rec,\theta} E_{rec,\theta}|^2 \quad , \quad (5.31)$$

yielding the (positive) value of  $C$ .

---

<sup>2</sup> Here, the ray phase is denoted as  $\psi$  instead of  $\theta$  in order to avoid confusion with the coordinate angle  $\theta$ .

## 5.4 Implementation of antenna directivity functions

In PROSIM, directivity functions can either be entered in formula form or, alternatively, be stored in a look-up table. The latter enables the use of measurement data without data reduction. In this section, two types of aperture antennas are treated: 1) sectorial-horn antennas<sup>1</sup> and 2) biconical-horn antennas. Radiation patterns of both these antennas are pre-implemented in PROSIM.

### 5.4.1 Sectorial-horn antennas

The analysis of the spatial  $E$ -field originating from a smooth walled sectorial-horn antenna has extensively been treated in [14] and [15]. The cross-sections of such an antenna are shown in Fig. 5.7.

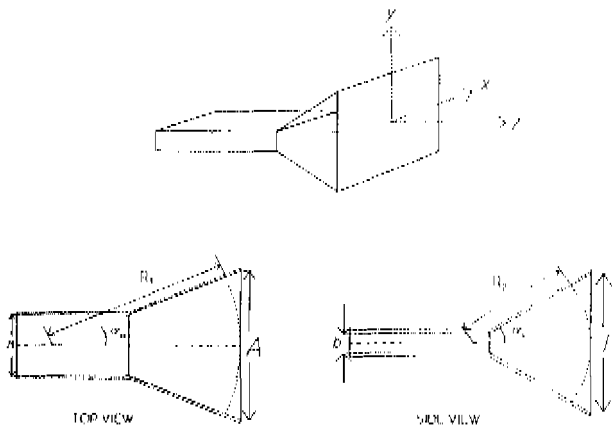


Figure 5.7: Cross-sections of the sectorial-horn antenna.

It can be considered as a taper section between the feeding rectangular waveguide and an opening aperture with cross-sectional dimensions to accommodate a mode impedance which approximates that of free space. The far-zone electric field can be determined by integrating the tangential fields which arise from the attached

<sup>1</sup> The sectorial-horn antenna exhibits a radiation pattern similar to the narrow beam of the circular-horn antenna used in some of our measurements (see Sections 3.3.5 and 3.6.3). Here, the sectorial-horn antenna is treated instead of the circular-horn antenna for the reason that the directivity function of the sectorial-horn antenna is much easier to analyse and therefore much easier to implement in PROSIM.

waveguide over the aperture. The aperture plane for the sectorial horn will be taken to be the  $xy$ -plane. Furthermore, we will assume that the waveguide carries the dominant  $TE_{10}$  rectangular waveguide mode. The aperture field is linearly polarized in  $y$ -direction and the amplitude distribution is, like that in the waveguide, a cosine taper in the  $x$ -direction. The far-zone electric field produced by the aperture field is given by [14] as

$$E_{\theta} = jk_0 \frac{e^{-jk_0 r}}{2\pi r} P_y \cdot \sin\phi \quad , \quad (5.32)$$

where  $r$  is the length of  $\underline{r}$  being the position vector from the origin in the aperture to the observation point in the far field.  $P_y$  is a two-dimensional Fourier transform of the aperture field  $E_{ap}$ , given by

$$P_y = \int_{S_{ap}} E_{ap}(\underline{r}') \cdot e^{jk_0 \underline{r}' \cdot \underline{z}'} dS' \quad , \quad (5.33)$$

where  $S_{ap}$  is the geometrical aperture surface.

The radiation pattern of the smooth walled sectorial-horn antenna is now completely determined for  $z > 0$  by its geometrical dimensions ( $A$ ,  $B$ ,  $L$ ). We have to determine the geometrical dimensions of the horn that will produce the desired 3-dB beamwidths in the two main planes: the one containing the electric field in the aperture (called the  $E$ -plane) and the one orthogonal to this (called the  $H$ -plane). The electric field in the aperture is linearly polarized along the  $y$ -axis. Hence; the  $H$ -plane corresponds to the  $\phi = 0$  plane cut and the  $E$ -plane to the  $\phi = 90^\circ$  plane cut.

We applied the design procedure as described in [15]. The design is based on an interpolation of the results obtained from many analysed horns. Those results are given in the form of the so-called "universal  $E$  and  $H$ -plane patterns" [14]. Based on these patterns, a set of geometrical dimensions ( $A$ ,  $B$ ,  $\alpha_E$ ,  $\alpha_H$ ) in the corresponding  $E$  or  $H$ -plane are generated producing the desired 3-dB beamwidth.

Not all of the combinations of  $E$  and  $H$ -plane dimensions are possible simultaneously since the perpendicular distance from the aperture plane to the waveguide-horn intersection plane must be equal in both planes. If we define this distance as the horn length  $L$ , then it implies that

$$\frac{A - a}{\tan\alpha_E} = \frac{B - b}{\tan\alpha_H} = 2L \quad , \quad (5.34)$$

where  $a$  and  $b$  are the a priori known waveguide dimensions. Note, that the definition

of the horn length  $L$  here differs slightly from that of the biconical-horn antenna since it is not measured from the (virtual) horn apex.

In order to determine the geometrical dimensions of the horn that will produce the desired 3-dB beamwidths in the two main planes we select a universal  $E$ -plane pattern producing the desired beamwidth and we determine the corresponding dimensions,  $A$  and  $L$ . The relation (5.34) can be used to generate a function  $B(L)$  for the  $H$ -plane. We will have a realizable horn antenna if this curve does intersect with a universal  $H$ -plane pattern producing the desired 3-dB curve in the  $H$ -plane. This procedure can be repeated for several other combinations of  $A$  and  $L$  producing a number of possible geometrical horn configurations with the desired 3-dB beamwidth in the  $E$  and  $H$ -plane. In this way, we designed six 57-59 GHz sectorial horns. Geometrical dimensions, 3-dB beamwidth and directivity of the designed horns are given in Table 5.3. The dimensions  $a$  and  $b$  of the attached waveguide are 2.388 mm and 4.775 mm, respectively, which complies with waveguide applied in the measurement setup.

Table 5.3: Dimensions of sectorial-horn antennas.

3-dB BW $H$ -plane (degrees)	3-dB BW $E$ -plane (degrees)	$A$ (mm)	$B$ (mm)	$\alpha_H$ (degrees)	$\alpha_H$ (degrees)	$D$ (dBi)
60	10	5.64	26.40	0.68	4.49	17.4
60	20	5.46	12.70	3.51	9.00	14.1
60	30	5.65	8.70	11.31	13.56	12.5
60	60	5.21	4.25	0.00	27.36	9.1
30	30	11.67	26.06	10.22	22.45	16.2
10	10	36.53	26.40	7.07	4.49	25.1

The aperture integration method applied is adequate in the main beam region and for moderate aperture sizes. For lower aperture sizes the radiation pattern is strongly influenced by the horn aperture flange structure. When we approach the  $\theta = \pi/2$  zone the error in the predictions increases and obviously the method is no longer valid beyond  $\theta = \pi/2$ . To obtain the radiated field in those regions for which the aperture integration method produces weak results one can use GTD techniques [16]-[18]. However, the main goal of this section is to investigate antenna effects on an indoor radio channel and we expect the zone beyond  $\theta = \pi/2$  to have little influence. Therefore, we simply assume the diffracted  $E$ -field in this zone to be constant. The

diffracted  $E$ -field can then be calculated using the relation

$$\int_{0 < \theta < \frac{\pi}{2}} P_{rad}(\Omega) d\Omega + \int_{\frac{\pi}{2} < \theta < \pi} P_{diff}(\Omega) d\Omega = P_t, \quad (5.35)$$

where  $P_t$  denotes the total power radiated by the horn.  $P_{rad}(\Omega)$  denotes the far field radiated power density calculated with aperture integration.  $P_{diff}(\Omega)$  denotes that part of the far field radiated power density with the horn diffraction which is assumed to be constant for  $\frac{1}{2}\pi < \theta < \pi$  and zero for  $0 < \theta \leq \frac{1}{2}\pi$ .

Fig. 5.8a and Fig 5.8b show, respectively, the  $E$ -plane and  $H$ -plane radiation pattern of a smooth walled sectorial-horn antenna design with a directivity  $D = 17.4$  dBi (see Table 5.3). Also included is the constant level of diffracted power for  $\frac{1}{2}\pi < \theta < \pi$ . The intersection of the dotted lines with the  $E$ -plane and  $H$ -plane radiation pattern indicate the 3-dB beamwidth in the  $E$ -plane and  $H$ -plane, respectively. The 17.4 dBi sectorial-horn antenna has 3-dB beamwidths of 10 and 60 degrees in the  $E$ -plane and  $H$ -plane, respectively.

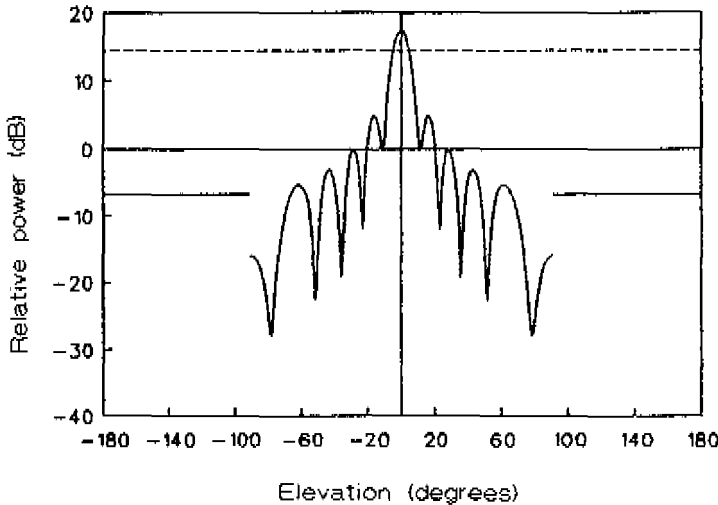


Fig. 5.8a: Radiation pattern of a 17.4 dBi sectorial-horn antenna in the  $E$ -plane.

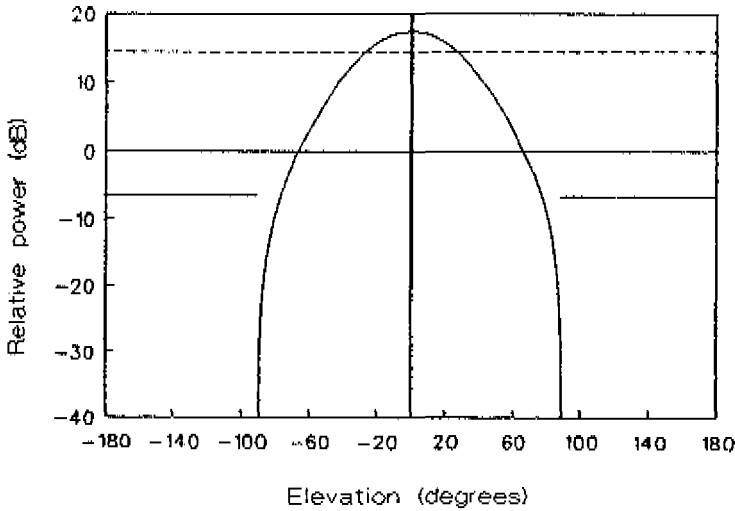


Fig. 5.8b: Radiation pattern of a 17.4 dBi sectorial-horn antenna in the  $H$ -plane.

#### 5.4.2 Biconical-horn antennas

The biconical-horn antenna has already been treated (see Section 3.3). Biconical-horn antennas consist of a radial line with spacing  $a$  and a biconical horn with (apex to aperture) length  $L$  and aperture width  $A$  (see Fig. 3.3). If the radial line is excited with the circularly polarised  $TE_{11}$  mode in the circular waveguide, then the biconical horn antenna exhibits an omnidirectional radiation pattern in the azimuth plane. The polarization is vertical for  $a < \frac{1}{2}\lambda_0$ . The radiation pattern in the elevation plane is determined by the horn dimensions  $A$  and  $L$  and can be calculated in the same way as the  $E$ -plane radiation pattern of a smooth walled sectorial horn (excited with the  $TE_{01}$  mode) described in the previous section.

Five different biconical horns have been designed for use in the simulations, all with different directivity and radiation pattern in the elevation plane. 3-dB beamwidth in the elevation plane, geometrical dimensions and antenna directivity of the designed antennas are listed in Table 5.4. The dimensions for the 9.0 dBi antenna are the same as those of the manufactured antennas applied in the measurements (which indeed showed a directivity of 9 dBi).

Table 5.4: Dimensions of biconical-horn antennas.

3-dB BW <i>E</i> -plane (degrees)	<i>B</i> (mm)	$\alpha_E$ (degrees)	<i>D</i> (dBi)
5	54.3	4.36	12.7
9	28.8	11.50	9.0
20	13.5	17.41	6.9
30	9.0	26.04	5.3
40	6.5	18.15	4.5

## 5.5 Simulation results and discussion

With the biconical-horn antennas described above we examined the accuracy of the GO model applied by comparing simulation results with measurement results. Since good agreement was found between the simulation and measurement results we continued with using PROSIM for a more thorough examination of the influence of the environment and antenna characteristics on rms delay spread (RDS) and normalized received power (NRP). In what follows, we present and discuss the results.

### 5.5.1 Comparison of simulation results with measurement results

The accuracy of the GO propagation model, on which PROSIM is based, is examined by comparing simulation results with results obtained from actual measurements. For this comparison we used the data obtained from the measurements.

Fig. 5.9 shows a typical measured and simulated power delay profile, both having 1 ns time-domain resolution. The environment under consideration is Room A described in Section 3.4. The model for this room is defined in the simulation software as a rectangular box with dimensions 24.3\*11.2\*4.5 m<sup>3</sup>. One long side is considered as entirely consisting of glass. The other sides are assumed to consist entirely of wood. The wall reflectivity is calculated according to the Fresnel reflection coefficients, given by (5.26), with material characteristics taken similar to those listed in Table 5.2. Only specular reflection and no diffuse scattering has been taken into account. A

scatter reduction factor as (5.10) has not been applied. The antennas applied are the 9 dBi biconical horn antennas. In the simulations, the base station antenna was located in the centre of the room at 3 m height as in the measurement setup. Per environment, 24 positions of the remote antenna have been examined. These positions were the same as those in the measurement setup.

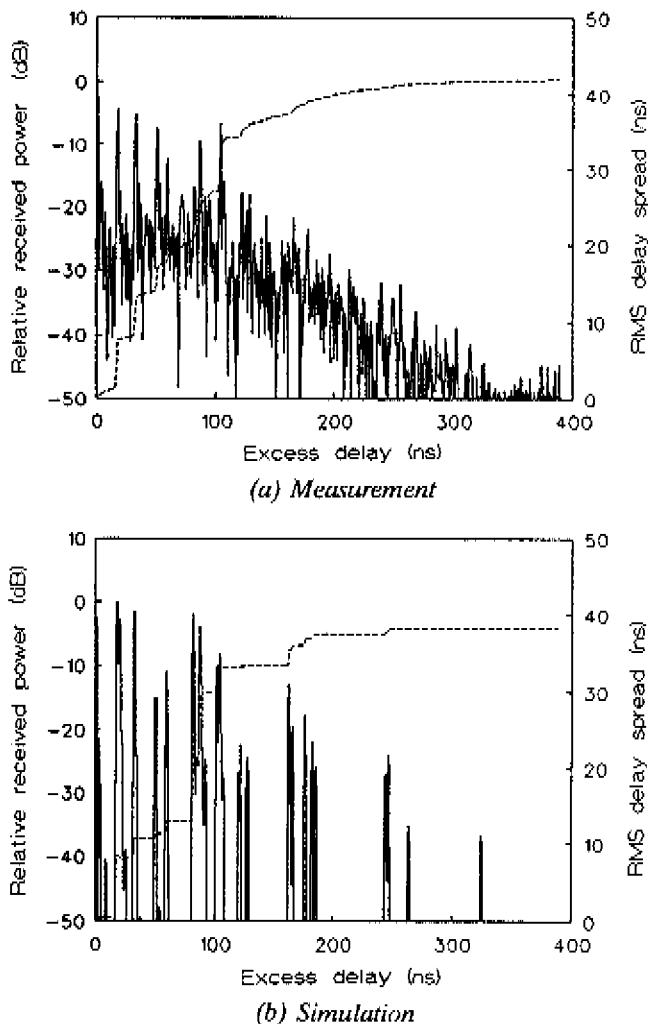


Fig. 5.9: Measured and simulated power delay profile and rms delay spread as function of maximum calculation time.



From Fig. 5.9 it occurs that the simulated and measured amplitudes of most dominant rays agree fairly well. In addition, it can be observed that the moments of occurrence of those dominant rays in the simulated profile agree well with the ones in the measured profile. However, in the measured profile the spacings in between the dominant rays are filled up with lower-level rays whereas in the simulated profile deep nulls are present. This difference may be attributed to diffraction and diffuse scattering effects which are not taken into account in the propagation model.

Fig. 5.9 also shows the RDS as a function of the maximum excess delay considered in calculating the rms delay spread (RDS). These curves give a good impression of the amount each individual ray contributes to the total RDS. We find that the weak rays in the measured profile which are present between the dominant rays do not yield a significant contribution to the total RDS. This fact clearly acts in favour of the accuracy of the model applied. For the profiles depicted in Fig. 5.9, it occurs that the timespan to be taken into account for calculating RDS should be at least about 200 ns. As with the measurement we took for the simulations a time span of 390 ns.

Fig. 5.10 depicts the CDF of the RDS values obtained from the measurements as well as the CDF of the corresponding values obtained from the simulations for 24 different positions of the remote-station antenna.

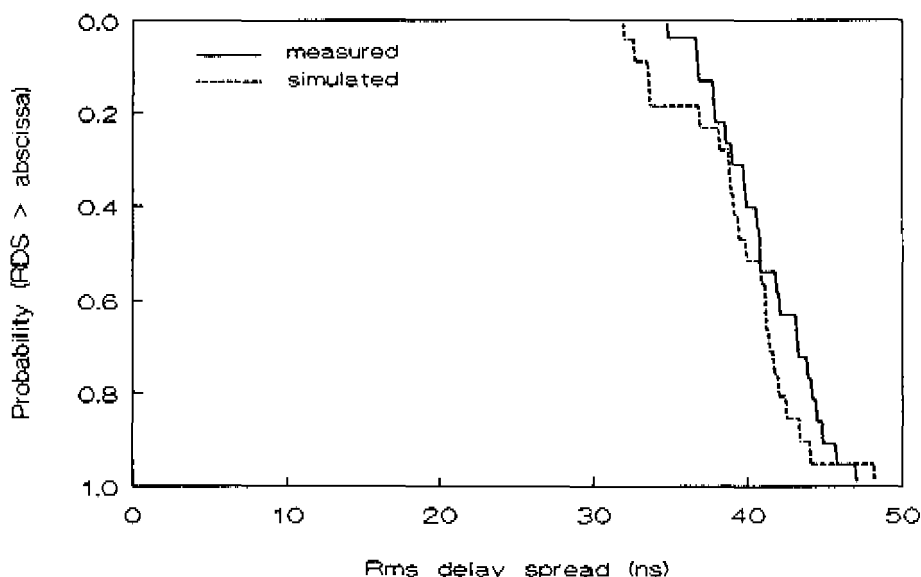


Fig. 5.10: Distribution functions of measured and simulated rms delay spread.

It occurs that the simulated CDF curve lies close to the measured CDF curve. This is also the case with the CDFs of the normalized received power (NRP) values. Although measured and simulated CDF curves show more deviation with respect to more irregularly shaped environments they are still in close agreement. There was, however, one clear exception. The measured and simulated CDF curves showed significant mutual differences of about 50% for Room F, the small ( $9.9 \times 8.7 \times 3.1 \text{ m}^3$ ) room with highly reflective (metal) walls. This was due to the limitation of the number of reflections to 4 in the simulation which causes the profiles to terminate too quickly.

The similarity observed between simulated and measured results confirms the assumption, that the channel characteristics of principal interest are mainly determined by the superstructure of the indoor environment (i.e., walls, ceiling, floor) and do not depend significantly on the details (i.e., tables, cabinets etc.) within that superstructure.

### 5.5.2 Additional simulations

In this section, the relation between NRP and RDS on the one hand and the shape and orientation of antenna radiation beams on the other is evaluated under both unobstructed LOS (indicated as "LOS") and obstructed LOS (indicated as "OBS") conditions. In addition, the influence of wall reflectivity on these parameters is examined. Antennas under consideration are the sectorial horn antennas and biconical horn antennas described in Section 5.4.

#### 5.5.2.1 Simulated configurations

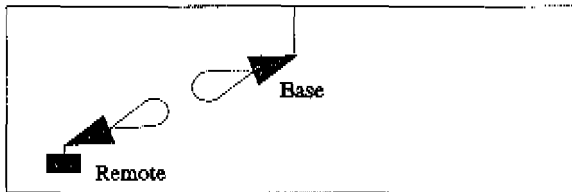
To examine the influence of wall reflectivity two rooms are considered; one room is a low reflective room with dimensions  $24.3 \times 11.2 \times 4.5 \text{ m}^3$ . The wall material has electrical properties such that, for perpendicular incidence, the average<sup>2</sup> return loss is 10 dB. The second room has exactly the same dimensions but the walls have a considerably lower average return loss of 1.5 dB. In both rooms, the receive antenna (representing the base-station antenna) is located at 3 metres height in the middle of the room, whereas the transmit antenna (representing the remote station antenna) is placed

---

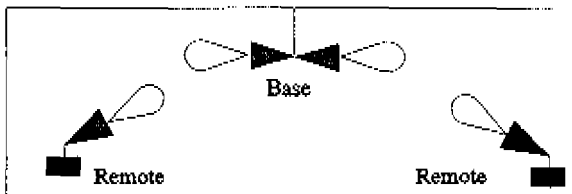
<sup>2</sup> I.e., the average of the six reflection coefficients for perpendicular incidence (4 walls, floor and ceiling).

1.4 metres above the floor at 24 randomly chosen positions throughout the room. For every position of the transmit antenna the power delay profile is calculated. Next, the NRP and RDS are derived from each profile obtained.

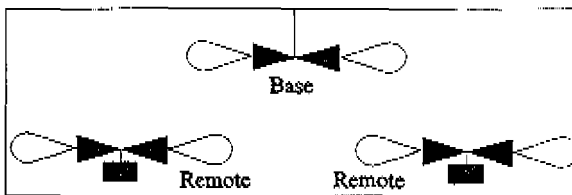
Simulations are performed for the three different antenna setups depicted in Fig. 5.11.



(a) Configuration C



(b) Configuration D



(c) standard configuration

Fig. 5.11: Simulated configurations.

Fig. 5.11a shows the antenna configuration with a sectorial horn at both the remote and base station, denoted as "Configuration C". In this configuration, the sectorial horns are pointing towards each other, eventually with a certain amount of mispointing in order to examine the effects of pointing errors. The orientation of the error angles at the remote and base station are mutually independent and randomly chosen.

Fig. 5.11b depicts the antenna setup with a sectorial horn at the remote station

and a biconical horn at the base station, denoted as "Configuration D". In this configuration, the sectorial horn at the remote station is pointing towards the biconical horn. Here, pointing errors are only introduced in the radiation beam of the sectorial horn at the remote station.

Fig. 5.11c shows the antenna setup with a biconical horn at both the remote and base station, which complies with the "Standard Configuration" as defined in Section 3.5. In this configuration, both biconical-horn antennas are radiating in the horizontal direction.

In addition to the effects of pointing errors, also the effects of an obstructed direct path are investigated. The results for obstructed LOS situations are derived from the results for unobstructed LOS situations by mathematical removal of the direct ray. This is justified by the observations made during the measurements, that obstruction of the LOS path by an object or person caused a total drop of the LOS ray power.

#### 5.5.2.2 Simulation results and discussion

For the three configurations, the results are presented in terms of NRP and RDS values. For various antenna beam directivity values and various pointing errors the smallest and largest of all (24) NRP values as well as the smallest and largest value of RDS are given for unobstructed as well as obstructed LOS. These values are useful indicators in estimating the level and spread of NRP and RDS that a receiver has to cope with under the given circumstances.

For Configuration C simulations have been performed with both antennas having dimensions, 3 dB beam widths and beam directivities as tabulated in Table 5.3. In the simulations the directivity of the remote-station antenna was always taken equal to the directivity of the base-station antenna. Table 5.5 lists the minimum and maximum NRP values obtained as well as the minimum and maximum RDS values obtained for various antenna directivity values and pointing errors for unobstructed LOS as well as for obstructed LOS.

Table 5.5: Minimum and maximum values for NRP and RDS obtained with Configuration C.

Ant. direct. (dBi)	LOS/ OBS	Pnt. err. (degr.)	NRP (dB)		RDS (ns)	
			min	max	min	max
low reflective room						
25.1	LOS	0	-40	-25	0	2
9.1	LOS	0	-70	-60	2	7
25.1	OBS	0	-108	-72	1	42
17.4	OBS	0	-104	-71	10	45
9.1	OBS	0	-91	-74	6	46
25.1	LOS	5	-73	-28	1	7
9.1	LOS	5	-90	-62	2	48
25.1	OBS	5	-108	-75	0	81
9.1	OBS	5	-110	-75	10	67
25.1	LOS	15	-91	-40	0	30
14.1	LOS	15	-88	-57	0	50
9.1	LOS	15	-90	-67	7	26
25.1	OBS	15	-110	-72	0	80
9.1	OBS	15	-108	-74	5	60
highly reflective room						
25.1	LOS	0	-40	-28	0	15
9.1	LOS	0	-70	-60	8	35
25.1	OBS	0	-90	-51	2	84
9.1	OBS	0	-78	-70	15	54
16.2	OBS	0	-85	-68	8	90
25.1	LOS	5	-65	-28	0	62
16.2	LOS	5	-79	-45	0	90
25.1	LOS	5	-88	-42	0	74
25.1	OBS	15	-90	-52	4	88

With respect to Configuration C we conclude that an antenna setup with 25.1 dBi sectorial horns at both ends yields the lowest RDS values and the highest NRP values when compared with the other examined configurations, provided that there is no obstruction of the LOS path and provided that the antenna beams are exactly pointing towards each other. Configuration C is, however, highly sensitive to LOS

obstruction and mispointing<sup>3</sup>. This is illustrated in Fig. 5.12 and Fig. 5.13, respectively, which show the NRP versus RDS for every position of the remote station. The combination of LOS obstruction and 5° mispointing results in a fairly uniform spread in RDS and NRP. A higher reflectivity of the walls results in higher NRP values as well as higher RDS values.

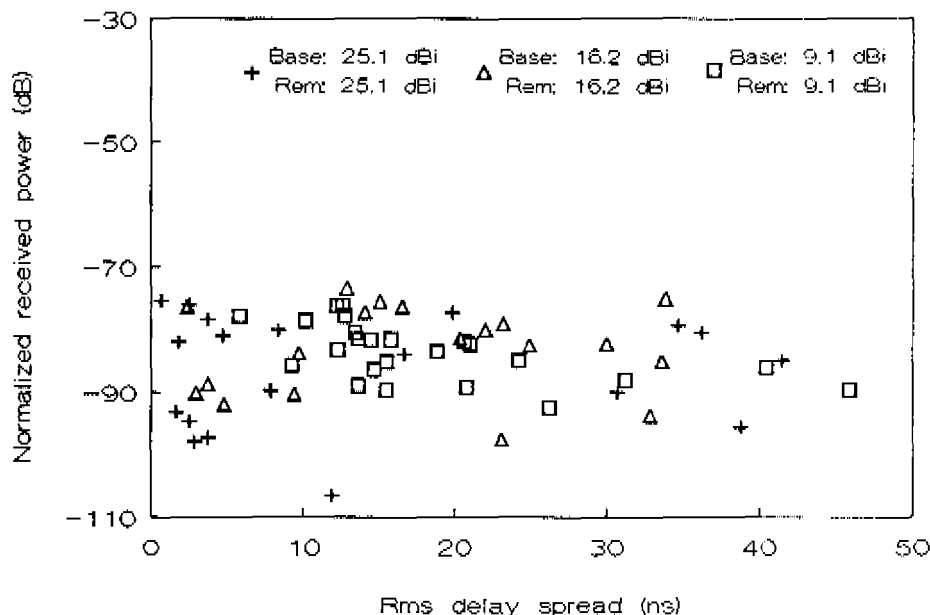


Fig. 5.12: Results for the low reflective room with Configuration C under OBS conditions.

<sup>3</sup> This conclusion is confirmed by additional experiments with an 11 Mbit/s digital radio communication link operating at 58 GHz in Room A. These experiments have been carried out in cooperation with the Physics and Electronics Laboratory (FEL-TNO) [20].

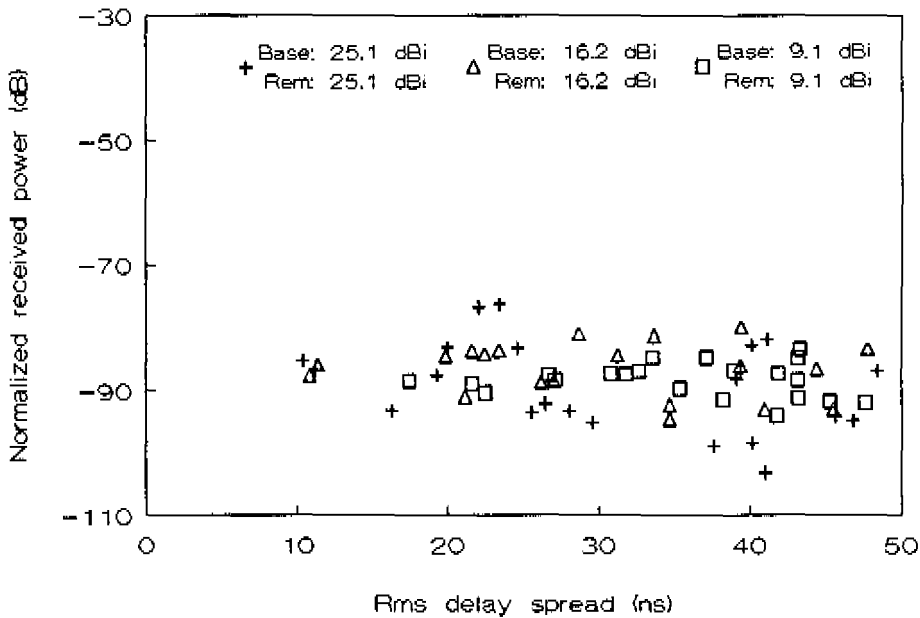


Fig. 5.13: Results for the low reflective room with Configuration C under OBS conditions.

For Configuration D, simulations have been performed with a sectorial horn at the remote station with beam directivity according to Table 5.3 and a 9 dBi biconical horn at the base station. Table 5.6 lists the minimum and maximum NRP values obtained as well as the minimum and maximum RDS values obtained for various beam directivity values of the remote station antenna and for various pointing errors under LOS as well as OBS.

As with Configuration C, it occurs that the Configuration D is highly sensitive to obstruction of the direct ray and mispointing. The effects of LOS obstruction and mispointing with  $5^\circ$  pointing error are demonstrated in Fig. 5.14 and Fig. 5.15, respectively. The difference with the Configuration C results is, however, that the minimum and maximum values for NRP and RDS for Configuration D are not so extreme. The spread in NRP values is significantly lower. This can be explained by the compensation effect described in Section 3.3.

Table 5.6: Minimum and maximum values for NRP and RDS obtained with Configuration D.

Ant. direct. (dBi)	LOS/ OBS	Pnt. err. (degr.)	NRP (dB)		RDS (ns)	
			min	max	min	max
low reflective room						
25.1	LOS	0	-65	-60	1	18
9.1	LOS	0	-81	-78	10	35
25.1	OBS	0	-102	-75	10	48
9.1	OBS	0	-100	-82	23	47
25.1	LOS	5	-92	-62	0	43
9.1	LOS	5	-90	-78	11	50
25.1	LOS	15	-98	-78	2	50
9.1	LOS	15	-88	-78	7	50
highly reflective room						
25.1	LOS	0	-62	-60	4	43
9.1	LOS	0	-75	-70	25	78
25.1	OBS	0	-85	-68	16	65
9.1	OBS	0	-80	-75	30	68

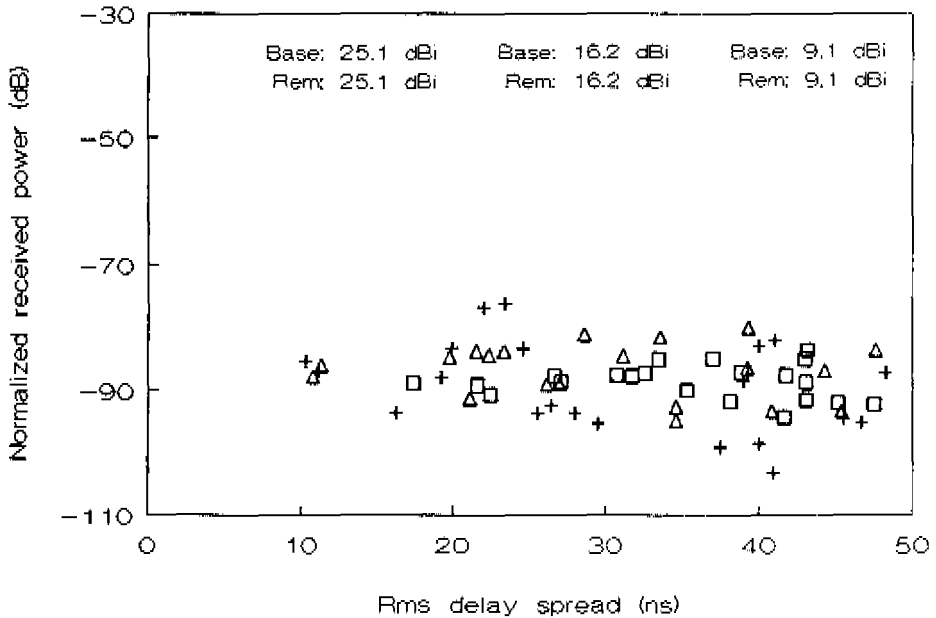


Fig. 5.14: Results for the low reflective room with Configuration D under OBS conditions.



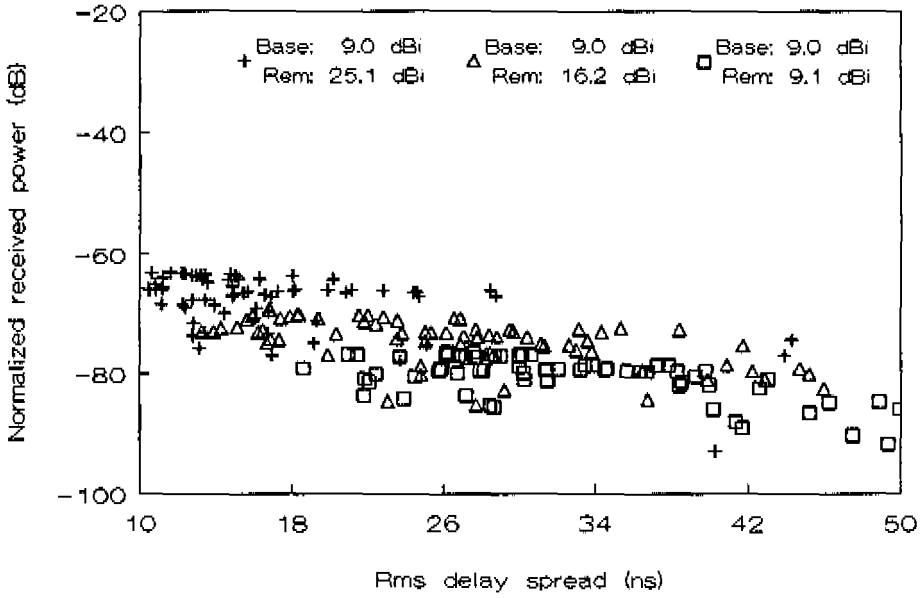


Fig. 5.15: Results for the low reflective room with Configuration D  $5^\circ$  pointing error.

For the Standard Configuration, simulations have been performed with biconical-horn antennas both having the same beam directivity value (one of those listed in Table 5.4). Table 5.7 lists the minimum and maximum NRP values obtained as well as the minimum and maximum RDS values obtained for the various beam directivity values of the antennas under LOS conditions as well as for OBS situations.

In contrast with the results obtained with Configuration C and Configuration D, it occurs that an increase in antenna directivity yields an increase of the RDS values (on average). Fig. 5.16 depicts the results obtained with a 9 dBi biconical horn at each end for both LOS and OBS. The differences in NRP values between those two cases are only a few dB. This indicates that the standard configuration is highly insensitive to LOS obstruction. Furthermore, the low spread in NRP values is striking. It perfectly demonstrates what is predicted and explained in Section 3.3 with respect to the uniformity in observed NRP values in case properly dimensioned biconical horns are applied. The standard configuration also yields the lowest spread in rms delay spread values. The low spread in the results has also been found for the highly reflective room with slightly higher NRP and RDS values on average.

*Table 5.7: Minimum and maximum values for NRP and RDS obtained with the standard configuration.*

Ant. direct. (dBi)	LOS/ OBS	NRP (dB)		RDS (ns)	
		min	max	min	max
low reflective room					
12.7	LOS	-84	-80	42	58
12.7	OBS	-84	-80	38	53
9.0	LOS	-82	-80	31	51
9.0	OBS	-83	-80	26	46
4.5	LOS	-82	-77	16	35
4.5	OBS	-89	-83	25	43
highly reflective room					
12.7	LOS	-68	-70	48	59
12.7	OBS	-68	-70	48	56
9.0	LOS	-68	-70	46	56
9.0	OBS	-68	-70	46	56
4.5	LOS	-76	-74	43	56
4.5	OBS	-77	-74	40	51

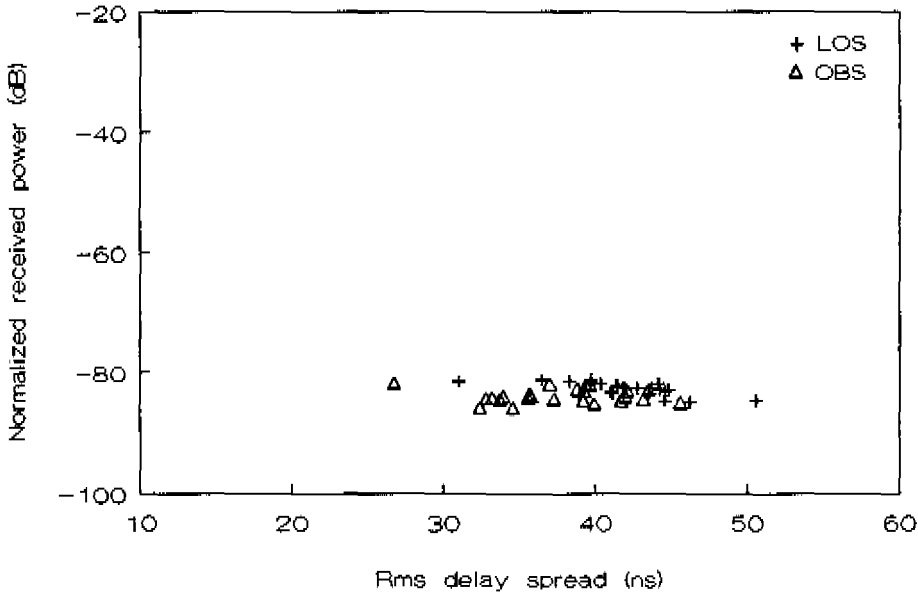


Fig. 5.16: Results for the low reflective room with the standard configuration under LOS and OBS conditions and with both antennas having 9 dBi beam directivity.

## 5.6 Summary and conclusions

A deterministic model of mm-wave indoor radio channels is discussed. As part of the deterministic modelling the significance of diffraction and scatter effects is examined. Typically, the diffracted power does not yield a significant contribution to the total received power. The surface roughness of building materials that can be typically found in indoor environments is such that the resulting scattering (diffuse reflection) does not contribute significantly to the total received power either. The dominant contributions are expected to come from specular reflections. We can calculate these contributions on the basis of the material characteristics  $\epsilon'$ ,  $\mu'$  and  $\sigma$  and eventually the material thickness and a factor that accounts for scatter loss.

Based on the above considerations, we propose a channel model on the basis of Geometrical Optics (GO) and we present the mathematical fundamentals for its implementation. The accuracy of the proposed model is examined by comparing simulation results with the data obtained from the measurements presented in Section

3.6. The indoor environments defined in the simulation software are simplifications of the corresponding real environments in which the measurements took place. Although the model only includes the superstructure (walls, floor and ceiling) and lacks details as tables and cabinets, the simulation results are in good agreement with the measurement results. This indicates that the results are mainly determined by the superstructure of the indoor environment.

After it was found that the GO-model yields accurate results, we performed computer simulations in order to gain a more detailed insight into the influence of environment and antenna characteristics on the most interesting channel parameters. For this, we defined antenna configurations with sectorial and/or biconical-horn antennas in the simulation software. A configuration with sectorial horns at both ends having the highest beam directivity considered yields the lowest rms delay spread and highest normalized received power when compared with other examined setups, provided that there is no obstruction of the LOS path and provided that the antenna beams are exactly pointing towards each other. A configuration with biconical horns at both ends yields results with respect to normalized received power and rms delay spread that are highly insensitive to LOS blocking. In addition, the uniformity in normalized received power values is observed as predicted and explained in Section 3.3. This setup also yields the lowest spread in rms delay spread values.

---

**References in Chapter 5**

- [1] T. Griesser and C.A. Balanis, "Reflections, diffractions, and surface waves for an interior impedance wedge of arbitrary angle", *IEEE Trans. Antennas Propagat.*, Vol. AP-37, No. 7, pp. 927-935, 1989.
- [2] J.B. Keller, "Geometrical Theory of Diffraction", *Journ. Opt. Soc. Am.*, Vol. 52, No. 2, pp. 116-130, 1962.
- [3] R.G. Kouyoumjian and P.H. Pathak, "A uniform GTD for an edge in a perfectly conducting surface", *Proc. IEEE*, Vol. 62, No. 11, pp. 1448-1461, 1974.
- [4] R. Tiberio, G. Pelosi and G. Manara, "A uniform GTD formulation for the diffraction by a wedge with impedance faces", *IEEE Trans. Antennas Propagat.*, Vol. AP-33, No. 8, pp. 867-873, 1985.
- [5] S.W. Lee and G.A. Deschamps, "A Uniform Asymptotic Theory of Edge diffraction", *IEEE Trans. Antennas Propagat.*, Vol. AP-24, No. 1, pp. 25-34, 1976.
- [6] J. Dijk, A. v.d. Vorst and L. Wijdemans, F.M. Boumans and W.T.E. Vaessen, "Microgolfdemping bij bouwmaterialen t.b.v. het stoor niveau in computerruimtes", Report Eindhoven University of Technology, Faculty of Electrical Engineering, Telecommunications Division, 1988. (in Dutch)
- [7] L.M. Correia and P.O. Frances, "Estimation of materials characteristics from power measurements at 60 GHz", *Proc. 5th Int. Symp. on Personal, Indoor and Mobile Radio Comm.*, The Hague, Sept. 1994.
- [8] P. Beckmann and A. Spizzichino, "The scattering of electromagnetic waves from rough surfaces", Pergamon Press, 1963.
- [9] B. Langen, G. Lober and W. Herzig, "Reflection and Transmission Behaviour of Building Materials at 60 GHz", *Proc. 5th Int. Symp. on Personal, Indoor and Mobile Radio Comm.*, The Hague, Sept. 1994.
- [10] J.W. McKnown, R.L. Hamilton, "Ray Tracing as a design Tool for Radio Networks", *IEEE Network Magazine*, Vol. 5, No 6, pp. 27-30, 1991.

- 
- [11] M. Kimpe, V. Bohossian and H. Leib, "Ray Tracing for Indoor Radio Channel Estimation, Proc. ICUPC '93, Ottawa, pp.64-68, Oct. 1993.
  - [12] G. Yang, S. Li, J-F. Lee and K. Pahlavan, "Computer Simulation of Indoor Radio Propagation, Proc. PIMRC '93, Yokohama, pp. 10-14, Sept. 1993.
  - [13] E.W.A.M. Ruis, "An Object-Oriented Programming approach to the modelling of mm-wave indoor radio channels", M.Sc.E.E. Thesis, Telecommunications Division, EUT, Febr. 1994.
  - [14] W.L. Stutzman and G.A. Thiele, "Antenna theory and design", New York, John Wiley and Sons, Inc., pp. 411-415, 1981.
  - [15] C.J. Sletten, "Reflector and lens antennas: analysis and design using personal computers", Boston, Artech House, Inc., pp. 92-100, 1988.
  - [16] J.B. Andersen, "Low and medium gain microwave antennas", The Handbook of Antenna Design, London, P. Peregrinus, Vol. I, Chap. 7, 1982.
  - [17] P.M. Russo and R.C. Rudduck, "A method for computing E-plane patterns of horn antennas", IEEE Trans. Antennas Propagat., Vol. AP-13, pp. 219-224, 1965.
  - [18] C.A. Mentzer, L. Peters and R.C. Rudduck, "Slope diffraction and its application to horns", IEEE Trans. Antennas Propagat., Vol. AP-23, No. 2, pp. 153-159, 1975.
  - [19] T. Holt, K. Pahlavan and J.F. Lee, "A graphical indoor channel simulator using 2D ray tracing", Int. Comm. Conf. '92, pp. 411-415, 1992.
  - [20] R. Overduin, P.F.M. Smulders, "Feasibility of broadband inroom radio communications at 60 GHz", Proc. 5th IEEE Int. Symp. on Personal, Indoor and Mobile Radio Communications, The Hague, pp. 119-126, Sept. 1994.

## CHAPTER 6.

# PERFORMANCE OF MILLIMETRE-WAVE INDOOR RADIO TRANSMISSION

### 6.1 Introduction

In the previous chapters, measurement results concerning the characteristics of mm-wave indoor radio channels were reported (Chapter 3) and statistically modelled (Chapter 4). In addition, simulation results generated according to a deterministic channel model were given (Chapter 5). These results and models can be used to estimate the performance of mm-wave indoor radio transmission. In this chapter a performance evaluation is presented which is directly based on *measured* impulse responses<sup>1</sup>. The objective of this performance evaluation is to assist in weighing design options such as antenna use, channel equalization complexity and application of external diversity.

In the next section the transmission performance is evaluated for the case that the

---

<sup>1</sup> Geerts [1] carried out a transmission performance evaluation based on the statistical model presented in Chapter 4. Fernandes et. al. [2] evaluated the transmission performance on the basis of the deterministic model presented in Chapter 5. The methods applied are basically the same as those presented in this chapter. Because of this and because there are no significant discrepancies in the results when compared with the results reported in this chapter we do not discuss these evaluations further.

modulation format applied is Quaternary Phase Shift Keying (QPSK) where no channel equalization is implemented. In Section 6.3, simulation results are presented and discussed. In Section 6.4 the Decision Feedback Equaliser (DFE) is presented and the transmission performance of a transmission system applying QPSK/DFE is evaluated. Results of QPSK/DFE simulations are presented and discussed in Section 6.5. The adaption to changes in the channel characteristics of the DFE are treated in Section 6.6. Finally, in Section 6.7, a summary is presented and conclusions are given.

## 6.2 Performance of QPSK

The modulation scheme considered is QPSK because this scheme is representative for more sophisticated schemes such as Offset QPSK and Gaussian Minimum Shift Keying (GMSK) which are envisaged for wireless LAN products [3,4,5]. These schemes can cope better with channel non-linearities or have improved bandwidth efficiency but they show similar performance with respect to probability of error. Therefore, we expect an evaluation of QPSK performance to yield a certain generality of the results. Because of the simplicity of the transmission system assumed in this section, it can be considered as a reference system allowing evaluation of performance gain due to more sophisticated receive techniques. As such, it provides insight in performance/complexity trade-off.

Fig. 6.1 shows the equivalent lowpass model of the indoor radio transmission link under study.

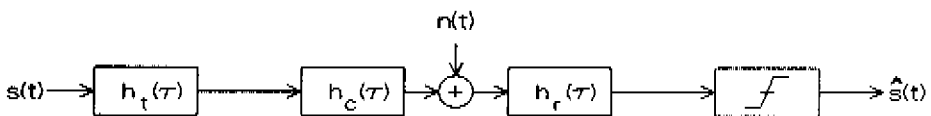


Fig. 6.1: Equivalent lowpass model of a QPSK indoor radio link.

$h_t(\tau)$  and  $h_r(\tau)$  are the (complex equivalent lowpass) impulse responses of the transmit filter and receive filter, respectively.  $h_c(\tau)$  here is the impulse response of the channel.  $n(t)$  represents Additive Gaussian Noise with single sided power spectral density  $N_0$  at the input of the receiver.  $s(t)$  represents the input data whereas  $\hat{s}(t)$  is the data after detection at the receiver. The input signal  $s(t)$  associated with the input data sequence  $\{s_k\}$  can be formulated as



$$s(t) = \sum_{k=-\infty}^{\infty} s_k \delta(t - kT_s) \quad , \quad (6.1)$$

where  $T_s$  is the symbol time, i.e., the time between successive symbol transmissions and  $\delta(\cdot)$  is the Dirac delta function. For QPSK modulation the data  $\{s_k\}$ , are selected from the set  $(a_k + jb_k)$  where  $\{a_k\}$ ,  $\{b_k\}$  are data sequences for the in-phase and quadrature channels, respectively, with  $a_k = \pm 1$ ,  $b_k = \pm 1$ .

The data sequence is shaped in such way that pulses have zeros periodically spaced in time at  $t = \pm T_s, \pm 2T_s, \pm 3T_s, \dots$ . A pulse shape widely in use in digital transmission on band-limited channels is generated by the *raised cosine* filter. This filter has impulse response

$$cr(\tau) = \frac{\sin \pi \tau / T_s}{\pi \tau / T_s} \frac{\cos \beta \pi \tau / T_s}{1 - (2\beta \tau / T_s)^2} \quad , \quad (6.2)$$

where  $0 \leq \beta \leq 1$  is the *rolloff factor*. The value of  $\beta$  will be taken 0.5 throughout this chapter according to common practice. The convolution with the data sequence (6.1) results in a *Nyquist pulse*. Commonly, the filtering is split equally between transmitter and receiver which means that  $h_c(\tau) = h_r(\tau)$  with  $h_c(\tau) * h_r(\tau) = cr(\tau)$  where  $*$  is the time domain convolution.

The complex equivalent lowpass impulse response of the communication link  $h_l(\tau)$  depicted in Fig. 6.1 can be written as

$$\begin{aligned} h_l(\tau) &= p(\tau) + jq(\tau) \\ &= cr(\tau) * h_c(\tau) \quad . \end{aligned} \quad (6.3)$$

The impulse response of the channel  $h_c(\tau)$  is given by (4.1). The subscript  $c$  is added to emphasize that the response of the *channel* is meant whereas the subscript  $l$  is used for the *overall link* response. Convoluting  $cr(t)$  with  $h_c(t)$  yields

$$h_l(\tau) = \sum_{n=1}^N \beta_n e^{j\theta_n} cr(\tau - \tau_n) \quad . \quad (6.4)$$

The received signal at sampling instant  $t_0$  follows from the time domain convolution of the input data sequence  $s(t)$  and the link response  $h_l(t)$  and the addition of a Gaussian noise process  $n(t)$ , being the result of convoluting  $n(t)$  and  $h_r(t)$ , yielding

$$\begin{aligned}
 r(t_0) &= \sum_{k=-\infty}^{\infty} s_k h(t_0 - kT_s) + n(t_0) \\
 &= \sum_{k=-\infty}^{\infty} [a_k p(t_0 - kT_s) - b_k q(t_0 - kT_s)] \\
 &\quad + j \sum_{k=-\infty}^{\infty} [b_k p(t_0 - kT_s) + a_k q(t_0 - kT_s)] \\
 &\quad + n_i(t_0) + j n_q(t_0) \quad ,
 \end{aligned} \tag{6.5}$$

in which  $n_i(t_0)$  and  $n_q(t_0)$  denote the in phase and quadrature components of  $n(t_0)$ , respectively. These components are assumed to be uncorrelated.

If the transmitted symbol of interest is indicated by  $s_0$ , then the intersymbol interference (ISI) follows from the summation over all  $k \neq 0$ . Rewriting the first term in the expression on the right hand side of (6.5) with expression (6.4) leads to

$$r(t_0) = s_0 \sum_{n=1}^N \beta_n e^{j\theta_n} \cdot cr(t_0 - \tau_n) + \left[ \sum' s_k \sum_{n=1}^N \beta_n e^{j\theta_n} \cdot cr(t_0 - kT_s - \tau_n) \right] + n(t_0) \quad , \tag{6.6}$$

where  $\sum'$  denotes the summation over all  $k \neq 0$ . The expression of the first term of the right part of (6.6) represents the received pulse whereas the expression between the square brackets represents the ISI. If the timing instant  $t_0$  cancels the delays  $\tau_n$ , so that the argument of the raised cosine in the ISI expression equals  $kT_s$ , then the shape of the raised cosine leads to zero ISI terms. When the symbol period is large when compared with  $t_0 - \tau_n$  the ISI terms are small, but when the symbol period decreases, and thus symbol rate increases, the argument becomes comparable to  $t_0 - \tau_n$  and starts to depart from the nulls in the raised cosine so that the ISI terms increase.

A symbol error occurs if

$$\begin{aligned}
 \sum' [a_k(p(t_0 - kT_s) - b_k q(t_0 - kT_s))] + n_i(t_0) &> -a_0 p(t_0) + b_0 q(t_0) \quad \vee \\
 \sum' [b_k(p(t_0 - kT_s) + a_k q(t_0 - kT_s))] + n_q(t_0) &> -b_0 p(t_0) - a_0 q(t_0) \quad ,
 \end{aligned} \tag{6.7}$$

The probability of a symbol error event  $P_s$  is

$$P_s \approx P_{s,i} + P_{s,q} \quad , \tag{6.8}$$

in which  $P_{s,i}$  and  $P_{s,q}$  denote the probability of symbol error for the in phase and quadrature channel, respectively, which both are assumed to be  $\ll 0.5$ . When Gray encoding is employed for symbol mapping and the adjacent phase is selected for the transmitted phase, the symbol error contains only one bit error. Thus, for Gray encoding the probability of bit error is

$$P_b = \frac{1}{2} P_s \approx P_{s,t} = P_{s,q} \quad (6.9)$$

In principle  $P_b$  can be determined by calculating all significant ISI samples. For this, however, considerable mathematical, programming and computational effort might be necessary [6,7]. The latter is especially true for calculation of the maximum feasible bit rate for a given  $P_b$  value which requires many calculations of  $P_b$  for different bit rate values. Considerable gain in computing time and required programming effort can be achieved by applying simple closed form expressions for upper and lower bounds on  $P_b$ . Milewski [8] derived expressions for close bounds for a (pseudo) random input data sequence.

The approach of [8] is based on the arrangement of ISI samples in decreasing order of magnitude  $|S_1| \geq |S_2| \geq \dots \geq |S_k| \geq \dots$ , where  $S_k$  is either  $p(t_0+kT_d)/p(t_0)$  or  $q(t_0+kT_d)/p(t_0)$ . Then, the upper and lower bounds on  $P_b$  can be expressed as

$$P_b \leq \frac{1}{2} \operatorname{erfc}((1-D_p)\sqrt{\gamma_b}) \cdot \prod_{k=1}^{\infty} \frac{1}{2} \left[ 1 + \frac{\operatorname{erfc}((1-D_p+2|S_k|)\sqrt{\gamma_b})}{\operatorname{erfc}((1-D_p)\sqrt{\gamma_b})} \right], \quad (6.10)$$

$$P_b \geq \frac{1}{2} \operatorname{erfc}((1-D_p)\sqrt{\gamma_b}) \cdot \prod_{k=1}^{\infty} \frac{1}{2} \left[ 1 + \frac{\operatorname{erfc}((1+D_p-2E_k)\sqrt{\gamma_b})}{\operatorname{erfc}((1+D_p-2E_k)\sqrt{\gamma_b})} \right], \quad (6.11)$$

where  $D_p$  denotes the peak distortion, i.e., the sum of all the significant ISI samples whereas  $E_k$  denotes the sum of the first  $k$  ISI samples.  $\gamma_b$  represents the ratio of the energy per bit  $E_b$  and  $N_0$  at the detector input. The proofs of (6.10) and (6.11) are outside the scope of this thesis but they are given by Milewski [8] in a comprehensive and heuristic way.

The timing instant  $t_0$  used for deriving the ISI samples, can be calculated in two different ways; according to the amplitude algorithm and according to the power algorithm.

The amplitude algorithm weighs the excess delays ( $\tau_n$ ) with the amplitudes ( $\beta_n$ ) of the different rays, thus

$$t_0 = \frac{\sum_{n=1}^{\infty} \beta_n \tau_n}{\sum_{n=1}^{\infty} \beta_n} \quad (6.12)$$

The power algorithm weighs the ray excess delays with the power, i.e., the square of the ray amplitude, thus

$$t_0 = \frac{\sum_{n=1}^{\infty} \beta_n^2 \tau_n}{\sum_{n=1}^{\infty} \beta_n^2} \quad (6.13)$$

### 6.3 Calculation results and discussion with respect to QPSK

#### 6.3.1 Parameters under consideration

The probability of bit error  $P_b$  is a simple and clear indication of the quality of the digital transmission. It can be argued, however, that it is a rather sensitive parameter since a small perturbation in system noise or channel characteristics can induce a large change of  $P_b$ . Therefore, we consider also another parameter, which is better suited to our purpose known as the *maximum bit rate*  $r_{b,max}$ , i.e., the maximum bit rate for which a given value (threshold) of  $P_b$  can be achieved. In what follows, this threshold will be denoted as  $P_{b,\phi}$ . Parameter  $r_{b,max}$  is a measure that indicates the performance of the entire transmission link (thus including the channel). A measure that is more indicative for the performance of the receiver alone is the *normalized maximum bit rate*  $R_{b,max} = \sigma_{ms} \cdot r_{b,max}$ . This parameter is a useful parameter in comparing different receiver structures whereas  $r_{b,max}$  more readily expresses the relationship between environments and feasible bit rate performance.

#### 6.3.2 Comparison of lower and upper Milewski bounds

In order to assess the suitability of the lower and upper Milewski bounds for our purposes we examined the tightness of these bounds for impulse responses typically encountered. In Fig. 6.2, the upper and lower bounds are presented versus  $E_b/N_0$  according to approximations of (6.10) and (6.11), respectively. These are approximations in the sense that only ISI factors up to  $j=40$  are taken into account.

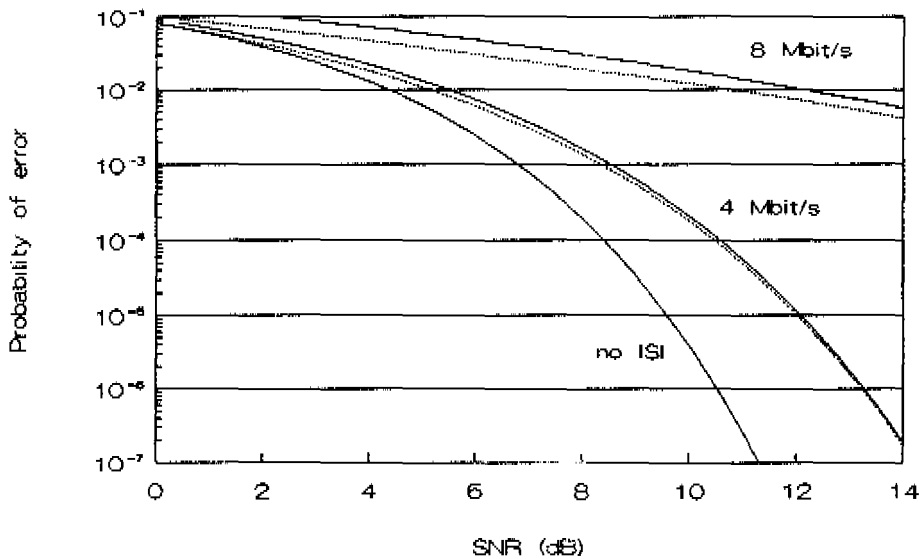


Fig. 6.2: Upper and lower Milewski bounds.

The impulse response under consideration was obtained in Room A with the standard measurement configuration as defined in Section 3.5. It is a typical sample with respect to "peakedness" and decay.

The bit rates considered are  $r_b=4$  Mbit/s and  $r_b=8$  Mbit/s. Also included is the curve for QPSK without ISI. When ISI is absent the upper as well as the lower Milewski bound comply with

$$P_b = \frac{1}{2} \operatorname{erfc} \sqrt{\gamma_b} \quad (6.14)$$

Fig. 6.2 shows that the upper bound lies close to the lower bound. Since the difference is caused by the ISI factors it tends to be especially small for the case that the ISI is small, i.e., for the data range of interest. However, even for  $r_b=4$  Mbit/s, for which the influence of ISI is considerable (when compared with the no-ISI curve), the bounds are close. This indicates that calculating the probability of bit error on the basis of one of these bounds yields satisfactory accuracy. However, we may not generalize this conclusion for all impulse responses obtained. Therefore, we calculated for each response both bounds. We only found differences between lower and upper bound that are comparable with those depicted in Fig. 6.2. This implies satisfactory accuracy of the results presented in the following which are based on

upper (thus; worst case) Milewski bounds.

### 6.3.3 Influence of timing algorithm

The influence of the algorithm, applied to determine the timing instant  $t_0$  on  $R_{b,max}$  has been determined for the LOS measurement subsets obtained in Room A and Room D with the standard measurement configuration. Fig. 6.3 and Fig. 6.4, show the (complementary) cumulative distribution functions (CDFs) for Room A and Room D, respectively.  $P_{b,th}$  is  $10^{-6}$  and there is no additive noise considered. This means that (6.10) and (6.11) have been applied to calculate  $\lim_{\gamma \rightarrow \infty} P_b$ .

The power algorithm shows superior performance when compared with the amplitude algorithm. This is also the case for the other measurement subsets. Therefore, the power algorithm is used in further simulations.

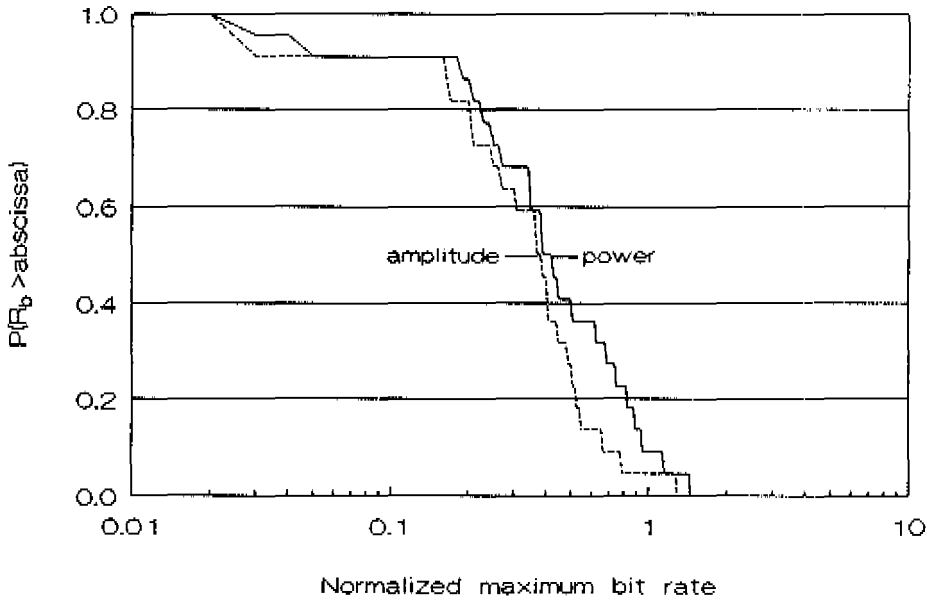


Fig. 6.3: Distribution functions of normalized maximum bit rate for amplitude and power algorithm, Room A,  $P_{b,th} = 10^{-6}$ .

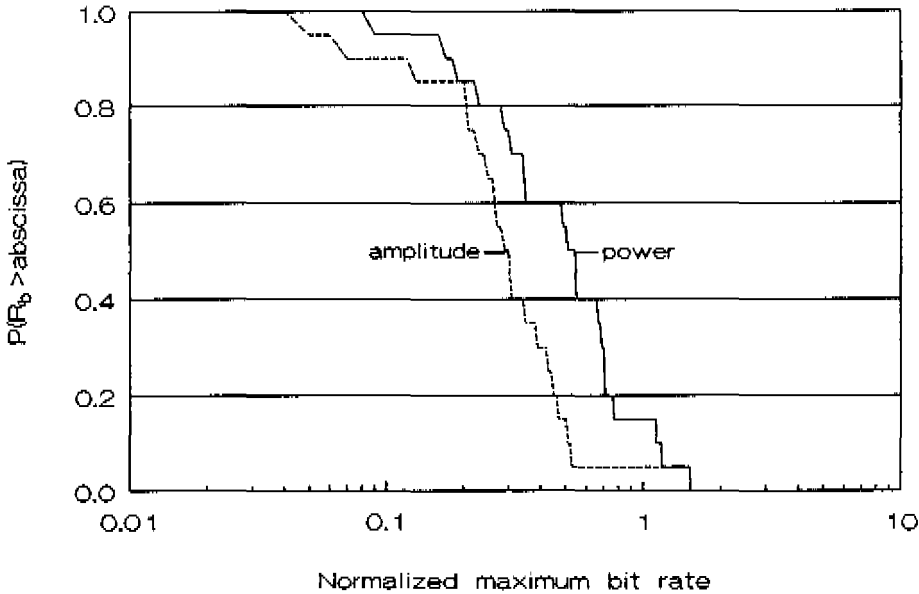


Fig. 6.4: Distribution functions of normalized maximum bit rate for amplitude and power algorithm, Room D,  $P_{b,th} = 10^{-6}$ .

#### 6.3.4 Influence of probability of bit error threshold.

In order to examine the influence of the parameter  $P_{b,th}$  we compared the  $R_{b,max}$  values obtained with  $P_{b,th} = 10^{-3}$  with those obtained with  $P_{b,th} = 10^{-6}$ . The measurement subset considered is the one obtained in Room A with the standard measurement configuration. CDFs for the LOS case and OBS case are depicted in Fig. 6.5 and Fig. 6.6, respectively.

For LOS as well as OBS the difference between the  $10^{-3}$ -curve and  $10^{-6}$ -curve is very small. This is also the case for the other measurement subsets. In addition the CDFs of  $r_{b,max}$  values show only a small difference for all measurement subsets under LOS as well as OBS conditions. From this, it can be concluded that parameter  $r_{b,max}$  as well as  $R_{b,max}$  are highly insensitive to the threshold  $P_{b,th}$ .

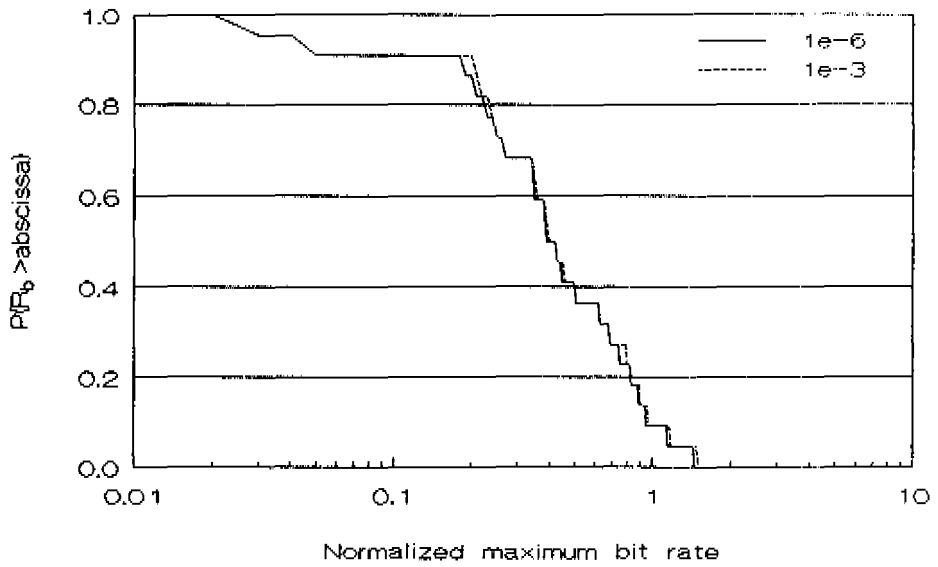


Fig. 6.5: Distribution functions of normalized maximum bit rate for different probability of bit error thresholds under LOS conditions.

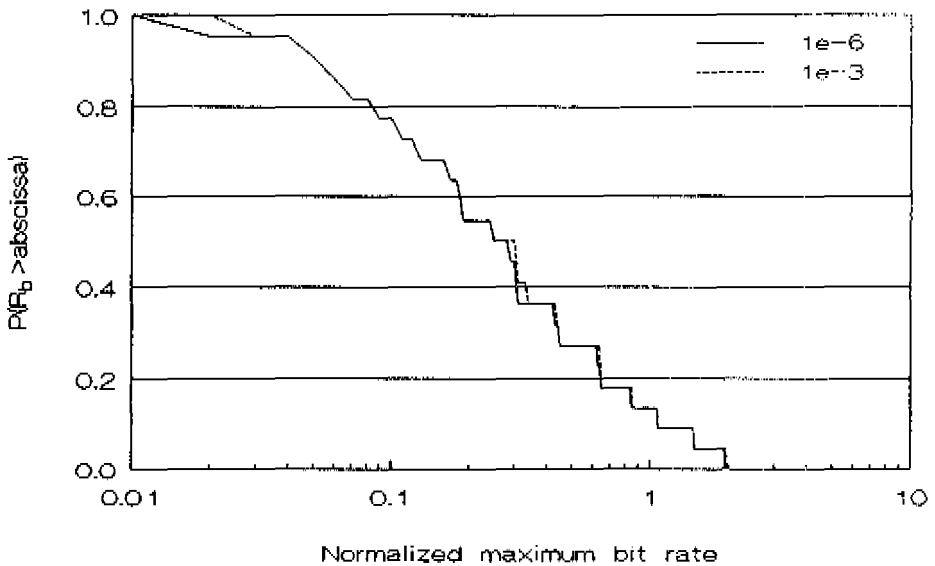


Fig. 6.6: Distribution functions of normalized maximum bit rate for different probability of bit error thresholds under OBS conditions.



### 6.3.5 Influence of SNR

In Table 6.1 the probability of bit error for various SNR values, i.e. for various values of  $E_b/N_0$ , is given for different bit rates. The response considered is one of those obtained in Room A with the standard configuration. With  $\eta$  is meant the calculation accuracy. The high probability of bit error values at high SNR demonstrate the bottoming effect due to ISI.

Table 6.1: Probability of bit error values for various SNR figures and bit rates.

$r_b$ (Mbit/s)	SNR (dB)				
	10	20	30	40	no noise
4	$2.10 \times 10^{-4}$	$2.86 \times 10^{-20}$	$< \eta$	$< \eta$	$< \eta$
6	$2.26 \times 10^{-3}$	$1.03 \times 10^{-10}$	$< \eta$	$< \eta$	$< \eta$
8	$1.84 \times 10^{-2}$	$3.48 \times 10^{-4}$	$5.67 \times 10^{-11}$	$< \eta$	$< \eta$
10	$1.43 \times 10^{-1}$	$7.09 \times 10^{-2}$	$6.25 \times 10^{-2}$	$6.25 \times 10^{-2}$	$6.25 \times 10^{-2}$
12	$2.50 \times 10^{-1}$	$2.50 \times 10^{-1}$	$2.50 \times 10^{-1}$	$2.50 \times 10^{-1}$	$2.50 \times 10^{-1}$

Considering the entire subset of impulse responses obtained in Room A with the standard configuration yields Fig. 6.7 in which the  $r_{b,max}$  values are given as function of the LOS distance for 1) the absence of noise and for 2) an  $E_b/N_0$  of 20 dB, whereas  $P_{b,th} = 10^{-6}$ . Figure 6.8 is the translation of Fig 6.7 to a CDF of  $R_{b,max}$  values obtained.

From these figures it can be concluded that in case  $E_b/N_0 > 20$  dB an increase in  $E_b/N_0$  can result in an improvement of  $r_{b,max}$  of about 30% at maximum. In that  $E_b/N_0$  range, ISI is the primary factor that determines  $r_{b,max}$  and  $R_{b,max}$ . Values of these parameters may vary considerably with the environment.

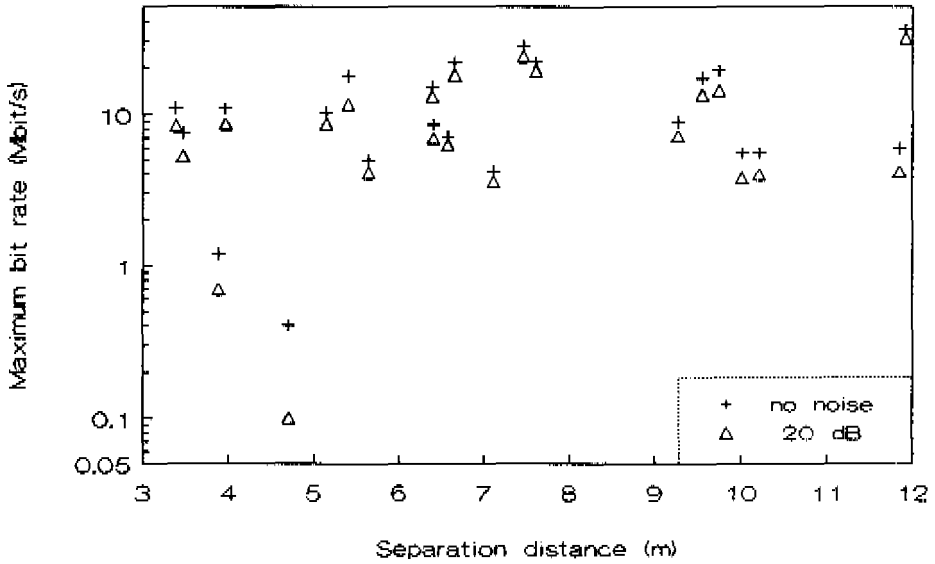


Fig. 6.7: Maximum bit rate for no-noise case and for the case that  $E_b/N_0$  equals 20 dB, Room A,  $P_{b,\text{th}}=10^{-6}$ .

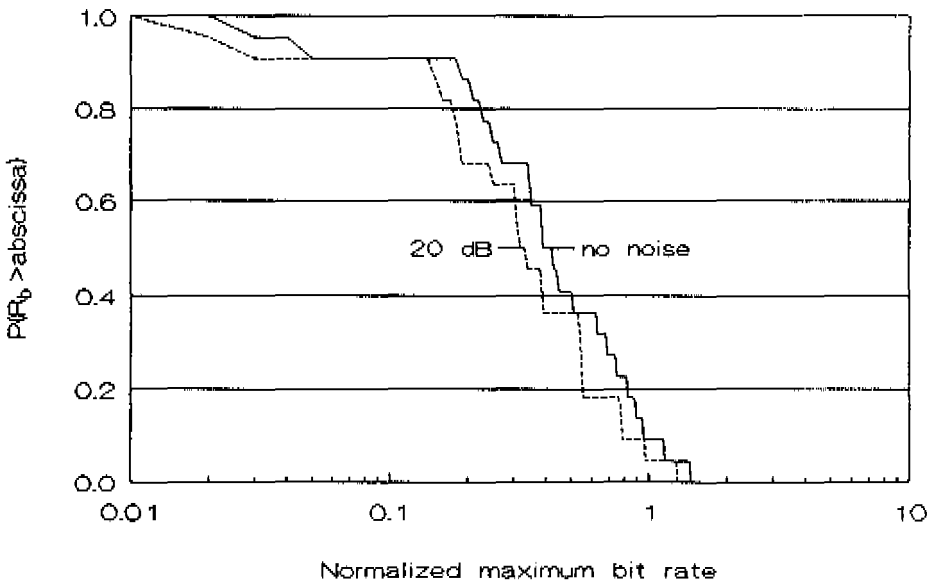


Fig. 6.8: Distribution functions of normalized maximum bit rate for the no-noise case and for the case that  $E_b/N_0$  equals 20 dB, Room A,  $P_{b,\text{th}}=10^{-6}$ .

### 6.3.6 Influence of measurement configuration

Additional simulations have been performed to examine the influence of the measurement configuration and to provide an overall impression of the feasible value of  $R_{b,max}$ . The results with respect to all measurement subsets obtained are listed in Table 6.2 in terms of the average and standard deviation of the  $R_{b,max}$  values obtained for both the LOS and OBS case.  $P_{b,th}$  was set again to  $10^{-6}$ . The first eight rows refer to the standard measurement configuration. The ninth row refers to Configuration A (see Section 3.6.3). The tenth and bottom row refer to Configuration B (see Section 3.6.3). It can be concluded from Table 6.2, that LOS values do not differ significantly from the corresponding OBS values. For all measurement subsets obtained taken together we get the outage probability  $P(R_{b,max} < 0.1) = 0.13$  whereas  $P(R_{b,max} < 0.05) = 0.05$ . Because  $R_{b,max} = \sigma_{rms} \cdot r_{b,max}$  the latter implies that for channels exhibiting an rms delay spread in excess of 50 ns less than 1 Mbit/s is feasible for an outage probability of 5%.

Table 6.2: Average and standard deviation of normalized maximum bit rate for LOS and OBS.

Env.	Config.	$R_{b,max}$ for LOS		$R_{b,max}$ for OBS	
		average	std. dev.	average	std. dev.
A	standard	0.51	0.36	0.40	0.44
B	standard	0.52	0.32	0.66	0.70
C	standard	0.56	0.34	0.48	0.30
D	standard	0.56	0.36	0.48	0.18
E	standard	0.48	0.36	0.48	0.32
F	standard	0.56	0.36	0.58	0.34
G	standard	0.54	0.38	0.50	0.42
H	standard	0.52	0.44	0.52	0.38
A	A	0.42	0.37	0.58	0.37
A	B	0.52	0.50	0.46	0.35
F	B	0.48	0.40	0.49	0.35

### 6.3.7 Influence of external diversity

The improvement effect of antenna diversity is examined by considering the average of three  $R_{b,max}$  values based on three impulse responses with equal amplitude profiles but mutually uncorrelated phase profiles. In that case the average of all  $R_{b,max}$  values increases from 0.51 to 0.58. Assuming an average rms delay spread of 60 ns this indicates that an average bit rate is feasible of about 10 Mbit/s. The average of standard deviation values decreases from 0.38 to 0.22, whereas an outage probability is achieved as good as  $P(R_{b,max} < 0.2) = 0.02$ . This indicates a feasible bit rate of about 3.3 Mbit/s for an outage probability of 2%.

### 6.4 Performance of QPSK/DFE

In Section 2.6 it was indicated that the ISI due to multipath can be combatted effectively by applying some form of channel equalization. In general, for the use of an equalizer to remove ISI from noisy linear channels three different approaches are possible: 1) the linear equalizer (LE) [9], 2) the decision feedback equalizer (DFE) [10], and 3) the maximum likelihood sequence estimator (MLSE) [11]. In practice the choice of techniques hinges on the compromise between complexity and desired performance.

The LE consists of a transversal tapped delay line filter. Detection takes place on its output data. It is tailored for simplicity and cost effectiveness, sacrificing performance. The DFE has the same structure as the LE except that the reconstructed data sequence is filtered and reinserted into the signal path. This feedback of the data serves to cancel ISI due to past digits for which decisions have already been made. Since in the absence of decision errors this can be done exactly without noise enhancement, it follows that the DFE should have superior performance. Moreover, it has been established by Salz [12] that when the channel exhibits a deep selective fade approaching a null, the DFE greatly outperforms the LE. The MLSE determines the most likely transmitted data sequence. It gives optimum performance at the expense of increased computation and storage requirements. The complexity of the MLSE using the Viterbi algorithm is exponential in the length of the channel impulse response. There is also (possibly long) delay in the decision process. Due at least in part to implementation considerations, little improvement has been observed over the much simpler adaptive DFE on dispersive channels [13].

In what follows, we will focus on DFE because of its highly competitive properties when compared with the LE and MLSE concepts. Fig. 6.9 shows the DFE structure.

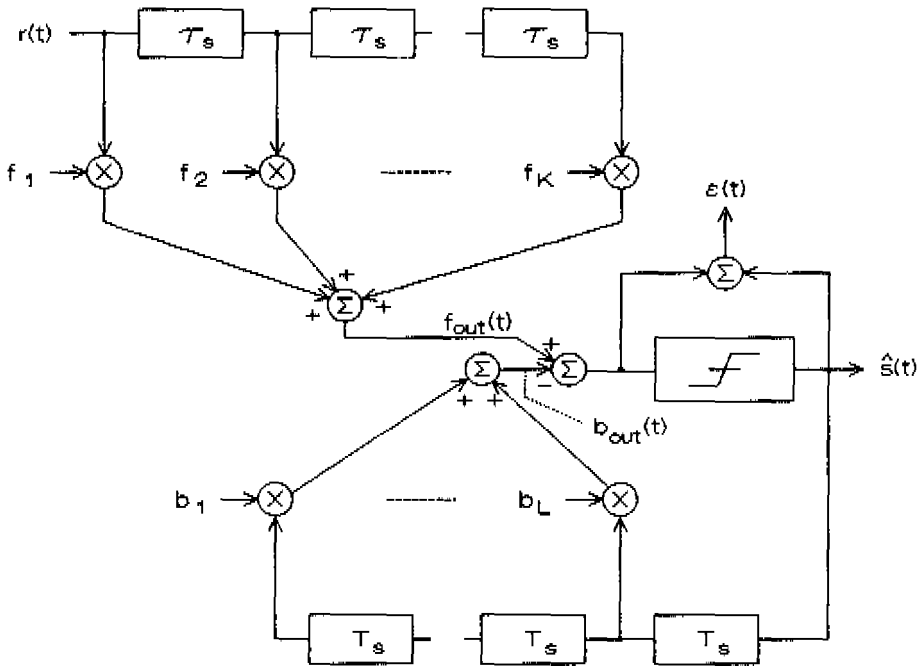


Fig. 6.9: Structure of Decision Feedback Equalizer.

The forward filter consists of a tapped delay line filter with tap spacing equal to  $\tau_s$ . The forward tap gains are denoted as  $f_1, \dots, f_K$ , where  $K$  is the total number of forward taps. The feedback filter consists of a tapped delay line filter with tap spacing equal to the symbol length. The feedback taps are denoted as  $b_1, \dots, b_L$ , where  $L$  is the total number of feedback taps.

The *forward filter* acts like a normal LE operating on the received signal,  $r(t)$ . It is used to reduce the effects of *future digit ISI*, i.e., the *precursors*. The impulse response of the forward filter is

$$f(t) = \sum_{i=1}^K f_i^* \delta(t - i\tau_s) \quad , \quad (6.15)$$

The  $*$  denotes the complex conjugate and  $\delta(\cdot)$  the Dirac delta function. With the received signal at sample time  $t_0$  given in (6.5) the output of the forward filter becomes

$$f_{out}(t_0) = \sum_{i=1}^K f_i^* \left[ \sum_{k=-\infty}^{\infty} s_k h_f(t_0 - i\tau_s - kT_s) + n(t_0 - i\tau_s) \right] \quad (6.16)$$

with  $h_f(\cdot)$  the overall transfer function as expressed by (6.4) including the transfer functions of the transmit and receive filter. The output is sampled at the symbol rate and held for the symbol duration.

The *feedback filter* linearly operates on the reconstructed data  $\{\hat{s}_k\}$  and is used to eliminate *past digit ISI*, i.e., the *postcursors*. As a consequence of this, errors in the decision process will tend to produce more errors which might result in error propagation. This phenomenon, however, has been shown to have only a small effect on a particular channel realization when the ISI and noise is not excessive [14]. Therefore, we make the assumption that the detected symbols are known and that past decisions are correct. Then, the ISI contribution in these symbols can be cancelled exactly by subtracting past symbol values with appropriate weighing from the equalizer output. The impulse response of the feedback filter containing  $L$  taps can be described as

$$b(t) = \sum_{i=1}^L b_i \delta(t - iT) \quad (6.17)$$

The output of the feedback filter becomes at the decision time for the symbol  $s_k$

$$b_{out}(kT_s) = \sum_{i=1}^L b_i \hat{s}(kT_s - iT_s) \quad (6.18)$$

For QPSK modulation the decision process takes the form

$$\hat{s} = \text{sgn}[\text{Re}(f_{out} - b_{out})] + j \text{sgn}[\text{Im}(f_{out} - b_{out})] \quad (6.19)$$

where  $\text{sgn}[\cdot]$  is the signum function.

A conventional DFE minimizes the mean-square-error (MSE). By introducing  $\epsilon(kT_s)$ , defined as the difference between the analog input of the decision device and the output of the decision device at time  $kT_s$ , and using the expressions in (6.16) and (6.18) the MSE minimization problem can be stated as

$$\min_{f_i, b_i} E[\epsilon^2(kT_s)] \quad (6.20)$$

with

$$\epsilon(kT_s) = \left[ \sum_{l=1}^K f_l^* \left[ \sum_{k=-\infty}^{\infty} s_k h_l(t_0 - i\tau_s - kT_s) + n(t_0 - i\tau_s) \right] - \sum_{l=1}^L b_l \hat{s}(kT_s - iT_s) \right] - \hat{s}(kT_s) \quad , \quad (6.21)$$

where the expression between the square brackets is the input of the decision device.

For minimizing this MSE, the feedforward and feedback taps are updated, simultaneously, according to some algorithm that guarantees convergence. Section 6.6 deals with update algorithms and associated dynamic (i.e., convergence) characteristics of DFEs.

The performance of DFE/QPSK operating on mm-wave indoor radio channels can be estimated on the basis of the theoretical framework given by Mosen [16]. Mosen addresses the processing of joint optimal diversity combining and adaptive DFE for combatting fading on HF channels which poses a similar set of problems as the mm-wave indoor radio channel since both types are characterized by severe multipath and slow fading. The basic performance measure is the average probability of error  $\bar{P}_b$ , already introduced in Section 2.5. The theoretical approach for the calculation of the average probability of bit error developed in [16] includes the influence of the finiteness of the transversal filter used to realize the forward filter of the DFE. The radio link considered consists of an ensemble of  $D$  external diversity paths as shown in Fig. 6.10. The individual channels are considered to be independent of each other. As a consequence of this independence we may write

$$E\{h_i(t)h_j^*(t+\Delta t)\} = \delta_{ij}\delta(\Delta t)E_b p(t), \quad i, j = 1, 2, \dots, D \quad , \quad (6.22)$$

where  $\delta_{ij}$  and  $\delta(\cdot)$  are the Kronecker delta and continuous delta function, respectively.  $E_b$  is the average received energy per bit per diversity channel. The power delay profile  $p(t)$  here represents a unit area function (i.e.,  $\int_{-\infty}^{\infty} p(t)dt=1$ ).

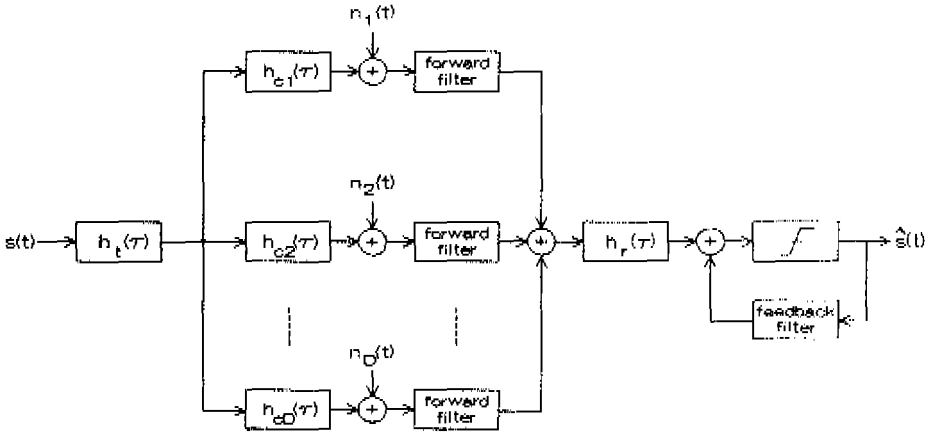


Fig. 6.10: Equivalent lowpass model of a DFE/QPSK indoor radio link with  $D$  diversity branches.

The analytic procedure developed by Mosen provides an estimate of the ISI effect on the average probability of bit error. For this, perfect (noiseless) determination of tap weights is assumed. Furthermore, it is assumed that the interference symbols  $s_i$ ,  $i \neq 0$ , are Gaussian distributed and that the ISI after equalization can be well approximated by an equivalent additive Gaussian noise term. Based on these assumptions, the average probability of error of a QPSK/DFE link is given by [16] as

$$P_b = \frac{1}{2} \prod_{k=1}^K \left(1 + \frac{E_s}{N_s} \lambda_k\right)^{-D} \quad (6.23)$$

where the  $\lambda_k$  are the eigenvalues of the matrix  $\underline{\underline{G}}^{-1} \underline{\underline{C}}(t_0)$ . The elements of the matrix  $\underline{\underline{C}}(t_0)$  are given by

$$C_H(t_0) = \int_{-\infty}^{\infty} cr(t_0 - k\tau_s - u) cr(t_0 - l\tau_s - u) p(u) du \quad (6.24)$$

where  $\tau_s$  is the equalizer tap spacing of the forward filter, while  $cr(\cdot)$  is the impulse response of the transmit and receive filters (raised cosine with  $\beta=0.5$ ). The elements of matrix  $\underline{\underline{G}}$  are given by



$$G_{kl} = cr(k\tau_s - l\tau_s) + \frac{E_b}{2N_0} \sum_{i=1}^l C_{kl}(t_0 - iT_s) \quad , \quad (6.25)$$

where  $l$  is the number of significant future ISI pulses and  $t_0$  the sampling instant. The calculation of the inverse matrix of  $\underline{G}$  can be performed by application of single-value decomposition as described by Press et. al. [12]<sup>1</sup>. Note, that the feedback coefficients play no part in the analyses. This is because the output of the feedback section of the DFE is a weighted sum of noise-free past decisions.

## 6.5 Calculation results and discussion with respect to QPSK/DFE

### 6.5.1 Parameters under consideration

Based on (6.23) to (6.25), the average probability of error is calculated as function of the normalized bit rate  $R_b = \sigma_{rms} \cdot r_{b,max}$ . From the results obtained the normalized maximum bit rate  $R_{b,max} = \sigma_{rms} \cdot r_{b,max}$  is derived for an average probability of bit error. Fig. 6.11 shows CDFs of  $R_{b,max}$  values obtained in Room A with the standard configuration for  $P_b = 10^{-3}$ . There is no external diversity applied (i.e.,  $D=1$ ).  $E_b/N_0$  is 40 dB. The DFE uses 3 forward taps. The steep slopes of the curves in Fig. 6.11 indicate a fairly uniform performance throughout the room. This equality in performance is observed for all measurement subsets and thus for all the environments considered. A consequence of this uniformity in performance is that the performance can be characterized well by just one average of all approximately 20 obtained  $R_{b,max}$  values per measurement subset.

---

<sup>1</sup> We first tried to find the LU-decomposition and to calculate the inverse matrix by back-substituting. The implementation of this method, however, did not lead to satisfactory results; Calculating the unit matrix  $I = \underline{G}\underline{G}^{-1}$  resulted in non-diagonal elements of factors 100. Therefore a more powerful method had to be used to calculate the inverse matrix of matrices that are numerically very close to singular.

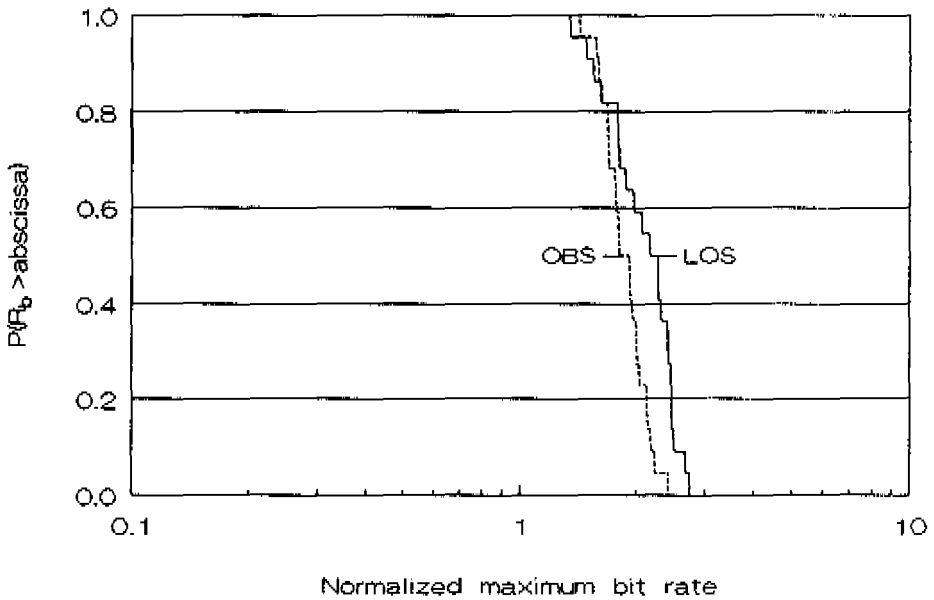


Fig. 6.11: Distribution functions of normalized maximum bit rate values, Room A.

### 6.5.2 Influence of timing algorithm

The first step in determining the QPSK/DFE performance was to examine the influence of the algorithm applied to determine the timing instant  $t_0$  on  $R_{b,max}$  for both the LOS and OBS case. As for QPSK, the power algorithm showed superior performance when compared with the amplitude algorithm. Therefore, the power algorithm is used in further simulations.

### 6.5.3 Influence of SNR

Fig. 6.12 shows the average probability of error versus  $R_b$  for a radio link in Room A for LOS as well as for OBS and for  $E_b/N_0$  values of 30, 40 and 50 dB. Again, we consider a 3 (forward) taps DFE without external diversity.

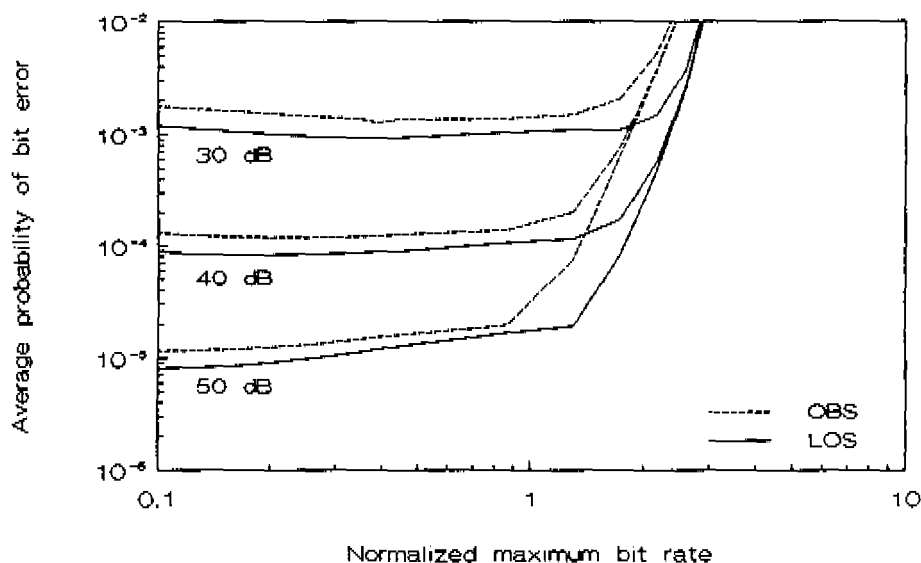


Fig. 6.12: Average probability of bit error versus normalized maximum bit rate for various SNR values, Room A.

At low  $R_b$  values the  $E_b/N_0$  ratio is mainly determining the average probability of error, because the thermal noise dominates the ISI. With increasing  $R_b$ , the probability of error first decreases, because the DFE uses the internal diversity resulting from the increased multipath. At higher bit rates, where the span of the equalizer becomes too small to handle the channel dispersion encountered, the average probability of error increases sharply to an unacceptable level.

Fig. 6.12 shows that obstruction of the direct LOS path has only a minor effect on the performance. This desirable feature is encountered in all the environments under consideration in case biconical-horn antennas are applied.

#### 6.5.4 Influence of number of forward taps

The influence of the number of forward taps is shown in Fig. 6.13, for 3, 5 and 7 taps without external diversity for a LOS link in Room A.  $E_b/N_0$  is 40 dB.

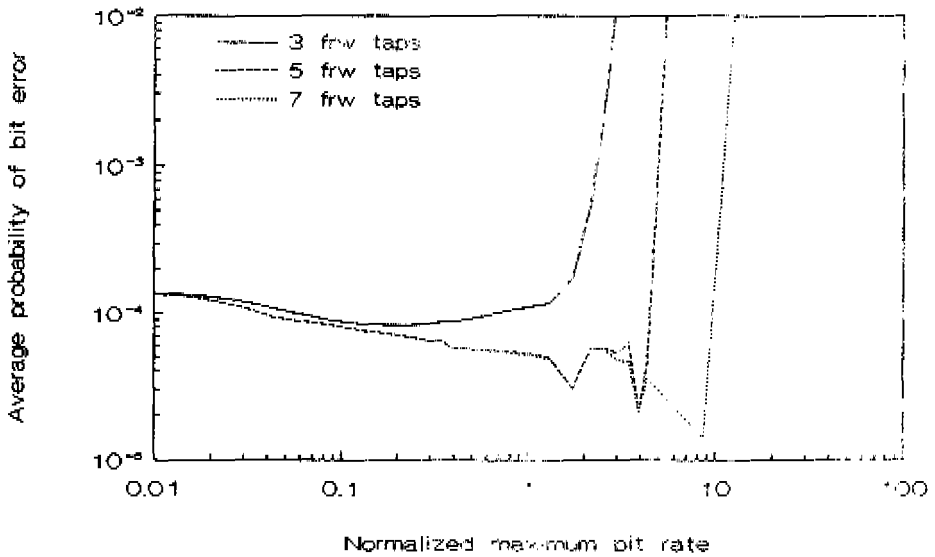


Fig. 6.13: Average probability of bit error versus normalized maximum bit rate for various numbers of forward taps, Room A.

In Table 6.3, the averages of  $R_{b,max}$  values for  $\bar{P}_b = 10^{-3}$  are listed for 3, 5 and 7 forward taps for each measurement subset. Increasing this number increases the span of the equalizer and thus increases the  $R_{b,max}$  value. In this table, the environments are subdivided in three classes: a) Large rooms, i.e., Room B,C and D. b) Long narrow structure (a corridor), i.e., Environment E. c) Small rectangular rooms, i.e., Room A,F,G and H. The large rooms exhibit the largest  $R_{b,max}$  values under LOS circumstances. This indicates that, under LOS conditions, there is a levelling effect on equalizer performance in the sense that an equalizer does not perform "proportionally worse" in a larger, more dispersive, environment.

Increasing the amount of forward taps from 3 to 5 results in an average increase in  $R_{b,max}$  of about a factor 3. The implementation of two more forward taps is less effective in the sense that "only" an average improvement factor of 1.7 is achieved. These results fairly comply with results found by Sexton and Pahlavan [17] with respect to the performance of DFE operating on similar though theoretical channels.

Table 6.3: Maximum normalized bit rate for various number of forward taps for LOS and OBS.

Class	Env.	LOS			OBS		
		3	5	7	3	5	7
Large	B	3.2	8.2	15.8	1.7	5.1	9.1
	C	3.5	9.7	18.0	1.8	5.0	11.6
	D	3.2	8.6	13.6	2.1	6.0	10.3
Long	E	2.7	9.7	12.0	2.3	6.7	11.4
	F	2.0	6.5	10.6	1.9	6.4	10.8
Small	G	2.2	6.4	10.5	1.5	4.7	7.1
	H	1.9	4.7	8.7	1.7	4.5	7.8
	A	2.3	6.3	11.4	1.8	6.1	10.0

Table 6.4 lists  $r_{b,max}$  values that correspond with the values of  $R_{b,max}$  given in Table 6.3. The values in Table 6.4 indicate that there is no clear relationship between environment dimensions and  $r_{b,max}$  values.

Table 6.4: Maximum bit rate for various number of forward taps for LOS and OBS.

Class	Env.	LOS $r_b$ (Mbit/s)			OBS $r_b$ (Mbit/s)		
		3	5	7	3	5	7
Large	B	95	244	471	53	160	285
	C	54	148	275	28	78	180
	D	54	145	230	36	101	174
Long	E	40	144	178	33	97	164
	F	47	153	250	45	151	255
Small	G	104	303	498	84	264	399
	H	65	160	297	61	163	281
	A	53	145	262	44	150	246

### 6.5.5 Influence of number of backward taps

As already stated, the feedback coefficients play no part in determining the equalizer performance since the output of the feedback section is assumed to be a weighed sum of noise-free and error free past decisions. The required number of backward filter taps  $L$  is mainly determined by the impulse response width and symbol time  $T_s$ . An assessment according to [14] yields  $B \approx 2\sigma_{ms}/T_s$ , which results in  $B \approx 3$  for some tens of Mbit/s. A backward filter span exceeding the impulse response width might work counter productive since the problem of error propagation raises with the amount of backward taps.

### 6.5.6 Influence of measurement configuration

Table 6.5 lists  $R_{b,max}$  values obtained in Room A with Configuration A as well as  $R_{b,max}$  values obtained with Configuration B and  $R_{b,max}$  values obtained with the standard configuration for 3, 5 and 7 forward taps. Again,  $E_b/N_0$  is 40 dB and  $P_b = 10^{-4}$ .

*Table 6.5: Comparison of maximum normalized bit rate for different measurement configurations.*

Configuration	LOS			OBS		
	3	5	7	3	5	7
A	7.3	19.4	31.3	1.7	5.8	8.8
B	4.6	14.0	23.1	2.3	7.1	12.8
standard	2.3	6.3	11.4	1.8	6.1	10.0

Configuration A yields the highest values of  $R_{b,max}$  for LOS situations. However, when the line-of-sight path becomes blocked, the performance drops significantly. This drop is much smaller for the standard configuration because the omnidirectional biconical antennas provide more path diversity.

### 6.5.7 Influence of external diversity

Fig. 6.14 shows  $P_b$  for a DFE with 3 forward taps in combination with dual antenna diversity ( $D=2$ ) for an  $E_b/N_0$  ratio of 40 dB.

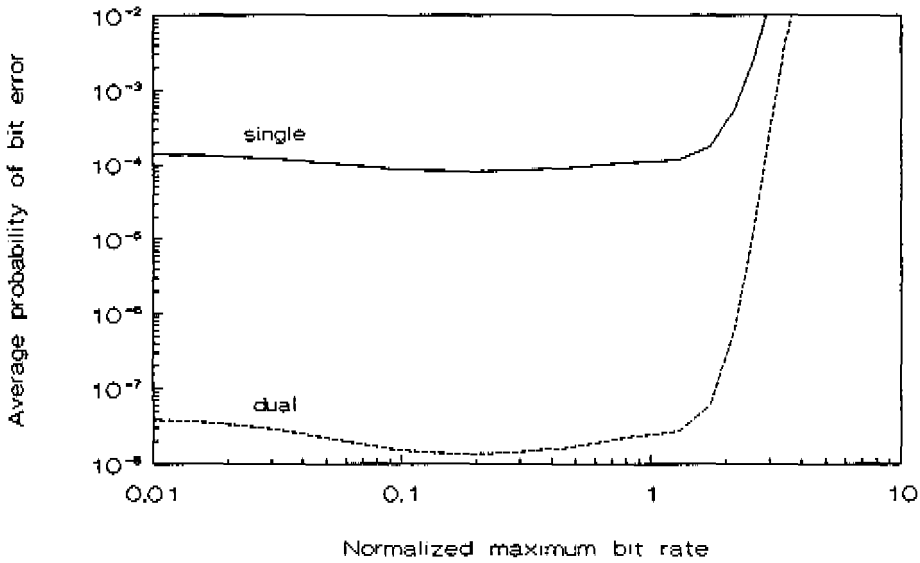


Fig. 6.14: Average probability of bit error versus normalized maximum bit rate for no and dual external (antenna) diversity, Room A.

In comparison to the no-diversity case ( $D=1$ ),  $P_b$  decreases with a factor  $3 \cdot 10^4$  for small  $R_b$  values. A similar improvement is also reported by Pahlavan and Howard [18] for measurement data obtained in indoor areas at 910 MHz. With  $D=2$  instead of  $D=1$  only a slight increase of the  $R_{b,max}$  value can be observed. This indicates, that diversity mainly helps to overcome stringent  $P_b$  requirements.

## 6.6 Implementation aspects

### 6.6.1 Adaption of equalizer coefficients

In the previous sections (6.4 and 6.5), we implicitly considered DFE performance after adaption of the equalizer coefficients to the channel impulse response. In addition to this steady-state performance, a crucial item regarding channel equalization is the adaption itself to changes in the channel impulse response. Especially in the case of transmission of *short* message blocks there is an additional requirement of a fast start-up of the equalizer in order to achieve acceptable throughput efficiency. Typically, an adaptive equalizer adjusts its tap coefficients during an

initial *training period* in which a data sequence, known at the receiver, is received<sup>1</sup>. A *short* training sequence is required in broadband wireless LANs, where the tributary terminals transmit short message blocks in a time sharing fashion to a centrally located base station. Subsequent received message blocks can originate from terminals located at totally different positions. Therefore, the equalizer should feature considerable agility to adapt to the subsequent characteristics of the channels the equalizer has to operate on.

The adaption time (i.e., the training period) adds to the overhead of the transmission capacity. In order to allow determination of the available transmission capacity for the actual information (net bit rates, see Chapter 7) it is necessary to estimate the adaption time in terms of number of iterations (symbol times). This figure, however, depends highly on the implementation of equalizer convergence, i.e., on the specific adaption algorithm applied. In what follows, we therefore investigate the suitability of the various iterative adaption algorithms that are conceivable for our application.

The final choice should be based on three major items, viz.,

- 1) fast initial convergence during the *training phase*.
- 2) accurate (fast and stable) tracking of the time-varying channel characteristics during the *information* or *tracking phase*.
- 3) sufficiently low computational complexity. By computational complexity we mean the number of operations to be performed in one iteration. This is especially relevant for the high bit rate applications we consider. With the devices currently available, additions and multiplications need about the same computation time, whereas divisions cannot be performed with only one instruction, but need a dedicated macro-instruction. This indicates that the number of divisions should be small [20].

Other items related with adaption time overhead are the establishment of carrier and clock recovery, the application of fractional tap spaced equalization and the application of off-line processing. These topics are dealt with in Section 6.6.7 to 6.6.10.

With respect to algorithms for iterative adaption of equalizer tap coefficients two main classes can be distinguished, i.e., the classical *Least Mean Square* (LMS) [21]

---

<sup>1</sup> Adaptive channel equalization can also be performed without resorting to a known training sequence, see for instance [19]. However, with that approach, the equalizer convergence is relatively slow (in the order of  $10^6$  iterations) since data symbols are not known at the receiver.



algorithms (also denoted as *Stochastic Gradient* (SG) algorithms) and the *Recursive Least Squares* (RLS) [22] algorithms. The first class includes the *Gradient Steepest-Descent* (GSD) [23] and the *Gradient Adaptive Lattice* (GAL) [24] algorithms. The second class comprises the *Kalman* [25], *Fast-Kalman* (FK) [26], *Square-Root Kalman* (SRK) [27] and the *Least Squares Lattice* (LSL) [28] algorithms. These RLS algorithms seek the minimum of the least squares (LS) to estimate the minimum MSE set of tap coefficients, which yields much faster equalizer convergence than can be achieved by applying the classical LMS algorithms which seek the minimum of the MSE itself. The latter will be clarified in the next section.

### 6.6.2 Achievement of fast convergence

The LS minimization problem for a DFE at time  $kT_s$  can be stated as

$$\min_{f_i, b_i} \sum_{n=0}^k |\epsilon(nT_s)|^2, \quad (6.26)$$

where  $\epsilon(\cdot)$  denotes the difference between the input and output of the decision device as expressed in (6.21). Minimizing according to (6.26) thus yields the coefficients  $f_i$  and  $b_i$ . For minimizing the LS, the forward and feedback taps can be updated simultaneously according to

$$f_i[(k+1)T_s] = f_i[kT_s] - \kappa_{i,f}[kT_s] \cdot \epsilon[kT_s] \quad \text{with } i=1,2,\dots,K, \quad (6.27)$$

$$b_i[(k+1)T_s] = b_i[kT_s] + \kappa_{i,b}[kT_s] \cdot \epsilon[kT_s] \quad \text{with } i=1,2,\dots,L, \quad (6.28)$$

where  $\kappa_{i,f}(kT_s)$  and  $\kappa_{i,b}(kT_s)$  are the elements of the  $N=K+L$  dimensional complex Kalman gain vector  $\underline{\kappa}_N(kT_s)$ . Notice, that control is applied to each tap coefficient through the corresponding element of  $\underline{\kappa}_N(kT_s)$  which greatly accelerates the equalizer's adaption, independent of the channel's dispersion characteristics [25,29,30]. In contrast, the gradient algorithm minimizing the basic MSE, expressed by

$$f_i[(k+1)T_s] = f_i[kT_s] - \alpha r^* [kT_s - iT_s] \cdot \epsilon[kT_s] \quad \text{with } i=1,2,\dots,K, \quad (6.29)$$

$$b_i[(k+1)T_s] = b_i[kT_s] + \alpha s^* [kT_s - iT_s] \cdot \epsilon[kT_s] \quad \text{with } i=1,2,\dots,L, \quad (6.30)$$

has only one variable parameter, i.e., the step size  $\alpha$ . Therefore, RLS adaption yields much faster equalizer convergence than that achieved by the simple gradient algorithm. The convergence rate of RLS adaption turns out to be independent of the channel characteristics as long as the length of the channel's impulse response essentially remains below the equalizer span. On the other hand, the convergence rate depends strongly upon the total number of equalizer taps  $N$ . It is found by

Eleftheriou and Falconer [31] and Cowan [32], that the convergence of RLS algorithms defined as the number of iterations needed to decrease the estimated MSE 20 dB below the initial value is within  $2N$  iterations.

### 6.6.3 Achievement of low complexity

It turns out that the least complex algorithm is the GSD. However, its speed of convergence is 400 to 500 symbols, which is much too low for our applications since the message blocks to be transmitted consist only of a few hundred symbols so that the initial training period would lead to an unacceptable overhead of 200 to 300 percent. In addition, the convergence shows a substantial dependence on the channel characteristics.

Apart from the GSD algorithm, the best method with respect to the number of additions and multiplications required is the SRK, but this algorithm requires  $N$  divisions. For large values of  $N$ , i.e.  $N \geq 7$ , the Kalman algorithm is the most complex, but it becomes competitive for  $N < 5$  [20]. The complexity of the Kalman algorithm comes from the fact that an  $N$  by  $N$  matrix must be adapted and stored once per iteration. Thus, on the order of  $N^2$  operations must be performed per iteration. This is in direct contrast with the GSD algorithm, in which on the order of  $N$  operations per iteration are required.

To overcome this limitation of the Kalman algorithm, several computational efficient modifications have been proposed in the literature. These fast algorithms exploit a certain shift-invariance property of successive equalizer contents [26] with the result that they require on the order of  $N$  operations per iteration, thereby maintaining the convergence properties of the Kalman algorithm. A major improvement of the Kalman algorithm is the FK algorithm which reduces the amount of operations per iteration to a number proportional to  $N$ . A full derivation of the FK is given in [33]. In addition, an abbreviated derivation is given in [26], which emphasizes the use made of the shifting property of the input vectors and of certain optimal predictor equations and associated relationships. A treatment of the complex version of the FK algorithm to be applied for the complex DFEs consisting of two branches (because of the quadrature-type modulation) can be found in [35].

Among the fast algorithms, the FK algorithm turns out to be the least complex for  $N \geq 10$  whereas for  $3 < N < 10$  the SRK algorithm is the least complex and for  $N \leq 3$  the Kalman algorithm is the least complex [20].

### 6.6.4 Achievement of accurate tracking

In the RLS algorithms, all previous equalizer input sequence vectors  $\mathbf{z}_n(kT_s)$  and errors  $\epsilon(kT_s)$  are assigned equal weight in determining the current tap coefficient estimates. This works well for a limited-duration initial start-up phase. However, steady-state operation usually requires that vectors  $\mathbf{z}_n(kT_s)$  in the distant past be "forgotten", in order to afford the possibility of tracking channel time variations and to avoid problems associated with digital round-off errors. The inclusion of an exponential weighing factor in the sum-of-squares criterion (6.26) to meet this steady state requirement is proposed in [26,28]. The minimization of an exponentially weighed square error at time  $kT_s$  can be written as

$$\min_{f_i, b_i} \sum_{n=0}^k \lambda^{(k-n)T_s} |\epsilon(nT_s)|^2, \quad (6.31)$$

in which  $\lambda$  is some positive number close to, but less than, 1. The inverse of  $1-\lambda$  is, roughly speaking, the memory of the algorithm [26].

Lim and Mueller [34] reported, however, an unstable behaviour of the FK algorithm when they included exponential weighing in their simulations of RLS algorithms using single precision floating point arithmetic although one would expect the opposite. Double precision arithmetic (i.e., 56-bits for the mantissa) was found to eliminate the instability. The Kalman and LSL algorithms did not show this instability. In addition, the SRK algorithm is known to have excellent numerical properties and has been shown to be very robust to round off noise in the computations [27].

With respect to mm-wave indoor radio communications the tracking problem is less relevant in comparison with the start-up and complexity problem since we expect only slow fading in a typical indoor environment at mm-wave frequencies as indicated in Section 2.3; the channel is expected to remain essentially constant over the equalizer span. Therefore, the information about the "past" contained in the equalizer tap coefficients is (almost) as important as the information about the present and future. Hence; for our application  $\lambda$  should be chosen very close to 1 or the exponential weighing should be simply omitted in order to optimally exploit all available information, which will act in favour of the initial convergence properties.

### 6.6.5 Adaptive lattice filtering

In the former, we assumed a tapped delay line equalizer structure. Another promising structure which has attracted considerable attention in the last few years, is based on

lattice filters. A lattice filter is obtained by cascading a number of stages. Within each stage coefficients are adapted without the need for global feedback, making extensive pipelining of computations possible. Therefore, multiple programmable processing elements can be used which can work in parallel to speed up the execution of a given algorithm. This multi processor [36] approach has two fundamental advantages. First, no increase in hardware is needed when the order of the filter is increased. Second, the same system can easily implement a variety of coefficient update algorithms without the need for redesign or modification of existing hardware [37].

Satorius and Pack [28] compared the convergence properties of lattice equalizers based on minimization of the MSE (GAL algorithm) and on minimization of the LS (LSL algorithm). By simulation, the LSL algorithm is shown to converge in 40 to 50 iterations in a situation where the GAL algorithm needs about 120 iterations. As for transversal equalizers, the convergence rate is about  $2N$ . The price paid for this improvement is increased complexity beyond that of the FK and SRK algorithm.

Based on computer simulations [38,39] and analyses [40], it can be said that among the fast RLS algorithms, the LSL algorithm exhibits the smallest tendency toward numerical instability for  $\lambda < 1$ .

#### 6.6.6 Achievement of accurate carrier recovery

Hitherto, we have implicitly assumed that carrier phase for demodulation has been properly estimated. However, in practice there might be a significant phase shift between the carrier signal and local reference signal which exhibits jitter. This phase jitter acts as a real random sequence  $\phi_n$ , affecting the phase angle of the channel output samples. When its time constant is much larger than the equalizer settling time, it can be assumed to cause a constant phase shift. In that case, it can be adaptively compensated by the equalizer. Similar conditions hold for a frequency offset (i.e., the perturbation of the carrier frequency  $f_0$  by a small amount  $\Delta f$ ). Since the equalizer can track small amounts of phase jitter and frequency offset, we can shift the discussion towards the problem of having available a sufficiently accurate reference signal for coherent demodulation. For rapid acquisition, as required for receiving shorts data packets at high data rates, we can apply open loop recovery of a pilot which is received along with the actual information signal.

### 6.6.7 Achievement of accurate clock recovery

For most equalizers proper recovery of the symbol clock is necessary before proper adaption can take place. A method of recovering a symbol rate clock with appropriate timing phase is to modulate the pilot with a basic clock having a low clock rate when compared with the actual symbol rate, so that no significant ISI is encountered. Open-loop clock recovery can easily be applied when *binary* PSK is used for this.

Another method is to extract the clock information from the received message signal itself. In that case, the clock recovery system has to cope with the ISI of the signal on which it operates<sup>2</sup>. A well known system is early-late (EL) clock recovery (see, e.g., [41]). Clock recovery with only slightly degraded performance due to ISI is claimed by [42] by applying some modified form of EL although problems arose when deep signal fades were encountered.

### 6.6.8 Fractional tap spaced equalization

A general problem with respect to clock synchronization is formed by the fact that the performance of equalizers critically depend on the symbol clock phase derived in the receiver in case the tap spacing is taken equal to the symbol spacing  $T_s$ . The reason for this is that

- 1) the equalizer cannot suppress noise at frequencies outside the Nyquist band,  $|f| \leq 2T_s$ . Hence; the burden of rejecting such noise components is placed entirely on the filters preceding the equalizer.
- 2) adequate equalization is not possible for all symbol clock phases, since the equalizer cannot alter the relative magnitudes and phases of signal components which in the spectrum are  $1/T_s$  Hz apart and which in the course of sampling the equalizer output at a clock rate  $1/T_s$  become superimposed.

Ungerboeck [43] addresses the possibility of eliminating the need for precise clock-phase control by applying *fractional tap spacing*, i.e., choosing a tap spacing smaller than  $T_s$ . It is shown that

---

<sup>2</sup> Clock recovery after equalization, which removes this distortion, cannot be applied as the equalizer would be required to work before the clock recovery system could operate properly, since an equalizer requires symbol synchronization for correct operation.

- 1) with fractional tap spacing the MSE becomes, within a large time interval, practically independent of the clock phase allowing rather simple clock recovery schemes to be used.
- 2) The final LMS error after adaption is slightly smaller when compared with the symbol-spaced equalizer.
- 3) Less critically designed filters may be used in the receiver section preceding the equalizer.
- 4) For the same length of the equalizer delay line, a fractionally spaced equalizer converges at practically the same speed with respect to the MSE.

In general, the tap spacing may be represented as

$$\tau_s = \xi \cdot T_s, \quad \xi = \frac{I}{J} \leq 1, \quad (6.32)$$

where for the digital implementation  $I$  and  $J$  should be relative prime integers. The cost of fractional tap spacing would then primarily be a  $J$ -times higher analog/digital (A/D) conversion rate,  $J$ -times more memory stages for the equalizer delay line, and  $I/L$ -times more multiplications for the same length of the equalizer delay line in terms of total delay.

### 6.6.9 Off-line processing

In the former, the problem of *real time* adaption and carrier and clock recovery are considered. This results in additional overhead due to the fact that part of the training sequence must be assigned to carrier and clock recovery training. An alternative method, which might relax these requirements substantially, is off-line processing. This means that the received message block is completely stored before starting its processing. If this is done in an oversampling mode the appropriate clock and carrier phase can be found without additional overhead at the cost of a delay in the order of the total message block. An additional side benefit of this approach is that the training sequence can be placed in the middle of the data packet in-between the actual information bits. The adaptive equalizer can start the adaption procedure from the information bits close to this training sequence (denoted as "midamble"), and works rightward and leftward. This makes the equalizer adaption process less vulnerable for changes of the channel characteristics and phase jitter. Another advantage of this approach is that subsequent message blocks can be processed in parallel. Hence; a multiple of low-effort processors can be applied instead of one high-effort processor. This form of regularity (much of the same) thus implies a

reduction of the implementation problem.

A strategy that can be followed to compute the optimum decision instant  $t_0$  and the carrier phase  $\phi_0$  corresponding to the minimum peak distortion is given in [20]; initially, the magnitude  $M(t)$  of the correlation function  $R_{ps}(t)$  of the received preamble sequence  $P$  is computed, starting from the in-phase and quadrature components  $R_{ps}^I(t)$  and  $R_{ps}^Q(t)$ :

$$M(t) = \sqrt{[R_{ps}^I(t)]^2 + [R_{ps}^Q(t)]^2} \quad , \quad (6.33)$$

and  $t_0$  is given by the peak instant of  $M(t)$ . As already indicated, the search for  $t_0$  is performed by applying a sampling rate higher than the bit rate. The received preamble sequence  $P$  is then synchronized according to the value of  $t_0$  obtained. Finally, the carrier phase can be calculated as

$$\phi_0 = -\text{arctg} \left[ \frac{R_{ps}^Q(t_0)}{R_{ps}^I(t_0)} \right] \quad . \quad (6.34)$$

## 6.7 Summary and conclusions

In this chapter, a performance evaluation is presented which is directly based on the measured impulse responses. The objective of this performance evaluation is to assist in weighing design options as antenna use, channel equalization complexity and application of external diversity.

First, the transmission performance is evaluated for the case that the modulation format applied is Quaternary Phase Shift Keying (QPSK) whereas no channel equalization is implemented. For this case, it can be concluded that the values of maximum bit rate  $r_{b,max}$  and associated normalized maximum bit rate  $R_{b,max}$  obtained under LOS conditions do not differ significantly from the corresponding ones obtained under OBS conditions. For all measurement subsets together, we get the outage probability  $P(R_{b,max} < 0.1) = 0.13$  whereas  $P(R_{b,max} < 0.05) = 0.05$ . The latter implies that for typical rms delay spread values, e.g., 60 ns less than 1 Mbit/s is feasible for an outage probability of 5%. It also occurs that the average of  $R_{b,max}$  values does not depend significantly on the indoor environment considered and the type of antennas applied.

The improvement effect of antenna diversity is examined by considering the average

of three  $R_{b,max}$  values based on three impulse responses with equal amplitude profiles but mutually uncorrelated phase profiles. In that case, the average of all  $R_{b,max}$  values increases from 0.51 to 0.58. Assuming an average rms delay spread of 60 ns, this indicates that an average bit rate is feasible of about 10 Mbit/s. The average of standard deviation values decreases from 0.38 to 0.22, whereas an outage probability is achieved as good as  $P(R_{b,max} < 0.2) = 0.02$ . This indicates a feasible bit rate of about 3.3 Mbit/s for an outage probability of 2%.

With respect to indoor mm-wave radio links employing QPSK/DFE the performance is evaluated of a finite tap DFE operating on a 58 GHz indoor radio channel. The evaluation includes the influence of the  $E/N_0$  ratio, the number of forward taps, antenna directivity and external (antenna) diversity on the performance.

The application of a DFE with 3 forward taps yields a  $r_{b,max}$  value of about 30 Mb/s. It is shown that the number of forward taps has a profound influence on the the value of  $R_{b,max}$ ; an increase from 3 to 7 forward taps results in an average improvement of about a factor 5.

A significant average improvement of  $r_{b,max}$  and  $R_{b,max}$  values can be obtained by applying a high gain circular horn antenna at the base station or remote station instead of a biconical-horn antenna. The best results are achieved if the remote station is equipped with a circular horn. In that case, a factor 3 improvement is observed under LOS conditions. The performance is severely deteriorated, however, if the LOS-path becomes obstructed. In contrast, the results show that indoor mm-wave links in which biconical-horn antennas are applied at both the receiving and transmitting end are relatively insensitive to obstruction of the direct LOS ray.

The application of dual antenna diversity on top of DFE enables a  $3.10^4$  times lower probability of bit error  $P_b$  for the same  $r_{b,max}$  value. It can also be used to increase the  $r_{b,max}$  value slightly or it can be applied to reduce the received power penalty for the same value of  $P_b$ .

With respect to the implementation of a DFE operating on mm-wave indoor channels, the Fast Kalman algorithm without exponential weighing offers the best trade-off of convergence, tracking and complexity properties in case the DFE has a transversal structure with a minimum of about 10 taps. For an equalizer having a smaller amount of taps the Square Root Kalman algorithm offers the most favourable characteristics. In both cases, the convergence rate does not dependent strongly on the channel characteristics and amounts to about  $2N$  iterations.

A promising and competitive alternative, allowing more convenient processing, is a lattice DFE with LSL adaption, which offers a comparable convergence at the cost of a slightly higher complexity.



---

In order to eliminate the need for precise clock-phase control, the tap spacing in the feed-forward section should be taken smaller (e.g. a factor  $\frac{1}{2}$ ) than the symbol time. The resulting fractionally spaced equalizer converges at practically the same speed for the same length of the equalizer delay line.

**References in Chapter 6**

- [1] R. Geerts, "Simulatie van Indoor Radio Channels in de mm-Wave Frequency Band", training period report, Telecommunications Division, EUT, Dec. 1993. (in Dutch)
- [2] F. Fernandes, J. Nascimento, A. Gusmão, R. Dinis and J. Neves, "Performance evaluation of mm-wave digital radio transmission", Proc. of the IEEE Second symposium on Communications and Vehicular Technology in the Benelux, Louvain-la-neuve, pp. 95-100, Nov. 1994.
- [3] S.A. Gronemeyer and A.L. McBride, "MSK and Offset QPSK Modulation", IEEE Trans. on Commun., Vol. COM-24, No 8, pp. 809-820, 1976.
- [4] S. Nakajima and N. Furuya, "Gaussian Filtered and Amplitude Limited MSK", Trans. of the IECE of Japan, Vol. E64, No 11, pp. 716-723, 1981.
- [5] D.C. Cox, "Wireless Network Access for Personal Communications", IEEE Commun. Mag., pp. 96-115, 1992.
- [6] F.S. Hill, Jr., "The computation of Error Probability for digital Transmission", Bell Sys. Tech. J., pp. 2055-2077, 1971.
- [7] O. Shimbo and M.I. Celebiler, "The Probability of Error due to Intersymbol Interference and Gaussian Noise in Digital Communication Systems", IEEE Trans. on Commun., Vol. COM-19, No. 2, pp. 113-119, 1971.
- [8] A. Milewski, "New simple and efficient bounds on the probability of error in the presence of intersymbol interference and Gaussian noise", IEEE Trans. on Commun., Vol. COM-25, No. 10, pp. 1218-1222. 1977.
- [9] J.G. Proakis, "Digital Communications", New York, McGraw-Hill, 1989, 2nd ed.
- [10] C.A. Belfiore and J.H. Park Jr., "Decision Feedback Equalisation", Proc. of the IEEE, Vol. 67, No. 8, pp. 1143-1157, 1977.

- [11] G.D. Forney, "Maximum-likelihood sequence estimation of digital sequences in the presence of intersymbol interference", *IEEE Trans. Inform. Theory*, Vol. IT-18, No. 3, pp. 363-378, 1972.
- [12] J. Salz, "Optimum Mean-Square Decision Feedback Equalization", *Bell Sys. Tech. J.* Vol. 52, No. 8, pp. 1341-1373, 1973.
- [13] D.D. Falconer, A.U.H. Sheikh, E. Eleftheriou and M. Tobis, "Comparison of DFE and MLSE Receiver Performance on HF Channels", *Trans. on Comm.* Vol. COM-33, No 5, pp. 484-486, 1985.
- [14] P. Mosen, "Adaptive Equalisation of the slow Fading Channel", *IEEE Trans. Com.*, Vol. 22, No. 8, 1974.
- [15] R. Agusti, F. Casadevall, J.J. Olmos, "Performance of Fractioned and Nonfractioned Equalizers with High-Level QAM", *IEEE J. on Sel. Areas in Commun.*, Vol. SAC-5, No. 3, pp. 476-483, 1987.
- [16] P. Mosen, "Theoretical and measured performance of DFE modem on fading multipath channel", *IEEE Trans. Com.*, Vol. COM-25, pp. 1144-1153, 1977.
- [17] T.A. Sexton, K. Pahlavan, "Channel Modeling and Adaptive Equalization of Indoor Radio Channels", *IEEE J. on Sel. Areas in Commun.*, Vol. SAC-7., No. 1., pp. 114-120, 1989.
- [18] K. Pahlavan, S.J. Howard, "Decision Feedback Equalisation of the Indoor Radio Channel", *IEEE Trans. on Commun.* Vol. COM-41, No. 1., pp. 164-170, 1993.
- [19] D.N. Godard, "Self-Recovering Equalization and Carrier Tracking in Two-Dimensional Data Communication Systems", *IEEE Trans. on Comm.*, Vol. COM-28, No. 11, Nov. 1980.
- [20] "Digital land mobile radio communications", COST 207 Final report, Luxembourg, ISBN 92-825-9946-9, Sept. 1988,.
- [21] B. Widrow, M.E. Hoff, Jr., "Adaptive switching circuits", *IRE WESCON, Conc. Rec.*, Part 4, pp. 96-104, 1960.

- [22] C.L. Lawson and R.J. Hanson, "Solving Least Squares Problems", Prentice Hall, Englewood Cliffs, N.J., 1974.
- [23] W. Murray, "Numerical Methods for Unconstrained Optimization, Academic Press, New York, 1972.
- [24] L.J. Griffiths, "An adaptive lattice structure for noise-cancelling applications", Proc. IEEE Intern. Conf. Acoust., Speech, and Signal Processing, Tulsa, pp. 87-90, 1978.
- [25] D.N. Godard, "Channel Equalization Using a Kalman Filter for Fast Data Transmission," IBM J. Res. Develop., pp. 267-273, 1974.
- [26] D.D. Falconer, L. Ljung, "Application of Fast Kalman Estimation to Adaptive Equalization", IEEE Trans. on Commun., Vol. COM-26, No. 10, pp. 1439-1446, 1978.
- [27] F.M. Hsu, "Square root Kalman filtering for high-speed data received over fading dispersive HF channels", IEEE Trans. Inform. Theory, Vol. IT-28, No. 5, pp. 753-763.
- [28] E.H. Satorius, J. Pack, "Application of Least Squares Lattice Algorithms to Adaptive Equalization", IEEE Trans. on Comm., Vol. COM-29, pp. 136-142.
- [29] R.D. Gitling, F.R. Magee, Jr., "Self-Orthogonalizing Adaptive Equalization Algorithms", IEEE, Trans. on Commun., Vol. COM-25, pp. 666-672, 1977.
- [30] R.W. Chang, "A New Equalizer for Fast Start-Up Digital Communication", Bell. Sys. Tech. J., pp. 1969-2014, July-Aug. 1971.
- [31] E. Eleftheriou, D.D. Falconer, "Tracking Properties and Steady-State Performance of RLS Adaptive Filter Algorithms", IEEE Trans. on Acoust. Speech and Sign. Proc., Vol. 34, No. 5, pp. 1097-1110, 1986.
- [32] C.F.N. Cowen, "Performance comparisons of finite linear adaptive filters", IEE Proc., Vol. 134, Pt. F, No. 3, pp. 211-216, 1987.
- [33] L. Ljung, M. Morf and D.D. Falconer, "Fast Calculation of Gain Matrices for Recursive Estimation Schemes", Int. J. Control, 1978.

- 
- [34] T.L. Lim, M.S. Mueller, "Rapid equaliser start-up using least-squares algorithms", *Int. Conf. Comm. '80, Conf. Record*, pp. 57.7.1 - 57.7.5, June 1980.
- [35] G. D'Aria, V. Zingarelli, "Adaptive baseband equalisers for narrowband TDMA/FDMA mobile radio systems", *Proc. Int. Conf. on Digital Land Mobile Radio Communications, Venice, 1987*.
- [36] D.P. Agrawal, "Advanced Computer Architecture", IEEE Computer Society Press, Washington DC, 1986.
- [37] M.D. Meyer, D.P. Agrawal, "Adaptive Lattice Filter Implementations on Pipelined Multiprocessor Architectures", *IEEE Trans. on Commun.*, Vol. COM-38, No. 1, pp. 122-124.
- [38] M.S. Mueller, "Least-squares algorithms for adaptive equalizers". *Bell Sys. Tech. J.*, Vol. 60, pp. 1905-1925.
- [39] F. Ling, D. Manolakis, J.G. Proakis, "New forms of LS lattice algorithms and the analysis of their round of characteristics", *Proceedings ICASSP '85, Tampa, Fla.*, pp. 1739-1742.
- [40] S. Ljung, L. Ljung, "Error propagation properties of recursive least-squares adaption algorithms", *Automatica*, Vol. 21, pp. 157-167.
- [41] W.C. Lindsey, "Synchronization Systems in Communications", Prentice Hall, Englewood Cliffs, N.J., 1972.
- [42] W.T. Webb, R. Steele, "A 32 Mbit/s mobile radio link", to be published in *IEE Proc. Pt. I*.
- [43] G. Ungerboeck, "Fractional Tap-Spacing Equaliser and Consequences for Clock Recovery in Data Modems", *IEEE Trans. on Commun.* Vol. COM-24, No. 8, pp. 856-864, 1976.

## CHAPTER 7.

# APPLICATION OF THE ASYNCHRONOUS TRANSFER MODE IN INDOOR WIRELESS LANS

### 7.1 Introduction

Indoor wireless LANs intended for supporting a wide range of B-ISDN services should be *efficient* in terms of resource usage and must provide *flexibility* with respect to information transfer, since the range of supported services will impose a wide spectrum of traffic characteristics in terms of average bit rate, peak bit rate etc. Hence; the transfer technique applied in a broadband wireless LAN should be efficient as well as flexible in terms of capacity requirements and should be sufficiently robust to guarantee acceptable end-to-end delay/loss characteristics. Real-time applications like voice and (real-time) video pose stringent delay requirements (time transparency) whereas data traffic requires correct delivery at the destination of the bits transmitted by the source (semantic transparency).

Conceptually, the most efficient transfer technique with respect to resource usage and the most flexible transfer technique in terms of bandwidth requirements is packet switching. However, the initial packet switching networks, such as those based on X.25, do not allow the transport of services with stringent delay constraints. In addition, they suffer from high complexity. The quality of the transmission media was such that in order to guarantee an acceptable end-to-end quality, error control was

performed on every link. As technology improved, the error rate figures of the transmission media reduced. Hence; the quality of transmission systems increased which enabled the packet switching concept to evolve towards a *transfer mode*<sup>1</sup> with only a minimal error recovery functionality in the network, thus allowing the error performance required with low transfer delay. The transfer mode that has been chosen for providing high-speed flexible transfer is the *Asynchronous Transfer Mode (ATM)* initially proposed by Coudreuse [2] and Turner [3] and standardized by CCITT SG XVIII (now ITU T SG 13) [4]. According to the definition of ATM given by the ITU, it refers to a transfer mode in which the information is organized in *cells*; it is asynchronous in the sense that the recurrence of cells containing information from an individual user is not necessarily coupled to the network transmission rate. A *cell* is an information unit of fixed length consisting of a header and an information field. In the ATM context the term "cell" is used instead of "packet" in order to make a distinction between an information unit identified by a label at layer 3 of the OSI reference model (a packet) and an information unit identified by a label at the ATM layer of the B-ISDN protocol reference model (a cell) [5].

With respect to radio networking it is important to notice that the ATM concept was developed with the idea that high quality of transmission is guaranteed, which is certainly true for the present optical fibre technology. Transmission via the radio medium, however, is much less reliable and might depend strongly on environment conditions as extensively discussed in the former chapters. This difference in transmission quality is not essential since fibre technology can not completely prevent the appearance of transmission errors either. Therefore, ATM still accommodates a simplified form of error control being end-to-end error control and header error control. Thus, we have to examine whether this simplified form of error control is sufficient for the achievement of the required error performance of wireless LANs. If so, ATM can be adopted without modification. When it occurs that the error control capability of ATM is insufficient for wireless LANs, then it has to be determined in which way error control functionalities can be added to standard ATM in order to make it suitable for wireless LANs.

A second major difference between fibre-based transmission and radio-based transmission is that in fibre-based networks bandwidth is a relatively abundant commodity whereas in radio-based networks the available bandwidth is relatively limited.

---

<sup>1</sup> According to the vocabulary of terms for broadband aspects of ISDN recommended by the ITU the term "transfer mode" refers to aspects covering transmission, multiplexing and switching in a telecommunication network [1].

As with transmission quality this difference is not essential since the need for efficient broadband network access facilities exists as well for fibre-based networks. Multi-access protocols currently developed and implemented for fibre-based access are therefore also candidates for radio-based access eventually with enhanced error control capability. Furthermore, we probably just have to accept that indoor radio LANs cannot be dimensioned for offering each users "bandwidth-hungry" services like 150 Mbit/s High Definition Television simultaneously<sup>2</sup>.

In summary, the following questions have to be addressed:

- 1) Is end-to-end error control in combination with header error control sufficient for wireless LANs? When this is not the case, it has to be determined which error control functionalities can be added to standard ATM (and where and how) in order to make it suitable for mm-wave indoor wireless LANs.
- 2) Which multi-access protocol, originally intended for fibre-based access, is also suitable for radio-based access possibly in combination with enhanced error control capability?<sup>3</sup>

In considering these questions, we start with a general description of B-ISDN and OSI concepts that are relevant to our discussion (Section 7.2). These concepts are reconsidered in the specific context of radio networking in Section 7.3. A multi-access protocol for ATM-based indoor wireless LANs is described in Section 7.4. Finally, a summary and conclusions are given in Section 7.5.

---

<sup>2</sup> In this respect, it should be noted that developments in the field of source coding have great impact on the applicability of wireless LANs for typical broadband services. These developments have led to the establishment of the MPEG-1 standard, for instance, according to which a high quality video signal is coded in a 1.5 Mbit/s bit stream. Another example is the MPEG 2 standard according to which High Definition Television is coded in a 20 Mbit/s bit stream.

<sup>3</sup> Of course, it is also instructive to examine the suitability of the traditional solutions for radio access for our purpose. This is done by Sonnemans [6] and Maessen [7] under the guidance of the author. These investigations revealed an appropriate solution similar to the one described in Section 7.4 and needs therefore no further treatment.



## 7.2 Basic network concepts

### 7.2.1 Evolution of system concepts

A substantial part of the discussion is focused on additional error control measures. Therefore, it is instructive to discuss the relationship between B-ISDN protocols and conventional OSI protocols since network concepts according to the OSI protocol reference model are based on the assumption that conventional transmission media cannot guarantee an acceptable end-to-end quality without error control on every link, as shown in Fig. 7.1a. This error control is supported by a protocol that includes core functions such as error checking and error recovery (forward error correction / retransmission). In high-quality networks only core functions of that protocol need to be implemented on a link-by-link basis whereas the other functions can be implemented on an end-to-end basis (Fig. 7.1b). For fibre-based network technology, which features very high quality transmission in terms of probability of bit error  $P_b$  (e.g.,  $P_b = 10^{-10}$ ), this idea is extended further; in the case of B-ISDN, most of the error recovery functions also have been shifted to the edges of the network (Fig. 7.1c).

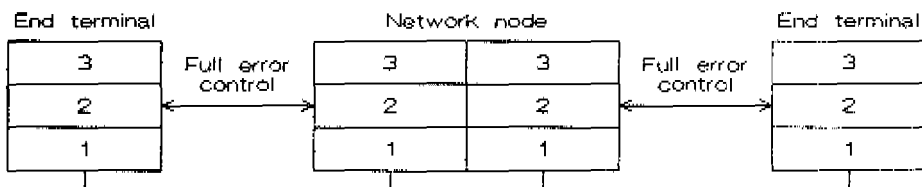


Fig. 7.1a: Full error control on each link (X.25)

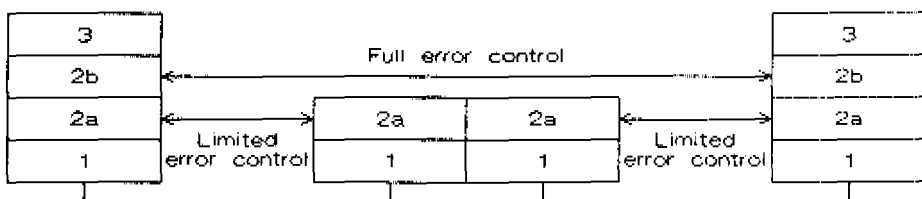


Fig. 7.1b: Limited error control on each link

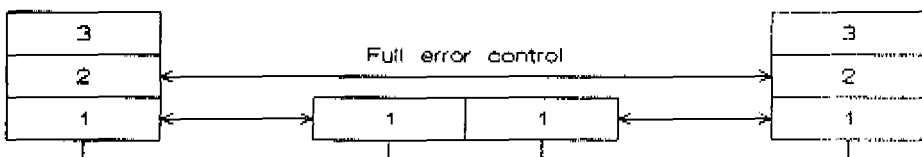


Fig. 7.1c: End-to-end error control (B-ISDN)

Fig. 7.1: Evolution in system concepts

## 7.2.2 ATM concept

### 7.2.2.1 Protocol reference model

As part of the ATM concept, the functions that are responsible for time transparency as well as the functions responsible for semantic transparency are shifted to the edges of the network. This is done by merging two well-known concepts, namely packet switching and time division multiplexing (TDM). Each of these techniques has been modified as follows:

- There is no error control (on the data field) nor flow control on a link-by-link basis.
- The transfer is connection oriented at the lowest level; all information is transferred in a virtual circuit assigned for the complete duration of the connection.
- ATM cells have a fixed and small length which allows the use of very high speed switching nodes.
- The functionality of the cell headers is limited; the primary functionality in the cell headers is the identification of the virtual path and the virtual circuits. In addition, some error control on the header is provided.
- There is no fixed time relation between time slots and ATM cells inside the network; there is no identification by the time position of a cell (this is the meaning of the "A" in the acronym "ATM"). That explains the need to have a header field containing a virtual circuit identifier. The size of an ATM cell is set to 53 octets, the header being 5 octets long and the cell information field is 48 octets.

The B-ISDN protocol reference model (PRM) for ATM, as recommended by CCITT, is depicted in Fig. 7.2. A similarity with the OSI PRM is the layered architecture. A characteristic property is that it contains several planes; a user plane to transport user information, a control plane to transport signalling information (out-of-band signalling) and a management plane to perform network maintenance as well as layer functions.

Three layers are defined: the *physical layer*, which mainly transports information, the *ATM layer* which mainly performs switching and multiplexing and the *ATM adaptation layer*, which is mainly responsible for adapting service information to the ATM stream. These layers will be described in more detail.

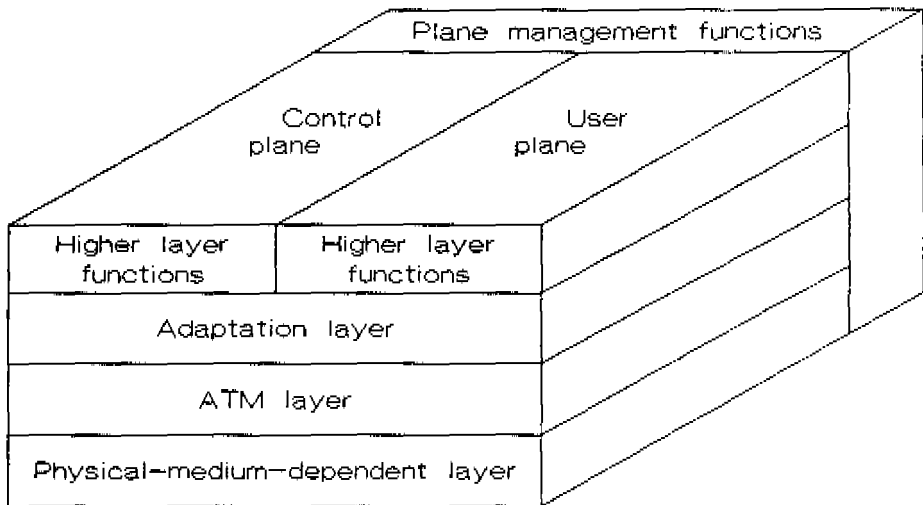


Fig. 7.2: B-ISDN ATM protocol reference model.

### 7.2.2.2 Physical layer

The physical layer (PL) consists of the *physical-medium-dependent (PMD) sublayer* and the *transmission convergence (TC) sublayer*. The PMD sublayer is responsible for the correct transmission and reception of bits on the physical medium. Its functions are medium dependent (optical, copper, radio).

The main function of the TC sublayer is mapping of the ATM cells to the transmission system used (synchronous, plesiochronous, or cell based hierarchies). The TC sublayer communicates with the PMD sublayer using bit streams, and with the higher ATM layer in terms of error-free ATM cells.

### 7.2.2.3 ATM layer

The main functions performed in the ATM layer as defined by CCITT [8] are:

- Multiplexing and demultiplexing of cells of different connections onto a single cell stream. For this, the *virtual channel (VC)* concept is introduced which describes the unidirectional transport of ATM cells associated with a common unique identifier value, the VC identifier (VCI) which is contained in the cell

header. In addition, the *virtual path (VP)* concept is introduced as being a bundle of VCs. Hence; a cell header also contains a VP identifier (VPI).

- The cell header is extracted before the cell is delivered to the adaptation layer and added after the cell is received from the adaptation layer.
- Translation of the VCI might be required at ATM switching nodes.
- Access flow control can be implemented on the user network interface.

#### 7.2.2.4 ATM adaptation layer

The ATM layer, as defined by CCITT [9], is not tailored to any specific application. As a consequence, it is not directly usable for many applications. The ATM adaptation layer (AAL) enhances the services provided by the ATM layer according to the requirements of specific services. These services can be user services as well as control and management services.

In the area of services, four classes of service were defined: These classes are denoted A,B,C and D. This classification was based on whether or not a timing relationship must be maintained between source and destination, whether or not the application requires a constant bit rate, and whether the transfer is connection-oriented or connectionless, as shown in Fig. 7.3.

Criteria \ Class	A	B	C	D
Timing relationship between source and destination	Required		Not required	
Bit rate	Constant	Variable		
Connection mode	Connection-oriented			Connection-less

Fig. 7.3: Service classes for the AAL.

An example of a class A service is circuit emulation, which is by definition connection oriented. In circuit emulation, a constant-bit-rate (CBR) is used. CBR services clearly require the maintenance of a timing relation including the control of the peak bit

rate. An example of a class B service is variable-bit-rate (VBR) video, such as might be used in a teleconference. Here, the application is connection oriented and timing is important, but the bit rate varies depending on the amount of activity in the scene. Classes C and D correspond to data transfer applications. In both classes, the bit rate may vary and no particular timing relationship is required; difference in data rate are handled by the end systems using buffers. The data transfer may be connection oriented (class C) or connectionless (class D).

CCITT has recommended four types of AAL to support the four service classes: type 1, 2, 3/4 and 5. Although the AAL types are in accordance with the service classes, the user is free to select any AAL type for any service class. There is also the possibility to have an empty AAL for users who may find the ATM services sufficient for their requirements.

The AAL can be subdivided into a sublayer that provides cell segmentation and reassembly to interface to the ATM layer and a more service specific convergence sublayer to interface to the bearer services being carried.

### 7.2.3 Mapping of protocol data units

The AAL maps the *AAL protocol data unit* (AAL PDU), i.e., the total sequence of the AAL header, payload and trailer, into the payload field of the ATM cell and vice versa. The ATM layer in turn maps the *ATM PDU*, i.e., ATM cell, into the payload of the *PL PDU*, i.e., PL payload and PL overhead part attached and vice versa. The overhead part of the PL PDU consists of synchronization bits, an equalizer training sequence (see Section 6.6), multi access control bits and (eventually) error control bits. An example of the mapping of protocol data units is shown in Fig. 7.4. This figure includes the structure and dimensioning (number of bits for the various parts) of the different PDU's. The AAL PDU refers exclusively to the AAL 3/4 type. The structure and dimensioning shown for the PL PDU is by no means established and is just an example of what might be appropriate for a wireless LAN.

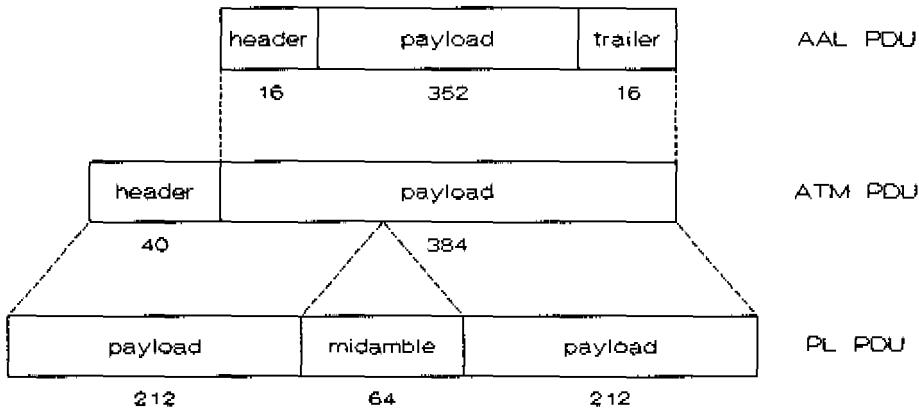


Fig. 7.4: Mapping of the protocol data units.

### 7.2.3 B-ISDN Reference points

For an analysis of network architectures, a functional reference architecture model for the network can be used, which is a conceptual division of network functions [4]. Fig. 7.5 provides a conceptual model for a B-ISDN reference configuration consisting of *functional groupings* partitioned by *reference points*  $R$ ,  $S_B$  and  $T_B$ . Functional groupings are arrangements of physical equipment or combinations of equipment. Reference points are conceptual points used to separate groups of functions. The subscript  $B$  indicates broadband reference points. The terminal equipment functions that follow ISDN recommendations are denoted as B-TE1 whereas the terminal equipment functions that do not follow ISDN recommendations are denoted as B-TE2. These B-TE2 functions use a broadband terminal adapter (B-TA) to achieve connection with a broadband network. The  $R$  reference point is for non-ISDN physical interfaces which require B-TAs to convert their own protocols to the ATM-supported  $S_B/T_B$  interface of the network termination (NT). User equipment complying with B-ISDN standards can be directly connected at the  $S_B$  and  $T_B$  reference points. The  $S_B/T_B$  interface is based on ATM and has the same capacity as the loop interface ( $U_B$ ) which is the designation for the physical interface between the NT and the local exchange. The NT2 functions contain local switching between  $S_B$  interfaces, multiplexing of several  $S_B$  interfaces onto the  $U_B$  interface and concentration functions. The B-NT2 functions may be performed by terminal controllers, PBX (private branch exchanges) and LANs. A B-NT2 that performs PBX or LAN functions is termed a *distributed B-NT2*. B-NT1 functions terminate the transmission

line from the local exchange. The function of this grouping is to provide the physical layer interworking of the  $T_B$  and  $U_B$  interfaces.

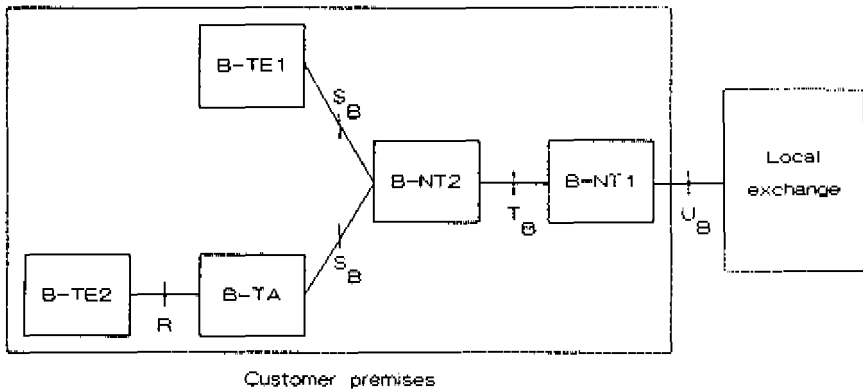


Fig. 7.5: B-ISDN reference points.

### 7.3 Wireless LAN concepts based on ATM

#### 7.3.1 Distributed B-NT2

In the B-ISDN context, a wireless LAN can be considered as a (radio) distributed B-NT2. Such a B-NT2 is depicted in Fig. 7.6. It consists of a set of medium adapters (MAs) and a base station (BS). The MAs adapt the B-ISDN protocols running across the  $S_B$ -interfaces to the protocols of the wireless LAN. They provide a medium access mechanism to ensure that all B-TEs get access to the network. The functions of the MAs will not be standardized by CCITT. The BS adapts the B-ISDN protocols running across the  $T_B$ -interface to the wireless LAN protocols. The wireless LAN may use its own protocols tailored to meet the special requirements imposed by the rudeness of the radio medium as long as the B-TE1s, B-TE2s/B-TAs and B-NT1 are connected via the standardized  $S_B$  and  $T_B$  interfaces, respectively. In the following, the combination of B-TE1 and MA or B-TE2, B-TA and MA is termed a *remote station* (RS).

The wireless LAN offers a shared bandwidth of some tens of Mbit/s (per carrier) amongst all connected users while fibre-based ATM can offer each user a dedicated 155 Mbit/s access. However, incompatibility at the edges of the wireless LAN due to its limited capacity can be prevented by establishing a transfer contract

that is adapted to the limited capacity of the wireless LAN in the connection setup phase. The signals passing the  $S_B$  and  $T_B$  interfaces can then be mapped on the signals with lower bit rates in the B-TAs and BS. In what follows, we describe and discuss the way in which the ATM cells can be transferred most reliably and efficiently after the transfer contract has been established. Relevant to this discussion is 1) the duplexing method to be applied, 2) the error control measures to be taken and 3) the multi-access method to be applied. Duplexing as well as error control are discussed in the next section whereas multiple access is treated in Section 7.4.

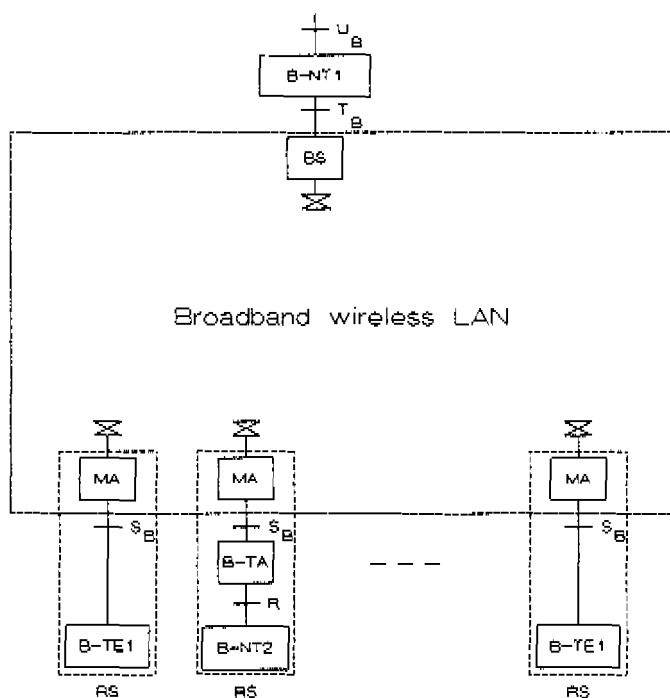


Fig. 7.6: Example configuration of a radio distributed B-NT2.

### 7.3.2 Duplexing methods

In practice, transmission and reception within one and the same frequency band cannot be performed simultaneously by a radio transceiver. Reason for this is the huge difference (e.g., 60 dB) between transmit and receive power, which makes subtraction of the received signal from the (known) transmitted signal too unreliable



to be of use, even when these signals are orthogonal. One duplexing method that can be imagined for ATM is random transmission/retransmission of ATM cells within one and the same frequency band. With this method, however, the resulting efficiency is low due to collisions of cells. In addition, time transparency as necessary for real time services may not be guaranteed due to excessive (re)transmission delays.

In what follows, we discuss the two remaining duplex methods commonly applied in radio communications, viz., Time Division Duplex (TDD) and Frequency Division Duplex (FDD). In a TDD system a single carrier is used for the transmission of both upstream and downstream traffic. FDD, on the other hand, uses different carriers for the two directions of transmission. The duplexing method applied has an impact on radio-network design, implementation and frequency use. We will discuss the criteria on which a choice in favour of one of the two candidate duplex methods can be based. For this, we assume a system in which channel equalization is applied for each channel.

For each direction, the line symbol rate in a TDD system must be at least twice that of a FDD system to attain the same transfer capacity because TDD uses only one carrier, instead of two in a FDD system. Therefore, the channel equalizer must be more complex for the TDD system and there must be at least twice as much signal power available at the input of the demodulator for the same transmission performance.

TDD has an advantage with respect to the application of diversity; diversity reception with efficient combining techniques, such as maximum-ratio combining can be achieved without the need for multiple antennas at each RS. Instead, antenna diversity is implemented only at the BS and efficient signal combining can be performed when data symbols are received from an RS; when the BS next transmits to that RS, it uses the same combining ratio, making use of the reciprocity property of the radio channel. The reciprocity property cannot be exploited in an FDD system since FDD uses separate channels for the two directions of transmission which are not instantaneously reciprocal. This, however, does not imply that transmit diversity techniques cannot be applied in FDD systems; in the literature various transmit diversity techniques are proposed for FDD systems. These techniques can be classified into three broad categories. The first category uses feedback information from the receiver to configure the transmitter [14,15]. In the second category feed-forward information is used from the transmitter to train the receiver [16,17]. The third category uses multiple transmit antennas and channel coding to provide diversity [18,19].

Another design consideration is whether a duplexer is required in the BS and

RSs. A duplexer is required when simultaneous reception and transmission is performed as in most FDD systems<sup>4</sup>. TDD does not require a duplexer because in this scheme the receiver is switched out during the transmit burst.

Furthermore, the selection of a duplex scheme has consequences with respect to RF filtering; in FDD two filters are required, each having half of the total RF bandwidth, whereas in TDD only one RF filter is required having the total RF bandwidth.

In an FDD system, BS-to-RS transmissions cannot interfere with RS-to-BS transmissions. The downstream traffic can be a continuous (uninterrupted) stream of data symbols. When compared with TDD this 1) facilitates acquisition of the received signal at the RSs and 2) eliminates the necessity of guard times between downstream bursts thus saving capacity.

A second implementation consideration is that of equipment utilization. In a heavily loaded TDD system, designed to operate at the maximum symbol rate as dictated by the time dispersion of the channels and the complexity constraints of the equalizer, each RS effectively sits idle half the time. Therefore, for a given amount of traffic, a TDD system will require (more than<sup>5</sup>) twice as much transceiver capacity as an FDD system, significantly increasing the cost.

The fact that FDD employs two frequency bands implies that an additional guard band must be respected when compared with TDD which only uses one frequency band. On the other hand, TDD must accommodate twice the symbol rate, when compared with that of FDD for the same transmission capacity, which results in a larger sequence required for equalizer training which also requires extra bandwidth.

Table 7.1 summarizes the relative strengths and weaknesses of both duplex methods. In general, the most important advantage of TDD, when compared with FDD, is the more extended possibility to implement transmit diversity schemes, which eliminate the need for multiple antennas at the RSs. This might be a significant advantage for systems with small RSs (e.g., handsets), but for our purposes this advantage is of minor importance since we consider systems with larger RSs that can be easily

---

<sup>4</sup> Duplexers might not be necessary in FDD systems employing Time Division Multiple Access (TDMA) since with TDMA systems, the transmit time slot and receive time slot of the RSs can occur at different times. However, according to the ATM scheme proposed in Section part 7.4, cells must be simultaneously transmitted and received by the BS and RSs.

<sup>5</sup> This is due to the fact that for higher bit rates the equalizer training sequences must be longer resulting in extra transmission overhead (see Section 6.6.2).

equipped with two or more small-sized mm-wave antennas. For the achievement of transmission over indoor radio channels at symbol rate values in excess of the coherence bandwidth the equalizer functionality becomes of utmost importance. Hence; for time-dispersion-limited symbol rates as we envision, a system employing FDD matches the characteristics of indoor radio channels best.

*Table 7.1 Comparison of FDD and TDD.*

Criteria	FDD	TDD
Transmitted Peak power required	< half of TDD	> twice FDD
Symbol rate required	< half of TDD	> twice FDD
Equalizer complexity	Less complex	More complex
Antenna diversity implementation	More complex	Less complex
Duplexer required at BS	Yes	No
Duplexer required at RS	Yes	No
Burst acquisition required at BS	Yes	Yes
Burst acquisition required at RS	No	Yes
Upstream burst synchronization req.	Yes	Yes
Downstream burst synchr. req.	No	Yes
RF filters required	Two filters	One filter
Equipment utilization	> twice TDD	< half of FDD
Required amount of spectrum	Similar	Similar

### 7.3.3. Error control

As far as the control of bit errors is concerned, the performance requirements for candidate B-ISDN wireless services are commonly given in terms of maximum cell loss rate [13,20,21,22]. In cable-based ATM networks cell loss is primarily caused by network saturation. In these networks, bit errors due to noise and inter-symbol interference can also cause cell loss when it affects the cell header, but this is only a second order effect. In wireless networks, bit errors tend to appear much more frequently. In this discussion concerning error control, we assume that the influence of bit errors on cell loss is acceptable in case the cell-loss rate due to bit errors does not exceed the cell-loss rate due to network saturation.

In general, there are two candidate categories of techniques for controlling transmission errors in data transmission systems: the forward error control (FEC) scheme and the automatic-repeat-request (ARQ) scheme [17].

In an FEC system, an error-correcting code is used which allows the receiving terminal to locate and correct a limited number of errors in a received block of data. FEC codes add redundant parity check bits to the data bits in a way that allows errors to be located within a code word. In general, twice as many errors can be detected by an FEC code as can be corrected. In an FEC system, there is always a finite possibility that an error will not be corrected, resulting in incorrect data being received. A method to reduce cell loss is implementing FEC at the AAL layer. Another method is to implement (additional) measures at ATM layer level by which more errors can be corrected in the ATM cell header. Such measures, however, would require additional cell overhead and are therefore incompatible with the current CCITT standard I.361 concerning the format of ATM cells. A better method is to implement additional FEC in the PL since the major advantage of this approach is that the PL carries the ATM cells in a completely transparent way.

With respect to FEC there are two different types of error detecting and -correcting codes in common use today; *convolutional codes* and *linear block codes*.

Convolutional coding is a more powerful technique than linear block encoding. The information contained in any one data bit is spread through several bits of codewords. Decoding convolutional codes, however, is a complex process that requires decisions on the most likely transmitted data sequence when a codeword is received in error. Because of this complexity, the application of convolutional coding can be ruled out for error correction of received cells.

Linear block codes are a class of error-detecting and -correcting codes that can be easily implemented. Cyclic codes form an important subclass of linear block codes. These codes are attractive for the reason that encoding and decoding can be implemented easily by employing shift registers and logic gates. The Bose, Chaudhuri and Hocquenghem (BCH) codes form the most powerful group of error-correcting cyclic codes yet devised [23].

The encoder for a block code divides the information sequence into message blocks of  $k$  information bits each. In case of cell-based transmission, each cell can be treated as a message block. The encoder transforms each message block into a codeword of  $n$  bits.  $n$  is called the *block length*. Such codeword thus contains  $n-k$  redundant bits. These  $n-k$  bits are called parity check bits. The encoder can generate  $2^k$  different possible code words, corresponding to  $2^k$  different possible messages at its output. This set of  $2^k$  code words of length  $n$  is called an  $(n,k)$  block code. The ratio  $R=k/n$  is called the code rate.

BCH codes with the capability of correcting  $t$  errors have a blocklength  $n=2^m-1$  with  $m$  being an integer and  $m \geq 3$ . The number of parity checkbits equals  $n-k \geq mt$  for  $t < 2^{m-1}$ .

The message block to be protected consists of the ATM cell (424) and a MAC-field of 8 bits (see Section 7.4, the sequence for equalizer training/synchronization is bypassed). Consequently,  $k=432$ . This implies that  $m$  must be at least 9. We can minimize the required coding overhead, i.e., the minimum required number of parity bits  $k_{min}$  by taking  $m=9$  which results in  $n=511$  and  $k_{min}=n-9t$ . The BCH(511,502) code for instance has the potential to correct 1 bit error in whatever place of 511, or it can detect 2 errors, a burst of 9 or less, 99.6 % of the bursts of length 10, 99.8 % of longer bursts. Alternatively, the BCH(511,493) code has the capability to correct 2 errors in whatever place of 511. In addition, it can correct 1 burst error up to 9 bits, whereas it can detect all burst errors up to 18 bits [24]. The additional error detecting potential makes BCH codes well suitable for application in hybrid FEC/ARQ schemes.

In an ARQ system, a code with good error-detecting capability is used to determine whether or not a received block of data is error free. If there are too many errors in the received block of data, then the receiver communicates this to the transmitter via a return link and the corrupted data block is retransmitted. Provided that all errors introduced by the link are detected, retransmission of the corrupted data block can be repeated until the data are received correctly. ARQ can provide high system reliability and may be well suited for indoor applications since round-trip delays are very short (only a few symbol times at maximum). This enables very short retransmission delay. In ATM cell-by-cell transmission a retransmitted block of data would be obviously an ATM cell. It should be noticed, that retransmitted cells may experience additional cell delay introduced by the multi access protocol yielding increased cell delay jitter. This problem can be alleviated by applying only a simple form of ARQ as *single retransmission*. In this scheme, the retransmission strategy is as follows: when in a received cell more errors are detected than the number of errors that can be corrected the cell is retransmitted once and only once, eventually with priority over initially transmitted calls. Additional measures might be necessary in order to maintain cell sequence integrity. ARQ can be implemented in the PL as well as in the AAL. For this, the AAL PDU contains a sequence number for the detection of lost and misinserted cells. The AAL can provide ARQ functions tailored to specific services; the application of ARQ can be restricted for instance, to services that require a low bit error rate but do not require a strict timing relation between source and destination (Class C and D services). From an implementation point of view it might be advantageous to leave ARQ over to the AAL located in the B-TEs since this option eliminates the need for implementing AAL functions in the wireless LAN. However, a drawback of this approach is that the resulting quality of transmission is not a feature of the wireless network itself but of the terminals attached. In other

words, the terminals do not experience a LAN that guarantees the (error) performance of a the cable-based distributed NT-2 on which their error control facilities at AAL level are based. Therefore additional ARQ measures can be implemented best at PL level.

### 7.3.3 Feasibility of reliable ATM-cell transmission

The possibility of supporting B-ISDN services by an indoor wireless LAN depends on

1. The performance requirements by the different services.
2. The applied wireless-LAN technology.

ad 1. Table 7.2 lists some candidate B-ISDN wireless services [13,20,21,22] with estimated bit rate, typical session duration and maximum cell loss rate.

ad 2. In this section we consider a wireless-LAN with features as listed in Table 7.3.

*Table 7.2: Performance requirements for broadband wireless services.*

Service	Max. $P_{cell}$	Av.rate (Mbit/s)	Peak rate (Mbit/s)	Typical session length
Video teleconferencing	$10^{-5}$	0.3-2	10	30 min.
Video telephony	$10^{-5}$	0.06-2	6	3 min.
High volume transfer	$10^{-9}$	1-20	1-20	10-100 Mbit
High resolution image retrieval	$10^{-9}$	4-45	4-45	8 Mbit
Portable multimedia	$10^{-9}$	1-10	10-100	30 min.
Manufacturing (Robotics)	$10^{-9}$	0.01-3	0.01-3	continuous

Table 7.3: Parameter values and descriptions of the system under study.

Parameter	Value/Description
Transmit power	17dBm
Carrier frequency	58 GHz
Separation distance	25 m
Front-end noise figure	9 dB
Additional losses	2 dB
Transfer method	ATM-cell based
Duplex type	FDD
Antennas	Biconical-horn antennas (7 dBi gain)
Antenna diversity order	1 or 2
Modulation	QPSK
Channel equalization	no or DFE with 3,5 or 7 forward taps
Error correction	no, 1 or 2 random errors per cell
Retransmission	no or single retransmission
Implementation margin	2 dB
Cell-loss probability	$10^{-9}$ or $10^{-5}$

From the data listed in Table 7.2 and Table 7.3, it can be estimated to which extend antenna diversity and error control needs to be implemented for the support of a specific B-ISDN service. This can be done by determining the *maximum allowed line bit rate*, i.e., the *line bit rate* at which the maximum allowed cell-loss probability occurs. The term "line bit rate" is used to denote the bit rate at which the individual PL PDU's (excluding guard times) are transmitted. As an example, we derive the feasible line bit rate for

- Maximum allowed probability of cell loss:  $P_{ck} = 10^{-9}$
- Diversity order:  $D=2$
- Error-correcting capability:  $t=2$
- No retransmission

The first step is to determine the maximum allowed probability of bit error at the physical layer (and thus experienced by the ATM PDU's)  $P_{b,PL}$  for  $P_{ck} = 10^{-9}$ . For this, we assume that bit errors appear randomly and that an ATM cell becomes lost in case the header of the ATM cell contains more bit errors than the number of correctable bit errors. Hence; we can determine  $P_{b,PL}$  by considering the binominal distribution

$$P_{cb} = \sum_{i=0}^N \binom{N}{i} P_{b,PL}^i (1 - P_{b,PL})^{N-i} \quad (7.1)$$

in which  $N$  is the number of bits in the header of the ATM cell and  $u$  is the error correcting capability of the ATM cell header. According to [8],  $N=32$  and  $u=1$ . Substituting these figures together with  $P_{cb}=10^{-9}$  in (7.1) yields  $P_{b,PL}=1.4 \cdot 10^{-6}$ .

The second step is to determine the *probability of line bit error*, i.e., the probability of bit error at the input of the BCH decoder, required for  $P_{b,PL}=1.4 \cdot 10^{-6}$ ,  $t=2$  and  $D=1$  which we denote as  $P_{b,line}(P_{b,PL}, t, D) = P_{b,line}(1.4 \cdot 10^{-6}, 2, 1)$  can be calculated according to

$$\sum_{i=1}^k P_{b,PL}^i (1 - P_{b,PL})^{k-i} = \sum_{i=1}^k P_{b,line}^i(P_{b,PL}, t, D) (1 - P_{b,line}(P_{b,PL}, t, D))^{k-i} \quad (7.2)$$

Substituting  $k=432$  together with  $P_{b,PL}=1.4 \cdot 10^{-6}$ ,  $t=2$  and  $D=1$  in (7.2) yields  $P_{b,line}(1.4 \cdot 10^{-6}, 2, 1) = 3.5 \cdot 10^{-4}$ .

The third step is to determine the  $P_{b,line}$  required for  $P_{b,PL}=1.4 \cdot 10^{-6}$ ,  $t=2$  and  $D=2$ . It follows directly from (6.23) that  $P_{b,line}(P_{b,PL}, t, 2)$  can be derived from  $P_{b,line}(P_{b,PL}, t, 1)$  according to

$$P_{b,line}(P_{b,PL}, t, 2) = \sqrt{\frac{1}{2} P_{b,line}(P_{b,PL}, t, 1)} \quad (7.3)$$

which yields  $P_{b,line}(1.4 \cdot 10^{-6}, 2, 2) = 1.3 \cdot 10^{-2}$ .

The fourth step is estimation of the value  $E_b/N_0$  required for  $P_{b,line}(1.4 \cdot 10^{-6}, 2, 2) = 1.3 \cdot 10^{-2}$ . This can be done by applying (6.23) to (6.25). Alternatively, we can estimate the required  $E_b/N_0$  by interpolating or extrapolating the results given in Fig. 6.12. For normalized bit rate values up to about 2 and a line bit error rate of  $1.3 \cdot 10^{-2}$  we find for  $E_b/N_0 = 22$  dB.

Finally, we can determine the line bit rate  $r_{b,line}$  by

$$10 \log r_{b,line} = \frac{C}{N_0} - \frac{E_b}{N_0} \quad (\text{dB}) \quad (7.4)$$

The figures in Table 7.3 yield  $C/N_0=98$  dB for  $N_0$  is  $kT$ , ( $k$  is Boltzmann Constant,  $T$ , is 290 K noise temperature). Substituting this value together with  $E_b/N_0=22$  dB in (7.4) yields  $r_{b,line}=40$  Mbit/s. The minimum number of forward taps the channel



equalizer should have can be determined on the basis of the worst-case rms delay spread value obtained, being 100 ns. The span of the applied channel equalizer must be sufficient large to accommodate the inter-symbol interference. According to Fig. 6.14, the minimum required number of forward taps for  $r_{b,line}=40$  Mbit/s amounts to 5.

It follows directly from (7.4), that each 3 dB that can be gained in the link budget offers a factor 2 increase in maximum bit rate provided that the span of the applied channel equalizer is sufficient large.

The *net bit rate*, i.e., the effective bit rate at which the AAL payload is transmitted, can be determined for the upstream traffic according to

$$r_{b,net} = \frac{n_{AAL,inf}}{n_{ATM} + n_{PL,oh} + n_{guard}} r_{b,line} \quad (7.5)$$

in which

- $n_{AAL,inf}$  is the number of AAL information bits contained in the payload field of the AAL PDU.  $n_{AAL,inf}$  is 376 for AAL type 1 and 352 for AAL type 3 and 4. ( $n_{AAL,inf}$  for AAL type 2 is not yet standardized).
- $n_{ATM}$  is the total number of bits contained in the ATM PDU.  $n_{ATM}$  amounts to 424.
- $n_{PL,oh}$  is the number of PL overhead bits contained in the midamble field of the PL PDU.  $n_{PL,oh}$  depends on the implementation of the PL functionalities. A significant part of the PL overhead is likely to be formed by the sequence for equalizer training/synchronization. As stated in section 6.6.2, the length of this sequence should be at least  $2N$  symbols, where  $N$  is the total number of forward + backward taps. A 10 taps equalizer in combination with quaternary modulation should thus be at least 40 bits. In addition, the PL overhead might contain 9 or 18 CRC bits as stated in the previous section. Furthermore, about 8 bits are necessary for medium access control (see Sections 7.4.2 and 7.4.3). It can therefore be estimated that  $n_{PL,oh}$  amounts to 59 or 68 bits when two spare bits are taken into account, which can be used for acknowledgement and priority identification.
- $n_{guard}$  is the number of bits corresponding to the guard time  $t_{guard}$  that must be respected between consecutive transmitted cells. Hence;  $n_{guard} = t_{guard} \cdot r_{b,line}$ . A guard time of 300 ns can accommodate differences in RS-to-BS separation distances of up to 60 m, which is sufficient for our purposes.

Substituting the given parameter values in (7.5) yields an estimated aggregate over-

head of 30%<sup>6</sup>. For  $C/N_o = 98$  dB and  $E_b/N_o = 22$  dB, this yields  $r_{b,net} = 28$  Mbit/s. If the cell transmission rate is the same for both directions, then the aggregate overhead in the down stream traffic equals the overhead in the upstream traffic. In the continuous downstream traffic no guard times need to be respected. The resulting extra bits can be used for additional performance improvement.

According to the previous procedure, feasible line bit rate values are determined for the parameters as listed in Table 7.3. The results are listed in Table 7.4a and 7.4b for  $P_{cb} = 10^{-9}$  and  $P_{cb} = 10^{-5}$ , respectively. The values between brackets denote the required number of forward taps of a DFE on basis of 100 ns rms delay spread according to Fig. 6.14. The addition "(no)" indicates that for the net bit rates below 0.35 Mbit/s (or equivalently, for line bit rates below 0.5 Mbit/s) no channel equalization needs to be implemented (see Section 6.3).

*Table 7.4a: Feasible net bit rates for  $P_{cb} = 10^{-9}$ .  
t: number of correctable errors / cell  
D: diversity order*

$P_{cb} = 10^{-9}$	D=1	D=2
t=0	3.5 kb/s (no)	1.7 Mb/s (3)
t=1	1.7 kb/s (no)	14 Mb/s (3)
t=2	0.7 Mb/s (3)	28 Mb/s (5)

*Table 7.4b: Feasible net bit rates for  $P_{cb} = 10^{-5}$ .  
t: number of correctable errors / cell  
D: diversity order*

$P_{cb} = 10^{-5}$	D=1	D=2
t=0	300 kb/s (no)	2.2 Mb/s (3)
t=1	1.7 Mb/s (3)	44 Mb/s (5)
t=2	11 Mb/s (3)	70 Mb/s (7)

It follows from Table 7.4a and 7.4b that, without the implementation of ARQ, the error correction capability should be at least one error per ATM cell to achieve bit rate values in the order of some tens of Mbit/s. It is even possible to achieve 16 Mbit/s without the implementation of antenna diversity in case two bit errors can be corrected in the received cell for services that allow a maximum probability of cell

<sup>6</sup> In optical networks this aggregate overhead is about 20% [22].

loss of  $10^{-5}$ . From Table 7.2 it follows, however, that typical target wireless services as portable multimedia require a probability of cell loss as low as  $10^{-9}$ . For such a low value, net bit rates in the order of some tens of Mbit/s can only be achieved by implementing antenna diversity. Hence, for our purposes,  $t$  should be at least 1 and  $D$  should be 2. In that case, a bit rate of 20 Mbit/s can be obtained with a DFE having only 3 forward taps. A factor 2 increase in feasible bit rate can be obtained by implementing  $t=2$  instead of  $t=1$  or, alternatively, by taking measures that result in a 3 dB gain in the link budget. The minimum required number of taps in the forward section of the DFE should then be 5.

In order to examine the reduction of cell loss that can be achieved by a simple form of ARQ we consider the single retransmission scheme as described in the introduction of this section. In that case, the effective probability of cell loss  $P_{cl}$  equals the loss probability of a cell when it is transmitted for the first time  $P_{cl1}$  times the loss probability of its retransmitted version  $P_{cl2}$ . We assume that changes in the channel occur so slow that we may take  $P_{cl1} = P_{cl2}$ . Furthermore, we assume that the acknowledgement channel (return link) is error free. For this ARQ scheme, the feasible bit rate can be determined by first calculating  $P_{b,PL}$  according to

$$P_{cl} = P_{cl1} \cdot P_{cl2} = \left[ \sum_{i=0}^N \binom{N}{i} P_{b,PL}^i (1 - P_{b,PL})^{N-i} \right]^2 \quad (7.6)$$

Finally,  $r_{b,net}$  is calculated using (7.2) to (7.5). Table 7.5 lists the results for  $P_{cl} = 10^{-9}$ .

*Table 7.5: Feasible net bit rates for  $P_{cl} = 10^{-9}$  with single retransmission.  
t: number of correctable errors / cell  
D: diversity order*

$P_{cl} = 10^{-9}$	$D = 1$	$D = 2$
$t = 0$	0.4 Mb/s (3)	28 Mb/s (5)
$t = 1$	2.8 Mb/s (3)	56 Mb/s (7)
$t = 2$	4.4 Mb/s (3)	88 Mb/s (9)

From this table, it follows that the application of single retransmission might increase the feasible bit rate significantly. It even occurs that when applying single retransmission, error correction is not necessary for the achievement of some tens of Mbit/s, provided that antenna diversity is still implemented. On the other hand, retransmission increases cell delay variation which might be unacceptable for real-time services.

## 7.4 Medium-Access Control

### 7.4.1 General concept

The access to the shared medium is arbitrated by the *Medium-Access Control* (MAC) protocol. Common protocols for shared medium access in fibre-based ATM networks such as Distributed Queue Dual Bus [11] or Orwell slotted ring [12] cannot be applied in wireless LANs with an economic use of the available network resources since a single RS-to-RS connection might involve many individual RS-to-RS links. Therefore, we propose a wireless network in which the communication between tagged RSs always takes place via the BS. The master of the MAC protocol, which assigns the available network capacity upon demand among the various RSs, can be located in the BS. With respect to the flexible transfer required such a centralized control system is desirable since it can control the status of the overall system and it can easily vary the capacity of each RS according to the needs of each individual RS. In addition, the BS fulfils a gateway function to the ATM backbone net. In order to approach the ATM concept as much as possible the transmission takes place on a cell-by-cell basis. The fact that the transfer is asynchronous implies that an ATM cell generated by an RS must wait at the RS until the BS has authorized that RS to send a cell. Therefore, each RS must have a buffer to accomodate these waiting cells. The number of cells waiting in each RS buffer must be known to the central control in order to enable a good match of available network capacity with the capacity needs of the RSs. In general, the MAC protocol is defined by

- the way the central control is informed about the number of cells that are waiting in the buffer of each RS.
- the way the RSs are informed when a cell can be sent (i.e., the permission to access the medium).
- the way the available capacity is distributed among the RSs.

The main function of the MAC protocol in an ATM/FDD-based wireless LAN is to avoid collisions of the upstream traffic (i.e., the ATM cells originating from the different RSs). It should aim at

- *Efficiency*: The overhead introduced by the protocol should be low.
- *Performance*: The average delay and delay variation introduced by the MAC protocol should be kept within the bounds defined by the quality of service requirements.
- *Fairness*: One RS should not be subject to more access delay than another.

The MAC protocol presented in the following sections is similar to the MAC protocol proposed by Casals et. al. ([25]-[27]) for an ATM oriented passive optical network<sup>8</sup>. It uses a request/permit mechanism; each RS advertises its capacity requirements by means of *requests*, which are sent to the master of the protocol located in the BS. Using these requests, together with parameters agreed at call set-up, the MAC protocol allocates dynamically the available capacity for upstream traffic to the various RSs by means of a well defined *capacity allocation algorithm*. The RSs are then informed about the allocated bandwidth by means of *permits*. In what follows, we give a detailed description of the various components of the protocol.

### 7.4.2 Requests

Each RS is allowed to send two types of requests:

- *Requests coupled to the upstream ATM cells.* An upstream cell originating from a certain RS is preceded by a MAC information field (e.g., 8 bits long) containing the number of cells waiting in queue at that RS for (upstream) transmission.
- *Requests contained in dedicated request blocks.* When only requests coupled with upstream cells are used, a RS can only reveal its bandwidth needs when it is allowed to send an ATM cell. This could not only lead to a slow response to changing traffic situations but a RS may even never be able to declare its required transmission capacity. Therefore, the protocol is provided with a second type of request. The so called *request blocks* contain<sup>9</sup> requests originating from a number of consecutive RSs *not* coupled to upstream cells. A request block has the same length as an upstream cell. It is issued during an idle period, which allows the protocol to respond fast.

Fig. 7.7 shows the upstream information structure for ATM cells and request blocks.

---

<sup>8</sup> This MAC protocol has been defined in the RACE project R2024 Broadband Access Facilities, and is currently being implemented in the demonstrator system of this project.

<sup>9</sup> A Request block also contains a dedicated timeslot in which a new station can send a request for registration. A randomized retransmission strategy can be used to avoid persistent collisions and large retransmission delays. When the BS receives a request for registration it initiates a registration procedure and it appoints an address to the newly tagged RS.

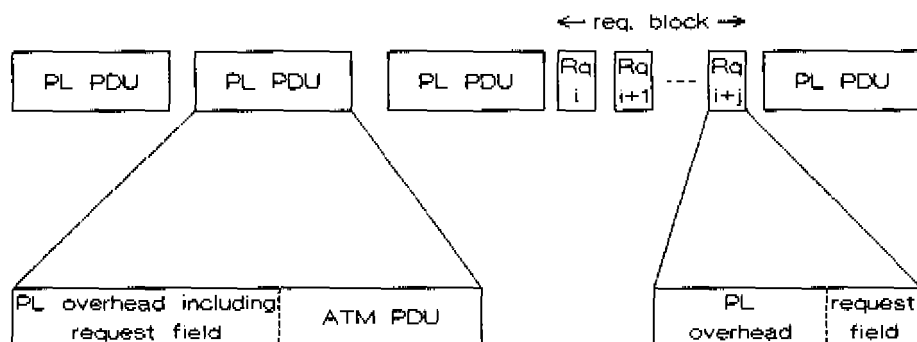


Fig. 7.7: Upstream information structure.

### 7.4.3 Permits

The MAC protocol allocates the available capacity among the RSs on the basis of the information contained in the Requests. The RSs are informed about the allocated capacity by means of *permits*. Such a permit authorizes the RS to send one cell. We distinguish two types of permits:

- *Permits for ATM cells.* When according to the allocation algorithm an RS is allowed to send a cell, then the BS issues a permit containing the address of this RS (e.g., 7 bits long) and adds it to a downstream ATM cell. Downstream traffic is broadcasted and hence; no coupling between this downstream cell and the permit is needed. An additional bit, namely the permit class bit CL, is added to indicate that the permit addresses an ATM cell (CL=1).
- *Permits for request blocks.* When, during a time slot, no permit is generated for an ATM cell, the BS issues a permit for a request block (permit class bit CL=0). In this case, the permit field contains the address of the RS that is the first to send a request in the request block.

Hence; the BS issues permits for request blocks whenever it has no permits for ATM cells to send. Therefore, the idle periods of the upstream traffic (i.e., no ATM cells are sent) are used for transmitting request blocks. In that way, the upstream capacity spared is exploited to increase the reaction speed of the protocol on changing traffic situations. Fig. 7.8 shows the downstream traffic structure, both for permits for ATM cells and permits for request blocks.

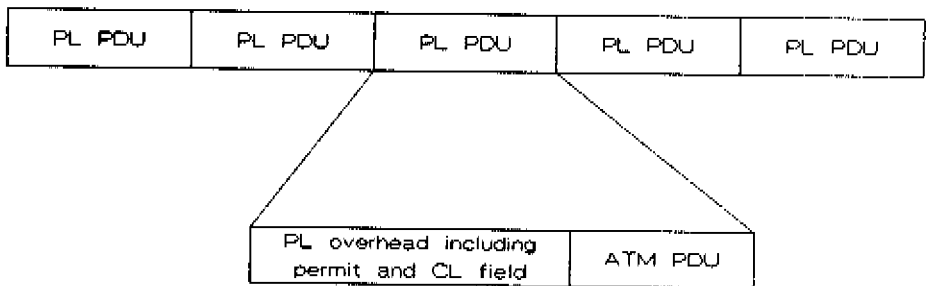


*Fig. 7.8: Downstream information structure.*

#### 7.4.4 Capacity allocation algorithm

In this section, we describe how the capacity is allocated among the RSs, or equivalently, how the permits are distributed. The main characteristics of the permit distribution algorithm are

- The peak bit rate per RS is enforced by spacing the cells.
- A global FIFO discipline is used (over all RSs) to minimize cell delay variation and to achieve fair access.
- The available buffer capacity in the RSs is used to store the cells that wait for transmission (distributed buffering).

In order not to exceed the maximum allowed peak bit rate the MAC protocol enforces a minimum time spacing between consecutive cells of a RS proportional to the inverse of the peak bit rate a RS is allowed to produce, as agreed upon at an initial negotiation procedure between RS and BS. The number of new cell arrivals is deduced from the requests and the necessary permits are assigned to the RS. These permits are then put into a FIFO queue together with permits for the other RSs with the constraint of minimum time spacing between two consecutive permits for the same RS. In this way, the actual queuing takes place in the RSs, while the central control in the BS maintains a permit FIFO queue, by which the transmission instants and the order in which the different RSs are emptied are governed.

In order to show how the permit distribution algorithm can be efficiently implemented we consider  $N$  RSs,  $RS_1, \dots, RS_N$ , each provided with a buffer. Let  $t_i$  be the number of slots between two consecutive cells originating from  $RS_i$  under peak bit

rate conditions.  $RS_i$  is said to be *ready to send a cell*, whenever a cell is present in the buffer of  $RS_i$  and the number of time slots since the last transmission of  $RS_i$  is at least  $t_i$ .

The central controller in the BS maintains a global permit FIFO queue and two counters for each RS:

- The *global permit FIFO queue* contains permits for RSs corresponding to cells which are ready to send. A permit for  $RS_i$  is put in the global permit FIFO queue this RS has a cell ready to send.
- Two counters per RS are maintained, a *countdown counter* and a *request counter*. For  $RS_i$  we have that
  - the countdown counter  $CNTDOWN\_CNTR(i)$  is given the value  $t_i$  at the moment the permit for  $RS_i$  is put in the permit FIFO queue. Its value is decreased by 1, at each time slot of the outgoing line. Counting down stops as soon as  $CNTDOWN\_CNTR(i) \leq 0$ .
  - the request counter  $REQ\_CNTR(i)$  is increased each time a request comes in by the number of arrivals since the last request. It is decreased by 1 whenever a permit for  $RS_i$  is put in the global permit FIFO queue.

When the conditions  $CNTDOWN\_CNTR(i) \leq 0$  and  $REQ\_CNTR(i) > 0$  are both satisfied then

- 1) a permit for  $RS_i$  is put into the global permit FIFO queue,
- 2)  $REQ\_CNTR(i) := REQ\_CNTR(i) - 1$ .

When this permit comes at the head of the permit FIFO queue, it is sent to  $RS_i$  and the first cell in the buffer of  $RS_i$  is transmitted.

If at the end of the countdown process (i.e., as soon as  $CNTDOWN\_CNTR(i) \leq 0$ ),  $REQ\_CNTR(i) = 0$ , then the countdown process stops, and when the next request for this RS arrives, besides increasing  $REQ\_CNTR(i)$ , the countdown process of  $RS_i$  will start again. This makes the two above conditions true, so that a permit is put immediately in the global FIFO queue.

Fig. 7.9 shows an example to illustrate the operation of the permit distribution algorithm.



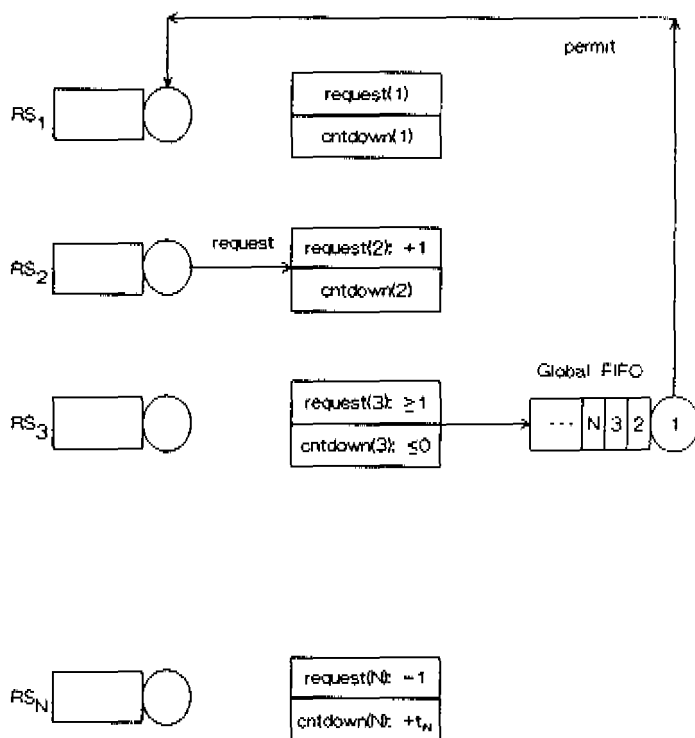


Fig. 7.9: Operation of the MAC protocol.

In this example,

- The BS issues a permit for  $RS_1$ .
- A request, originating from  $RS_2$ , is sent to the BS resulting in an increase of  $REQ\_CNTR(2)$ .
- The conditions  $REQ\_CNTR(3) \neq 0$  and  $CNTDOWN\_CNTR(3) \leq 0$  are satisfied, hence; a permit for  $RS_3$  will be put in the global FIFO queue.
- A permit for  $RS_N$  has been put in the global FIFO queue,  $REQ\_CNTR(N)$  is decreased by 1 and  $CNTDOWN\_CNTR(N)$  is increased by  $t_N$ .

#### 7.4.5 Robustness of the protocol

In order to operate correctly, the RSs must declare their capacity requirement through the number of newly arrived cells since the last request. This value is added to *REQ\_CNTR*. However, the loss of a request may lead to the situation that cells remain in the RS buffer forever. In order to avoid this situation, the request contains the queue length of the RS. The MAC controller must be able to compute the number of new arrivals from this queue length. For this, it must maintain the number of permits that have been generated for which the upstream cell has not been received yet for the reason that the permit is still waiting in the global FIFO to be transmitted. From this number and the new queue length, the BS can compute the number of newly arrived cells since the last request.

#### 7.4.6 Initiation of equalizer tap coefficients

The BS receives consecutive cells from different RSs. Hence; the tap coefficients of the BS channel equalizer must be adapted for each received cell. In order to aid this cell-by-cell adaption process the equalizer can be initiated with the most actual tap coefficients which for each RS-to-BS channel are contained in a look-up table. This is possible because of the slow-fading conditions assumed (see Section 2.3.2) and because the BS receives only cells from RSs that are authorized by the BS itself so that at the BS it can be determined, on forehand, via which RS-to-BS channel a cell comes in. The tap coefficient values that result at the end of the adaption process (by means of the training sequence contained in the physical layer preamble) are used to update to values contained in the equalizer coefficient look-up table.

### 7.5 Summary and conclusions

In this chapter, we discussed how information transfer can be achieved in broadband indoor wireless LANs on the basis of the Asynchronous Transfer Mode (ATM).

In order to identify the most suitable method for duplexing the upstream and downstream ATM cells we provided an assessment of the relative advantages and disadvantages of two commonly applied duplex methods, viz., Time Division Duplex (TDD) and Frequency Division Duplex (FDD). As a result of this, it occurs that FDD is the most suitable option to accommodate the transmission at high bit rates as required.

In order to examine the need to add error control measures to standard ATM, for applying it in mm-wave indoor wireless LANs, we considered a mm-wave FDD/ATM-based indoor wireless LAN in which the base station (BS) as well as the remote stations (RSs) are equipped with biconical-horn antennas as described in Section 3.3. From this examination it occurs that, for cell loss requirements imposed by typical broadband services, the error control capability accommodated by ATM, as applied in fibre-based networks, is insufficient for the wireless LAN under consideration; for the achievement of several tens of Mbit/s (per carrier), as might be required for broadband services such as high volume transfer and high resolution image, some form of forward error correction and/or retransmission must be added. For this purpose, the BCH codes form an attractive group of error correcting codes; the BCH (511,502) code has the potential to correct 1 bit error in a received ATM cell. Alternatively, the BCH(511,493) code can correct 2 random errors in a cell. A considerable reduction of cell loss can also be achieved by applying a simple retransmission scheme according to which a cell, in which uncorrectable errors are detected, is retransmitted once and only once. BCH codes can also be used for the detection of errors. This makes them especially suitable for hybrid error correction/retransmission schemes. It occurs that these error control measures are only sufficiently effective in case dual diversity is applied. The most suitable place to implement these measures is in the physical layer.

A multi-access protocol for wireless access is described. This protocol uses a request/permit mechanism to control the access to the shared medium; each RS declares its required capacity by sending requests to the master of the protocol located in the BS. The available capacity is allocated by means of a strategy that approximates a global FIFO queue in such way that the peak bit rate is enforced. The RSs are informed about the capacity obtained by means of permits. Such a permit authorizes the RS to send a cell. The MAC protocol is thus cell based, meaning that an issued permit initiates the transmission of a single cell.

---

**References in Chapter 7**

- [1] ITU, Telecomm. Standardization Sector, SG 13, Rec. I.113, "Vocabulary of Terms for Broadband Aspects and Aspects of ISDN", Geneva, Jan. 1993.
- [2] J.P. Coudreuse, "Les reseaux temporel asynchrones: du transfert de données à l' image animée", *L'echo des recherches*, No 112, pp. 33-40, 1983.
- [3] J.S. Turner, L.F. Wyatt, "A packet network architecture for integrated services", *Proc. of Globecom '83*, pp. 45-50, Nov. 1983.
- [4] CCITT Recommendation I.121, "broadband aspects of ISDN, Fascile III.7, Melbourne, 1988.
- [5] M. de Prycker, "Asynchronous transfer mode: solution for broadband ISDN", Ellis Horwood Limited, 1994, 2nd Edition.
- [6] R. Sonnemans, "ATM in an indoor radio network; a feasibility study", M.Sc.E.E. Thesis, Telecommunications Division, EUT, Aug. 1990.
- [7] R.B. Maessen, "The use of ATM in an inhouse radio network", M.Sc.E.E. Thesis, Telecommunications Division, EUT, June 1992.
- [8] CCITT Recommendation I.361, "B-ISDN ATM Layer Specification", Geneva, 1991.
- [9] CCITT Recommendation I.362, "B-ISDN ATM Adaption Layer (AAL) Functional Description", Geneva, 1992.
- [10] CCITT Recommendation I.321, "B-ISDN ATM Protocol Reference model and its Application", Geneva, 1991.
- [11] Standard IEEE 802.6, "Distributed Queue Dual Bus (DQDB) subnetwork of a Metropolitan Area Network (MAN)", IEEE, New York, 1990.
- [12] R.M. Falconer, J.L. Adams, "Orwell: a protocol for an integrated services local network", *British Telecom Techn. J.* Vol. 3, No. 4, 1985.

- [13] IEEE Std. 802.11, "Wireless-Access Method and Physical Layer Specifications", IEEE P802.11 Committee, 1992.
- [14] W.C. Jakes, "Microwave Mobile Communications", John Wiley and Sons, New York, 1978.
- [15] J.H. Winters, "Switched Diversity with Feedback for DPSK Mobile Radio Systems", IEEE Trans. on Veh. Technol., Vol. VT-32, pp. 134-150, 1983.
- [16] N. Seshadri and J.H. Winters, "Two Signaling Schemes for Improving the error performance of Frequency-Division-Duplex (FDD) Transmission Systems using Transmitter Antenna Diversity", Proc. of the IEEE Veh. Technol. Conf., Secaucus, New Jersey, pp. 508-511, May 1993,.
- [17] A. Wittneben, "Base Station Modulation Diversity for Digital SIMULCAST", Proc. of the IEEE VEH. Technol. Conf., St. Louis, Missouri, pp. 848-853, May 1991.
- [18] A. Hiroike, F. Adachi and N. Nakajima, "Combined Effects of Phase Sweeping Transmitter Diversity and Channel Coding", IEEE Trans. on Veh. Technol., Vol. VT-41, pp. 170-176, May 1992.
- [19] V. Weerackody, "Characteristics of a Simulated Fast Fading Indoor Radio Channel", Proc. of the IEEE Veh. Technol. Conf., Secaucus, New Jersey, pp. 231-235, May 1993.
- [20] D. Raychaudhuri, N. Wilson, "Multimedia Personal Communication Networks (PCN): System Design Issues", Workshop Record, Third WINLAB Workshop on Third Generation Wireless Information Networks, East Brunswick, New Jersey, 28-29, April 1992.
- [21] T. Kwok, "Communications requirements of Multimedia Applications: A preliminary study", ICWC '92, Vancouver, BC, June 1992.
- [22] J.B. Lyles, D.C. Swinehart, "The Emerging Gigabit Environment and the Role of Local ATM", IEEE Communications Magazine, pp. 52-58, 1992.
- [23] S. Lin, D.J. Costello, "Error Control Coding: Fundamentals and Applications", Prentice-Hall, Inc. Englewood Cliffs, New Jersey, 1983.

- 
- [24] W.W. Peterson, D.T. Brown, "Cyclic Codes for Error Detection", Proc. of the IRE, Vol. 49, No. 1, pp. 228-235, 1961.
  - [25] O. Casals, J. Garcia and C. Blondia, "A medium Access Control Protocol for an ATM Access Network", Proc. of 5th Int. Conf. on Data Comm. Syst. and their Performance, Raleigh, North Carolina (USA), Oct. 1993.
  - [26] T. Apel, C. Blondia, O. Casals, J. Garcia and K. Uhde, "Implementation and Performance Analysis of a Medium Access Control Protocol for an ATM Network", to appear in Proc. of Architecture and Protocols for High speed networks, Dachstuhl Seminar, Kluwer Academic, 1993.
  - [27] C. Blondia, O. Casals and J. Garcia, "Performance Analysis of a MAC Protocol for a Broadband Network Access Facility", Symp. on Teletraff. Anal. of ATM Syst. '93, Eindhoven 1993.

## CHAPTER 8

### SUMMARY AND CONCLUSIONS

The transmission capacity required for broadband wireless LANs can only be accommodated in the millimetre-wave frequency band from about 25 GHz to 65 GHz. The mm-wave bands are of special interest for indoor applications because of the possibility of frequency reuse between neighbouring rooms. The severe attenuation of most inner walls, at these frequencies, causes that the relationship between cell boundaries and the physical layout of the indoor environment to be more easily determined, facilitating indoor cell planning.

In *Chapter 2*, the propagation characteristics expected to occur in a typical, thus reflective, indoor environment are treated, analytically. It is shown to be plausible that the mm-wave indoor radio channel may be considered as practically constant over many symbol periods for symbol rates of interest ( $> 1$  Msymb/s). It is also shown that the mm-wave indoor radio channel can be considered as a discrete multipath channel that might be highly frequency selective for the high symbol rates of interest (tens of Msymb/s). It is indicated that considerable performance gain can be achieved by exploiting the inherent diversity associated with the frequency selective nature of the channel.

In order to assess important parameters like feasible diversity gain, as required for the development, design and network planning of wireless LANs, it is essential to

provide accurate information about the characteristics of mm-wave indoor radio channels. Since we consider a wireless LAN in which the transceivers are fixed during operation, we are primarily interested in the transmission performance dependence on the spatial positions of the transceivers involved.

*Chapter 3* treats the channel measurements performed to obtain a set of impulse responses that allows for statistically significant conclusions. The frequency-stepping technique applied is described and discussed. It is shown that the aliasing-free range in the time domain of 400 ns is sufficient for reliable channel characterization. The antennas applied in the measurement setup received considerable attention since their radiation patterns have a great impact on the channel's characteristics. Furthermore, it is shown that biconical-horn antennas can be dimensioned in such way that the level of received power does not depend strongly on the separation distance between the transmit and receive antenna. With these antennas typical rms delay spread values range between 15 and 45 ns for small rooms whereas they are between 30 to 70 ns for the larger ones. Obstruction of the direct path causes only slight changes in rms delay spread.

In *Chapter 4*, a statistical model is developed for the complex equivalent-lowpass impulse response of the indoor mm-wave radio channel. The objective is to provide a compact summary of the overall channel characteristics for an environment or class of environment types. The resulting statistical model is based on the measurement data obtained as well as physical reasoning. The relation between the model parameters and environment properties (wall dimensions and return loss figures) is described by simple first order approximations. This makes the model readily applicable to a variety of other comparable indoor environments.

The assumption that the mm-wave indoor radio channel may be regarded as a discrete multipath channel, as posed in Chapter 2 and confirmed by the measurement results, implies that the channel response can be described by an ensemble of "rays" each characterized by an amplitude, phase and excess delay value.

The ray occurrence in an impulse response is modelled as a discrete uncorrelated scattering process. The probability density functions are very similar for all subsets of measurement data obtained in the various indoor environments. In all environments it was found that the ray amplitude at a certain excess delay fits a Rayleigh distribution. The normalization parameter of this distribution can be modelled as a function of excess delay by a constant level part up to 60 ns followed by an linear decrease (dB value). The rays arrive with independent uniformly distributed phases. The ray arrival process is modelled as a Poisson process with a mean interarrival time per measurement subset ranging from 1 to 3 ns. Dominance of



the direct LOS-ray is modelled by taking the level part, which occurs ahead of the response, 0 to 13 dB below the level of the direct LOS ray. OBS situations are modelled by completely omitting the direct LOS ray.

In *Chapter 5*, a deterministic model of mm-wave indoor radio channels is developed which accepts a detailed description of the indoor environment. As such, it complements the statistical model. As part of the deterministic modelling, the significance of diffraction and scatter effects is examined. Typically, the diffracted power does not yield a significant contribution to the total power at 60 GHz. The surface roughness of building materials that can be typically found in indoor environments is such that the resulting scattering (diffuse reflection) does not contribute significantly to the total received power, either. The dominant contributions are expected to come from specular reflections. Therefore, we propose a channel model based on Geometrical Optics (GO) and we presented the mathematical fundamentals for its implementation.

Results of a GO-based ray-tracing simulation programme are compared with measurement results. The indoor environments, defined in the simulation software are stylized versions of the corresponding real environments in which the measurements took place. Although the idealized versions only include the superstructure (walls, floor and ceiling) and lack details as tables and cabinets, the simulation results are in good agreement with the measurement results. This indicates that the results are mainly determined by the superstructure of the indoor environment.

After it was found that the GO-model yields accurate results, we performed computer simulations in order to gain a more detailed insight into the influence of environment and antenna characteristics on the most interesting channel parameters. For this, we defined configurations with sectorial and/or biconical-horn antennas in the simulation software. A configuration with sectorial horns at both ends, having the highest directivity considered (25.1 dBi), yields the lowest rms delay spread and highest received power when compared with other examined configurations, provided that there is no obstruction of the LOS path and provided that the antenna beams are exactly pointing towards each other. A configuration with biconical horns at both ends yields results, with respect to received power and rms delay spread that are highly insensitive to LOS blocking. In addition, the uniformity in received power for different positions of the remote station is observed. This configuration also yields the lowest spread in rms delay spread values.

*Chapter 6* contains a performance evaluation of data transmission via mm-wave indoor radio channels. This evaluation is directly based on the measurement results obtained. The application of a Decision Feedback Equalization (DFE) with 3 forward

taps yields a feasible bit rate of some tens of Mbit/s. It is shown that the number of forward taps has a profound influence on the maximum feasible bit rate; an increase from 3 to 7 forward taps results in an average improvement of about a factor 5. Obstruction of the direct LOS path does not significantly deteriorate the performance when biconical-horn antennas are applied, as expected. The application of dual antenna diversity, in addition to DFE, enables a  $3 \cdot 10^4$  times lower probability of bit error for the same bit rate.

In *Chapter 7*, we examined in which way information transfer can be achieved in broadband wireless LANs on the basis of the Asynchronous Transfer Mode (ATM). Frequency Division Duplex was identified as the most suitable method for duplexing the ATM upstream and downstream traffic. Dual antenna diversity as well as additional error control should be implemented in order to meet the stringent ATM-cell loss rate requirements for typical broadband services. It was indicated that the BCH(511,502) and BCH(511,493) codes are attractive candidates for error correction/detection. The most suitable place to implement these measures is in the physical layer.

Finally, a multi-access protocol for ATM-based transmission in wireless LANs is proposed. This protocol uses a request/permit mechanism to control the access to the shared medium. The available capacity is allocated by means of a strategy which approximates a global FIFO queue in such way that, for each tagged remote station, the peak bit rate is enforced.

In conclusion, it is believed that a dedicated wireless access of 155 Mbit/s for each user, as can be afforded by fibre-based networks, would be an unrealistic design objective. It is estimated, on the other hand, that sufficiently reliable transmission at a rate in the order of some tens of Mbit/s per carrier (e.g., 34 Mbit/s standard rate) is feasible. A way to achieve this is the combined application of (low complexity) Decision Feedback Equalization, two-fold antenna diversity with biconical-horn antennas and additional error control using BCH codes. Hence; a system that uses, e.g., 5 carriers can afford an aggregate network capacity that equals the standard rate of 155 Mbit/s. Allocation of this capacity can be done in a flexible way according to the principles of ATM and by application of a suitable multi-access protocol such as the one proposed in this thesis.

---

**List of acronyms**

AAL	ATM Adaptation Layer
ACTS	Advanced Communications Technologies and Services
ARQ	Automatic Request for Retransmission
ATM	Asynchronous Transfer Mode
AWGN	Additive White Gaussian Noise
BCH	Bose, Chaudhuri and Hocquenghem
B-ISDN	Broadband Integrated Services Digital Network
B-NT	Broadband Network Termination
BS	Base Station
B-TA	Broadband Terminal Adaptor
CBR	Continuous Bit Rate
CDF	Cumulative Distribution Function
CDMA	Code Division Multiple Access
CLAN	Cableless Local Area Network
COST	European Cooperation in the field of Scientific and Technical research
CRC	Cyclic Redundancy Check
DFE	Decision Feedback Equalization
DPSK	Differential Phase Shift Keying
DRIVE	Dedicated Road Infra-structure for Vehicle safety in Europe
EFTPOS	Electronic Funds Transfer at Point of Sale
EL	Early Late
EM	Electromagnetic
ERC	European Radiocommunication Committee
ETSI	European Telecommunications Standards Institute
FDD	Frequency Division Duplex
FEC	Forward Error Correction
FIFO	First In First Out
FK	Fast Kalman
FSK	Frequency Shift Keying
GAL	Gradient Adaptive Lattice
GMSK	Gaussian Minimum Shift Keying
GO	Geometrical Optics
GSD	Gradient Steepest Descent
GSM	Global System for Mobile (communications)
GTD	Geometrical Theory of Diffraction
HDTV	High Definition Television
HF	High Frequency

---

IF	Intermediate Frequency
IFT	Inverse Fourier Transfer
INIRC	International Non-Ionizing Radiation Committee
IRPA	International Radiation Protection Association
ISDN	Integrated Services Digital Network
ISI	Intersymbol Interference
ITU	International Telecommunication Union
LAN	Local Area Network
LE	Linear Equalizer
LMS	Least Mean Square
LO	Local Oscillator
LOS	Line-Of-Sight
LS	Least Squares
LSL	Least Squares Lattice
MA	Medium Adaptor
MAC	Multiple-Access Control
MLSE	Maximum Length Sequence Estimation
M <sup>3</sup> IC	Millimetre-wave Monolithic Integrated Circuit
M <sup>3</sup> VDS	Millimetre-wave Multichannel Multipoint Video Distribution Service
MMSE	Minimum Mean Square Error
MPE	Maximum Possible Exposure
MPEG	Moving Pictures Expert Group
MPM	Multipath Margin
MSE	Mean Square Error
NRP	Normalized Received Power
NT	Network Termination
OBS	Obstructed Line-Of-Sight
OSI	Open Systems Interconnection
PDF	Probability Density Function
PDP	Power Delay Profile
PDU	Packet Data Unit
PL	Physical Layer
PMD	Physical-medium-dependent
PO	Physical Optics
PROSIM	PROPagation SIMmulation
PSK	Phase Shift Keying
QPSK	Quaternary Phase Shift Keying
RACE	Research into Advanced Communications Europe
RDS	Rms Delay Spread

---

RF	Radio Frequency
RLAN	Radio Local Area Network
RLS	Recursive Least Squares
RS	Remote Station
SG	Stochastic Gradient
SNR	Signal-to-Noise Ratio
SRK	Square-Root Kalman
SWR	Standing Wave Ratio
TA	Terminal Adaptor
TC	Transmission Convergence
TDM	Time Division Multiplex
TDMA	Time Division Multiple Access
TE	Terminal Equipment
UAT	Uniform Asymptotic Theory
UHF	Ultra High Frequency
US	Uncorrelated Scattering
UTD	Uniform Theory of Diffraction
VBR	Variable Bit Rate
VC	Virtual Channel
VCI	Virtual Channel Identifier
VHSIC	Very High Speed Integrated Circuit
VP	Virtual Path
VPI	Virtual Path Identifier
WLAN	Wireless Local Area Network

## Korte samenvatting

Het onderwerp van dit proefschrift is de haalbaarheid van draadloze lokale netwerken voor breedbandige toepassingen zoals voorzien voor Breedband-ISDN. De behandeling van dit onderwerp is gebaseerd op de aanname dat transmissie plaats vindt over millimetergolfradiokanalen binnen een inhuisongeving.

Een methode wordt besproken voor het meten van de breedbandige karakteristieken van het beschouwde kanaaltipe. Vervolgens worden de meetresultaten gepresenteerd welke zijn verkregen volgens deze methode. Tevens wordt een deterministisch kanaalmodel ontwikkeld op basis van Geometrische Optica (GO). De toepasbaarheid, beperkingen en nauwkeurigheid van dit GO-model worden besproken. Resultaten van op dit model gebaseerde kanaalsimulaties worden gepresenteerd. Deze resultaten geven een indicatie van de invloed van omgeving en antennestralingspatronen op de kanaalkarakteristieken.

De maximaal haalbare bitsnelheid wordt geëvalueerd bij transmissie over millimetergolfradiokanalen op basis van de gemeten kanaalkarakteristieken. Deze evaluatie omvat ondermeer het verbeteringseffect van kanaalegalisatie afhankelijk van het aantal vertragingselementen van de toegepaste kanaalegalisator. Tevens wordt de invloed van de ruis, antenne-"diversity" en antennestralingspatroon beschouwd.

Ten slotte wordt beschreven hoe op eenvoudige en flexibele wijze transmissie van informatie kan plaatsvinden in breedbandige draadloze lokale netwerken op basis van de Asynchronous Transfer Mode. In deze context wordt een protocol voor botsingsvrije meervoudige toegang voorgesteld.

## Epilogue

After the finishing of this Ph.D. work, the research in the field of broadband wireless LANs in our group, i.e., the Telecommunications Division of the EUT, did not stop. The activities continued in the framework of the ACTS project MEDIAN (Wireless Broadband Customer Premises Network/Local Area Network for Professional and Residential Multimedia Applications) initiated and managed by IMST<sup>1</sup>. One of the objectives of this project is to evaluate and optimize the performance of a wireless LAN, suitable for multimedia applications, by means of system simulation. Furthermore, a pilot system should be implemented for examination and demonstration of the system concept. This system will consist of one base station and two (wireless) remote stations. The transmission of information between the remote stations will take place via the base station according to the principles of ATM. Additionally, the base station will be connected to the fixed ATM network in order to demonstrate interoperability with the environment. The system will be tested in various user environments. Characteristics that distinguish the MEDIAN concept from conventional wireless LANs are

- 1) the unprecedented aggregate user information transport capacity (totally up to 155 Mbit/s),
- 2) the applied frequency band (62-63 GHz),
- 3) the flexibility in the assignment of network capacity, (this will be achieved by application of ATM),
- 4) the internetworking capability with the fixed ATM network.

The main contribution of our group to the project concerns the definition of interworking functions between the wireless LAN and the fixed ATM network. In this context, items will be addressed as resource allocation, addressing, routing, priority mechanisms etc. The problem of interworking also addresses items as channel coding in view of the objective to match the degree of reliability of the wireless LAN to that of the fixed network. Hence; our group will contribute to the design of the system architecture and to the specification of system parameters. Analyses and system simulations of parts of the transmission system, and of the whole transmission system (including the millimetre-wave channel), are dealt with. The consortium partners involved with the system simulation work agreed to take the statistical channel model presented in this dissertation as a starting point. The influence of the antennas on the channel characteristics, and therefore on the entire system, has been identified as an

---

<sup>1</sup> Institut fuer Mobil- und Satellitenfunktechnik, Kamp Lintfort, Germany

important item to take into consideration. Initially, the antennas described in this dissertation will be applied. In addition, we will design an extended set of antennas with different radiation patterns in order to demonstrate the potentials and limitations of the various options. Finally, we will participate in integration and testing of the pilot system.



---

## List of scientific publications

### Chapter 1

- [1.1] P.F.M. Smulders, "Feasibility considerations of broadband indoor networks", Proc. of the Int. Symp. on Subscriber Loops and Services '91, Amsterdam, pp. 76-80, April, 1991.

### Chapter 3

- [3.1] P.F.M. Smulders and A.G. Wagemans, "Mm-wave biconical horn antenna for near uniform coverage in indoor pico-cells", *Electronic Letters*, Vol 28, pp. 679-681, 1992.
- [3.2] P.F.M. Smulders and A.G. Wagemans, "Wideband indoor radio propagation measurements at 58 GHz", *IEEE, Electronic Letters*, Vol. 28, No. 13, pp. 1270-1271, 1992.
- [3.3] P.F.M. Smulders and A.G. Wagemans, "Wide-band Measurements of 58 GHz Indoor Radio Channels", *URSI, Proc. 3th Int. Symp. on Signals, Systems and Electronics*, Paris, pp. 692-696, Sept. 1992.
- [3.4] P.F.M. Smulders and A.G. Wagemans, "Wideband measurements of mm-wave indoor radio channels", *Proc. of the IEEE 3th Int. Symp. on Personal, Indoor and Mobile Radio Commun.*, Boston, pp. 329-333, Oct 1992.
- [3.5] P.F.M. Smulders and A.G. Wagemans, "Frequency Domain Sounding on mm-wave Indoor Radio Channels", *Int. Conf. on Universal, Person. Commun. '93*, Ottawa, pp. 636-640, Oct. 1993.
- [3.6] P.F.M. Smulders and J. Lähteenmäki, "Measurements of indoor radio channels at 60 GHz", *Joint COST 231/235 workshop on Mobile Communications*, Prague, April 1994.
- [3.7] P.F.M. Smulders and A.G. Wagemans, "Biconical Horn Antennas for Uniform Coverage in Indoor Areas at Mm-Wave Frequencies", *IEEE Trans. Veh. Technol.*, Vol. VT-43, No. 4, pp. 897-901, 1994.

- [3.8] P.F.M. Smulders and A.G. Wagemans, "Frequency-Domain Measurement of the Millimeter Wave Indoor Radio Channel", *IEEE Trans. on Instrumentation and Measurement*, Vol. 44, No. 6, 1995.

#### Chapter 4

- [4.1] P.F.M. Smulders and A.G. Wagemans, "A Statistical Model for the Mm-wave Indoor Radio Channel", 3th Int. Symp. on Personal, Indoor and Mobile Radio Comm., Boston, pp. 303-307, Oct. 1992.

#### Chapter 5

- [5.1] P.F.M. Smulders, "Geometrical optics model for millimetre-wave indoor radio propagation", *Electronic Letters*, Vol. 29, pp. 1174-1176, 1993.
- [5.2] P.F.M. Smulders, "Deterministic Modeling of mm-Wave Indoor Radio Propagation", *Proc. of IEEE First Symp. on Commun. and Veh. Technol. in the Benelux*, Delft, pp. 3.1-1 - 3.1-7, Oct. 1993.
- [5.3] P.F.M. Smulders and G.J.A.P. Vervuurt, "Influence of Antenna Radiation Patterns on Mm-wave Indoor Radio Channels", *Int. Conf. on Universal, Person. Commun. '93*, Ottawa, pp. 631-635, Oct. 1993.
- [5.4] R. Overduin, P.F.M. Smulders, "Feasibility of Broadband Inroom Radio Communications at 60 GHz", *Proc. of the IEEE 5th Int. Symp. on Personal, Indoor and Mobile Radio Comm.*, The Hague, pp. 119-126, Sept. 1994.
- [5.5] P.F.M. Smulders and J.J.G. Fernandes "Wide-band Simulations and Measurements of Mm-Wave Indoor Radio Channels", *Proc. of the IEEE 5th Int. Symp. on Personal, Indoor and Mobile Radio Comm.*, The Hague, pp. 501-504, Sept. 1994.
- [5.6] J.J.G. Fernandes, P.F.M. Smulders and J.C. Neves, "Simulation results on mm-wave indoor radio channel modeling and comparison with measurements", *Proc. of the IEEE 2nd Symp. on Communications and Vehicular Technology in the Benelux*, Louvain-la-Neuve, pp. 89-94, Nov. 1994.
- [5.7] P.F.M. Smulders, "Deterministic Modelling of Indoor Radio Propagation at 40-60 GHz", *Wireless Personal Communications*, Vol. 1, No. 2, pp. 127-135, 1995.

- [5.8] J.J.G. Fernandes, J.C. Neves and P.F.M. Smulders, "Mm-Wave Indoor Radio Channel Modelling Vs. Measurements", *Wireless Personal Communications*, Vol. 1, No. 3, pp. 211-219, 1995.

### Chapter 6

- [6.1] P.F.M. Smulders and H.T. Müskens, "Bit rate performance of millimetre-wave indoor radio systems", *Electronic Letters*, Vol. 28, No 23, pp. 2152-2153, 1992.
- [6.2] P.F.M. Smulders and H.T. Müskens, "Performance of Decision Feedback Equalization in mm-Wave Indoor Radio Systems", *Proc. of the IEEE 2nd Int. Symp. on Univ. Personal Commun.*, Ottawa, pp. 890-893, Oct. 1993.

### Chapter 7

- [7.1] P.F.M. Smulders, "Error Control in ATM-Based Indoor Radio LANs", *Proc. of the IEEE 5th Int. Symp. on Personal, Indoor and Mobile Radio Comm.*, The Hague, pp. 237-241, Sept. 1994.
- [7.2] P.F.M. Smulders and C. Blondia, "Application of the Asynchronous Transfer Mode in Indoor Radio Networks", *Proc. of the IEEE/ICCC Regional Meeting on Wireless Computer Networks*, The Hague, pp. 839-843, Sept. 1994.

### Chapter 8

- [8.1] P.F.M. Smulders, "Characteristics of Millimetre Wave Indoor Radio Channels", *Tijdschrift van het Nederlands Elektronica- en Radiogenootschap*, deel 60, No. 1, pp. 25-29, 1995.

---

## Account of scientific results

Several students made major contributions to this work as part of their M.Sc. graduation work. These contributions are listed below.

### Chapter 3

The measurements, reported in Section 3.2, have been carried out by the author in cooperation with A.G. Wagemans. Mr. Wagemans also measured the radiation properties of the antennas in the anechoic room at the Electromagnetics Division under the guidance of T. Knoben. Furthermore, he performed the numerical elaboration of the raw measurement data which led to Fig. 3.10 and to the results with respect to normalized received power and rms delay spread presented in Section 3.6.

### Chapter 4

The data reduction process, as described in Section 4.2, is proposed and carried out by A.G. Wagemans. He also contributed to the modelling of ray phases, ray amplitudes and ray interarrival times by fitting the measurement data and applying the Chi-Square test. The distribution functions and probability density functions shown in Sections 4.3 to 4.5 are the result of his contribution.

### Chapter 5

A simulation package for geometric ray tracing has been written by M. Melters in PASCAL. This first version, which has been of great value for this Ph.D work, was upgraded by E. Ruis. Mr. Ruis added some convenient options and converted the PASCAL program to a C++ version, which resulted in a considerable gain in computing time. Furthermore, he builded a beautiful Graphics User Interface around the engine. This resulted in the simulation package called PROSIM (PROPagation SIMulation) which is extensively used by various institutes.

The implementation of the antenna directivity functions in software (Section 5.4) has been performed by G. Vervuurt. He also generated the simulation results, with respect to normalized received power and rms delay spread, presented in Section 5.5.

**Chapter 6**

The numerical elaboration of Eq. (6.10) to (6.13) as well as (6.22) to (6.24) has been performed by H. Müskens. Mr. Müskens calculated the results, with respect to (average) probability of error and (normalized) maximum bit rate, presented in Section 6.3 and 6.5.

## Acknowledgements

First of all, I would like to express my gratitude to my first promotor, Gert Brussaard, for his continuous support in many different ways. I would like to thank him for his carefully reading drafts of this thesis and for all the stimulating discussions. Furthermore, I would like to thank my second promotor Hans de Stigter for initiating this Ph.D. research. Thanks to his foresight with respect to the relevance of this topic the output of the research may contribute to an important development in telecommunications, i.e., the advent of broadband wireless LANs. I also want to thank him for triggering my mind with all kind of useful suggestions and critical remarks. Next I am grateful to Wim van Erten and Ramjee Prasad for the proofreading of earlier versions of this thesis.

I am indebted to all my colleagues who contributed a great deal of insight and to the numerous students who contributed to the results of this Ph.D. work and to the nice atmosphere in the group.

Furthermore, I wish to thank STW (Foundation of Technical Sciences) for their financial support which made it possible for the Telecommunications Division to purchase the expensive measurement equipment.

I also want to thank my beloved wife Gerdi and my dear children Tessa and Remco for being so patient when yet another weekend was used for working on my dissertation.

The opportunity I got from my parents to do the study of my own choice, has finally been the main condition for the finishing of this thesis. This is more than enough reason to dedicate this thesis also to them.

## Curriculum vitae

Peter Smulders was born in Eindhoven, The Netherlands, on May 23, 1957. He graduated from Eindhoven University of Technology in 1985. In September 1985 he joined the Propagation and Electromagnetic Compatibility Department of the Research Neher Laboratories of the Netherlands PTT. While he was with PTT he was doing research in the field of compromising emanation from civil data processing equipment.

In June 1988 he moved to the Eindhoven University of Technology as a staff member of the Telecommunications Division. Next to his lecturing duties he performed research in the field of mobile communication systems and broadband wireless LANs. This research work addressed propagation as well as system and implementation aspects. The work on this thesis started in 1990. He is currently involved in the ACTS project MEDIAN -Wireless Broadband CPN/WLAN for Professional and Residential Multimedia Applications.

He is a member of working group 3 of the European COST 231 project ("Evolution of land mobile radio -including personal- Communications). He is co-founder and present board member of the James Clerk Maxwell Foundation. He is a member of the Executive Committee of the IEEE Vehicular Technology/Communications Society Joint Chapter, Benelux Section.



**STELLINGEN**

**BEHORENDE BIJ HET PROEFSCHRIFT**

**BROADBAND WIRELESS LANS:**

**A FEASIBILITY STUDY**

**P.F.M. SMULDERS**

**EINDHOVEN, 4 DECEMBER 1995**



- 1) J.E. Mitzlaff suggereert ten onrechte, dat het gebruik van antennes met een hoge antennewinst automatisch leidt tot een lage kanaaldispersie.
  - J.E. Mitzlaff, "Radio Propagation an Anti-Multipath Techniques in the WIN Environment", IEEE Vetw. Mag., pp. 21-26, 1991.
  - Dit proefschrift par. 3.6.
  - Dit proefschrift par. 5.6.
  
- 2) P. Yegani en C.D. McGillem veronderstellen in hun beschouwing over het aankomst process van echo's ten onrechte dat er geen onderlinge overlapping van echo's optreedt. Dit leidt tot een Weibull verdeling van het aankomst process terwijl een Poisson verdeling realistischer en eenvoudiger te hanteren is.
  - P. Yegani en C.D. McGillem, "A statistical model for line-of-sight (LOS) factory radio channels", IEEE, Proc. 39th Veh. Tech. Conf., pp. 496-503, 1989.
  - P. Yegani en C.D. McGillem, "A statistical model for the obstructed factory radio channels", IEEE, GLOBECOM '89, Vol. 3. pp. 1351-1355, 1989.
  - Dit proefschrift, par 4.5.
  
- 3) Het incorporeren van diffractie-effecten in een deterministisch model voor millimetergolfpropagatie binnen een gebouw leidt niet tot een wezenlijke verbetering van de modelbenadering.
  - Dit proefschrift par. 5.2.
  
- 4) Het toepassen van infra-rood voor breedbandige draadloze communicatie is uit veiligheidsoverwegingen af te raden.
  - Dit proefschrift, par. 1.3
  
- 5) De evolutie van breedbandige draadloze netwerken wordt gefrustreerd door een gebrek aan samenwerking tussen ontwikkelaars van radionetwerken en hun vakbroeders die zich toeleggen op de problematiek van service-integratie.
  - Dit proefschrift, par. 1.1.

- 6) De CCITT Recommendatie I.430, waarin de laag-1 karakteristieken van de ISDN S-bus zijn gespecificeerd, geeft onvoldoende garantie voor een aanvaardbaar risico van compromitterende uitstraling.
  - A.H.J. Norp en P.F.M. Smulders, "Effects of configuration parameters on the radiation of the ISDN S-bus", Proc. Int. Conf. on EMC, Zurich, pp. 713-718, March 1991.
  - P.F.M. Smulders, "ISDN subscriber line security", Communications International, Vol. 18, No. 6, pp. 8-10, June 1991.
  
- 7) De techniek van de zelfstoppende odometer zoals voorgesteld door L. Sallows biedt een fundamentele algoritmische structuur voor "brute-force" verificatie en verdient daarom ruimere bekendheid.
  - L. Sallows, "op zoek naar een pangram", Intermediair, 22e jaargang 6 - 7 februari, 1986
  
- 8) Het Assessment Center, de Rolls Royce onder de middelen voor personeelsselectie, is niet alleen veel duurder en tijdrovender dan de simpele intelligentietest, maar heeft ook een geringere voorspellende waarde.
  
- 9) Verslagen van spontane paranormale verschijnselen zijn ontoereikend om het werkelijke bestaan van het paranormale te bevestigen.
  
- 10) Binnen het wiskunde-onderwijs dient meer aandacht te worden besteed aan wiskundige ongelijkheden en hun toepassingen voor optimalisatieproblemen.
  
- 11) Door de wijdverbreide misvatting dat men appels niet met peren mag vergelijken worden er te veel appels en te weinig peren gegeten.